

THE UNIVERSITY OF SYDNEY

DOCTORAL THESIS

---

# An Experimental Study of Gridded and Virtual Cathode Inertial Electrostatic Confinement Fusion Systems

---

*Author:*

Richard BOWDEN-REID

*Supervisor:*

A/Prof. Joseph KHACHAN

*A thesis submitted in fulfilment of the requirements  
for the degree of Doctor of Philosophy*

*in the*

Department of Plasma Physics and Nuclear Fusion  
School of Physics

September 2019

# Declaration of Authorship

I, Richard BOWDEN-REID, declare that this thesis titled, *An Experimental Study of Gridded and Virtual Cathode Inertial Electrostatic Confinement Fusion Systems* and the work presented in it are my own. I confirm that:

- This work was done wholly or mainly while in candidature for a research degree at this University.
- Where any part of this thesis has previously been submitted for a degree or any other qualification at this University or any other institution, this has been clearly stated.
- Where I have consulted the published work of others, this is always clearly attributed.
- Where I have quoted from the work of others, the source is always given. With the exception of such quotations, this thesis is entirely my own work.
- I have acknowledged all main sources of help.
- Where the thesis is based on work done by myself jointly with others, I have made clear exactly what was done by others and what I have contributed myself.
- Sections of Chapter 3 of this thesis are published as:  
“Evidence for Surface Fusion in Inertial Electrostatic Confinement Devices” *Physics of Plasmas*, **25**, 112702, 2018, <https://doi.org/10.1063/1.5053616>

I designed the study, analysed the data and wrote the drafts of the manuscript.

Signed:

---

Date:

---

*“Fusion works. All you have to do is go outside at day time or go outside at night and look up; There are billions of fusion reactors, every star is a fusion reactor and not one of them is toroidal.”*

Robert Bussard

THE UNIVERSITY OF SYDNEY

## *Abstract*

Faculty of Science  
School of Physics

Doctor of Philosophy

### **An Experimental Study of Gridded and Virtual Cathode Inertial Electrostatic Confinement Fusion Systems**

by Richard BOWDEN-REID

Inertial electrostatic confinement (IEC) fusion is a technique that aims to use electric fields to confine and heat ions. The concept makes use of concentric electrodes to accelerate and focus ions thereby creating the conditions necessary for nuclear fusion to occur. IEC cathodes may be *mechanical*, taking the form of metallic grids or *virtual*, formed through the localisation of a net negative space charge. An experimental study has been carried out into the operation of IEC devices of both types with the view to furthering understanding as to how such devices may be implemented as net energy producing fusion reactors. The phenomenon of surface fusion in a gridded IEC was examined and the total fusion rate found to be dominated by interactions between energetic ions and neutral targets adsorbed on cathode surface. The material and temperature of the IEC cathode were found to have a profound influence on the observed fusion rate, with graphite seen to perform exceptionally well when compared to transition metal cathodes. The first example of a gridded IEC device manufactured from graphite is described. The research indicates that great improvements in the fusion efficiency of gridded IEC machines are possible through careful choice of grid material and the implementation of active cathode cooling. Also described is the design and construction, as well as initial operation of MCVC-0, a successor to previous Polywell style devices constructed at The University of Sydney. The device makes use of a biconic cusp magnetic field to confine electrons in space, thereby generating a virtual cathode. Biased and floating Langmuir probe measurements were used to examine potential well formation in the new machine, as well as diagnose the fundamental plasma parameters of temperature and density. Preliminary experimental work indicates poor performance of MCVC-0 with respect to virtual cathode formation and these shortcomings are addressed in terms of non-isotropic electrical conductivity in magnetised plasmas. The plasma conductivity model is extended to previously published virtual cathode machines and is shown to adequately describe the observed device behaviour, providing a possible alternate physical explanation for virtual cathode formation.

## *Acknowledgements*

I would like to extend my utmost thanks to all those without whom this project would not have been possible.

First and foremost to A/Prof Joe Khachan, who is the epitome of what a supervisor should be. Who, despite his sometimes crushing work load, is always able find time for his students, whether to provide assistance in the lab, advice on a problem or to proofread a thesis. I am enormously thankful that I am able to refer to Joe, not merely as a supervisor, but also as a mate.

To the CSIRO and the folks at the Queensland Centre for Advanced Technologies, John Malos, Mark Kochanek, Craig Smith and Craig James, whose support and interest in this project made possible things I had not previously imagined.

I am also extremely grateful to the extraordinarily talented staff of the School of Physics Mechanical Workshop, Michael Paterson, Terry Phieffer, James Gibson, Caleb Gudu, David Cassar, Darren Moran and Sean Devaney, each and every one of whom, at one stage or another, have provided assistance or advice on some element of this project, from helping to identify an obscure thread, to totally fabricating large, complex components of experimental apparatus. Likewise to our resident electronics gurus Wayne Peacock, Peter Axtens and Phil Dennis who were always happy and willing to assist with the design, repair or troubleshooting of any piece of electrical gadgetry, be it the smallest amplifier or the largest power supply. Gentlemen, it has been a master-class.

To my friends and colleagues, John Hedditch, Ralf Wilson, Daan Van Schijndel, Nico Ranson, Joe Builth-Williams and Adam Israel, who have each served as invaluable sounding boards and lab minions, all the while helping me perfect the art of articulating affection through insults. While our exuberant discussions (or arguments?) about physics, politics, history, sociology, psychology, engineering, the general state of the world and what to have for lunch may not necessarily be conducive to getting any work done, they do, at the very least, make the office a truly joyous place to work.

And finally to my parents David and Bronwen, and my sisters Ellen and Rebecca, for putting up with the oddity, for actively taking an interest, and for happily nodding along, even when you'd lost track of what I was rambling about. I love you all.

# Contents

<b>Declaration of Authorship</b>	<b>i</b>
<b>Abstract</b>	<b>iii</b>
<b>Acknowledgements</b>	<b>iv</b>
<b>Contents</b>	<b>v</b>
<b>1 Introduction</b>	<b>1</b>
1.1 Nuclear Fusion . . . . .	1
1.1.1 Fusion Rate and cross section . . . . .	3
1.2 Fusion Methods . . . . .	5
1.2.1 Magnetic Confinement Schemes . . . . .	5
1.2.1.1 Magnetic Mirror Confinement . . . . .	6
1.2.1.2 Cusp Confinement . . . . .	8
1.2.1.3 Toroidal Magnetic Confinement . . . . .	8
1.3 The Argument for Deuterium Fuel . . . . .	10
1.4 Inertial Electrostatic Confinement (IEC) . . . . .	11
1.4.1 Simple Energy Balance in IEC Devices . . . . .	12
1.5 Virtual Cathode IEC . . . . .	16
1.5.1 Polywell . . . . .	17
1.6 Aim of This Thesis . . . . .	20
<b>2 Experimental Apparatus</b>	<b>22</b>
2.1 Vacuum System . . . . .	22
2.2 Translational Stage . . . . .	23
2.3 Electron Gun . . . . .	23
2.4 Neutron Detection . . . . .	26
2.4.1 Analogue Count Acquisition . . . . .	26
2.4.2 Digital Count Acquisition . . . . .	27
2.4.3 Calibration . . . . .	27
2.5 Deuterium Gas Generation . . . . .	30
<b>3 Surface Fusion in IEC Devices</b>	<b>31</b>
3.1 Experimental apparatus . . . . .	33
3.2 Pressure hysteresis in IEC devices . . . . .	34

3.2.1	Experimental Method . . . . .	34
3.2.2	Results and Discussion . . . . .	36
3.3	Fusion on metal surfaces . . . . .	38
3.3.1	Experimental Method . . . . .	40
3.3.2	Results and Discussion . . . . .	40
3.4	High performance IEC Grid Based on Graphite . . . . .	45
3.4.1	Experimental Method . . . . .	46
3.4.2	Results and Discussion . . . . .	47
3.4.3	High Power Operation of Graphite IEC Grid . . . . .	48
3.4.4	Results and Discussion . . . . .	50
3.5	Summary . . . . .	52
<b>4</b>	<b>Magnetically Confined Virtual Cathode Machine (MCVC-0)</b>	<b>53</b>
4.0.1	Magnetic field coils . . . . .	54
4.0.2	Coil Cases / Electrodes . . . . .	56
4.0.3	Field Coil Sub-assembly . . . . .	57
4.0.4	Coil Terminal Contacts . . . . .	57
4.0.5	Support Frame . . . . .	57
4.1	Power Supplies . . . . .	61
4.1.1	Pulsed Capacitor Bank Power Supply (PCPS) . . . . .	61
4.1.1.1	Theoretical <i>LCR</i> circuit response . . . . .	61
4.1.1.2	Capacitor Bank Layout . . . . .	65
4.1.1.3	Capacitor Bank Control and Automation . . . . .	67
4.1.2	High Voltage Bias Power Supply . . . . .	68
4.2	Coil Temperature Monitoring . . . . .	69
4.3	Programmable Pulse Generator . . . . .	70
4.4	System Control Hierarchy . . . . .	71
<b>5</b>	<b>Langmuir Probe Diagnostic</b>	<b>74</b>
5.1	Biased Langmuir Probe Theory . . . . .	74
5.2	Langmuir Probe Construction . . . . .	76
5.2.1	High Impedance Floating Probe . . . . .	77
5.2.2	Biased Langmuir Probe . . . . .	78
5.2.3	Current Sense Amplifier Offset . . . . .	79
<b>6</b>	<b>Electro-Magnetic Fields In MCVC-0</b>	<b>82</b>
6.1	Magnetic Fields . . . . .	82
6.1.1	Simulated magnetic fields . . . . .	82
6.1.2	Eddy Currents . . . . .	84
6.1.3	EMF probe measurements . . . . .	85
6.2	Electric Potential . . . . .	88
6.2.1	Laplace Solver . . . . .	88
6.2.2	MCVC potential . . . . .	90
<b>7</b>	<b>Preliminary Plasma Studies in MCVC-0</b>	<b>92</b>
7.1	Generalised Experimental Procedure . . . . .	92
7.2	Unbiased Operation . . . . .	93
7.2.1	Spatial Variation of Plasma Parameters . . . . .	96

7.2.2	Electron Temperature from Variable Impedance Floating Probe . . . . .	101
7.3	Low Voltage Operation (500V) . . . . .	103
7.3.1	Potential Well Scaling with Magnetic Field Strength . . . . .	107
7.3.2	Off-Axis Langmuir Probe Measurements . . . . .	108
7.3.3	Validation of Floating Probe Diagnostic . . . . .	112
7.4	High Voltage Operation (1-6 kV) . . . . .	114
7.5	Summary . . . . .	118
<b>8</b>	<b>Plasma Conductivity in MCVC / Polywell Devices</b>	<b>121</b>
8.1	Laplace Equation in Anisotropic Conductive Media . . . . .	121
8.2	Anisotropic Laplace Equation in a Penning Trap . . . . .	125
8.3	Anisotropic Laplace Equation in MCVC-0 . . . . .	127
8.4	Imperfect Electrode Shielding in MCVC-0 . . . . .	129
8.5	Anisotropic Laplace Equation in Polywell Systems . . . . .	135
8.5.1	WB6-Mini . . . . .	135
8.5.2	High Energy Power Source Experiment . . . . .	139
8.6	Implications for Magnetic Virtual Cathode Machines . . . . .	140
8.6.1	Summary . . . . .	145
<b>9</b>	<b>Conclusions and Future Work</b>	<b>147</b>
<b>Bibliography</b>		<b>150</b>

# Chapter 1

## Introduction

Since the beginning of the Industrial Revolution in 1760, Human development has been driven by the consumption of fossil fuels. The mechanisation, through steam power, of major industries led to explosive increases in productivity and drove exponential population growth across the globe. Such was the rate of this growth, that the global population more than doubled in the next 150 years, from 800 million in 1750, up to 1.65 billion in 1900. Growth continued to accelerate throughout the 20<sup>th</sup> Century such that by the time of its publication in 2014 the United Nations Population Report placed global citizenship at just over 7.2 billion, with projected growth expected to reach 10 billion by the year 2050 [1]. There has been increasing concern in recent years about the long term sustainability of population growth, particularly in developing nations. Each of the major quality-of-life indices, improved water access, life expectancy, infant mortality rate, average years of schooling, electricity access and gross national product have been closely correlated with per capita energy consumption [2–4], with access to plentiful and reliable energy being identified as a leading factor in relieving extreme or chronic poverty [5]. Nations such as India and China have subsequently invested heavily in new power generation infrastructure in attempts to raise living standards for their ever growing populations.

### 1.1 Nuclear Fusion

Sources of nuclear energy provide a potential solution to the growing global demand for energy generation. When a hydrocarbon fuel is burned energy is derived from the rearrangement of chemical bonds into a new configuration. The total bond enthalpy in the initial fuel molecules is found to be marginally larger than that in the final products, and it is this change that leads to the release of excess energy during the reaction. The amount of energy released per molecule tends to be very small, however, ( $\sim 5\text{ eV}$ ) and hence millions of tonnes of fuel are required to generate the 160,000 TerraWatt hours consumed across the globe each year [6].

Reaction						%	Yield (MeV)	
$^2_1D$	+	$^3_1T$	$\rightarrow$	$^4_2He$	+	$^1_0n$	-	17.6
$^2_1D$	+	$^2_1D$	$\rightarrow$	$^3_2He$	+	$^1_0n$	50	3.27
			$\rightarrow$	$^3_1T$	+	$^1_1p$	50	4.03
$^2_1D$	+	$^3_2He$	$\rightarrow$	$^4_2He$	+	$^1_0n$	-	18.3
$^3_1T$	+	$^3_1T$	$\rightarrow$	$^4_2He$	+	$2^1_0n$	-	11.3
$^3_1T$	+	$^3_2He$	$\rightarrow$	$^4_2He$	+	$^1_0n$	+ $^1_1p$	51
			$\rightarrow$	$^4_2He$	+	$^1_0n$	+ $^1_1p$	6
			$\rightarrow$	$^4_2He$	+	$^2_1D$		43
$^1_1p$	+	$^6_3Li$	$\rightarrow$	$^4_2He$	+	$^3_2He$	-	4
$^2_1D$	+	$^6_3Li$	$\rightarrow$	$2^4_2He$			-	22.4
$^3_2He$	+	$^6_3Li$	$\rightarrow$	$2^4_2He$	+	$^1_1p$	-	16.9
$^1_1p$	+	$^{11}_5B$	$\rightarrow$	$3^4_2He$			-	8.7

TABLE 1.1: Common nuclear fusion reactions. Reproduced from [7]

Nuclear processes do not derive energy from chemical bonds, but rather from the rearrangement of protons and neutrons within the nuclei of atoms. When a heavy atom such as Uranium-235 undergoes nuclear fission, the process of splitting to form two or more lighter atoms, the total mass of the final products is smaller than that of the initial atom. This excess mass, or so called “mass defect”, is converted directly into energy according to Einstein’s famous energy-mass relation  $E = mc^2$ , resulting in the release of very large quantities of energy ( $> 1 \times 10^6$  eV) *per atom*. Nuclear reactors are therefore extremely attractive as a possible replacement for fossil fuel based energy generation. Unfortunately, due to concern about the safe storage and processing of long-lived uranium waste, as well as serious nuclear accidents as occurred in Chernobyl and Fukushima, public and political opinion has been heavily swayed away from fission based nuclear energy.

Nuclear fusion, the process by which light elements combine to form heavier ones, is also a very high yielding process and represents a possible alternative to traditional fission technologies. Fusion reactors may be fuelled by a variety of light elements such as deuterium and tritium (isotopes of hydrogen) as well as more exotic fuels like Helium-3, Lithium-6 and Boron-11. For a selection of relevant fusion reactions and their products see Table 1.1. These processes produce benign reaction products such as Helium-4, thereby eliminating the need to store large amounts of long lived radioactive waste. Unlike fission reactors which require careful monitoring in order to prevent an uncontrolled run-away reaction, fusion reactions require a constant input of driving energy to maintain. In the event of a mechanical failure within a fusion plant, the reaction will quench, removing the risk of reactor melt down. Further, the absolute quantity of

nuclear material within a fusion reactor is very small (a few grams) compared with that in a comparable fission facility ( $\sim 10\text{-}30$  Tonnes).

### 1.1.1 Fusion Rate and cross section

For any given interaction, the *cross section*,  $\sigma$ , provides a measure of the probability that the interaction will occur. The cross section results from a pseudo-classical interpretation of the atomic processes wherein target atoms are regarded as having a characteristic *area* that may be struck by another incident particle. In this way, the quantum mechanical detail of the interaction is discarded in favour of a single quantitative measure [8]. For an infinitesimal volume of area  $A$  and a depth  $\Delta x$ , containing a density of targets  $n$ , the number of target atoms is given as

$$N = nA\Delta x. \quad (1.1)$$

If the target atoms are each assigned a classical area  $\sigma$ , then the total area occluded by targets is

$$A_{occl} = n\sigma A\Delta x \quad (1.2)$$

and so the probability that an incident particle undergoes an interaction while traversing the volume is

$$p = \frac{A_{occl}}{A} = n\sigma\Delta x. \quad (1.3)$$

For a particle flux  $\Gamma(x)$  entering the slab, the emergent flux on the other side is therefore given by

$$\Gamma(x + \Delta x) = (1 - n\sigma\Delta x)\Gamma(x) \quad (1.4)$$

which may be re-arranged and integrated to give the particle flux as a function of distance according to

$$\Gamma(x) = \Gamma_0 \exp(-n\sigma x). \quad (1.5)$$

Interaction cross sections are a function of the particle collision energy and hence there exist numerous models for the computation of fusion cross sections for various reactions. Equation 1.1.1 provides an empirical form by which  $\sigma_f$  may be calculated, in units of  $\text{m}^2$ , for the most common reactions of interest [9]

$$\sigma_f(E) = 1 \times 10^{-28} \cdot \frac{A_5 + A_2 [(A_4 - A_3 E)^2 + 1]^{-1}}{E [\exp(A_1 E^{-1/2}) - 1]} \quad (1.6)$$

where  $E$  is the kinetic energy of the incident particle, in units of keV, relative to a stationary target. The coefficients  $A_1 - A_5$  are given in Table 1.2 while plots of reaction cross section are provided in Figure 1.1. An improved form of has also been developed by Bosch and Hale [10, 11]. In a two species reactor, the fusion rate per unit volume is found by integrating over

Reaction	A <sub>1</sub>	A <sub>2</sub>	A <sub>3</sub>	A <sub>4</sub>	A <sub>5</sub>
D(d,n) <sup>3</sup> He	46.097	372	$4.36 \times 10^{-4}$	1.220	0
D(d,p)T	47.88	482	$3.08 \times 10^{-4}$	1.177	0
D(t,n) <sup>4</sup> He	45.95	50200	$1.368 \times 10^{-4}$	1.076	409
D( <sup>3</sup> He,p) <sup>4</sup> He	89.27	25900	$3.98 \times 10^{-4}$	1.297	647

TABLE 1.2: Empirical coefficients for computing fusion cross sections. Reproduced from [9].

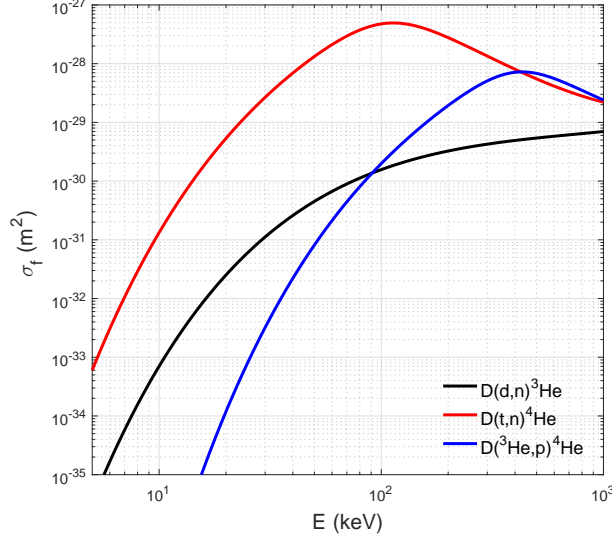
all particles in the system according to

$$\text{Rate Vol}^{-1} = n_1 n_2 \iint \vec{v}_1 \sigma_f(|\vec{v}_1 - \vec{v}_2|) f_1(\vec{v}_1) f_2(\vec{v}_2) d\vec{v}_1 d\vec{v}_2 = n_1 n_2 \langle \sigma v \rangle \quad (1.7)$$

where  $n_1, n_2$  are the densities of the two species,  $\sigma_f(v)$  is the speed dependent cross-section and  $f_1(\vec{v}_1)$  and  $f_2(\vec{v}_2)$  are the velocity distributions functions. The integral term is known as the reactivity and is often written as  $\langle \sigma v \rangle$ . In most cases  $f_{1,2}(\vec{v}_{1,2})$  are given by Maxwell-Boltzmann, or *thermal* distributions

$$f(\vec{v}) = \left( \frac{m}{2\pi k_B T} \right)^{3/2} \exp \left( -\frac{m|\vec{v}|^2}{2k_B T} \right) \quad (1.8)$$

where  $m$  is the particle mass,  $T$  is the distribution temperature and  $k_B$  is the Boltzmann constant.

FIGURE 1.1: Fusion cross sections  $\sigma_f(E)$  for selected fusion reactions given a projectile of energy  $E$ , incident upon a stationary target atom.  
Calculated according to Equation 1.1.1.

## 1.2 Fusion Methods

A substantial hurdle to nuclear fusion is the mutual repulsion of charged nuclei. In order for two nuclei to fuse they must approach each other to within  $10^{-15}$  m, the range over which the strong nuclear force operates, which for two singly charged nuclei corresponds to a coulomb barrier of approximately 1.44 MeV. Although it is not generally possible to obtain large numbers of particles at these energies, quantum tunnelling permits lower energy particles (10-200 keV) to pass through the coulomb barrier and undergo fusion. The goal is therefore to create and confine a gaseous plasma of sufficiently high temperature (100 million Kelvin) and density ( $10^{20}$  m<sup>-3</sup>) for substantial fusion to take place.

Such extreme temperatures render physical containment vessels impossible and so we are limited to confinement schemes that prevent the plasma making contact with the inner walls of the device. In electric and magnetic fields charged particles experience the *Lorentz force*, which is given by

$$\vec{F}_{Lorentz} = \underbrace{q\vec{E}}_{Electric} + \underbrace{q\vec{v} \times \vec{B}}_{Magnetic} \quad (1.9)$$

where  $\vec{E}$  and  $\vec{B}$  are the electric and magnetic fields, and  $q$  and  $v$  are the particle charge and velocity respectively. Numerous confinement schemes have been proposed that make use of either the magnetic or electric components, or some combination of the two. In the sections below we describe some of the attempted schemes and discuss the pros and cons of each.

### 1.2.1 Magnetic Confinement Schemes

Magnetic confinement devices aim to exploit the second term in the Lorentz force expression to contain fusion plasmas. The cross-product within the magnetic term means that forces are always perpendicular to the velocity of the particles, and hence charged particles will tend to prescribe spiral paths along magnetic field lines. A particle of mass  $m$  will trace a spiral with a radius of

$$r_g = \frac{mv_\perp}{q|B|} \quad (1.10)$$

where  $v_\perp$  is the velocity transverse to the field line and  $r_g$  is called the gyro-radius. If the magnitude of the magnetic field is sufficiently large that

$$r_g \ll L_{Device} \quad (1.11)$$

where  $L_{Device}$  is the characteristic scale of the fusion machine, then the particle may be confined within the device. Magnetic configurations may be “open”, where magnetic field lines are allowed to exit the trapping region, or “closed”, wherein the field lines complete loops within

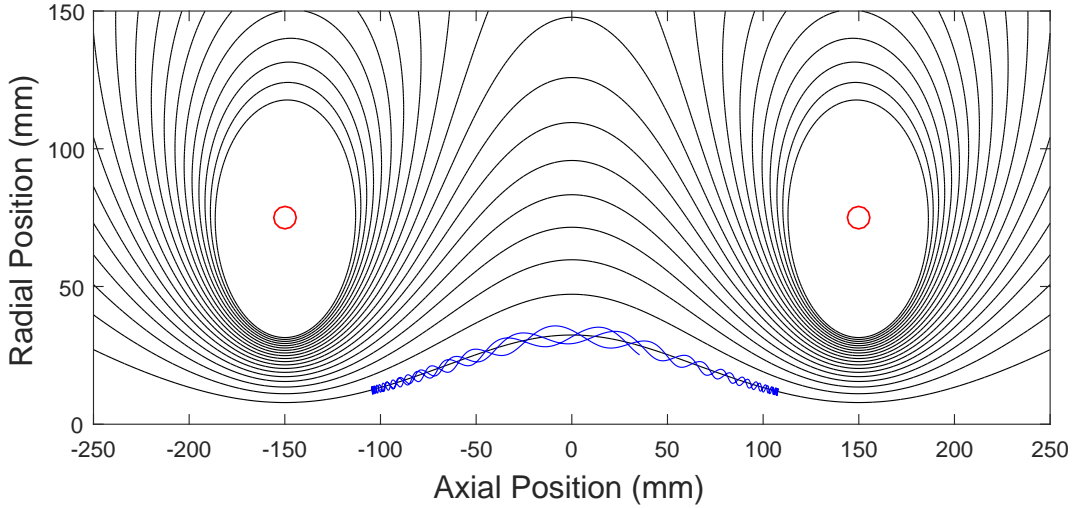


FIGURE 1.2: Magnetic field configuration in a twin coil mirror machine. Coil positions are denoted by red circles and an example electron orbit is given in blue.

the confinement volume. Cusp and Mirror machines fall into the category of open devices while Tokamaks and Stellarators are closed.

### 1.2.1.1 Magnetic Mirror Confinement

Mirror devices aim to confine plasmas by using magnetic field gradients to reflect electrically charged particles. The simplest mirror configuration is formed by a single pair of coils, coaxially aligned such that their magnetic moments point in the same direction. If the coil spacing is substantially larger than their radii then the resulting magnetic field exhibits a minimum between the two coils allowing particles to be trapped within the device. Figure 1.2 illustrates one such mirror field, including an example trajectory of a trapped electron. The electron is seen to orbit along field lines until it is reflected by one of the mirrors and returned to the core. This is called the magnetic mirror effect and may be illustrated by considering the motion of a single electron as it travels along a magnetic field line in a monotonically increasing field  $B(z)$ . If the electron velocity is initially  $v(0)$  then the conservation of kinetic energy gives

$$\frac{1}{2}m_e v^2(0) = \frac{1}{2}m_e \left( v_{\parallel}^2(z) + v_{\perp}^2(z) \right) \quad (1.12)$$

where  $v_{\parallel}$  and  $v_{\perp}$  are the velocity components parallel and perpendicular to the magnetic field respectively. The quantity  $\mu$ , given by

$$\mu = \frac{m_e v_{\perp}^2(0)}{2B(0)} = \frac{m_e v_{\perp}^2(z)}{2B(z)} = Constant \quad (1.13)$$

is called the first adiabatic invariant and is a constant of motion so long as the magnetic field varies slowly relative to the size of the electron gyro-radius,  $r_g$ . Writing  $v_{\perp}$  in terms of  $\mu$  results

in

$$\begin{aligned} v^2(0) &= v_{\parallel}^2(z) + \frac{B(z)}{B(0)} v^2(0) \sin^2(\alpha). \\ \alpha &= \tan^{-1} \left( \frac{v_{\perp}(0)}{v_{\parallel}(0)} \right) \end{aligned} \quad (1.14)$$

which becomes

$$v_{\parallel}^2(z) = v^2(0) \left[ 1 - \frac{B(z)}{B(0)} \sin^2(\alpha) \right] \quad (1.15)$$

For the electron to pass a specified point  $z$ , we require that the solutions for  $v_{\parallel}$  in Equation 1.15 are real. That is

$$1 - \frac{B(z)}{B(0)} \sin^2(\alpha) > 0 \quad (1.16)$$

or

$$\sin^2(\alpha) < \frac{B(0)}{B(z)} = R_m \quad (1.17)$$

which is called the mirror ratio. The value of  $\alpha$  for which Equation 1.15 is equal to zero is called the *loss cone angle* and describes the boundary in  $(v_{\parallel}, v_{\perp})$  space between particles that are reflected and transmitted by the magnetic field. The loss cone may never be completely closed, as this requires an infinite magnetic field strength  $B(z)$ . Mirror devices therefore exhibit a persistent, non-zero flux of particles being lost from the trapping volume as collisions continually scatter particles into the loss region. A review of magnetic confinement by Post [12] describes the multitude of configurations devised in attempts to reduce losses from mirror machines. The tandem mirror and thermal barrier configurations in particular aimed to limit particle losses by adding a pair of smaller bottles at the ends of the main confinement volume wherein higher density plasmas could be generated. By carefully controlling the relative electron and ion densities in the end regions it is possible to generate electric fields which serve to *plug* the openings in the main mirror, increasing plasma confinement, in some cases by over an order of magnitude.

Electrostatic plugging through the use of focusing electrodes has also been proposed, with Dolan [13] providing an in depth review. The principle behind electrostatic plugging may be illustrated through re-examination of the mirror ratio, this time inclusive of a monotonic electrostatic potential  $\Phi(z)$ . The conservation of energy expression then becomes

$$\frac{1}{2} m_e v^2(0) - e\Phi(0) = \frac{1}{2} m_e (v_{\perp}^2(z) + v_{\parallel}^2(z)) - e\Phi(z) \quad (1.18)$$

which, using the same approach as previous, gives

$$v_{\parallel}^2(z) = v^2(0) \left( 1 - \frac{B(z)}{B(0)} \sin^2(\alpha) \right) + \frac{2e}{m_e} (\Phi(z) - \Phi(0)) \quad (1.19)$$

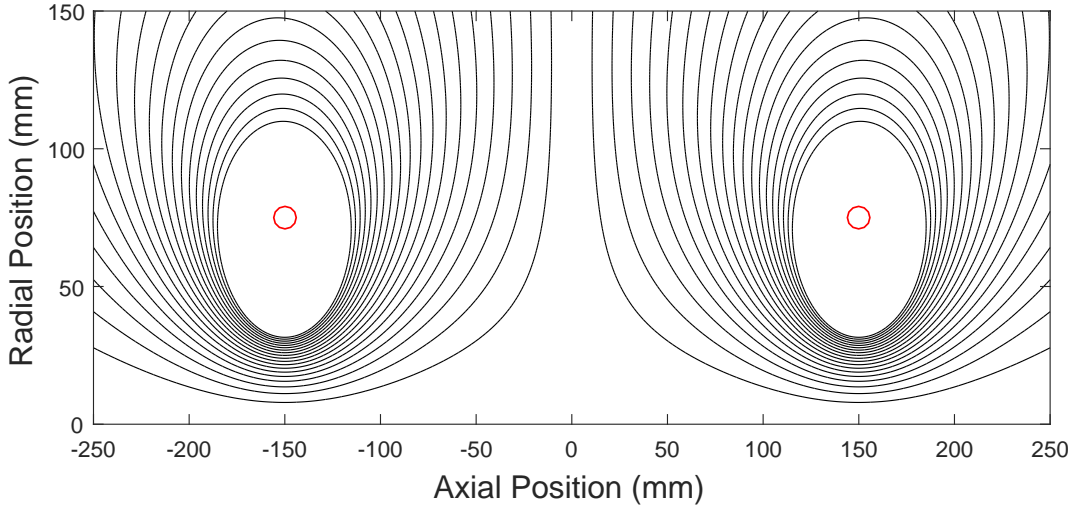


FIGURE 1.3: Magnetic field configuration in a biconic cusp.

$$\sin^2(\alpha) < R_m \left[ 1 + \frac{2e}{m_e v^2(0)} (\Phi(z) - \Phi(0)) \right] \quad (1.20)$$

This corrected value of  $R_m$  contains additional forcing terms that depend on  $\Phi$  and it is therefore possible to find values of  $\Phi$  for which Equation 1.20 has no solution. When the expression on the right hand side of Equation 1.20 is less than zero the loss cone is closed completely, eliminating particle losses. When the right hand side is greater than one the magnetic mirror ceases to function and all particles are lost. Electrostatic approaches of this type are naturally limited as an electric field that is confining for electrons will naturally promote the loss of ions and vice-versa.

### 1.2.1.2 Cusp Confinement

An alternative arrangement to the magnetic bottle is the magnetic cusp, produced by inverting one of the coils shown in Figure 1.2 such that like magnetic poles face each other, as shown in Figure 1.3. The resulting configuration has a point of zero magnetic field, or a *magnetic null*, in the central region where the field contributions due to the two coils cancel out. Although the cusped field exhibits enhanced magneto-hydrodynamic stability over mirror configurations, the large cylindrical loss surface in the equatorial plane of the device, coupled with the randomisation of the magnetic moment each time a particle transits the null region, means that the particle confinement times in cusped fields are greatly reduced [14–17].

### 1.2.1.3 Toroidal Magnetic Confinement

By far the most ubiquitous fusion device globally is the toroidal magnetic confinement machine, or Tokamak, wherein a circular array of coils generates a closed loop magnetic field and a

toroidal confinement volume. Particles spiralling along field lines are able to continually orbit the device, thereby eliminating the losses typical of open field systems. The magneto-hydrodynamic stability of the torus configuration is further improved through the addition of a poloidal field, which may be generated by the plasma current circulating in the machine. Additional smaller coils permit control over the shape and position of the plasma within the device. Tokamaks represent the most advanced pathway towards a net energy fusion machine, with confinement of high temperature plasmas ( $>100$  million degrees) achieved over long times scales (1-10 seconds). At the time of writing, the world record for the highest fusion power ever generated is 16.1 MW, held by the Joint European Torus (JET), corresponding to an energy gain of  $Q = 0.67$  [18]. The Japanese tokamak JT-60 produced plasma conditions equivalent to  $Q = 1.25$  for a 50:50 deuterium-tritium fuel mixture, however as this result has been extrapolated from deuterium-deuterium fusion experiments it remains theoretical [19]. The International Thermonuclear Experimental Reactor (ITER) currently under construction in France is projected to operate at a fusion gain of  $Q \approx 10$ , generating  $\sim 500$  MW of fusion power from only 50 MW of heating power. It is hoped that the success of the ITER project will lead to the eventual construction of DEMO, a demonstration tokamak power plant [20].

Advances in Tokamak technology have been tempered however, by the discovery of numerous plasma instabilities and anomalous particle loss mechanisms. One such loss is associated with particle drift transverse to magnetic field lines. When a particle moving in a magnetic field is acted on by a second force  $\vec{F}$ , it will undergo a drift motion in a direction that is orthogonal to both the magnetic field and the applied force. The drift velocity is given by

$$\vec{V}_D = \frac{1}{q} \frac{\vec{F} \times \vec{B}}{||\vec{B}||^2} \quad (1.21)$$

where  $q$  is the particle's charge, and may result from electric and gravitational forces, but also pressure differentials within the plasma as well as gradients and curvature in the magnetic field [21, 22]. The so called curvature and grad-B ( $\nabla \vec{B}$ ) drifts present particular challenges for tokamaks, as the tight, circular paths transcribed by field lines result in large drift fluxes of particles outwards toward the chamber walls. This has resulted in continual growth in the size of new machines, such that the ITER vacuum vessel will be nearly 20 metres in diameter and 12 metres tall. While tokamaks will almost certainly constitute the first generation of energy producing fusion reactors, it remains to be seen whether machines of such scale will ever be economically viable.

### 1.3 The Argument for Deuterium Fuel

It may be seen in Figure 1.1 that the reaction between deuterium and tritium exhibits reactivities,  $\langle \sigma v \rangle$  that are, in general, many orders of magnitude larger than the D-D and D-He3 alternatives. It is for this reason that the majority of modern fusion approaches, such as those discussed above, have focused on the D-T reaction as a potential energy source [8]. The need for tritium fuel however, makes this process unattractive.

Tritium is a short-lived, synthetic isotope of hydrogen with a decay half life of just over 12.3 years [23, 24]. The material poses a radiological hazard, not simply due to the potential for leaks, but also due to the high degree of retention in fusion systems, which renders devices highly radioactive [25]. Due to its short half life, tritium must be manufactured continually in order to keep a fusion reactor fuelled. Tritium breeding has therefore been proposed, whereby lithium metal blankets are applied to the walls of fusion devices and tritium is generated through nuclear reactions between the lithium atoms and the emerging fusion neutrons:



In order for the fusion reaction to be self sustaining, the breeding blankets must give a tritium breeding ratio (TBR) of greater than unity

$$TBR = \frac{\text{Tritium Production Rate}}{\text{Tritium Consumption Rate}} > 1 \quad (1.23)$$

and while breeding simulations show that this condition is possible, variations due to the selected nuclear data libraries introduce large uncertainties into the findings [26–30]. Subsequently, tritium breeding technologies have yet to be experimentally validated. Prior to reactor start-up an initial tritium inventory of several kilograms is required from other sources. Tritium is currently sourced from heavy water uranium reactors in Canada and South Korea, which together account for approximately 4 kg of tritium produced per year. However many of these facilities are ageing such that, without substantial investment in new generation, the global tritium stockpile is likely to peak at  $\sim 60$  kg some time in the early 2020's. With the time-line of large scale fusion projects such as ITER and DEMO encountering extensive delays [20] the tritium inventories available to start these devices is in question [31]. Tritium free or tritium lean start-up profiles have been suggested as a means to circumvent limited inventories, however these approaches significantly lengthen commissioning times of new reactors [32, 33].

Deuterium, by contrast, is a vastly abundant element accounting for approximately 0.0156% of oceanic hydrogen. A single kilogram of seawater therefore contains enough potential fusion energy to replace far larger quantities of fossil or hydrocarbon based fuels. Table 1.3 compares

Fuel	Energy Density MJ per kg	Mass Equivalent to 1kg Water (kg)	Mass Equivalent to 1kg D <sub>2</sub> gas (kg)
Water (D)	1970		
Deuterium Gas	$6.0 \times 10^7$		
Coal	24	82	$2.5 \times 10^6$
natural gas	55.5	35	$1.1 \times 10^6$
Gasoline (petrol)	44.4	44	$1.4 \times 10^6$
Diesel	48	41	$1.3 \times 10^6$
LPG	46.4	42	$1.3 \times 10^6$
Ethanol fuel (E100)	26.4	75	$3.3 \times 10^6$
Methanol fuel (M100)	19.7	100	$3.0 \times 10^6$
Uranium (in breeder)	$8.02 \times 10^7$	$2.5 \times 10^{-5}$	0.75

TABLE 1.3: Energy density of common fuels compared to Deuterium

the energy content of 1 kg each of sea water and refined deuterium gas against several commonly used chemical fuels. The above calculations have only taken into account fusion energy that is derived from deuterium-deuterium reactions, with subsequent burn-up of the generated tritium and helium-3 being neglected. Earth's oceans, which exceed 1.3 billion cubic kilometres, represent some  $2.2 \times 10^{13}$  kg of deuterium, a reservoir of stored energy unsurpassed by any other. With deuterium enrichment and isolation technologies well established and capable of operating at an industrial scale [34], the development of a fusion technology able to harness this reserve, without the need for auxiliary support in the form of tritium generation will vastly simplify the transition to a fusion based energy economy.

## 1.4 Inertial Electrostatic Confinement (IEC)

Inertial electrostatic confinement (IEC) fusion offers an alternative approach to magnetic confinement, opting instead to exploit the electric component of the Lorentz force. First proposed by Oleg Lavrent'ev in 1950 [35–38], the approach aims to contain and heat fusion plasma within a spherically symmetric electric field, and in this way mimic the radial gravitational well present in stars. Lavrent'ev conceived of a device in which a quasi-spherical wire grid was biased at a large negative voltage relative to the enclosing vacuum chamber or, in some cases, a second gridded anode. Positive ions generated in the inter-electrode gap are accelerated by the strong electric fields and are focused into a dense fusion region at the core of the inner grid. Although Lavrent'ev's machine was never built in the Soviet Union, American inventor Philo Farnsworth independently devised and tested a similar device [39]. Robert Hirsch and Gene Meeks, working under Farnsworth, also successfully demonstrated a small scale electric fusion device based on Lavrent'ev's concept [40–42]. The Hirsch and Farnsworth devices, so called *fusors*, are depicted in Figure 1.4.

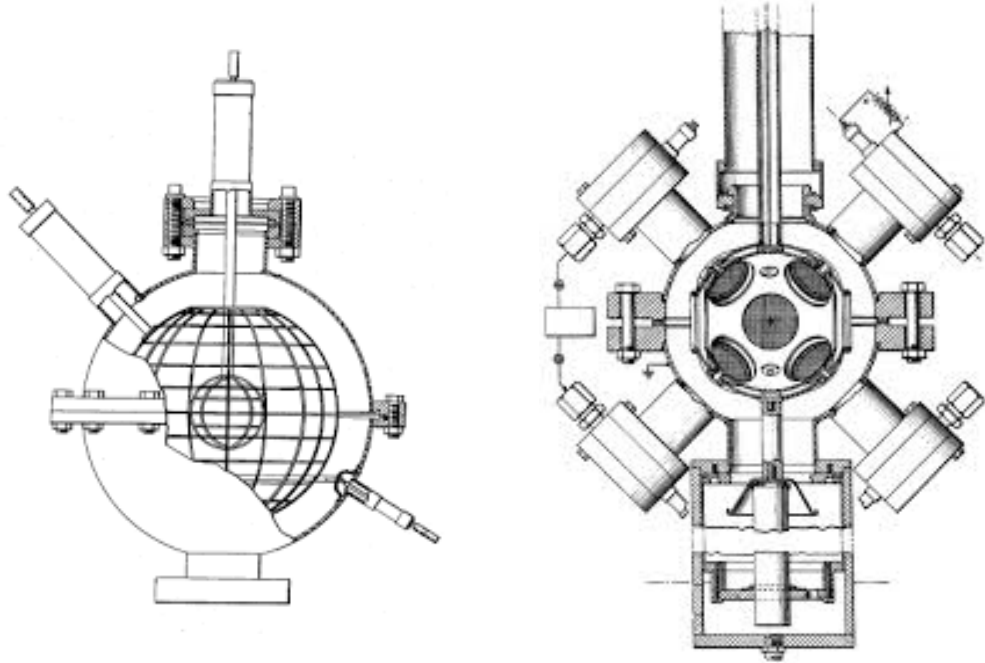


FIGURE 1.4: Inertial electrostatic confinement devices as constructed by Robert Hirsch and Gene Meeks [42] (Left) and Philo Farnsworth [39] (Right)

Obtaining nuclear fusion in an IEC device is almost trivial when compared to standard, thermonuclear style devices. This is due to the ease with which high energy ions (25 - 100 kV) may be obtained simply by increasing the applied system voltage. Small scale, deuterium fuelled machines routinely achieve neutron production rates of  $10^6 - 10^8 \text{ s}^{-1}$  in steady state operation and hence a great many IEC systems have been operated in the United States [43–49], Japan [50–54], Australia [55–58], Germany [59], the Netherlands [60], Iran [61–63] and Turkey [64].

#### 1.4.1 Simple Energy Balance in IEC Devices

Grid transparency represents an important problem in the study of IEC devices, as ion losses to the cathode constitute the largest energy loss within the system. Hirsch [65] used a simple statistical model to estimate an upper bound on the number of ions recirculating after  $k$  transits of the device core: Letting  $\eta \in (0, 1)$  be the transparency of the gridded cathode, that is the probability that an ion will survive a crossing with the grid without being collected, then we may write down an expression for the recirculating ion current  $I_r$  in terms of the collected current  $I_c$  as

$$I_r = [\eta + \eta^3 + \eta^5 + \dots + \eta^{(2k+1)}] I_c. \quad (1.24)$$

Taking the infinite limit of the geometric series gives the recirculation factor  $\delta$  as

$$\delta = \frac{I_r}{I_c} = \frac{\eta}{1 - \eta^2}. \quad (1.25)$$

Evaluating Equation 1.25 for  $\eta = 0.98$ , a practical upper limit on grid transparency, gives  $\delta \approx 25$ . Even in an idealised system, where all ion scattering mechanisms are neglected, it is nonetheless expected that an average ion will complete no more than 25 transits of the core before being collected on the grid. It is possible to extend Hirsch's approach in order to obtain limits on other device parameters, such as operating voltage and core density, required to derive net energy from such a device.

Consider a single ion incident on a focused sphere of plasma, with diameter  $d$ , present at the core of an IEC device. The probability that the ion undergoes fusion while traversing the core is given by Equation 1.3 as

$$p = n\sigma_f d. \quad (1.26)$$

In general the interaction probability is given more completely through rearrangement of Equation 1.5, however due to the extremely small magnitude of fusion cross sections ( $< 10^{-28} \text{ m}^2$ ) the use of the first order approximation in this case is appropriate. Assuming that the ion originates outside of the cathode, then we may therefore write down the probability that the ion fuses on its  $k^{\text{th}}$  transit of the core as

$$\mathcal{P}(k) = p\eta^{(2k-1)}(1-p)^{(k-1)} \quad (1.27)$$

The total probability that the ion will fuse before being lost is therefore

$$\mathcal{P}(k : 1 \rightarrow \infty) = \sum_{k=1}^{\infty} p\eta^{(2k-1)}(1-p)^{(k-1)} \quad (1.28)$$

$$\mathcal{P}_f = \frac{p\eta}{1 - \eta^2(1-p)} \quad (1.29)$$

In order to obtain net fusion power we require the energy released by the fusing ions to exceed that carried away by those ions striking the grid. That is

$$\mathcal{P}_f \left( \frac{1}{2}E_f - Z\Phi \right) - \left( 1 - \mathcal{P}_f \right) Z\Phi > 0 \quad (1.30)$$

where  $E_f$  is the energy released per fusion event and  $Z\Phi$  is the kinetic energy carried by an ion with charge  $Z$  accelerated through the potential difference  $\Phi$ . Both quantities are expressed in electron volts. As fusion events involves two particles, each ion only contributes  $E_f/2$  to the derived energy. Combining Equations 1.29 and 1.30 yields a break-even condition in terms of grid transparency  $\eta$  and the ion area density in the core  $\chi = nd$ :

$$\frac{\chi\eta\sigma_f}{1 - \eta^2(1 - \chi\sigma_f)} - \frac{2Z\Phi}{E_f} > 0. \quad (1.31)$$

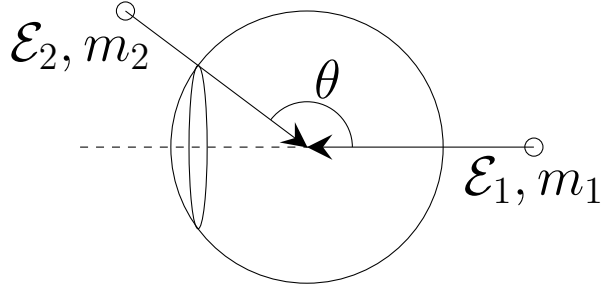


FIGURE 1.5: Two particle collision at the centre of an IEC device

Solving the boundary line for which Equation 1.31 equals 0 gives the minimum required area density for a given grid transparency as

$$\chi = \frac{\mathcal{R}(1 - \eta^2)}{\sigma\eta(1 - \mathcal{R}\eta)} \quad (1.32)$$

where

$$\mathcal{R} = \frac{2Z\Phi}{E_f} \quad (1.33)$$

In the idealised IEC system the core region comprises particles with isotropically converging velocity vectors and so computation of the effective fusion cross-section  $\sigma_{Eff}(E)$  involves averaging over all possible collision angles. As the expressions for fusion cross section described in Section 1.1.1 are those of an energetic particle incident on a stationary target, it is first necessary to compute the equivalent beam-target energy for two particles colliding at an arbitrary angle as shown in Figure 1.5. For two particles of masses  $m_1$  and  $m_2$ , and total energies  $\mathcal{E}_1$  and  $\mathcal{E}_2$ , colliding at an angle  $\theta$ , the collision energy in the centre of mass reference frame is given, in natural units, by

$$\mathcal{E}_{CoM} = [m_1^2 + m_2^2 + 2\mathcal{E}_1\mathcal{E}_2 - 2|\vec{p}_1||\vec{p}_2|\cos(\theta)]^{\frac{1}{2}} \quad (1.34)$$

where  $|\vec{p}|^2 = (\mathcal{E}^2 - m^2)$  and  $\mathcal{E} = E + m$ ,  $\vec{p}$  is the particle momentum,  $E$  is the kinetic energy, and all quantities  $m, p, E, \mathcal{E}$  are in electron volts. Moving to the lab frame, where particle 1 is incident on a stationary particle 2 ( $\mathcal{E}_2 = m_2$ ,  $|\vec{p}_2| = 0$ ) with energy  $\mathcal{E}_{1,lab}$ , the centre of mass energy reduces to

$$\mathcal{E}_{CoM} = [m_1^2 + m_2^2 + 2m_2\mathcal{E}_{1,lab}]^{\frac{1}{2}}. \quad (1.35)$$

For the two particle collision we may therefore write down the equivalent lab frame kinetic energy of a beam-like particle incident on a stationary target by equating the energies in the centre of mass frame:

$$E_{1,lab} = \frac{2\mathcal{E}_1\mathcal{E}_2 - 2(\mathcal{E}_1^2 - m_1^2)^{\frac{1}{2}}(\mathcal{E}_2^2 - m_2^2)^{\frac{1}{2}}\cos(\theta)}{2m_2} - m_1. \quad (1.36)$$

Using Equation 1.36 and the expressions in Section 1.1.1, we may write the effective, angle

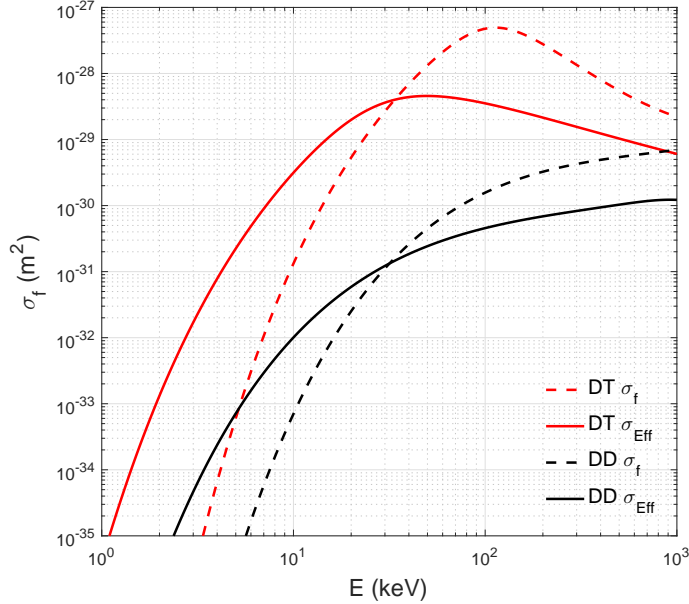


FIGURE 1.6: Beam-target and angle averaged, effective fusion cross sections as a function of particle energy. Dashed lines give cross sections for standard beam-target systems while solid lines give the corrected cross sections for the isotropically convergent ion focus.

averaged cross section for particles of uniform kinetic energy  $E = Z\Phi$  colliding in the core of an IEC device as

$$\sigma_{Eff} = \frac{1}{4\pi} \int_0^{2\pi} \int_0^\pi \sigma_f(E_{1,lab}) \sin(\theta) d\theta d\varphi \quad (1.37)$$

Numerical integration of Equation 1.37 yields the revised energy / cross section curves for the deuterium-deuterium and deuterium-tritium fusion reactions as given in Figure 1.6.

As expected, the adjusted fusion cross section in the isotropically convergent system displays a significant enhancement over the beam-target system at lower operating voltages ( $< 30$  kV). The values of  $\sigma_{Eff}$  were used to compute the break-even contours of Equation 1.31 and therefore establish minimum required core densities for energy generation at varying cathode voltages and transparencies. The results are given in Figure 1.7.

It is readily apparent that for all practically achievable grid transparencies,  $0.8 < \eta < 0.98$ , the minimum required density is unattainably high. For an  $\eta = 0.999$ , deuterium-tritium fuelled system, the required area density of targets is greater than  $2 \times 10^{23} \text{ m}^{-2}$ . Using the definition of  $\chi = nd$  we see that even with a focus region *one meter* in diameter, the ion density must exceed  $2 \times 10^{23} \text{ m}^{-3}$ , over three orders of magnitude greater than those currently obtained in thermonuclear devices. If we assume a D-T fuelled device with a 1 m core, operating at a typical Tokamak density of  $1 \times 10^{20} \text{ m}^{-3}$  with an applied accelerating voltage of 30 kV (corresponding to the minimum in the D-T break-even curve) then the required grid transparency for net energy operation is computed as  $\eta = 0.9999996$ . Such a grid may not be made from commonly used materials such as tungsten and rhenium, and this has led to the proposed use of magnetic fields

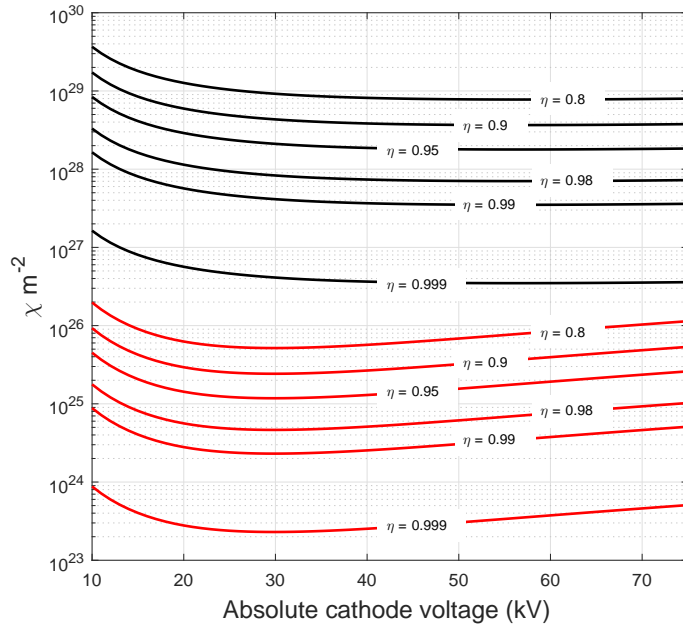


FIGURE 1.7: Break even contours for the deuterium-deuterium (black) and deuterium-tritium (red) fusion reactions. Contours are labelled with the corresponding cathode transparency.

to artificially enhance grid transparency [37, 38, 66] as well as the use of carbon nanotubes in the preparation of atomically thin grid wires [67].

The above results were calculated using a highly idealised model of the IEC system. We have assumed that all ions undergo collisions at energies equivalent to the accelerating cathode voltage and that deleterious effects such as ion scattering and charge exchange are absent. Finally, the energy balance does not include that energy which is carried away by electrons leaving the potential well, nor does it account for secondary electrons emitted from the grid. Despite this, the computed requirements on grid transparency and core density do not appear to be practically attainable and we therefore conclude that the canonical IEC device is unlikely to function as a net energy system. The devices instead find use as small scale neutron generators for the production of medical isotopes, neutron imaging and security applications. [47, 68–70].

## 1.5 Virtual Cathode IEC

In the previous section we demonstrated the difficulties presented by the use of a mechanical gridded electrodes. An alternative approach aims to replace the cathode with a *virtual* one, formed through the confinement of electrons in space [65, 71–73]. Specifically, applying a positive bias to the inner grid of the Hirsch-Farnsworth style fusor results in a central focus of electrons and a potential well is formed between the anode grid and the electron-rich core. Although relatively deep potential wells have been formed and significant ion heating obtained in this

way [74–78] the concept suffers from the same pathology as the fusor configuration; namely that energy losses to the grid wires are unacceptably high.

### 1.5.1 Polywell

The Polyhedral Well machine, or Polywell, is a hybrid electromagnetic device that was devised with the view to alleviate the shortcomings of gridded fusor and virtual cathode systems [79, 80]. Invented by Robert Bussard [81, 82], the device makes use of magnetic cusp trapping to confine a dense population of electrons, thereby generating a virtual cathode. The requirement that only electrons need be magnetically confined relaxes the design requirements on such a trap, in terms of both size and magnetic field strength, when compared with conventional thermonuclear machines. Further, the absence of grid electrodes enables a higher degree of ion recirculation within the core and hence the probability of fusion for any given ion is greatly improved.

Bussard described a device in which magnetic field coils are positioned on the faces of a regular polyhedron, most commonly a cube. The coils are oriented such that their magnetic moments point inwards, resulting in a high order multipole cusp with a central magnetic null. High energy electrons are injected into the core from electron guns stationed outside of the magnet coils and the resulting build up of negative space charge produces the desired virtual cathode, or “potential well”. Bussard reasoned that if the kinetic plasma pressure within the device could be made to approach the magnetic pressure, that is if

$$\beta = \frac{P_{\text{plasma}}}{P_{\text{magnetic}}} = \frac{nk_B T}{B^2 / 2\mu_0} \rightarrow 1 \quad (1.38)$$

then the diamagnetic circulation of electrons about magnetic field lines would serve to expel the applied field from the core. This “high beta” mode, sometimes referred to as the “wiffle ball” after the popular American children’s toy, was expected to exhibit the favourable particle trapping properties first described by Grad and Berkowitz [14, 15] leading to a sharp increase in device performance once the high beta mode was obtained. The majority of Polywell research has been conducted by the Energy Matter Conversion Corporation (EMC2) in the United States [87], which constructed and tested numerous Polywell devices between 1989 and 2015. Unfortunately, due to a policy on non-disclosure and intellectual property protection, very limited detail has been made available with regards to the technical features of their machines or the outcomes of experimental studies. Table 1.4 provides a summary of what is known about EMC2’s various machines. The “High Energy Power Source” experiment (HEPS) constructed in 1989-1990 by Directed Technologies Inc. (DTI) is the first known experimental Polywell. The device consisted of six,  $\sim 1.8$  metre diameter coils arranged around a cubic vacuum chamber, with multiple high current (20 A) electron guns used to inject electrons into the core. HEPS displayed promising performance, generating a potential well of  $\sim 8\text{-}9$  kV, approximately 80% of the injected electron

Device	Operational	$R_{coil}$ (cm)	$B_{cusp}$ (T)	$E_{inj}$ (keV)	$I_{inj}$ (A)	Notes
HEPS	1989	94	0.35	15	5-20	[83]
WB1	1994	5	0.08	1-2	4-5	Permanent magnets
WB2	1994-1996	10	0.13	1-2	1-4	Achieved $\beta = 1$ Air / Argon plasmas
WB3	1998-2000	10	0.24	15	3	Scaled up WB2 2.45GHz ECR heating
WB4	2003	15	0.5	15-30	2-4	D-D fusion reported $1 \times 10^4 \text{ s}^{-1}$ 2.45GHz ECR heating
PZLx-1	2003-2004	3	3.5	15	10-100	MHD stability tests
WB5	2005	-	-	-	-	-
WB6	2005	15	0.13	12.5	40	D-D fusion - $1 \times 10^9 \text{ s}^{-1}$ Coil cases conformal to $\vec{B}$ Device destroyed by arcing
WB7	2008	-	-	15	40-50	D-D fusion $(1 - 6) \times 10^5 \text{ s}^{-1}$
WB8	2010	-	>0.2	-	80	No connections between coils 500A arc source for initialisation 1MW neutral beam injection
High- $\beta$ Cusp	2011-2013	6.9	0.06-0.2	7	1-3	Wiffle Ball mode confirmation 700MW carbon plasma injection Displayed enhanced electron trapping in high $\beta$ mode [84]

TABLE 1.4: Summary of DTI and EMC2 Polywell machines. Where known, the coil radii, magnetic field strength and injected electron energy and current are given [83-86].

energy, however the machine lacked sufficient input power and the electron loss rate proved to be unacceptably high as magnetic field lines channelled electrons into the vacuum chamber wall [83]. EMC2 subsequently built several generations of smaller machines (WB1 - WB8) wherein the cubic array of coils resided within the vacuum system. Detail about these devices is primarily sourced from Robert Bussard's *Google Tech Talk*, given in 2006 [85]. Increasing system voltage and input power with each generation culminated in a deuterium-deuterium fusion rate of  $\sim 1 \times 10^4 \text{ s}^{-1}$  in WB4, though this result was observed only a handful of times at the end of the machine's life. A feature of the earliest generations of Polywells however was the use of square profile field coils in the generation of the magnetic field. As a result, large numbers of magnetic field lines intersected the corners of the biased Polywell coils leading to an unacceptably high electron loss rate. The sixth generation, WB-6 Polywell aimed to mitigate this effect through the implementation of "magnetic insulation", or "magnetic shielding", wherein the surfaces of the field coil cases are constructed such that they are everywhere conformal to the magnetic field. Particle losses must therefore occur in a direction perpendicular to the field and are greatly reduced. A fusion rate of  $\sim 1 \times 10^9 \text{ s}^{-1}$  was obtained in WB6, though the single observation coincided with the destruction of the machine through arcing of the coil power

supply and hence is likely spurious. The WB7 machine however, generated repeatable fusion rates of  $\sim 1 - 6 \times 10^5 \text{ s}^{-1}$ . Although the coils of WB6 and WB7 were magnetically shielded, the tube sections joining the coils together were not. These final loss surfaces were removed in the construction of WB8 in which each magnetic field coil was supported separately on struts from the vacuum chamber wall. No reported fusion results were found for the WB8 system. The most recent machine built by EMC2 aimed to confirm enhanced electron trapping in the high beta, wiffle ball mode. Earlier devices operated at insufficient power to obtain a dense, high beta plasma, and so a much smaller device was designed. Park successfully demonstrated the high beta effect in 2013 [84], though the measurement necessitated the use of 700 MW carbon plasma injectors in order to obtain a plasma of sufficient density.

A number of low beta polywell devices have also been operated at The University of Sydney (USYD) [88–94]. The work has been principally concerned with the phenomenon of potential well formation and characterisation of the electron trapping properties of the Polywell field configuration. A summary of the USYD devices is given in Table 1.5. The first USYD Polywell, constructed by Carr, consisted of teflon reels fastened together by aluminium brackets [88]. Electrons were injected using a hollow cathode style electron gun [95] and floating Langmuir probe measurements showed 100-200 V potential wells over a broad range of background gas pressures. Carr subsequently upgraded his machine in the image of WB6, using toroidal aluminium coil cases that were conformal to the magnetic field. The resulting machine, christened by Carr as WB6-Mini, operated at lower voltages than its predecessor ( $\sim$ 100-200 V) but produced potential wells of comparable relative depth ( $\sim$ 10-20 V). Carr also used biased Langmuir probe measurements to characterise the energies of the trapped electrons and proposed a novel energy distribution function [90]. Cornish [92, 93] conducted a survey of scaling laws within the Polywell, with particular consideration given to the dependence of virtual cathode formation on the size and spacing of the magnetic field coils. Finally, Studies conducted by Ren and Poznic examined electron density and energy distributions in a larger device using both biased Langmuir probe and radio frequency plasma wave techniques [94].

Further to experimental programs by EMC2 and USYD a number of computational studies have also been conducted using single particle orbital theory and particle-in-a-cell (PIC) methods. Potential well formation has been simulated by Kazemyzade et.al. [96] and the dependence on magnetic field strength examined. Gummersall [97] used single particle trajectories to derive scaling laws for electron confinement in terms of device dimensions, coil current and electron energy. The phenomenon of electron recirculation, wherein an electron that escapes from the Polywell travels along a field line and returns to the core, was also examined. Electron confinement time was similarly studied by Kollasch et.al. [98] through solution of the Laplace-Poisson equation. The work has an advantage over single particle simulation in that the results include electron induced electric fields. Finally, Rogers has conducted numerous PIC studies with the

Device	$R_{coil}$ (cm)	$B_{cusp}$ (T)	$E_{inj}$ (KeV)	$I_{inj}$ (mA)	Notes
Carr-1	2.5	0.38	15	1-5	Teflon coil Polywell Floating potential measurements Pressure Studies [88]
WB6-Mini	2.5	0.38	0.1-0.2	1-7	Electron energy distribution studies Electron trapping experiments [90]
Cornish-1	2.5-5	0.1-1.7	1	10-700	Polywell scaling laws Coil size Coil spacing [92]
Ren-1	9	0.065	0.5-2	10-100	Potential well studies Electron energy distribution studies [94]
MVCV-0	7.6	1	0.1-6	150	This Work

TABLE 1.5: Summary of Polywell machines built and operated at The University of Sydney.  
[88–94].

view to designing a break even Polywell reactor, particularly those that operate using exotic fuel mixtures [99–102].

## 1.6 Aim of This Thesis

The aim of this thesis is to detail research conducted into the operation of inertial electrostatic confinement devices, in both gridded and magnetic virtual cathode configurations. Our goal is that by further understanding the mechanisms of operation of these devices we may eventually come to realise a reactor that, when fuelled with deuterium gas, generates net fusion energy. In Chapter 2 we outline elements of the apparatus used throughout our studies, including the vacuum vessel, electron sources and fusion neutron detection techniques. Our first experimental work is discussed in Chapter 3, in which we explore the fusion performance of gridded IEC systems, with particular attention paid to the dependence on operating pressure and cathode material. The contribution to the fusion rate due to ion-neutral interactions on cathode surfaces is studied and found to be the dominant source in low power systems. The first known example of an IEC grid manufacture from graphite is also described. In Chapter 4 we detail the design and construction of the *Magnetically Confined Virtual Cathode* machine, MCVC-0, a successor to the Carr [91] and Cornish [93] Polywells, and in Chapter 5 we describe the floating and biased Langmuir probe diagnostics used to characterise the MCVC-0 plasma. In Chapter 6 the electric and magnetic field configurations within the new device are characterised and in Chapter 7

some preliminary experimental studies into the electric potential profiles within MCVC-0 are presented. Finally in Chapter 8 we review the results of the MCVC-0 study with reference to non-isotropic conductivity in plasma discharges. The theoretical framework is subsequently extended to some previously published Polywell experiments and the potential future of magnetic virtual cathode devices explored.

# Chapter 2

## Experimental Apparatus

The experimental work described in this thesis may be divided into two separate studies; The first relating to traditional gridded IEC systems and the second a novel magnetically confined virtual cathode machine. In this chapter we provide details about the elements of the experimental apparatus that are relevant to both projects. Discussion of those components specific to each of the projects will be given in later chapters.

### 2.1 Vacuum System

All experiments were conducted in a cylindrical, stainless steel chamber approximately 300 mm in diameter and height. Power and diagnostic feed-throughs accessed the chamber by way of vacuum ports about the circumference ( $4 \times \text{CF}2.75''$ ,  $4 \times \text{CF}1.33''$ ,  $1 \times \text{KF}50$ ), as well as the top and bottom end plates ( $1 \times \text{CF}2.75''$ ,  $2 \times \text{ISO}-63$ ). The chamber was evacuated by a Pfeiffer, THP330 turbo molecular pump with an Alcatel 2020 rotary vane pump operating as backing pump. The system routinely reached  $1 \times 10^{-6}$  Torr after less than 24 hrs pumping time. A glass fibre insulation blanket and 1 kW heating tape were used to bake the chamber to 165 °C thereby expelling adsorbed atmospheric water from the steel surfaces. A Varian,  $20 \text{ L s}^{-1}$  sputtering ion pump provided additional pumping at low pressures and resulted in an ultimate system pressure of  $1 \times 10^{-7}$  Torr. System pressure was monitored by way of a Pfeiffer PKR251 compact Pirani-Penning gauge in the range of  $1 \times 10^{-1} - 1 \times 10^{-6}$  Torr, while a Bayard-Alpert hot cathode gauge was used in the sub  $1 \times 10^{-6}$  Torr regime. Gas was emitted into the chamber through a leak valve, providing high resolution pressure control over the range  $1 \times 10^{-7} - 1 \times 10^{-1}$  Torr.

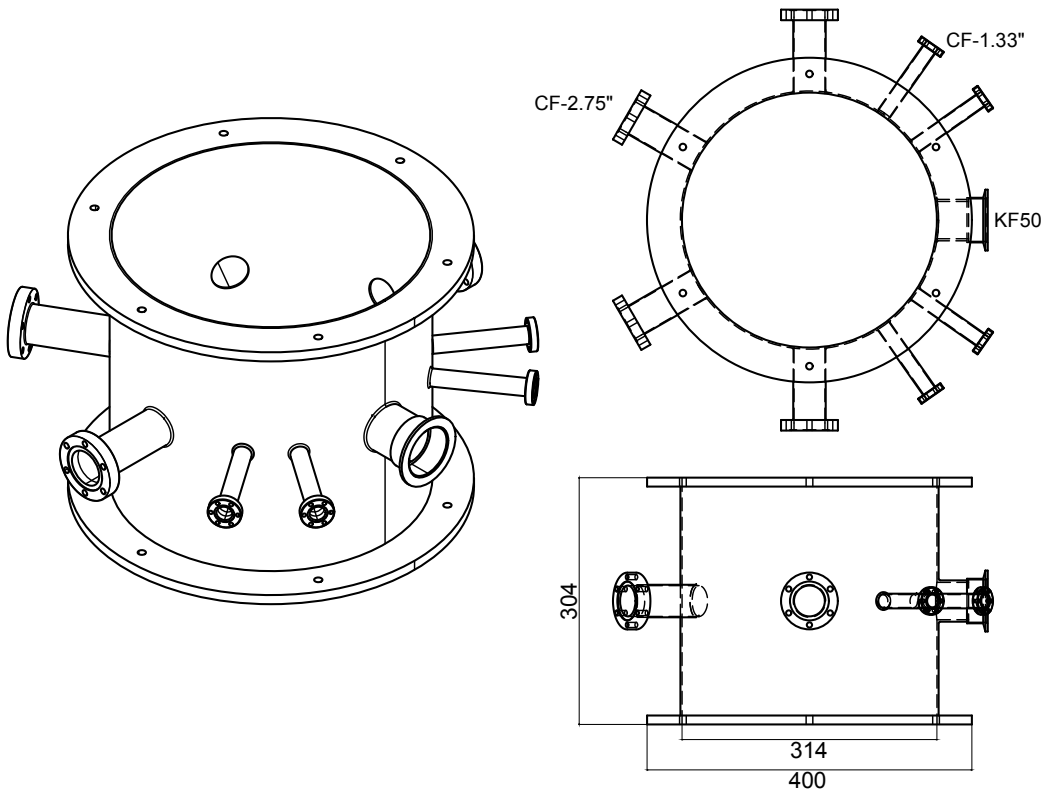


FIGURE 2.1: Vacuum chamber. All dimensions are in millimetres.

## 2.2 Translational Stage

Diagnostic instrumentation, such as magnetic field probes and Langmuir probes needed to be precisely positioned within the chamber, as well as moved while under vacuum. To this end a stepper motor controlled translational stage was implemented, resulting in a maximum possible translation distance of  $\sim 250$  mm with a spacial resolution of 0.1 mm. The stage was installed either horizontally on the vacuum chamber, at one of the equatorial ports, or vertically using the upper axial port.

## 2.3 Electron Gun

Both the IEC and MCVC systems required an external source of electrons. In the first case electron injection allowed for precise control of the IEC discharge current for a wide range of pressures, while in the second case an injected electron beam was necessary for the formation of a virtual cathode. A thermionic electron source was therefore constructed in the lower, axial vacuum port. Twelve volt, 50 Watt tungsten filaments were obtained from halogen light bulbs [103]. It was necessary to create a convenient and compact way to arrange multiple filaments

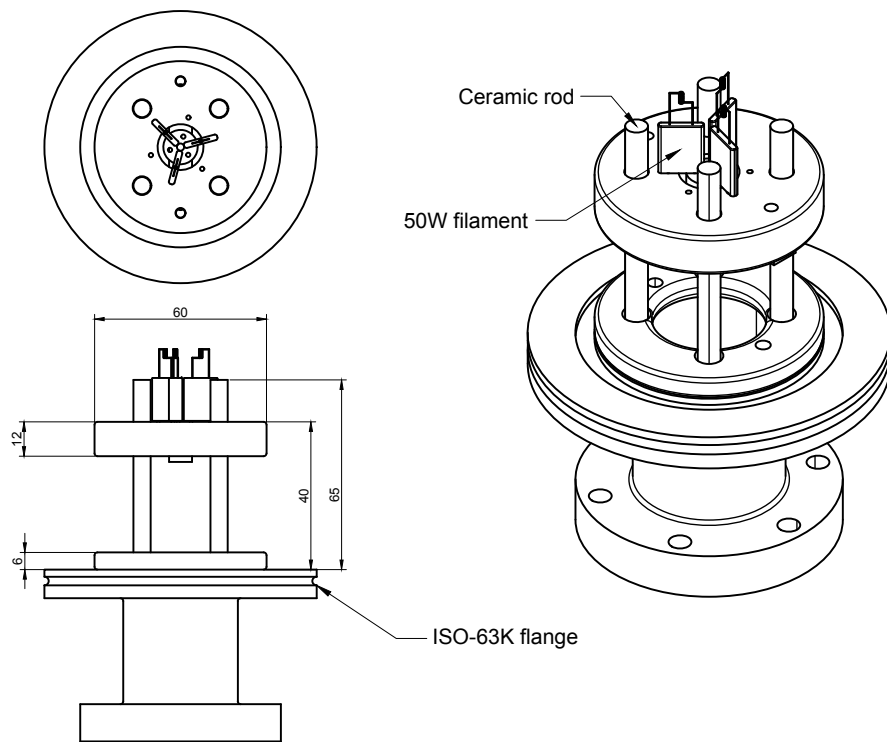


FIGURE 2.2: Electron gun assembly. All dimensions are in millimetres.

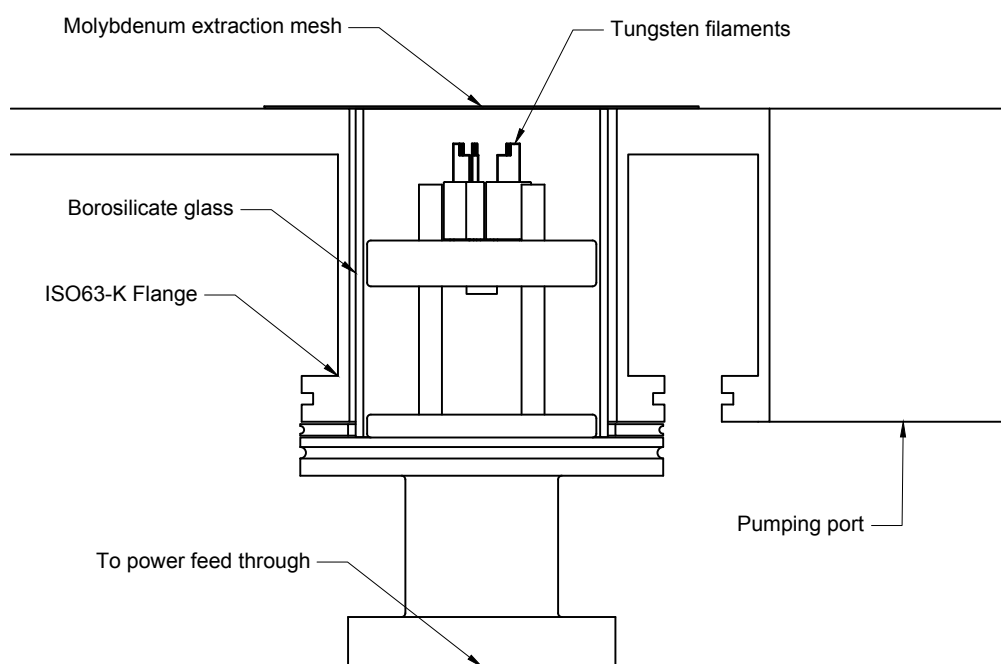


FIGURE 2.3: Electron gun assembly within vacuum port. All dimensions are in millimetres.

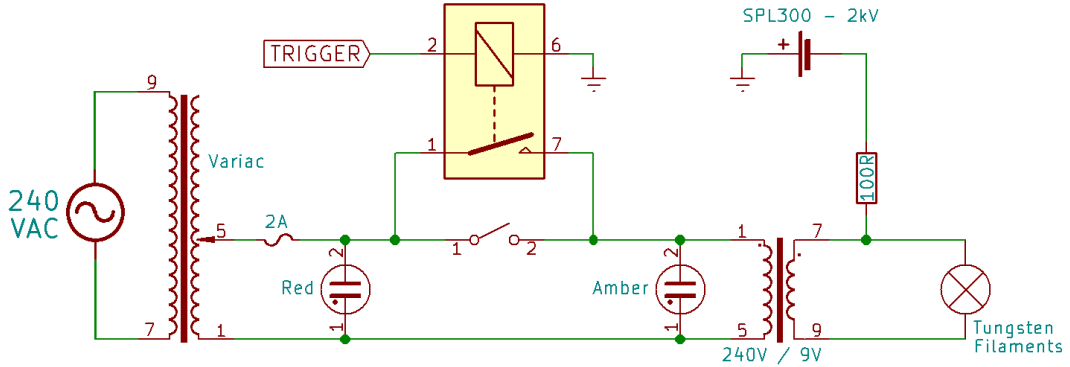
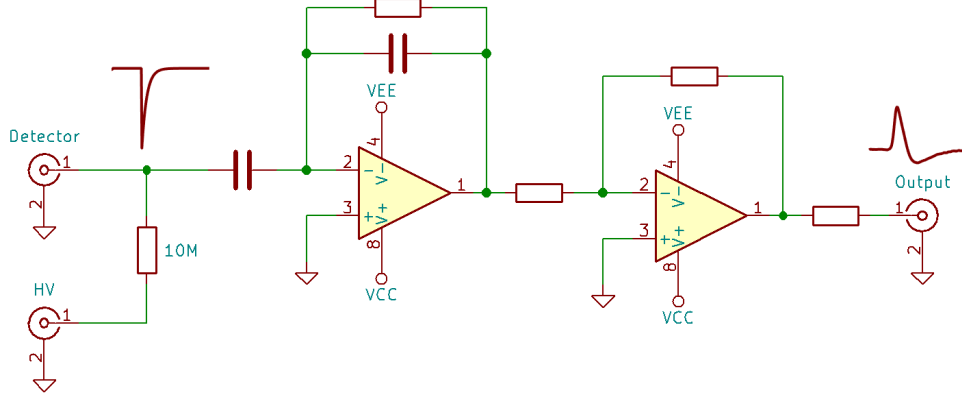


FIGURE 2.4: Biased AC power supply

in the electron gun assembly and so a three piece construction was devised wherein a small metallic plug was suspended within an outer housing via a ceramic strap. Two sets of 1.5mm diameter holes within the inner and outer components align to form 6 radial sockets, spaced by 6.35 mm, as required by our model of filament. This construction is demonstrated in Figure 2.2. Power was applied to the array via a single contact each on the central and outer elements.

The filament stage was supported on four 6 mm diameter ceramic rods such that it could be biased negatively with respect to the vacuum chamber. The assembly was mounted to an ISO63-K flange via a lower support plate. The height of the filament stage could be adjusted such that the filaments were recessed between 2 → 15 mm inside the vacuum port, depending on the desired operating voltage. A grounded molybdenum mesh (100  $\mu\text{m}$  wire, 30 wires per inch) spanned the port and served to accelerate the thermionic electrons as well as to electrically isolate the electron gun port from the main chamber. The entire electron gun assembly was sheathed with a 62 mm inside diameter borosilicate glass tube in order to provide additional electrical stand off between the floating filament stage and the wall of the vacuum port, as shown in Figure 2.3.

The filaments were heated by way of a custom built, variable 0-9 V, floating AC power supply. A 240 V/9 V, 250 W toroidal transformer provided high voltage isolation such that the secondary could be floated to  $\pm 2\text{kV}$  relative to the primary. Parallelled toggle and relay switches allowed for manual and remote control of the filament supply such that the filaments could be triggered by the main control system. An additional variable transformer provided continuous voltage control to the filaments and in this way the energy and current of the emerging electron beam could be controlled independently. See Figure 2.4 for a schematic of the filament power supply.

FIGURE 2.5: Generalised schematic for  ${}^3\text{He}$  neutron detector output amplifier

## 2.4 Neutron Detection

The D(d,n) ${}^3\text{He}$  fusion reaction was monitored by way of fast neutron detection. A pair of 24NH15, 25×150 mm, 4 atmosphere Helium-3 neutron detectors were provided by the Queensland Centre for Advanced Technologies. Cylindrical high density polyethylene blankets (dia. 200 mm) were placed around the tubes in order to moderate the emerging neutrons and aid in detection. The detectors were placed 400 mm from the centre of the vacuum chamber and were not moved for the duration of this project. The detectors were powered by a Canberra Scientific 3106D power supply and operated at a bias voltage of 1150 V. A generalised schematic of the signal amplification circuit is given in Figure 2.5. High voltage arcs within the vacuum system were found to generate spurious pulses in the output stage of the detection amplifier and so in order to obtain accurate neutron counts it was necessary to devise methods by which excess pulses could be identified and removed. The output signal was treated in one of two ways depending on the type of experiment being conducted, as described in the next two sections.

### 2.4.1 Analogue Count Acquisition

For long duration, steady state experiments neutron counts were acquired using an Ortec, Model 775 NIM counter module. Neutron counts were discriminated from arcs through the use of the *pulse* triggering mode on the Rigol 1074Z oscilloscope, wherein the oscilloscope was configured to trigger on pulses of between 2 - 5  $\mu\text{s}$  in duration with amplitudes greater than 100 mV. Trigger events were then counted by applying oscilloscope's TTL trigger output to the counter's input. Background count rates were generally less than 3 counts per minute.

### 2.4.2 Digital Count Acquisition

During programmed or pulsed operation of the experimental apparatus, or measurements of time varying fusion rates, it was not practical to manually record neutron counts using the analogue method. In these cases digital acquisition of the signal was achieved using a Model 3106D Picoscope and subsequent data processing used to remove arc pulses from the stored time series. A convolution filter was used wherein each data point  $y_i$  in the time series was replaced with a weighted sum of its previous neighbours according to

$$Y_i = \sum_{j=0}^n w_j y_{i-j}. \quad (2.1)$$

The weighting coefficients  $w_0 \rightarrow w_n$  were determined from the characteristic pulse response of the detectors; Several hundred neutron pulses were averaged to give a representative pulse and the resulting waveform was normalised such that

$$\sum_{j=0}^n w_j = 1. \quad (2.2)$$

The filter coefficients were then saved for use in all future data processing. Figure 2.6 shows the set of weighting coefficients in red as well as the raw detector response in blue. The filtered signal is given in the lower panel where it may be seen that the new, symmetric pulse has a greatly improved signal to noise ratio. An example of a detected arc pulse is given in Figure 2.7. The lower panel gives the time series following the application of the convolution filter and shows suppression of the arc signal relative to the neutron pulses. It was therefore possible to select a discrimination level for the filtered data such that arc counts were excluded from the total neutron count.

### 2.4.3 Calibration

Due to the unknown response of our detector set up for 2.45 MeV neutrons, the He3 counters were calibrated against a 12.5 cm Bonner Sphere. A Bonner sphere consists of a Lithium-6 Iodide scintillator crystal enclosed within a spherical polyethylene moderator. Bonner spheres of varying sizes are commonly used in neutron spectroscopy measurements and, therefore, have well characterised response curves [104–106]. The response of a selection of common Bonner sphere sizes are given in Figure 2.8. For an energy dependent flux of neutrons  $\Gamma(E) \text{ cm}^{-2} \text{ s}^{-1}$  incident on a detector of response  $R(E) \text{ cm}^2$ , the total number of counts per second is given by

$$\mathcal{R} = \int_0^\infty R(E)\Gamma(E)dE. \quad (2.3)$$

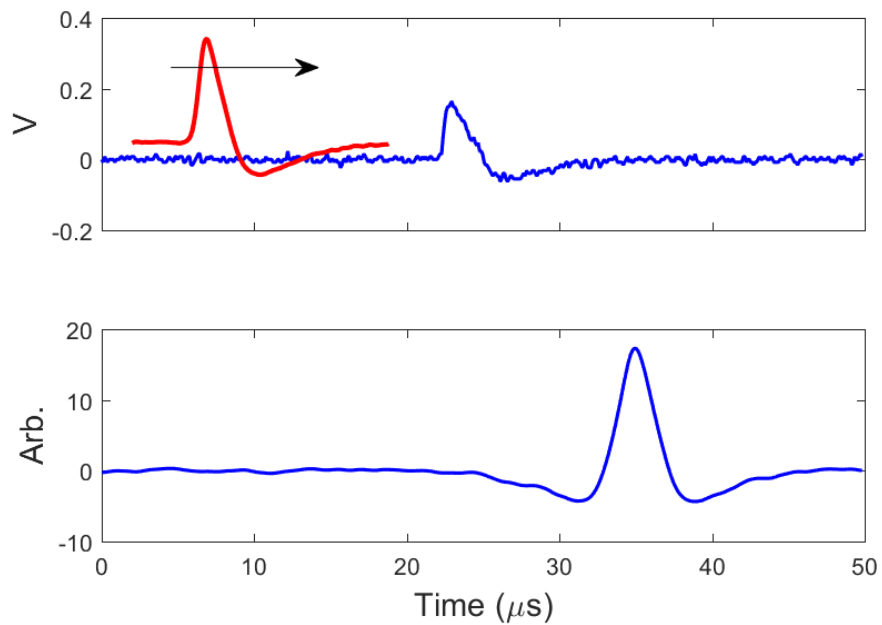


FIGURE 2.6: Neutron detector pulse before (top) and after (bottom) application of convolution filter. The weighting coefficients are given in red and have been deliberately off set for clarity.

---

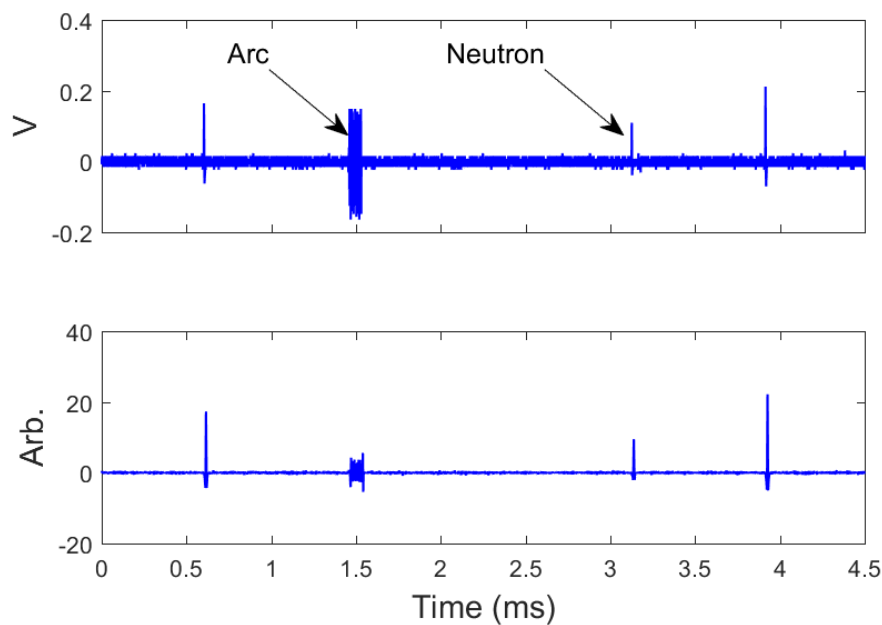


FIGURE 2.7: Neutron detector time series before (top) and after (bottom) application of convolution filter.

---

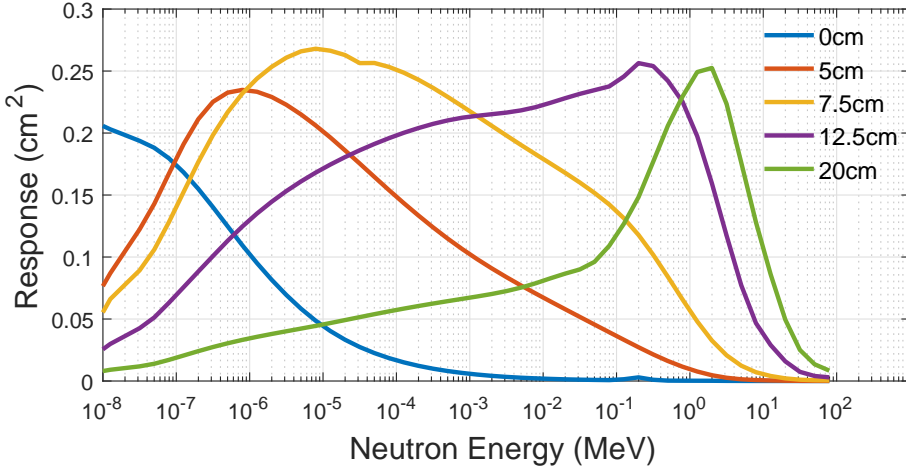


FIGURE 2.8: Bonner sphere response as a function of neutron energy.

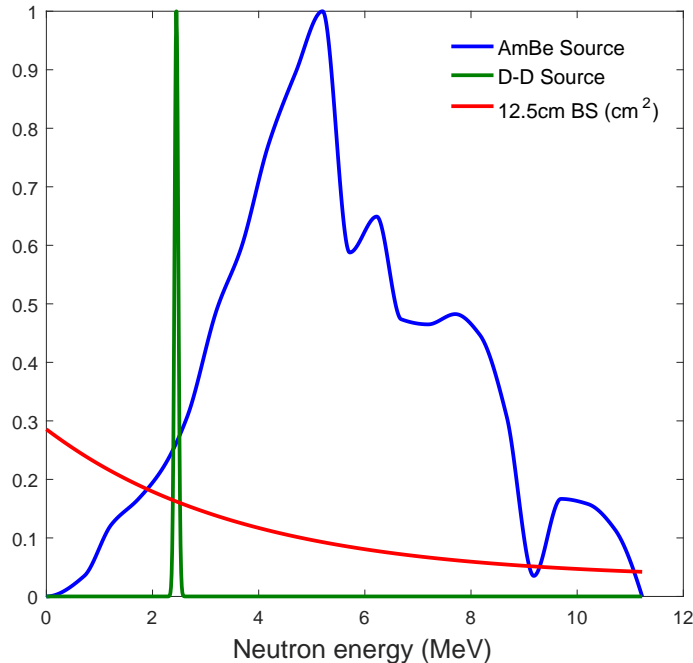


FIGURE 2.9: Normalised energy spectra for Americium-Beryllium and Deuterium-Deuterium neutron sources. The response of a 12.5 cm Bonner sphere is also shown.

A  $2.2 \times 10^6 \text{ s}^{-1}$  Americium-Beryllium (AmBe) neutron generator was used as a reference source. Neutrons are generated through spallation when  $\sim 5$  MeV alpha particles collide with Beryllium nuclei, resulting in a broad spectrum of neutron energies ranging from  $< 1$  eV through to 11 MeV. The peak normalised energy spectrum for an AmBe source is given in Figure 2.9 [107]. The Bonner sphere was placed 30 cm away from the neutron source. 2 cm of lead was used to exclude gamma radiation while having negligible effect on the emerging neutrons. Neutron counts were recorded for a period of 2 minutes resulting in an absolute count rate of 16.6 Hz. The neutron spectrum and response data presented above were used to evaluate Equation 2.3 and thereby estimate the expected count rate as  $\sim 18\text{-}19$  Hz. It was found that very small changes (1-2cm) in

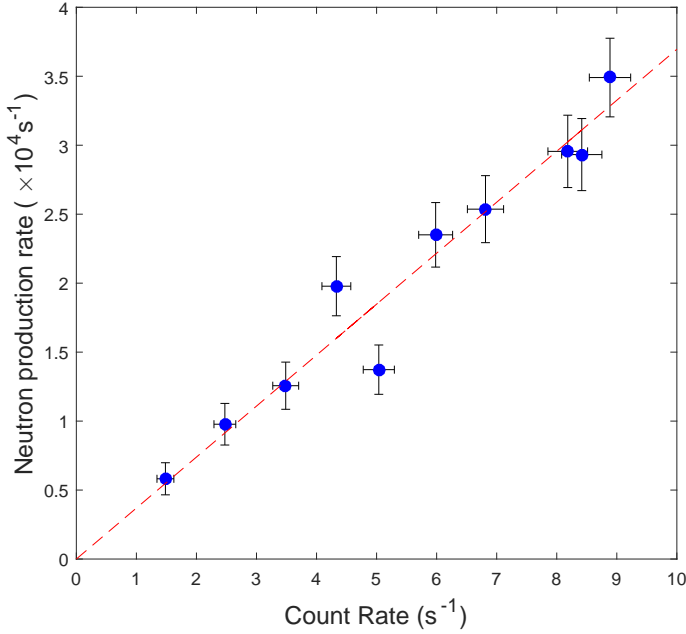


FIGURE 2.10: Neutron production rate as a function of Helium-3 detector count rate.  
(neutron production rate  $\approx 3400 \times$  counts per second)

the source-detector distance were sufficient to account for the deviation between the measured and calculated detection rate.

The Bonner sphere was then placed 30 cm away from a deuterium-deuterium fusion source, characterised by the production of mono-energetic, 2.45 MeV neutrons, as depicted in green in Figure 2.9. Fusion measurements were conducted such as to give neutron production rates over the range of  $5 \times 10^3 - 3.5 \times 10^4 s^{-1}$ . The absolute fusion rates were determined using Equation 2.3 as before and these results compared with the count rates obtained from the 24N15 detectors. The resulting calibration curve is presented in Figure 2.10. The error bars have been computed as Poisson uncertainties, approximated as the square root of the number of counts.

## 2.5 Deuterium Gas Generation

Deuterium gas was obtained through reverse fuel cell electrolysis of Deuterium Oxide. D<sub>2</sub>O (99.9%) was obtained from Sigma-Aldrich and electrolysed using a HydroFill-Pro fuel cell module. The generated D<sub>2</sub> gas was stored as a metal deuteride in HydroStik cannisters [108] and was determined to be > 99% purity through optical spectroscopy of the H<sub>α</sub> (656.28 nm) and D<sub>α</sub> (656.11 nm) Balmer lines.

## Chapter 3

# Surface Fusion in IEC Devices

Inertial electrostatic confinement devices are often described as “convergent ion focus” machines, in which it is assumed that the majority of fusion originates within a dense, high temperature core. Early theoretical approaches by Farnsworth and Hirsch assumed perfectly spherical, highly ionised systems in which the electron and ion motion were determined exclusively by the electric potential. Ion-ion fusion rates were subsequently calculated as

$$\mathcal{F} \approx n_1 n_2 \langle \sigma v \rangle_{avg}. \quad (3.1)$$

where  $n_1$  and  $n_2$  are the densities of the fusing fuels and  $\langle \sigma v \rangle_{avg}$  is the distribution averaged reactivity. No such IEC system has been built however, with practical devices instead operating in the low ionisation, low current discharge regime [48, 109–111], often with electron injection [43, 44], ion injection [50, 112, 113] or radio frequency initiation [114–116]. Ion motion in the discharge regime is mediated by momentum transfer and charge exchange interactions with background gas molecules and so the observed ion energy distributions vary significantly from those obtained through simple examination of the electric potential. Previous work [109, 114] has shown that at elevated pressures ( $1 \times 10^{-3} - 1 \times 10^{-2}$  Torr) peak ion energies may be as little as one quarter of the applied grid voltage. Coupled with low ion densities ( $10^8 - 10^{10} \text{ cm}^{-3}$ ) [117] this has led to ion-ion interactions often being neglected as a significant source of fusion with attribution instead being placed on ion-neutral collisions. IEC devices are therefore most accurately described as beam-target systems, in which energetic particles are incident on low energy target atoms. Fusion targets may exist as free molecules within the gas volume or be adsorbed on, or embedded within, the cathode surface and it is the purpose of this chapter to examine the relative contributions of these fusion domains to the absolute rate.

The relative magnitudes of gas verses surface fusion may be explored through simple comparison of the area density of targets traversed by an ion in the gaseous and surface domains. Making

use of the recirculation factor discussed in Section 1.4.1

$$\delta = \frac{I_r}{I_c} \approx \frac{\eta}{1 - \eta^2} \quad (3.2)$$

where  $\eta : 0 \rightarrow 1$  is the transparency of the cathode, the total area density of gaseous targets is subsequently estimated as

$$\mathcal{N}_{gas} \approx 2\delta R_c n_{gas} = 2\delta R_c P / k_B T \quad (3.3)$$

where  $n_{gas}$  is the gas number density,  $P$  is the system pressure,  $R_c$  is the cathode radius,  $k_B$  is the Boltzmann constant and  $T$  is the gas temperature. Table 3.1 gives indicative gas target densities for published IEC devices.

Adsorption and implantation of hydrogen and deuterium in metal surfaces have been well studied. Though surface hydrogen layers are very thin (0.1 - 100 nm), the corresponding target densities may be many orders of magnitude larger than those found within the background gas. The target area density is given by

$$\mathcal{N}_{surf} = n_{surf} d_{surf} \approx \mathcal{N}_{ads} + \int n_{emb}(x) dx \quad (3.4)$$

where  $n_{surf}$  and  $d_{surf}$  are the number density and thickness of the surface layer respectively. These terms may be re-written according to the surface density of an atomically thin adsorption layer,  $\mathcal{N}_{ads}$ , and the line integrated density of the embedded layer. Table 3.2 gives literature values for measured hydrogen target densities in both the adsorbed and embedded regions of various metals.

It is important to note that the area density of fusion targets encountered at the surface of the cathode is, in all cases, comparable to the number of gas targets encountered during an ion's entire lifetime within the focusing region [118–120]. Further, it is found that after bombardment with 25 keV D<sup>+</sup>, at relatively modest fluences ( $1 - 2 \times 10^{18} \text{ cm}^{-2}$ ), the embedded density within metal samples may exceed the number of gas targets by more than an order of magnitude [121].

Although numerous computational and experimental studies relating to surface and gaseous fusion sources in IEC machines have been performed [47, 52–54], it is not immediately clear which fusion region will dominate in any given IEC device. Achievable fusion rates may depend strongly not just on system operating parameters but also the materials from which the device is constructed. Cathode material and temperature may prove to be dominant factors in determining the ultimate fusion output.

In Section 3.2 an experiment is described by which the relative contributions due to gaseous and surface fusion are studied for a set of traditional IEC cathodes. Step function changes in

$R_c$ (cm)	$\eta$	$P$ (Torr)	$\mathcal{N}_{gas}$ (cm $^{-2}$ )	Ref.
7.5	0.93	$1.0 \times 10^{-3}$	$3.32 \times 10^{15}$	This work
7.5	0.83	$1.0 \times 10^{-3}$	$1.29 \times 10^{15}$	This work
4	0.8	$1.0 \times 10^{-3}$	$5.72 \times 10^{14}$	This work
6.25	0.85	$2.5 \times 10^{-2}$	$3.08 \times 10^{16}$	[110]
10	0.95	$2.5 \times 10^{-3}$	$1.57 \times 10^{16}$	[44]
5	0.92	$4.0 \times 10^{-3}$	$7.71 \times 10^{15}$	[43]
5.5	0.85	$7.5 \times 10^{-4}$	$8.13 \times 10^{14}$	[113]
5.7	0.9	$8.0 \times 10^{-3}$	$1.39 \times 10^{16}$	[40]

TABLE 3.1: Calculated target area densities for indicative IEC systems. In all cases the gas temperature has been assumed to be 300 K.

Material	$\mathcal{N}_{ads}$ (cm $^{-2}$ )	$\sim n_{emb}$ (cm $^{-3}$ )	$\sim d_{emb}$ (nm)	$\mathcal{N}_{emb}$ (cm $^{-2}$ )	Ref.
Ni	$3.4 \times 10^{14}$				[118]
W	$1.4 \times 10^{15}$				[119]
Mo	$1.3 \times 10^{15}$				[120]
Ta	$4.2 \times 10^{15}$				[120]
Nb	$4.2 \times 10^{15}$				[120]
Cu		$8.6 \times 10^{21}$	200	$2.9 \times 10^{17}$	[121]
Ti		$7.1 \times 10^{21}$	272	$6.0 \times 10^{17}$	[121]
316SS		$4.7 \times 10^{21}$	372	$2.3 \times 10^{17}$	[121]

TABLE 3.2: Indicative hydrogen target densities on selected metal surfaces. Values of implanted target density correspond to bombardment with 25 keV D $^+$ , at fluences of  $1 - 2 \times 10^{18} \text{ cm}^{-2}$ .

system pressure are used to examine how fusion rate evolves as a function of time. In Section 3.3 the dependence of surface fusion rate on cathode material is explored.

### 3.1 Experimental apparatus

The generalised chamber set-up used for IEC studies is depicted in Figure 3.1. Prior to all experiments the chamber was evacuated to below  $1 \times 10^{-6}$  Torr. IEC cathodes were suspended from a 5 mm diameter copper support rod insulated with nested layers of alumina ceramic tubing to give a total insulation thickness of  $\sim 3$  mm. The chamber served as the anode. A pair of 150 mm diameter, stainless steel IEC grids of different styles were obtained through collaboration with the Institute of Aerospace Engineering, Technische Universität in Dresden [59], see Figure 3.2. A disc grid was assembled from annuli laser cut from 1 mm thick sheet metal. The annuli were slotted such that the meridian rings keyed into a single equatorial ring before being spot welded at the poles. An additional pair of wire rings were added by threading 1 mm stainless steel wire through holes drilled in the longitudinal rings. A buckyball style grid was manufactured using sintered metal 3D printing and consisted of a spherical shell 2.5mm

thick, with thirty-two 45 mm circular openings. Neither grid had previously been exposed to deuterium. Neutron counts were obtained by using the digital acquisition method described in Section 2.4.2; The Picoscope was configured to record the neutron detector output for a ten second snap shot every half minute, as limited by the time taken to download and save the recorded data following each acquisition. Accompanying each snapshot was a corresponding time stamp, as well as the instantaneous values of system voltage and discharge current. Digital analysis was subsequently used to identify the number of neutron counts in each ten second interval and thereby determine the instantaneous fusion rate.

## 3.2 Pressure hysteresis in IEC devices

### 3.2.1 Experimental Method

The buckyball grid was installed in the vacuum chamber and the grid conditioned in hydrogen at 40 kV 1 mA for several hours before being allowed to cool. A 35 kV, 500  $\mu$ A hydrogen discharge was initiated at  $1 \times 10^{-2}$  Torr and the system allowed to run for a further 30 minutes to ensure the grid temperature had stabilised. The hydrogen supply was swapped with deuterium and the fusion rate monitored until an equilibrium was reached, at which time the pressure was lowered to  $1 \times 10^{-4}$  Torr. The discharge current was maintained at 500  $\mu$ A through adjustment of the electron gun current. The decay in fusion rate was monitored for a further 120 minutes. The current normalised fusion rate as a function of time is given in Figure 3.3. It should be noted that while care was taken to maintain the discharge current at 500  $\mu$ A, small fluctuations of  $\pm 10\%$  were unavoidable. We present current-normalised rates for this reason. The disc grid was treated to an identical pre-conditioning as described above and was similarly exposed to changing system pressure while maintaining a constant discharge of 35 kV and 350  $\mu$ A. A hydrogen discharge was initiated at  $1 \times 10^{-4}$  Torr and a 30 minute pre-heat conducted before deuterium was introduced and the fusion rate monitored until an equilibrium was reached. Over the following 200 minutes the pressure was increased in steps to  $1 \times 10^{-3}$ ,  $5 \times 10^{-3}$  and finally  $1 \times 10^{-2}$  Torr. Electron gun currents were pre-determined in order to maintain a constant 350  $\mu$ A discharge current over the pressure ranges. The period over which the pressure and electron gun values were adjusted generally lasted no more than 30 seconds. After a further 100 minutes of run time the pressure was once again lowered to  $1 \times 10^{-4}$  Torr and the decay in fusion rate observed. The time varying fusion rate for the disc grid is given in Figure 3.4 while the region averaged fusion rate as a function of pressure is given in Figure 3.5. Optical spectroscopy of the H <sub>$\alpha$</sub>  (656.28 nm) and D <sub>$\alpha$</sub>  (656.11 nm) Balmer lines later confirmed that the hydrogen-deuterium transition period lasted no more than 3-5 minutes. These experiments constituted the first exposure of both grids to deuterium gas.

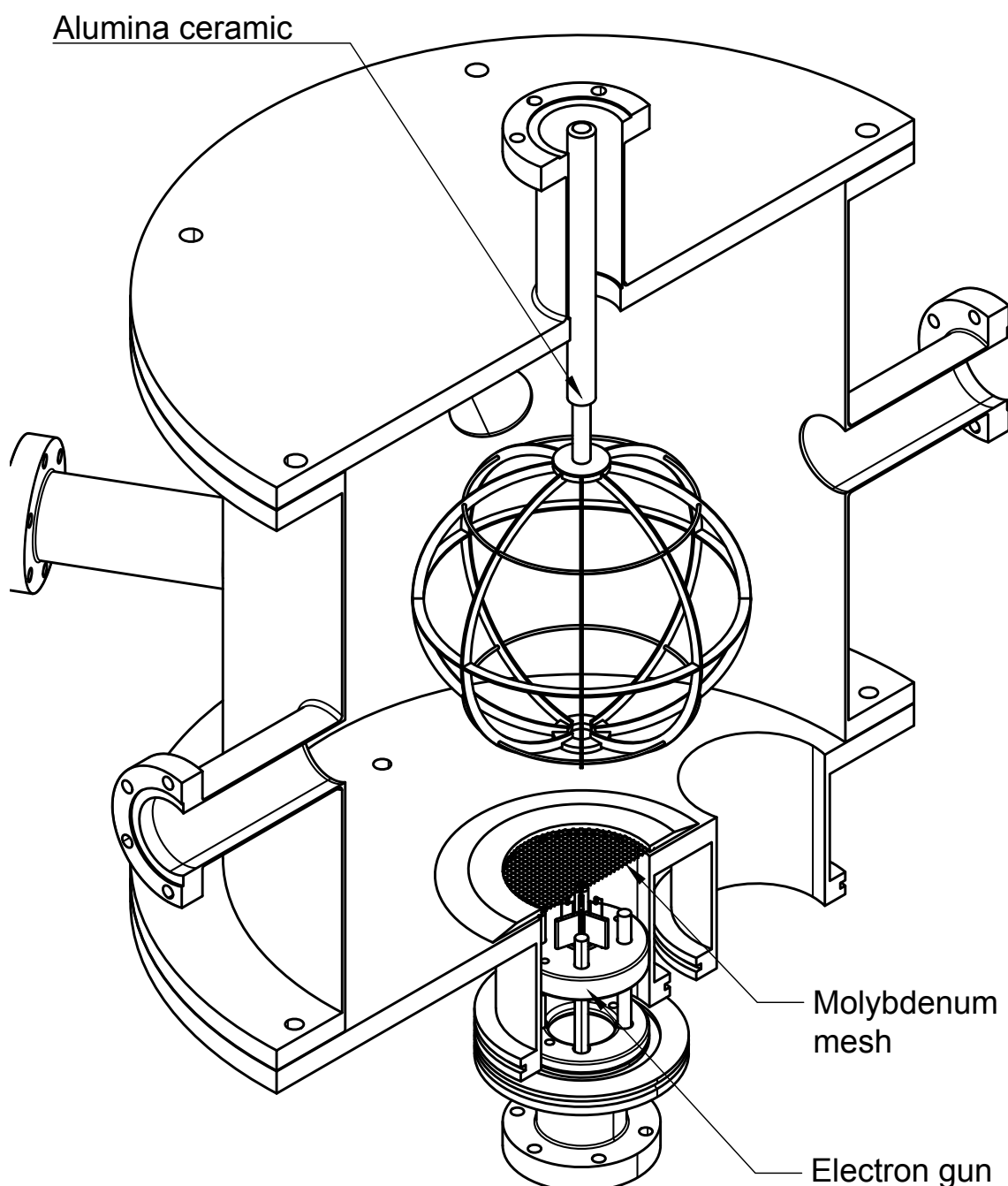


FIGURE 3.1: IEC experimental set up.

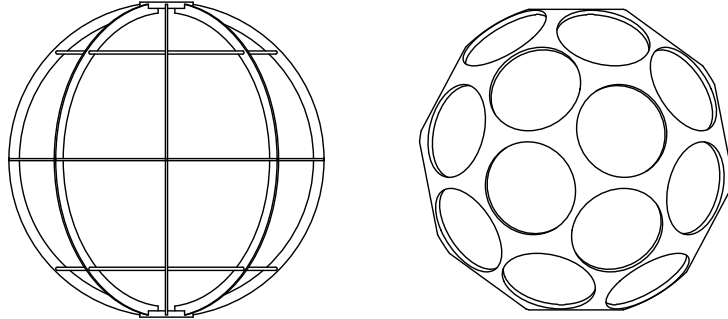


FIGURE 3.2: IEC grids. Disk grid (*Left*): area = 294 cm<sup>2</sup>, transparency = 92.6%. Buckyball grid (*Right*): area = 358 cm<sup>2</sup>, transparency = 82.7%.

### 3.2.2 Results and Discussion

For a system in which both gaseous and surface fusion occur, we can approximate the total fusion rate as

$$\mathcal{F} \approx \frac{I_c \sigma}{e} [\mathcal{N}_{gas} + \mathcal{N}_{ads} + \mathcal{N}_{emb}] \quad (3.5)$$

where  $I_c/e$  is approximately the ion fluence rate,  $\sigma$  is the distribution averaged fusion cross section and  $\mathcal{N}$  is the area density of targets in a given region. For small variations in pressure we expect  $\mathcal{N}_{gas}$  and hence the corresponding fusion rate contribution to scale proportionally. Larger changes in pressure are expected to deviate from linearity as the number of ion-neutral collisions moderate ion motion and hence alter the average cross section.  $\mathcal{N}_{ads}$  depends on the balance of adsorption and desorption at the cathode surface given as

$$\frac{d\theta}{dt} \approx \nu_a (1 - \theta)^2 \exp\left(\frac{-E_a}{k_B T_g}\right) - \nu_d \theta^2 \exp\left(\frac{-E_d}{k_B T_s}\right) \quad (3.6)$$

$$\theta = \mathcal{N}_{ads}/\mathcal{N}_0 \quad (3.7)$$

where  $\mathcal{N}_0$  is the surface density of adsorption sites,  $\theta$  is the occupancy fraction and  $\nu_{a,d}$  and  $E_{a,d}$  are the frequency factors and activation energies for adsorption and desorption respectively.  $T_{g,s}$  are the temperatures of the gas above the surface and the surface, respectively. In the case of constant temperature  $T_g = T_s = T$ , Equation 3.6 can be solved to give  $\theta(t)$  in the form of a hyperbolic tangent function

$$\theta(t) = \gamma_1 - \gamma_2 \tanh[\gamma_3(t - t_0)] \quad (3.8)$$

where  $\gamma_i$  are constants that depend on  $\mathcal{N}_0$ ,  $\nu_{a,d}$  and  $E_{a,d}$ . Setting Equation 3.6 to zero and solving for the steady state gives the well known result for the surface coverage as a function of pressure, known as the Langmuir isotherm for dissociative adsorption [122]

$$\theta = \frac{\sqrt{K_{eq}P}}{1 + \sqrt{K_{eq}P}} \quad (3.9)$$

where  $K_{eq}$  is an equilibrium constant. It has been assumed that the adsorption frequency coefficient,  $\nu_a$ , is proportional to the neutral particle flux and hence the pressure. Finally  $\mathcal{N}_{emb}$  is given by a balance of ion implantation rate and subsequent diffusion of ions back to the cathode surface where desorption may occur. We consider embedded fusion to be a minor contribution as will be discussed.

It is immediately apparent from Figures 3.3 and 3.4 that the observed fusion rates are not consistent with a model in which gas fusion dominates. The fusion rate for the buckyball grid is seen to rise very slowly, taking in excess of an hour to stabilise. The initial fusion rate, corresponding to the gaseous fusion rate, contributes only 23% of the final total, indicating that 77% of the observed fusion occurs at the cathode surface. The asymptotic approach is the result of time dependent accumulation of surface deuterium, whether through gas adsorption or ion implantation. The extensive conditioning procedure rules out changes in surface morphology as a contributing factor. Note in Figure 3.3 that when the system pressure, and hence  $\mathcal{N}_{gas}$ , was suddenly reduced by two orders of magnitude at 150 minutes, the fusion rate did not drop sharply as expected by a gas fusion model. Instead the instantaneous fusion rate remained relatively constant with only a small step reduction of  $\sim 20\%$  observed. It is possible that this gives a further measure of the gaseous contribution to the total, however as a corresponding effect is not observed in the disc grid results we regard the result as anomalous. Following the initial step in Figure 3.3, the fusion rate decays to match the new system conditions over a further  $\sim 50$  minutes. Such behaviour is consistent with the gradual desorption of gas from the cathode as described by Equation 3.6. The reduction in pressure results in a corresponding drop in the adsorption frequency factor,  $\nu_a$ , leaving desorption as the dominant process. The surface coverage and hence fusion rate decays according to Equation 3.8.

Note that the results for the disc grid in Figure 3.4, display a distinct departure in behaviour from that observed in the buckyball system. Step function increases in operating pressure resulted in corresponding step function responses in the fusion rate. The exponential approach as measured previously is absent and it is expected that this is the result of the initial pre-heat conditions chosen for the two grids. In the case of the buckyball grid, the system pre-heat in  $10^{-2}$  Torr hydrogen would have saturated the cathode surface with non-fusible targets. When the inlet gas was exchanged with deuterium the accumulation of fusion targets on the grid was limited by the hydrogen-deuterium exchange rate. By contrast, the disc grid was initially held at low pressure such that when additional deuterium was introduced to the system, fusible

targets were rapidly deposited on vacant binding sites. This observation further accounts for the marked similarity in time constants when comparing the rise and fall times for the buckyball grid. If the exponential rise in deuterium concentration is considered instead as an exponential decline of hydrogen coverage in response to a lowering of the partial pressure of hydrogen in the vacuum, we see that the two processes are equivalent and should be expected to exhibit similar dynamic behaviour. The cool down period of several hours following the conditioning of the grids was evidently long enough to purge the grids of hydrogen adsorbed during this process.

The rising steps in Figure 3.4 are partially consistent with gas fusion; that is, rapid increases in pressure result in immediate increases in fusion rate. The  $5 \times 10^{-3}$  to  $1 \times 10^{-2}$  Torr transition at  $t = 100$  minutes is of interest due to the initial reduction in fusion rate followed by a gradual recovery. It is postulated that this is the effect of ion moderation by the background gas initially reducing the fusion cross section, followed by a slow rise in the number of adsorbed deuterium targets due to improved convective cooling of the cathode [43]. In order to differentiate gaseous and surface sources the region averaged fusion rates were plotted against pressure and are given in Figure 3.5. A Langmuir isotherm was fitted and found to be in excellent agreement with the observed fusion data. The fusion rate therefore appears to obey the form

$$\mathcal{F} \approx \frac{I_c \sigma}{e} \mathcal{N}_{ads} = \frac{I_c \sigma}{e} \cdot \frac{\mathcal{N}_0 \sqrt{K_{eq} P}}{1 + \sqrt{K_{eq} P}}. \quad (3.10)$$

which is consistent with a surface fusion model.

Finally, the embedded contribution to the fusion rate must be addressed. During the experiment the disc grid experienced an ion flux of  $\sim 3.7 \times 10^{12} \text{ cm}^{-2} \text{ s}^{-1}$ , resulting in a total fluence of  $4.5 \times 10^{16} \text{ cm}^{-2}$  over the first 200 minutes of operation. Given the data in Table 3.2, it is expected that the area density of embedded deuterium would increase from zero to approximately  $6.5 \times 10^{15} \text{ cm}^{-2}$  over this period. The absence of an obvious increasing trend in the fusion data, particularly over the 100 - 200 minute interval, suggests that embedded fusion does not contribute significantly to the total.

### 3.3 Fusion on metal surfaces

It has been shown in Section 3.2 that the fusion rates measured in IEC systems display pressure and time dependencies consistent with surface fusion between energetic ions and adsorbed targets. The area density of targets on the metal surface, therefore, becomes an important consideration when designing new IEC systems. We wish to study the dependency of surface fusion rate on cathode material and so a 44 mm diameter stainless steel sample stage was constructed and fastened to the end of the high voltage stalk, in place of the IEC grid in Figure 3.1.

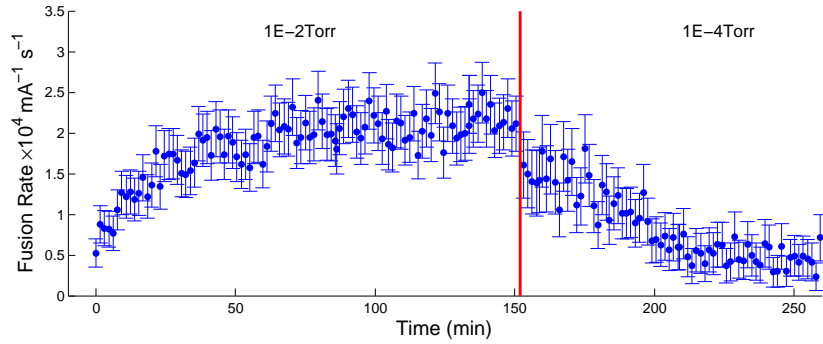


FIGURE 3.3: Buckyball grid fusion rate as a function of time for changing system pressure. 35 kV 500  $\mu$ A. The vertical line indicates the pressure change and each region is labelled according to pressure

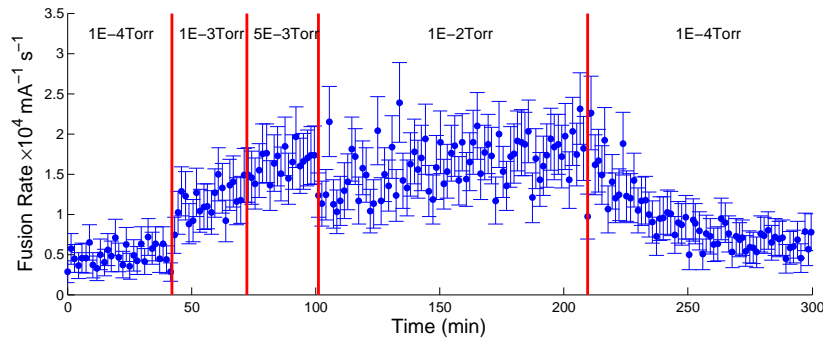


FIGURE 3.4: Disc grid fusion rate as a function of time for changing system pressure. 35 kV, 350  $\mu$ A. Vertical lines denote pressure changes and each region is labelled according to pressure

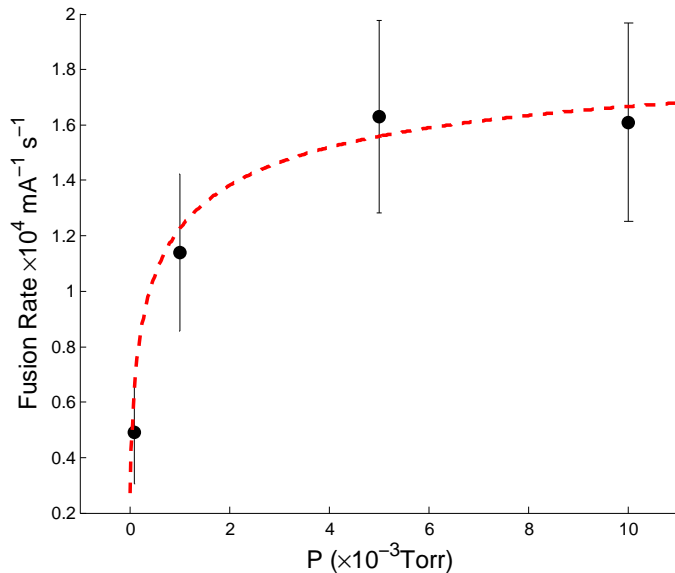


FIGURE 3.5: Disk grid fusion averaged over regions of constant pressure. Fitted Langmuir isotherm for dissociative adsorption is given by the dashed line.

Rectangular samples ( $30 \times 35$  mm) of various materials were prepared in order to study the material dependence of fusion rate in a deuterium discharge. The planar cathodes do not allow ion recirculation and, due to the extremely large size of the fusion mean free path relative to the vacuum vessel, almost all background gas fusion is eliminated.

### 3.3.1 Experimental Method

Samples of 316 Stainless Steel, Titanium, Molybdenum, Copper, Silver and Graphite were prepared. The pieces were thoroughly cleaned with methanol and affixed to the sample stage. Following pump down, deuterium gas was introduced and the pressure raised to  $1 \times 10^{-3}$  Torr. The sample was allowed to soak in deuterium for 15 minutes before a 35 kV, 1 mA discharge was initiated and the fusion rate monitored as a function of time. As the samples were not previously conditioned for high voltage operation the first few data points tended to be anomalously high due to arcing. These points were discarded. Arcing generally subsided within 45-90 seconds. Once the fusion rate had reached an equilibrium, the pressure was lowered to  $5 \times 10^{-4}$  Torr and finally to  $1 \times 10^{-4}$  Torr. Fusion measurements for each sample were conducted over about 15 minutes at each pressure.

### 3.3.2 Results and Discussion

Fusion rates as a function of time for select cathode materials are given in Figure 3.6. Rates have been normalised to their initial values such that the trends may be compared. Titanium and copper both exhibit behaviour comparable to that of molybdenum and so these samples have been excluded for clarity. Unlike the grids in Section 3.2, the planar cathodes were not pre-heated in hydrogen and hence the fusion rate evolves as the cathodes heat in the discharge. At low pressures radiative heat loss dominates, and so we may express the power balance as

$$\mathcal{C} \frac{dT}{dt} = \left[ \frac{1}{2} IV + A\sigma(T_0^4 - T^4) \right] \quad (3.11)$$

where  $T$  is the temperature of the sample,  $I$  and  $V$  are the system current and voltage respectively,  $A$  is the cathode area and  $\sigma$  is the Stephan-Boltzmann constant. A factor of one half is introduced to account for the approximate fraction of electrical power that is deposited into the cathode as opposed to the chamber wall.  $T_0$  is the ambient temperature and  $\mathcal{C}$  is the thermal capacitance of the cathode, given by the product of its mass and the specific heat capacity of the material from which it is made. It is assumed that the thermal capacitance of the cathode is dominated by that of the sample holder, with additional contributions due to the material samples regarded as negligible. Equation 3.11 may be solved to give an implicit form for  $T(t)$

as

$$t + t_0 = \frac{C}{4\gamma_1^3\gamma_2} [\ln(\gamma_1 + \gamma_2 T) - \ln(\gamma_1 - \gamma_2 T) + 2 \tan^{-1}(\gamma_3 T)] \quad (3.12)$$

where  $t_0$  is the integration constant and the following abbreviations have been used

$$\begin{aligned}\gamma_1 &= (\frac{1}{2}IV + \sigma AT_0^4)^{1/4} \\ \gamma_2 &= (A\sigma)^{1/4} \\ \gamma_3 &= \gamma_2/\gamma_1.\end{aligned}$$

Equation 3.12 has been used to compute the heating profile, estimating an equilibrium temperature of  $\sim 550$  K, after  $\sim 500$  seconds. All metal samples display a decaying trend in fusion rate with increasing temperature, consistent with the thermal desorption of adsorbed deuterium from the cathode surfaces. This deleterious effect of cathode temperature on fusion rate has also been observed in gridded IEC systems [51]. As the samples were exposed to approximately the same heating profiles, the varying decay rates for the different metals provide insight into the relative magnitudes of the activation energies  $E_{a,d}$  in Equation 3.6. In this way, the time series are reminiscent of thermal desorption spectroscopy (TDS) measurements in which samples are heated at a known rate in order to promote desorption and study gas trapping mechanisms [123]. It is noted that materials with larger equilibrium fusion rates also exhibit longer time constants during the decay phase; Stainless steel, the poorest performing material tested, undergoes rapid loss of deuterium for only modest increase in temperature, while the silver sample does not reach equilibrium even after 1500 seconds at 550 K.

Contrasted against the metal samples, graphite displays unique behaviour. Graphite appears to accumulate additional surface targets over the first 500 seconds leading to an almost ten fold increase in the fusion rate. TDS measurements have shown that very high temperatures ( $>800$  K) are required to liberate trapped hydrogen from graphite samples [124, 125], far higher than those obtained during this experiment. The second term in Equation 3.6 is therefore very small, leading to monotonically increasing surface coverage as a function of time. It is expected that IEC cathodes constructed from graphite would be capable of operating at higher powers without suffering the same drop in performance as seen in metal based grids.

Figure 3.7 provides a direct comparison of the equilibrium fusion rates for the various cathode materials as a function of operating pressure. It is important to note the large disparity between the samples, with almost two orders of magnitude variation between stainless steel and graphite. The observed fusion rates were found to be largely insensitive to changes in pressure and we attribute this to the order in which experiments were conducted. Measurements began at higher pressures which were reduced over time, revealing the same hysteresis effects as found in Section 3.2. Measurements were conducted over  $< 30$  minutes, far less than the characteristic desorption times measured previously. The exact mechanism by which one material produces a larger fusion

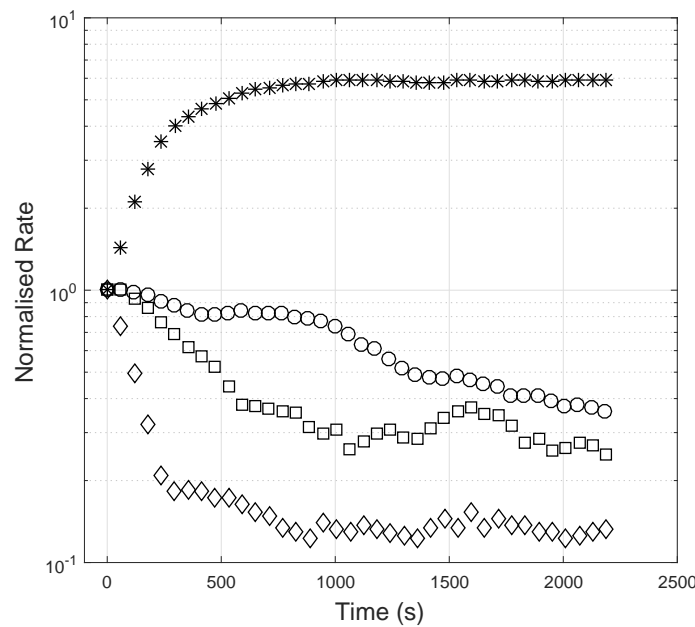


FIGURE 3.6: Evolution of fusion rate as a function of time for select cathode materials at 35 kV, 1 mA. Values are normalised to the initial rate.  $\diamond$  = 316 stainless steel,  $\square$  = Molybdenum,  $\circ$  = Silver,  $*$  = Graphite

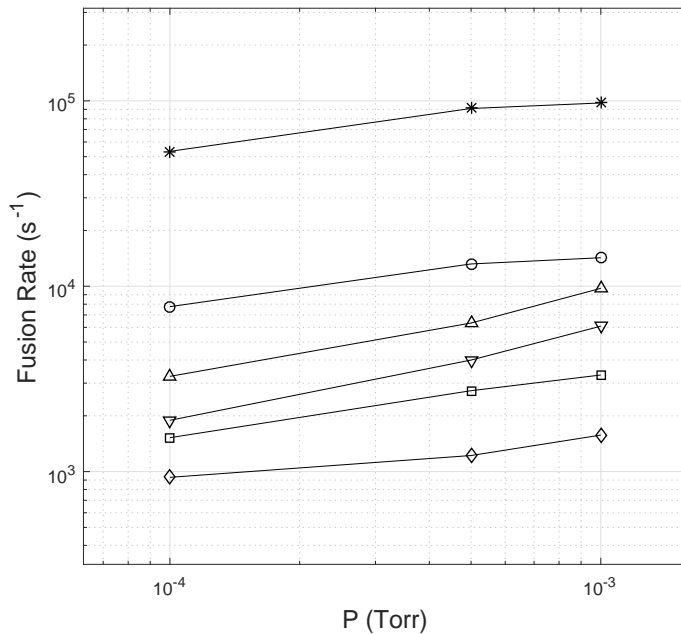


FIGURE 3.7: Surface fusion rate as a function of pressure for various cathode materials at 35 kV, 1 mA.  $\diamond$  = 316 stainless steel,  $\square$  = Molybdenum,  $\triangledown$  = Copper,  $\triangle$  = Titanium,  $\circ$  = Silver,  $*$  = Graphite

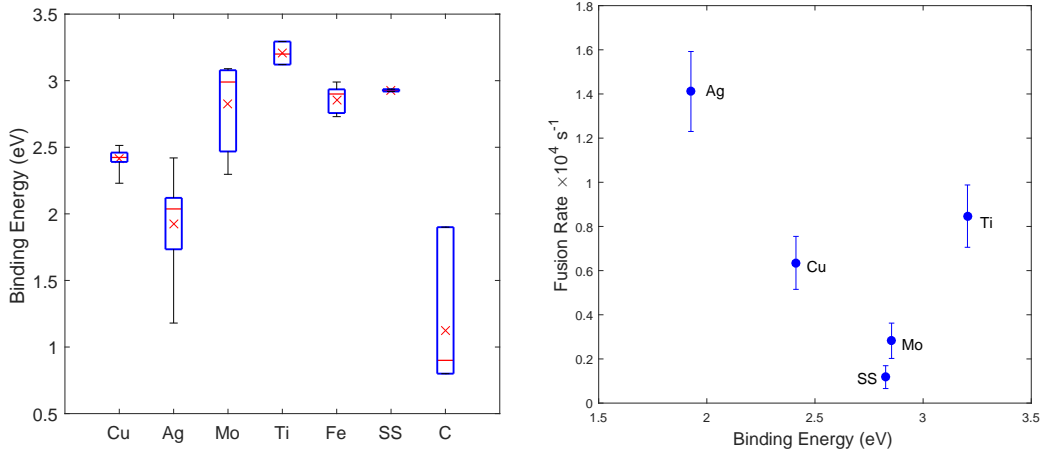


FIGURE 3.8: *Left:* Literature values for hydrogen binding energy in tested metals. Average and median values are denoted by red crosses and lines respectively. Blue boxes span the lower to upper quartile and whiskers indicate the limits of the datasets. *Right:* Fusion rate as a function of hydrogen binding energy; Graphite has been excluded due to the large disparity between the metal and graphite samples.

rate than another is not yet fully understood and is the topic of ongoing, unpublished work [126]. We may, however, briefly outline some important areas for future study by considering the simplest factors affecting surface target fusion rates. Namely, the density and bonding strength of surface bound deuterium, and the incident flux of energetic ions.

The hydrogen desorption energy,  $E_d$ , in Equation 3.6 determines the rate at which bound hydrogen may leave the cathode surface at a given temperature, with larger energies resulting in longer residency times. We would therefore expect materials with larger binding energies to exhibit larger fusion rates. Extensive computational and experimental studies have been conducted into hydrogen bonding in transition metals and graphite [124, 125, 127–131]. The left hand panel of Figure 3.8 summarises literature values of  $E_d$  in box and whisker format; The average and median values are denoted by red crosses and lines respectively while blue boxes span the lower to upper quartiles. Whiskers indicate the absolute limits of the datasets. The right hand panel gives the measured fusion rates for each metal plotted as a function of the average literature binding energy. It is seen that the fusion data appears to contradict the expected behaviour. Graphite and silver, the materials with the lowest literature values for  $E_d$  exhibits the largest measured fusion rates. Such a simple, binding energy based model is therefore insufficient to explain the observed fusion behaviour.

We therefore consider how the energetic ion flux into the cathode surface may change with the target material. When ions strike the cathode additional electrons, known as secondary electron, may be ejected from the metal surface. If the ions each liberate, on average,  $\gamma$  excess

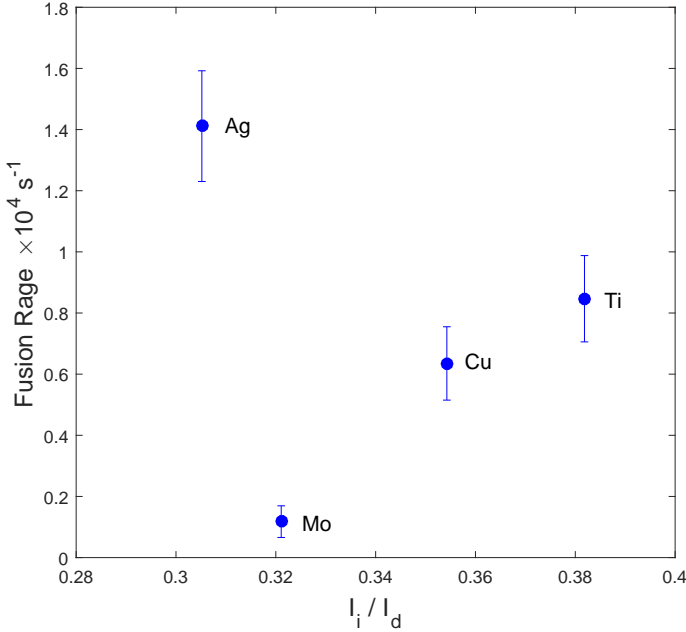


FIGURE 3.9: Fusion rates as a function of computed fractional ion current. Ion current fraction computed using Equation 3.13 using secondary electron coefficients in [132].

electrons, then the fraction of the total discharge current  $I_d$  carried by ions is given by

$$\frac{I_i}{I_d} = \frac{1}{2 + \gamma}. \quad (3.13)$$

Changes in the secondary electron coefficient between cathode materials may therefore result in different ion fluxes for equal discharge current and so we would expect materials with higher values of  $\gamma$  to exhibit lower fusion rates. Thermionic electron emission from hot cathodes will have an equivalent effect and it is for this reason that the use of incandescent grids should be discouraged. Zalm and Beckers [132] measured electron emission coefficients for four of our tested materials (Cu, Ag, Mo, Ti) under bombardment by  $H^+$  and  $H_2^+$  in the range of 5-20 keV. Their measurements were used to compute indicative fractional ion currents for each of the metal cathodes and the results plotted against our fusion rates in Figure 3.9. Molybdenum, copper and titanium appear to behave as expected, exhibiting a linear dependence on ion current. Silver once again displays disparate behaviour, exhibiting the largest fusion rate despite having the largest value of  $\gamma$ .

Of the two discussed explanations for material dependent fusion rates neither displays a convincing correlation to the measured data. It is likely that this is due to inconsistencies between the presented and literature experiments in terms of sample preparation and experimental conditions and methodologies, as well as gross oversimplification of the proposed models. Further work is required in which more careful sample preparation techniques are employed to ensure

consistent, well characterised cathode surfaces. Additionally a wider selection of cathode materials must be tested such that broader trends may become more obvious.

### 3.4 High performance IEC Grid Based on Graphite

In the previous section we have demonstrated that the fusion rate obtained through the use of planar cathodes displays a strong dependence on cathode material. In particular, graphite cathodes perform exceptionally, producing fusion rates almost two orders of magnitude larger than their metallic counterparts. This marked difference in behaviour may be directly attributed to the surface properties and hydrogen trapping capabilities of the cathode material and hence provides an additional means of probing the relative contributions of surface and gaseous fusion in IEC systems. Consider an IEC device in which the fusion rate is given simply as the sum of surface and gaseous contributions. If we operate cathodes that are made of materials 1 and 2, but which are otherwise geometrically identical, then we would expect the gas contribution to remain constant. If material 2 exhibits a fusion enhancement factor  $\alpha$  over material 1, then the observed fusion rates should therefore be

$$\mathcal{F}_1 = \mathcal{F}_{surf} + \mathcal{F}_{gas} \quad (3.14)$$

$$\mathcal{F}_2 = \alpha\mathcal{F}_{surf} + \mathcal{F}_{gas}. \quad (3.15)$$

Solving the equations simultaneously yields an expression for the fraction of fusion occurring on the surface of the material 1 cathode as

$$\frac{\mathcal{F}_{surf}}{\mathcal{F}_{surf} + \mathcal{F}_{gas}} = \left[ 1 + \left( \frac{\alpha\mathcal{F}_1 - \mathcal{F}_2}{\mathcal{F}_2 - \mathcal{F}_1} \right) \right]^{-1} \quad (3.16)$$

where we have made the implicit assumption that the secondary electron coefficients of the two cathode materials are equal. A pair of 100 mm diameter IEC grids were manufactured using the most disparate materials tested above; namely, 316 stainless steel, and graphite. The grids were constructed along similar lines to the disk grid described in Section 3.1, wherein annular pieces were slotted into a single equatorial ring and fixed at the poles. As spot welding was impossible for the graphite construction, the meridian sections were instead fitted into polar retaining blocks and threaded caps used to clamp them in place, as shown in Figure 3.10.

Due to limitations in the mechanical properties of graphite preparation of extremely thin grid wires were not possible. Instead the annular sections had a thickness of 4 mm and a depth of 10 mm. The resulting grid transparency was approximately 80%, computed at the spherical surface transcribed by the inside edges of the annuli.

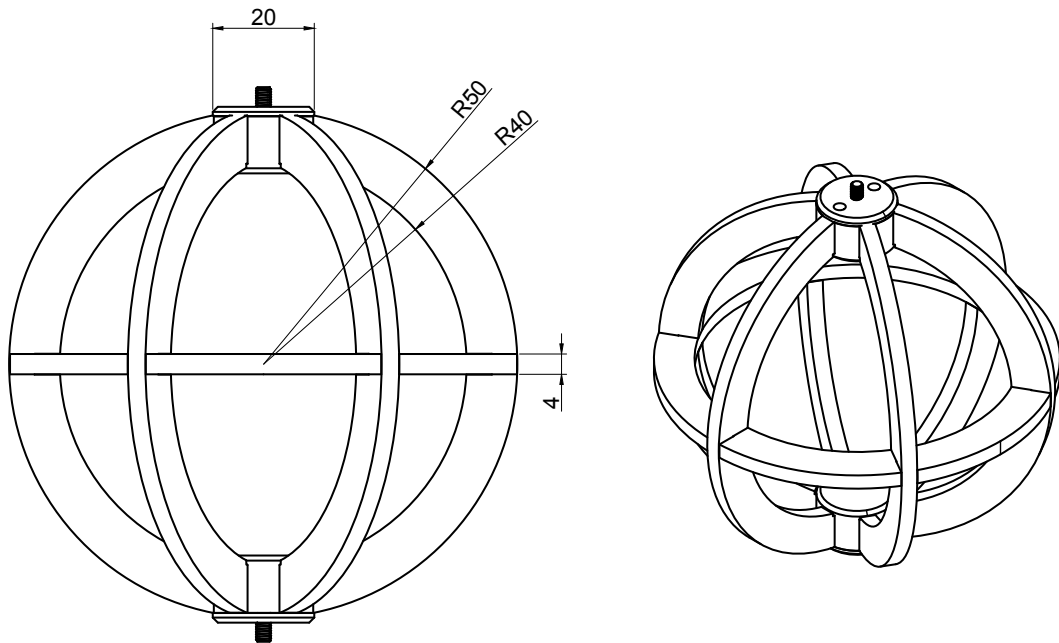


FIGURE 3.10: Matching stainless steel and graphite IEC grids for surface fusion diagnostic.  
Area =  $317 \text{ cm}^2$ , transparency = 80%.  
All dimensions are in millimetres.

---

### 3.4.1 Experimental Method

The grids were installed in the vacuum chamber as shown in Figure 3.1. An additional ceramic sheath was added to the high voltage stalk to increase the operating voltage to 50 kV. The grids were conditioned in hydrogen gas until the maximum operating voltage was reached. The system was then allowed to pump overnight to allow adsorbed hydrogen to dissipate. Due to the hysteresis observed in the fusion rate when lowering the gas pressure, fusion measurements as a function of pressure were taken in the increasing direction from lower to higher pressures. Similarly, due to the long settling times observed in the previous sections the fusion rate at each pressure was allowed to stabilise for 30 minutes before the count rate was recorded. Counts were acquired according to the method described in 2.4.1 over intervals of 60 seconds. 20 intervals were acquired at each pressure and averaged. Deuterium was introduced to the chamber at a pressure of  $2 \times 10^{-5}$  Torr and 50 kV, 150  $\mu\text{A}$  discharge initiated. Fusion measurements were obtained for pressures ranging  $2 \times 10^{-5}$  to  $5 \times 10^{-3}$  Torr for the steel grid and  $2 \times 10^{-5}$  to  $8 \times 10^{-4}$  Torr for the graphite grid. Above  $1 \times 10^{-3}$  Torr the graphite system arced uncontrollably and measurements were abandoned. In all cases the discharge current was maintained at the same value through

adjustment of the electron gun. Following a set of measurements the deuterium gas was shut off and the chamber pumped until the following day, approximately 15 hours. The  $2 \times 10^{-5}$  Torr data point was then repeated to examine the degree of deuterium retention. The resulting fusion rates are given in Figure 3.12

The stock material used to manufacture the graphite grid was different than that tested previously. The provenance and properties of both pieces were unknown. As such, the planar cathode measurement was repeated. A fresh plate of the new graphite was prepared, as was a new sample of 316 stainless steel. Both pieces were polished using 3000 grit emery paper, before being cleaned with methanol and installed on the sample stage as before. The operation voltage was limited by arcing to 40 kV, however this is not expected to significantly alter the fusion enhancement. Fusion rates were determined as above for a  $150 \mu\text{A}$  discharge at pressures ranging  $2 \times 10^{-5}$  to  $1 \times 10^{-2}$  Torr.

### 3.4.2 Results and Discussion

Fusion rate as a function of pressure is presented for planar cathodes in Figure 3.11. Notably, the large enhancement factor ( $\alpha \approx 60$ ) observed in Section 3.3 is absent, replaced instead by a peak value of  $\alpha = 3.46$  at  $1 \times 10^{-3}$  Torr. It is not known whether this is an artefact of the graphite sample itself or the different operating conditions. Further, the graphite sample displays a marked improvement with pressure as additional gas is introduced into the system, indicating increased uptake of deuterium with pressure. Beyond  $1 \times 10^{-3}$  the rate declines as a result of ion moderation in the background gas. The corresponding measurements for the gridded cathodes are given in Figure 3.12. The data appears almost linear on a semilog-x plot, consistent with Langmuir isotherm adsorption at low pressures. The graphite grid produces a fusion rate that is consistently  $\sim 2.2$  times larger than that of the stainless steel grid and so, with reference to Equation 3.16, we set  $\mathcal{F}_2 = 2.2\mathcal{F}_1$  and  $\alpha = 3.46$  to compute the surface fusion contribution in the stainless steel system as

$$\frac{\mathcal{F}_{surf}}{\mathcal{F}_{surf} + \mathcal{F}_{gas}} = \left[ 1 + \left( \frac{3.46 - 2.2}{2.2 - 1} \right) \right]^{-1} = 0.57. \quad (3.17)$$

While smaller than the 80% contribution determined in Section 3.2, the new value of 57% is still significant. It is postulated that devices with higher operating voltages should exhibit enhanced gas fusion as the kinetic energy gained by an ion over a collisional mean free path is dependent on the potential gradient. That is

$$E_{ave} \propto \lambda_{col} \frac{\Phi_0}{L} \quad (3.18)$$

where  $\lambda_{col}$  is the average collisional distance,  $\Phi_0$  is the operating potential and  $L$  is the characteristic length scale of the device. Hence fusion with gaseous targets should be enhanced at

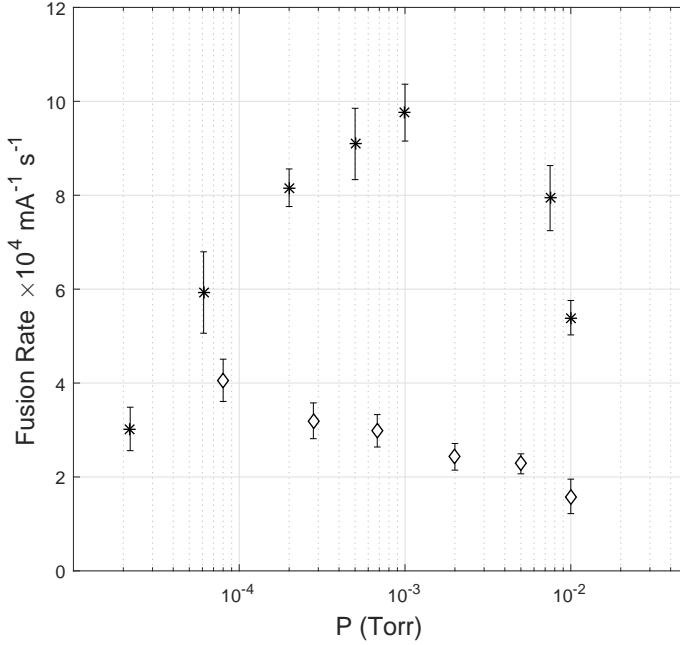


FIGURE 3.11: Fusion rate as a function of pressure for stainless steel and graphite plate cathodes. Discharge conditions were  $150\mu\text{A}$ ,  $40\text{kV}$ .  $\diamond$  = 316 stainless steel, \* = Graphite. Peak fusion enhancement  $\alpha = 3.46$  at  $1 \times 10^{-3}$  Torr.

higher voltages. Of particular interest is the behaviour of the fusion rate following a 15 hr pump out. The stainless steel grid ( $\circ$  in Figure 3.12) is seen to reset over night indicating the loss of deuterium from the grid. This is consistent with the observations made in Section 3.2, wherein 2-4 hours at reduced pressure was sufficient to deplete the surface of deuterium. Graphite, by contrast, appears to retain adsorbed gas during the pump out and exhibits a fusion rate that is consistent with the highest pressure to which the grid had previously been exposed. The red markers in Figure 3.12 indicate the projected fusion rates for  $1 \times 10^{-3}$  and  $3.5 \times 10^{-3}$  Torr and, although measurements were not possible at these pressures due to arcing, the deuterium accumulated during the attempts remains within the cathode. The repeated measurement at  $2 \times 10^{-5}$  Torr ( $\square$  in Figure 3.12) is therefore elevated considerably relative to the first.

### 3.4.3 High Power Operation of Graphite IEC Grid

It is apparent that the steel and graphite IEC grids did not behave as expected from the results in Section 3.3. The measured enhancement to the fusion rate due to graphite is small ( $\times 2-3$ ), even in the planar geometry. A significant difference between the experiments in Section 3.3 as compared to those in the previous section is the electrical power deposited into the cathode and hence, via Equation 3.11, the operating temperature. The equilibrium of Equation 3.11 is given by

$$T_{equ} = \left[ T_0^4 + \frac{IV}{2\sigma A} \right]^{1/4} \quad (3.19)$$

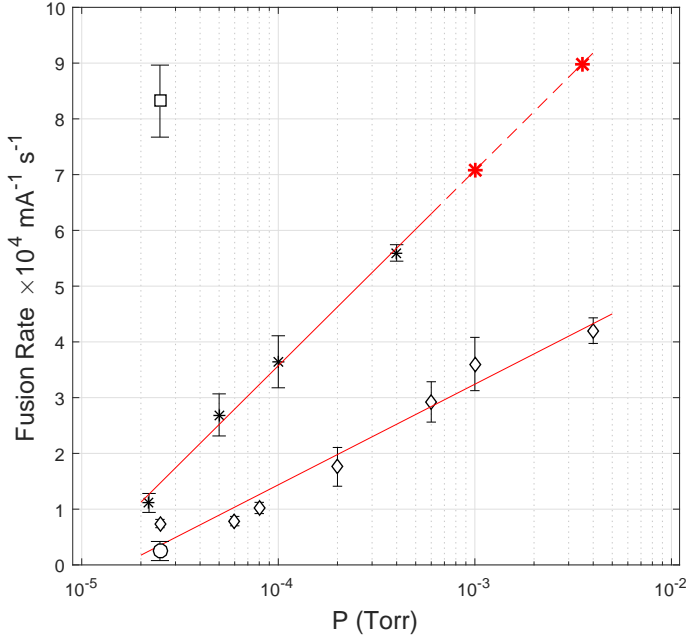


FIGURE 3.12: Fusion rate as a function of pressure for stainless steel and graphite IEC grids. Discharge conditions were  $150\mu\text{A}$ ,  $50\text{kV}$ .  $\diamond$  = 316 stainless steel,  $\circ$  = 316 stainless steel +15hr pump, \* = Graphite (red = projected),  $\square$  = Graphite +15hr pump.

and so we see that the *power per unit area* is the relevant quantity when comparing different cathodes. A summary of the previously described experiments is given in Table 3.3. Note the extremely large variation in power density, as well as the correlation between input power and fusion enhancement. With reference to the results in Figure 3.6, we note that while the graphite sample undergoes a  $\times 6$  increase in fusion rate over the first 1000 seconds of run time, the stainless steel sample undergoes a  $\times 6.7$  reduction. If we let

$$\mathcal{F}_{graph.}|_{t=0} = \alpha \mathcal{F}_{steel}|_{t=0} \quad (3.20)$$

$$\mathcal{F}_{graph.}|_{t=2000} = 6 \mathcal{F}_{graph.}|_{t=0} \quad (3.21)$$

$$\mathcal{F}_{steel}|_{t=2000} = \frac{1}{6.7} \mathcal{F}_{steel}|_{t=0} \quad (3.22)$$

then we compute the initial, cold cathode enhancement due to graphite to be merely

$$\alpha = \left. \frac{\mathcal{F}_{graph.}}{\mathcal{F}_{steel}} \right|_{t=0} = 1.5. \quad (3.23)$$

Large values of  $\alpha$  are therefore obtained, not simply due to the favourable qualities of graphite, but also due to the poor performance of stainless steel at elevated temperatures. In order to demonstrate this, the steel and graphite grids were operated at varying powers, ranging from 10 to 90 Watts. The grids were installed in the vacuum chamber and pumped to below  $1 \times 10^{-6}$  Torr. Deuterium was introduced and raised to a pressure of  $1 \times 10^{-3}$  Torr, the pressure

Experiment	Voltage (kV)	Current (mA)	Area (cm <sup>2</sup> )	Power Density (W cm <sup>-2</sup> )	$\alpha$	Note
Planar Cathodes	35	1	30	0.58	60	Figure 3.7
Planar Cathodes	40	0.15	30	0.10	3.5	Figure 3.11
Disk Grid	35	0.35	294	0.021	-	Section 3.2
Buckyball Grid	35	0.5	358	0.025	-	Section 3.2
Graphite Grid	50	0.15	317	0.012	2.2	Figure 3.12

TABLE 3.3: Comparison of described fusion experiments. The heating power deposited into the cathode is assumed to be half of the applied electrical power,  $0.5IV$ , with the balance absorbed by the vacuum chamber. Where applicable the measured enhancement ratio  $\alpha$  of graphite over stainless steel is given.

at which the maximum enhancement was observed in Figure 3.11. A discharge was initiated at 35 kV, 0.3 mA and the fusion rate allowed to stabilise. The count rate was recorded over ten, 1 minute intervals and averaged before the current was increased. The fusion rate was monitored as a function of discharge current over the range 0.3-2.5 mA.

### 3.4.4 Results and Discussion

Figure 3.13 gives the measured fusion rates as a function of power for the steel and graphite IEC grids. At currents below 0.6 mA ( $0.067 \text{ W cm}^{-2}$ ) the graphite and steel grids exhibit very little difference, following the expected linear trend with discharge current. The graphite grid continues this trend, with a high degree of linearity ( $R^2 = 0.9989$ ) over the first four data points. A small degree of roll-off is observed in the final data point, however this is also associated with a larger statistical uncertainty. The stainless steel grid however, reaches a threshold power density of around  $0.083 \text{ W cm}^{-2}$  beyond which the fusion rate plateaus. From Equation 3.19 we estimate the threshold temperature to be  $\sim 350 \text{ K}$ . The red, vertical line in Figure 3.13 indicates the current at which the power per unit area is equal to that used in Figure 3.11. At this power the graphite grid produces  $\sim 3.26$  times the fusion rate of its steel counterpart and so setting  $\mathcal{F}_2 = 3.26\mathcal{F}_1$  in Equation 3.16 gives

$$\frac{\mathcal{F}_{surf}}{\mathcal{F}_{surf} + \mathcal{F}_{gas}} = \left[ 1 + \left( \frac{3.46 - 3.26}{3.26 - 1} \right) \right]^{-1} = 0.92. \quad (3.24)$$

We therefore conclude that surface fusion remains dominant. Note that the power per unit area as used in Section 3.3 corresponds to a discharge current of 5.2 mA in the gridded system and was unattainable in this experiment.

From the above results we may construct an indicative model of how the fusion rate evolves within an IEC system as a function of increasing power. Figure 3.14 shows the characteristic behaviour of the surface and gaseous components to the total fusion rate; The surface and gaseous contributions, given in blue and red respectively, are expected to scale linearly with discharge

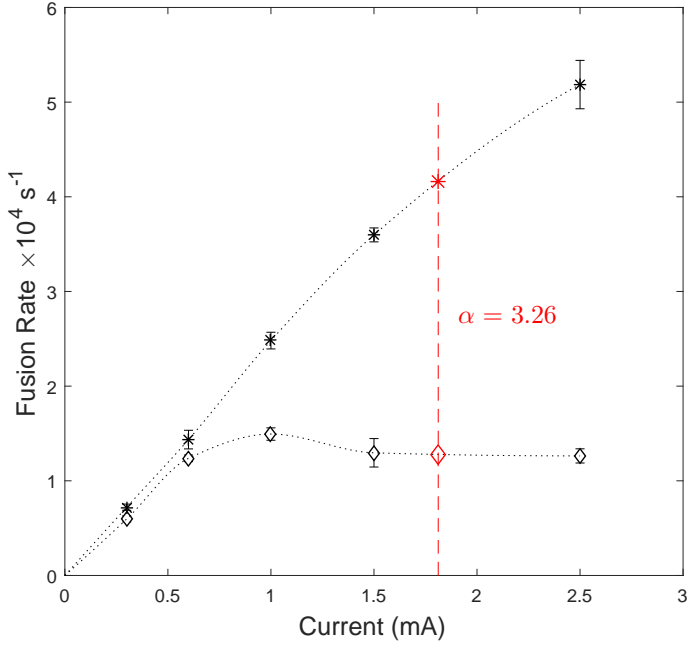


FIGURE 3.13: Fusion rate as a function of current for stainless steel and graphite IEC grids. Discharge conditions were  $1 \times 10^{-3}$  Torr, 35 kV.  $\diamond$  = 316 stainless steel, \* = Graphite. Dotted lines represent cubic spline interpolation of the measured data while the red, vertical line at  $I = 1.8$  mA indicates the power per unit area equivalent to that used in Figure 3.11. The computed value of  $\alpha = 3.26$  is in good agreement with that determined in the planar system.

current (power). Here we have allocated the gaseous component a gradient approximately one fifth that of the surface component, as consistent with the measurements in Section 3.2. Rarefaction of the background gas due to heating has been neglected in this picture. Increasing discharge power leads to heating of the cathode according to Equation 3.19, and thus the number of fusible targets on the surface is expected to decay exponentially, as given by Equation 3.6. The surface fusion is scaled accordingly, depicted in green in Figure 3.14. The total, measured fusion rate, computed as a sum of the surface and gaseous components is shown as a solid black line. In low power systems, such as those described above, the fusion rate is dominated by surface interactions as low grid temperatures mean that the number of target atoms bound to the cathode greatly exceeds that in the background gas. As the operating power is increased the fusion rate rolls off, reminiscent of the steel grid in Figure 3.13. In high power devices, such as those in which the grid is incandescent, the fusion rate asymptotes to that expected from a purely gas fusion system. In this way we reconcile our work with that of Cipiti [47] who concluded that surface interactions account for only 8% of the fusion obtained in the University of Wisconsin's IEC device. Regardless of this, it is apparent that the power efficiency of IEC machines could be greatly improved through the application of actively cooled cathodes, such that the surface interactions are not discarded during high power operation.

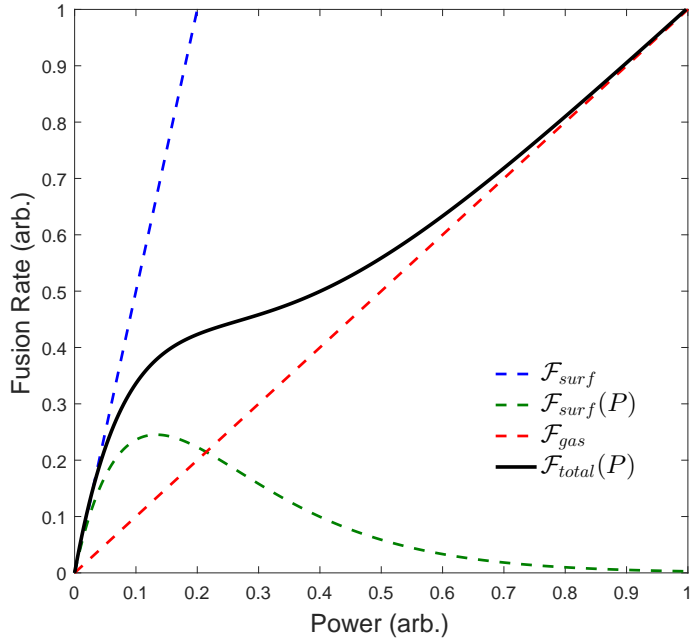


FIGURE 3.14: Generalised IEC fusion rate as a function of operating power. At low powers, where the grid temperature is relatively low, the fusion rate is dominated by surface interactions. At high powers, gaseous fusion dominates.

### 3.5 Summary

In this chapter we have explored the phenomenon of surface fusion in low power, gridded IEC systems. Fusion interactions in these devices are dominated by collisions between high energy ions and neutral targets adsorbed on the cathode surface and subsequently exhibit very strong dependencies on both the chosen cathode material, as well as the temperature at which that cathode is operated. Graphite was found to be an excellent material for use in IEC systems, with very high degrees of deuterium retention, even at elevated temperatures, indicating that graphite has the potential to serve as a cathode material in a future generation of high performance IEC devices. We have demonstrated the operation of one such IEC device, however uncertainties with respect to the grade of graphite used render these results incomplete. Further analysis is required to determine the exact properties that define an effective graphite cathode. Stainless steel cathodes were found to exhibit extremely poor performance at high temperatures and it is expected that this behaviour persists in other transition metal based cathodes. Such an observation suggests that huge improvements could be made in existing IEC machines through the implementation of actively cooled grids.

## Chapter 4

# Magnetically Confined Virtual Cathode Machine (MCVC-0)

The problem of cathode transparency in gridded inertial electrostatic confinement systems was explored in Section 1.4.1 and it was concluded that ion collisions with grid wires represent an insurmountable energy loss, even in the limit of extremely transparent grids ( $\eta > 0.999$ ). In the previous chapter we demonstrated that, in low power devices, ion collisions with neutral gas molecules adsorbed onto the grid wires may dominate the obtained fusion rate which, given the strong dependence on the *power per unit area* applied to the cathode, could potentially lead to the perverse scenario in which increasing cathode transparency may in fact *reduce* the absolute fusion output. We therefore wish to further investigate Polywell style devices with the view to extend work previously conducted by Carr [88–91] and Cornish [92, 93].

As shown in Table 1.5, the Carr and Cornish devices operated at very low power, with electron injection at energies of below 1 keV and beam currents of tens of milliamperes. The operation time scales of both devices were short, generally lasting no more than 1-2 ms. Our aim is to produce a device capable of achieving detectable deuterium-deuterium fusion and hence the operating voltage, pulse duration and available injection current must all be increased with respect to the Carr and Cornish machines. The design aims for the construction of the new device were as follows:

1. Must be constructed using only high vacuum compatible materials as given in the following

Metals - Stainless steel, Copper

Dielectrics - Glass, Ceramic

Polymers - Poly-ether-ether-ketone, Teflon

2. Achieve a peak magnetic field strength of 1 T for a minimum of 10 ms
3. Permit biasing of coil cases to 6 kV relative to the magnetic field coils
4. Support structure must tolerate high loads generated by the magnetic forces
5. Convenient mechanical assembly

The design requirements necessitated a magnetic coil construction that was considerably more robust than those used by Carr or Cornish. It was therefore not possible to build a six coil device within the confines of our existing vacuum chamber and so a two coil, biconic cusp configuration, such as that shown in Figure 1.3, was chosen. The resulting device can no longer strictly be referred to as a *Polywell* and hence we adopt the more general nomenclature of *Magnetically Confined Virtual Cathode*, with the designation of MCVC-0 being applied to our new machine. In the following sections we detail the design and construction of both the mechanical and electrical elements of the MCVC experiment and the devised solutions to the posed design problems are addressed.

#### 4.0.1 Magnetic field coils

The magnetic field coils constructed for the MCVC-0 device were subject to a number of stringent design constraints. The coils were required to fit inside the coil cases with sufficient clearance as to provide the required high voltage stand off as per design rule 3. Further constraint is applied via design rule 2, as the dimensions, wire gauge and number of turns contribute to the resistance and inductance of the coils and thereby influence the maximum obtainable coil currents and hence magnetic field strength. Due to the difficulty of hand winding efficiently packed coils, it was decided that a square profile coil offered the best opportunity for accurate turn placement. The inductance of a rectangular profile coil is approximated by

$$L \approx \frac{0.8r^2}{6r + 9h + 10w} N^2 \quad (4.1)$$

where  $r$  is the radius of the coil,  $h$  is its height,  $w$  is the radial width and  $N$  is the number of turns [133]. The resistance is similarly approximated as

$$R \approx \frac{8r\rho}{d^2} N \quad (4.2)$$

where  $d$  is the diameter of the wire and  $\rho = 1.71 \times 10^{-8} \Omega \text{ m}$  is the resistivity of annealed copper [134]. Both  $L$  and  $R$  tend to limit the maximum achievable pulse current for a given input power, and so we wished to minimise both quantities. Further detail of the coil design is given in Section 4.1.1 where the interplay between coil parameters and power supply requirements is

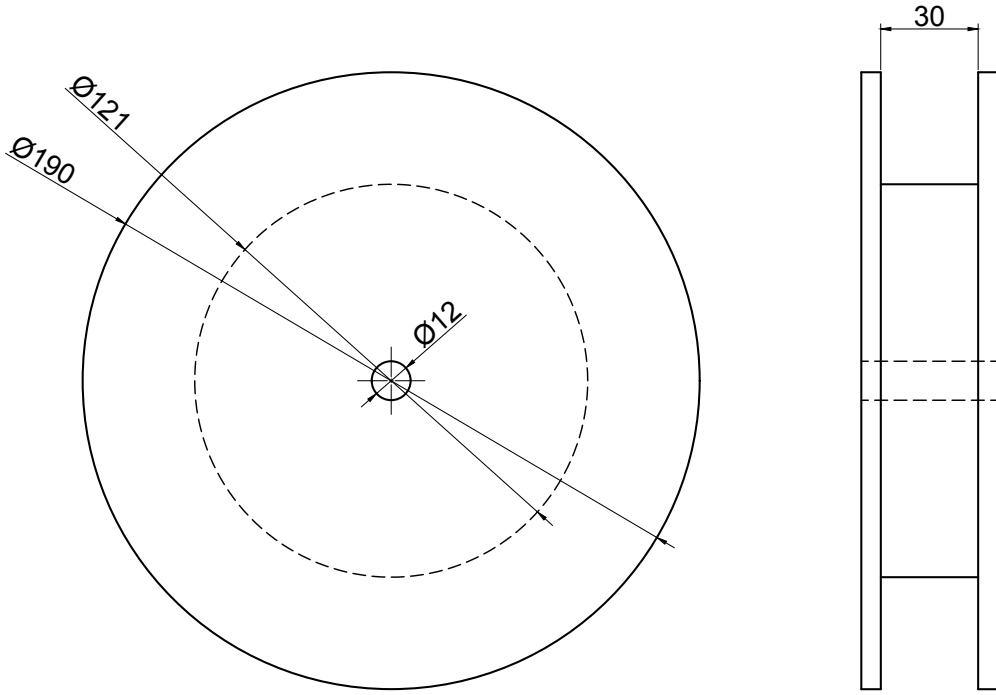


FIGURE 4.1: MDF coil former. All dimensions are in millimetres.

discussed. The final coil parameters were chosen as

$$r = 76 \text{ mm}$$

$$d = 2.65 \text{ mm}$$

$$N = 100$$

$$h = w = 30 \text{ mm} \approx d\sqrt{N}$$

$$L \approx 1770 \mu\text{H}$$

$$R \approx 0.15 \Omega$$

Grade II enamelled copper wire (1.8 kV, 200°C) was used in the preparation of the field coils. Coils were wound with the aid of a wooden former made from medium density multifibre board (Figure 4.1). The former was assembled from layers of 6 and 12 mm board such that it could be disassembled to allow removal of the finished coil. Captive cable ties, positioned within the former prior to winding, were used to bind the coil windings in place during removal. The coils were bound in teflon plumber's tape in order to prevent the coil windings from moving during handling. Once the coils were sufficiently secure, the cable ties that were added during winding

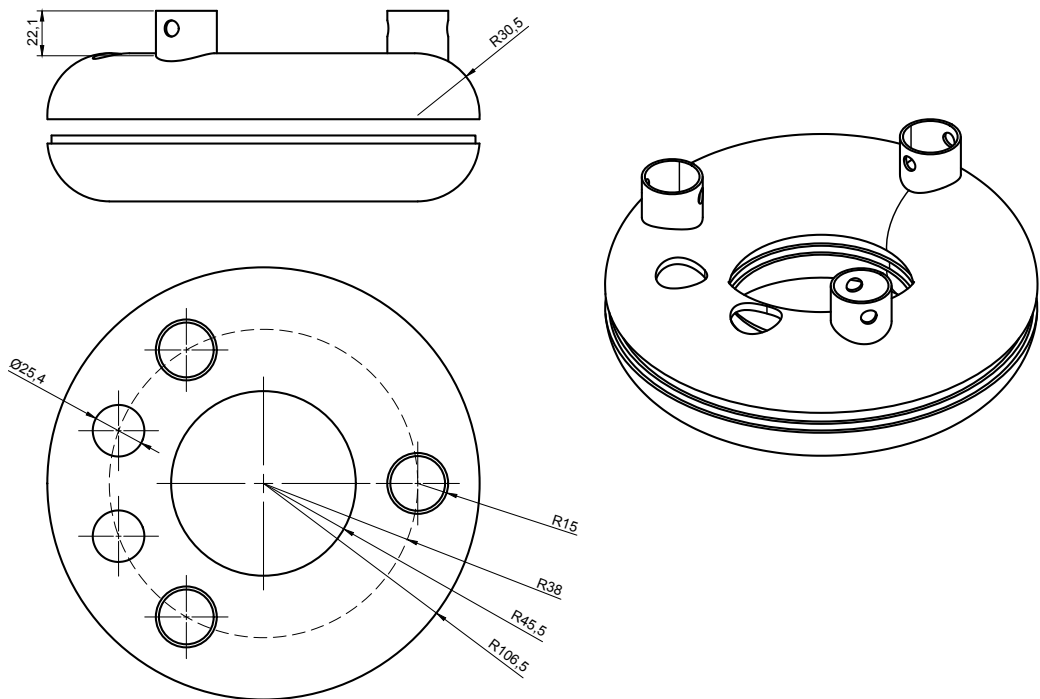


FIGURE 4.2: Magnetic field coil casing. All dimensions are in millimetres.

were removed.

#### 4.0.2 Coil Cases / Electrodes

The coils reside within toroidal metal cases which serve as the positive electrode in the MCVC system. High strength is required due to the large forces generated during a magnetic pulse. Previously coil cases have been constructed using metal spinning wherein sheet metal stock is spun on a lathe and pressed down over a timber form [91]. This technique however, is limited to thin walled, soft metals, such as aluminium, and as such was unsuitable for this project. The coil cases were instead constructed through the use of pre-formed, 316 stainless steel plumbing components. Sets of four 2 inch, 90 degree elbows were welded together to form tori with major and minor radii of approximately 76 and 30 mm respectively and a wall thickness of 4 mm. A total of four tori were prepared. The tori were cut into two asymmetric parts by cutting 2 mm proud of the torus central plane. The 2 mm of excess material was machined on a lathe to give interlocking spigots at the shell edges. The shells were then assembled and clamped before being machined to give a smooth outer surface.

Each of the finished tori were fitted with three  $\sim 30 \times 25$  mm sockets, positioned 120 degrees apart on the 76 mm major radius line. Two 25.4 mm holes with 40 degree spacing were drilled between two of the sockets to allow power feed-throughs to the coils within. The shell halves were held together with small stainless steel screw tabs. A finished coil case is depicted in Figure 4.2.

#### 4.0.3 Field Coil Sub-assembly

High voltage stand-off between the field coils and casings was achieved through the use of a vacuum gap. The coils were supported free floating within the tori using sets of interlocking insulating collars. The collars were made from poly-ether-ether-ketone (PEEK), a high temperature, ultra high vacuum compatible plastic and were prepared from a 16 mm board by water jet cutting.

In the region where the coil power passes through the electrode a teflon insert was used. Teflon was chosen as a material due to the high price of PEEK. The insert was machined to be conformal to the inner surface of a 120 degree section of the torus with tubular sections projecting through the openings in the coil case. An exploded view of the coil sub assembly is given in Figure 4.3

#### 4.0.4 Coil Terminal Contacts

Due to the large voltages on both the magnetic field coil (900 V) and electrode casings (6 kV), as well as the tight confines within the chamber, it was necessary to fully insulate the coil terminals to prevent arcing. In order to facilitate convenient connection between the coil ends (2.65 mm wire) and the high current cable used in this experiment, a set of 10 mm diameter copper lugs were manufactured. The lugs were drilled to accept the magnet wire and fastened in place with pairs of M3 $\times$ 3 grub screws. A teflon sheath was inserted between the lug and the projecting sections of the insert in order to give interleaved layers of insulation. In this way the surface tracking distance between the outer surface of the coil case and the coil itself was extended to over 80 mm. The cable end was passed through a threaded elbow section and inserted into a horizontal hole drilled in the lug. An M4 grub screw was used to secure the cable and ensure a good electrical connection. The top and side of the joint were then covered by a screw cap and the fore mentioned elbow. See Figure 4.4

#### 4.0.5 Support Frame

Designing a suitable support structure for the magnetic coils required the repulsive forces between the coils to be evaluated. Consider a pair of square profile field coils of radius  $r$ , minor

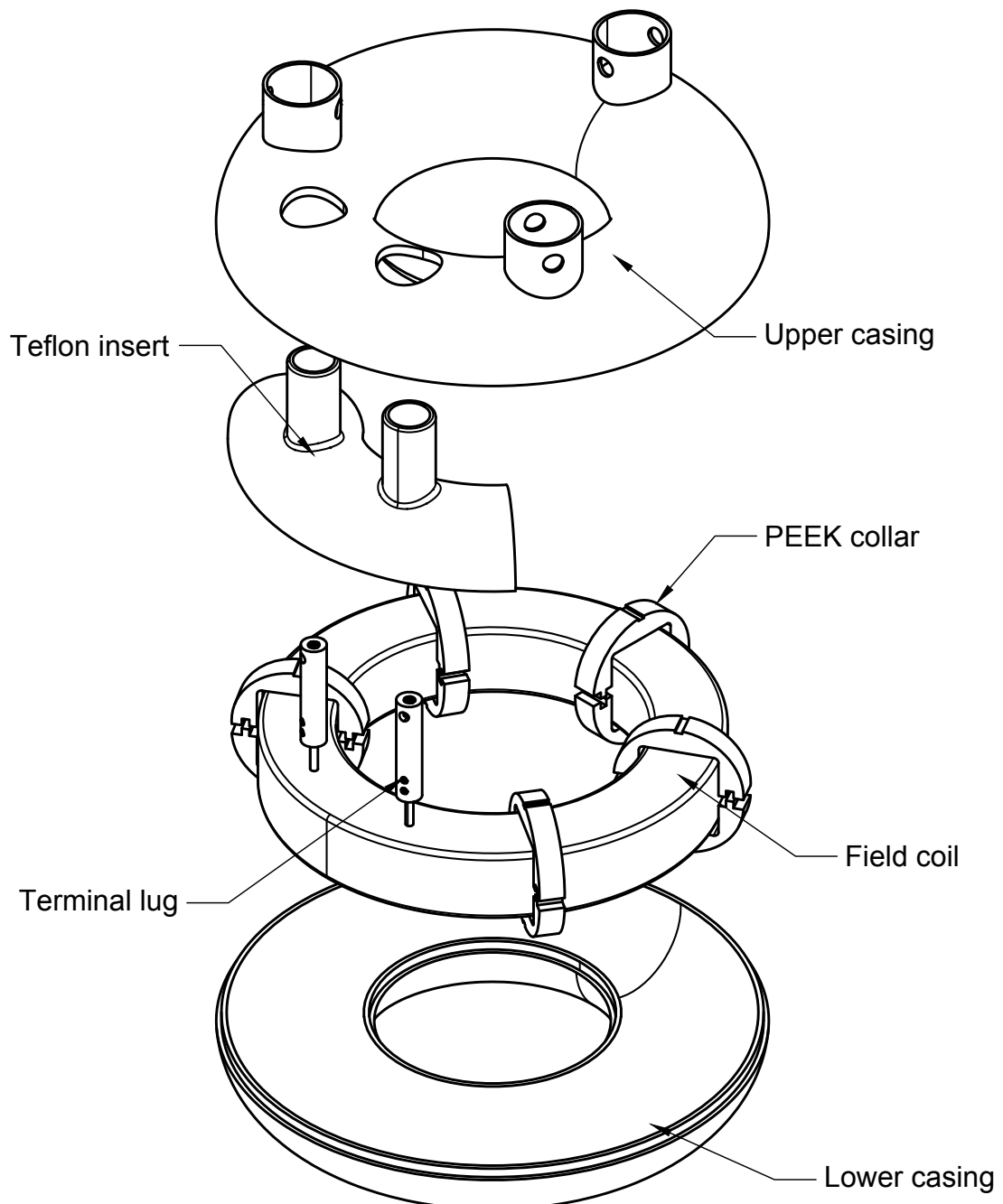


FIGURE 4.3: Magnetic field coil sub assembly.

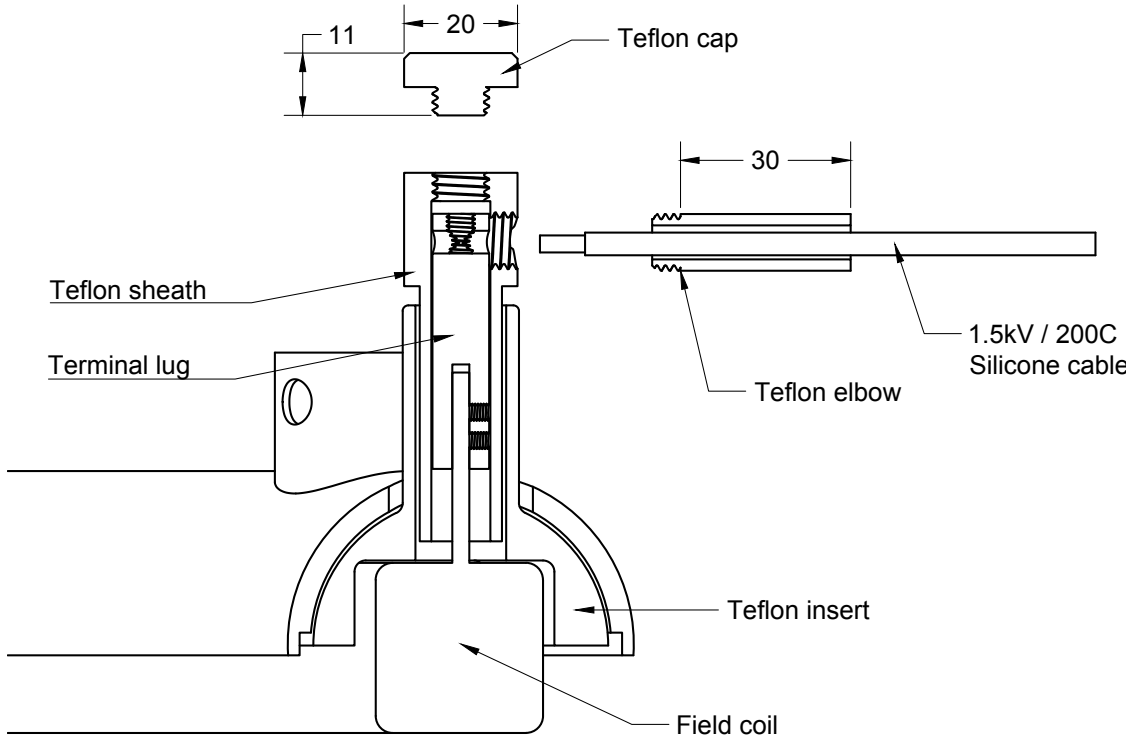


FIGURE 4.4: Coil terminal insulation assembly. All dimensions are in millimetres.

dimension  $2a$ , separated by a distance  $2S$  and carrying a total amp-turns current  $I$ . The coils are arranged such that their magnetic dipoles point in opposite directions, resulting in a cusped field such as that shown in Figure 6.2.

We wish to calculate the force on coil 2 due to the magnetic field generated by coil 1. The force acting on a current distribution  $J(\vec{r})$  in a magnetic field  $B(\vec{r})$  is given by

$$\vec{F} = \int \vec{J}(\vec{r}) \times \vec{B}(\vec{r}) d^3r \quad (4.3)$$

and so we may write the  $z$  component of the force on coil 2 as

$$F_z = 2\pi \int_{S-a}^{S+a} \int_{r-a}^{r+a} J_{\varphi, \text{Coil } 2}(\rho, z) B_{r, \text{Coil } 1}(\rho, z) \rho d\rho dz \quad (4.4)$$

where

$$J_{\varphi, \text{Coil } 2}(\rho, z) = \begin{cases} \frac{I}{4a^2} & (r - a) \leq \rho \leq (r + a), \\ & (S - a) \leq z \leq (S + a) \\ 0 & \text{elsewhere} \end{cases} \quad (4.5)$$

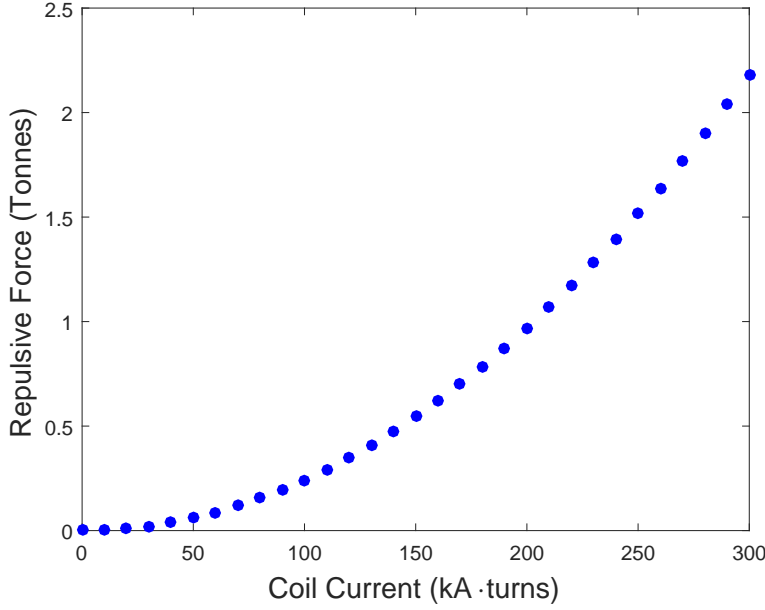


FIGURE 4.5: Repulsive force between cusped magnetic field coils.  
 $r = 76 \text{ mm}$ ,  $a = 15 \text{ mm}$ ,  $S = 50 \text{ mm}$

The magnetic field  $B_{r,Coil1}$  was calculated as described in Section 6.1.1. The integral in Equation 4.4 was then evaluated and the calculated forces for the described device are given as a function of coil current in Figure 4.5. It may be seen that the repulsive force between coils does not exceed 2.5 tonnes (24,500 N) and so a support structure was devised to provide  $\times 2$  redundancy.

In order to minimise the perturbation to the electric field due to the frame components, the frame was designed as a close fit into the cylindrical vacuum chamber. A pair of 12 mm thick, 305 mm diameter stainless steel plates were prepared via water jet cutting and formed the main coil support surfaces. Holes in the upper and lower plates allowed for location of the coils, anchoring of the frame within the vacuum chamber, access to the coil terminals as well as winching points for lifting the assembly via a crane. The end plates were fastened together by three vertical struts consisting of 50×10 mm stainless steel flat bar. The final assembly had a total weight of  $\sim 35 \text{ kg}$  and an estimated yield strength of  $> 6 \text{ tonnes}$ . The coil support structure is depicted in Figure 4.6. Following fabrication the support frame and coil cases were contaminated with residual cutting oils used in the manufacturing process. Further, untreated stainless steel is known to out-gas hydrogen in high and ultra high vacuum systems [135]. To improve the high vacuum compatibility of the apparatus, all steel components were baked at  $500^\circ\text{C}$  for 72 hours.

The magnetic field coils were mounted to the support frame by PEEK bushings, such that the coils could be biased relative to the support structure. The PEEK supports were machined with

multiple fins such as to increase the arc creep distance. In order to prevent sputtering damage the bushings were sheathed in 60 mm O.D. alumina ceramic tube.

## 4.1 Power Supplies

Due to the extremely high power requirements for driving both the magnetic field coils and the high voltage plasma circuit, it was necessary to build dedicated pulsed power supplies for this project. In this section we provide technical details on both the pulsed capacitor bank power supply (PCPS), and high voltage bias supply (HVBS) constructed for these purposes.

### 4.1.1 Pulsed Capacitor Bank Power Supply (PCPS)

In order to drive the large current pulses required by the MCVC coils a pulsed capacitor bank was designed and constructed. The basic circuit is given in Figure 4.7 and consists of an initially charged capacitor  $C$ , switched into a series  $LR$  load. In the case of the MCVC device, inductive and resistive impedance are of the same order of magnitude and so the circuit may not be simplified to a single load element. In order to prevent reverse charging of electrolytic capacitors, the inductor current is snubbed by diodes parallel to the MCVC coils.

#### 4.1.1.1 Theoretical $LCR$ circuit response

As the design requirements for the MCVC device are expressed in terms of magnetic field strength and pulse duration, it was necessary to identify the set of components  $L$ ,  $C$ , and  $R$ , as well as the initial charge voltage  $V_0$ , that gave the required pulse, while remaining practically attainable. It was therefore informative to formulate the theoretical response of the ideal circuit such that possible configurations could be explored. The governing equations for each of the circuit elements are

$$I = -C \frac{dV_c}{dt} \quad (4.6)$$

$$V_i = L \frac{dI}{dt} \quad (4.7)$$

$$V_r = IR. \quad (4.8)$$

where  $V_c$ ,  $V_i$ ,  $V_r$  are the voltages across the capacitor, inductor and resistor respectively and the diodes are considered to be ideal [136]. Combining Equations 4.6-4.8 gives a second order differential equation for the voltage on the capacitor as a function of time.

$$\frac{d^2V_c}{dt^2} + \frac{R}{L} \frac{dV_c}{dt} + \frac{1}{LC} V_c = 0 \quad (4.9)$$

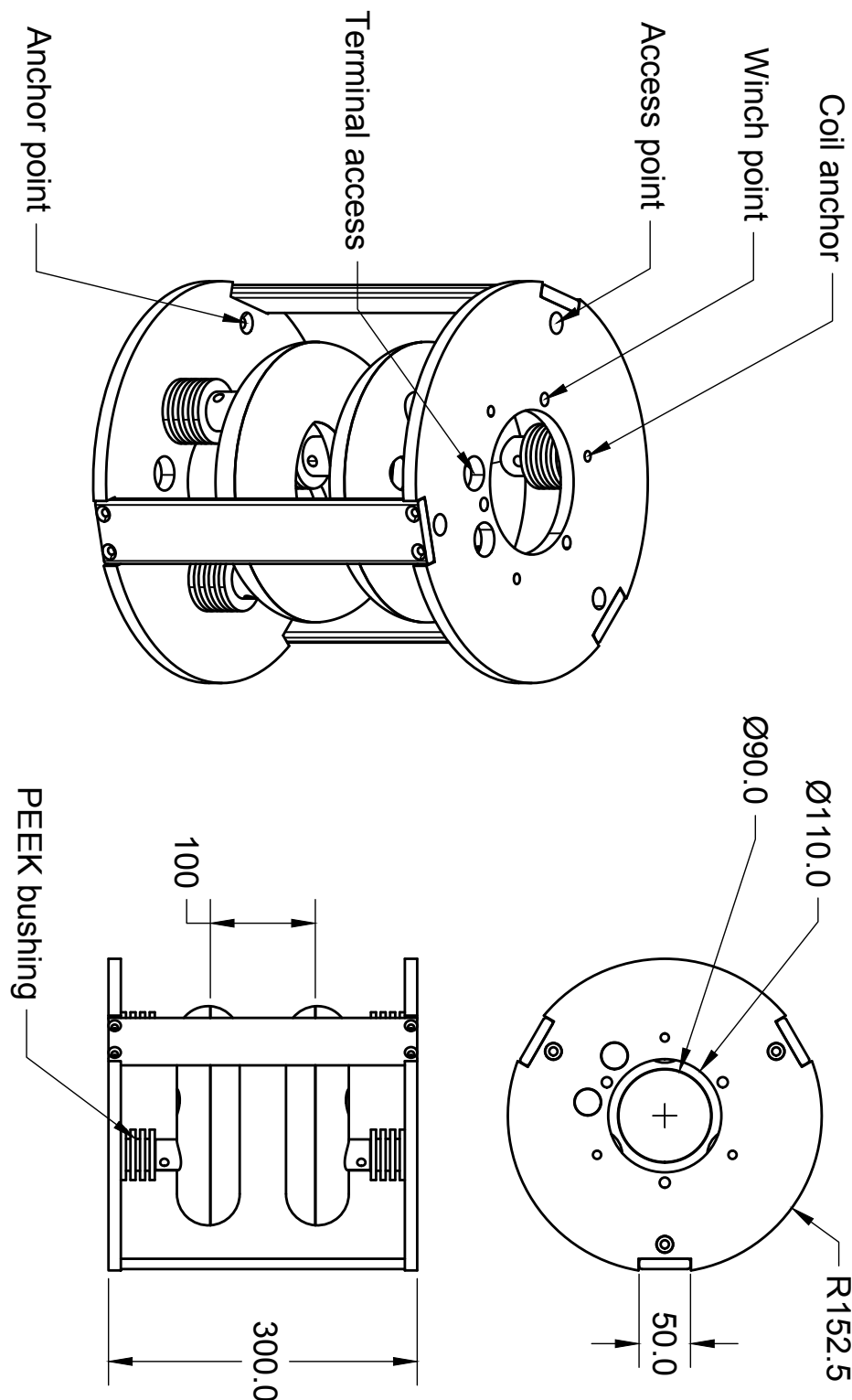
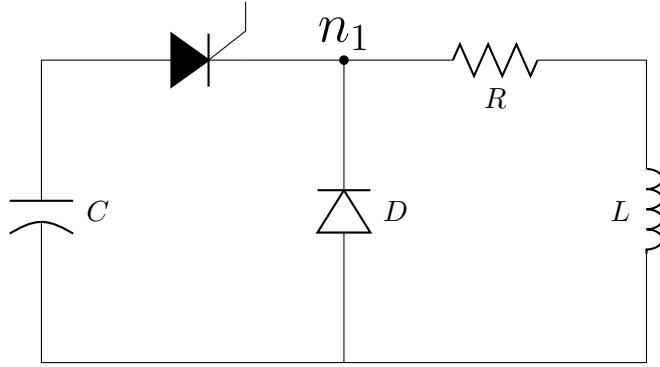


FIGURE 4.6: MCVC support frame. All dimensions are in millimetres.

FIGURE 4.7: Snubbed  $LCR$  circuit

Equation 4.9 may be solved to give

$$V_c(t) = V_0 e^{-\zeta \omega_n t} \left[ \cos(\omega_d t) + \frac{\zeta}{\sqrt{1 - \zeta^2}} \sin(\omega_d t) \right] \quad (4.10)$$

where  $V_0$  is the initial voltage on the capacitor and

$$\begin{aligned} \omega_n &= \frac{1}{\sqrt{LC}} \\ \omega_d &= \omega_n \sqrt{1 - \zeta^2} \\ \zeta &= \frac{R}{2} \sqrt{\frac{C}{L}}. \end{aligned}$$

$\omega_n$  is the natural frequency of the  $LC$  circuit,  $\omega_d$  is the damped frequency and  $\zeta$  is called the damping ratio. The corresponding current is calculated according to Equation 4.6 as

$$I(t) = \frac{\omega_n C V_0}{\sqrt{1 - \zeta^2}} e^{-\zeta \omega_n t} \sin(\omega_d t). \quad (4.11)$$

In the case where  $\zeta \geq 1$  Equation 4.11 is true for all time. If  $\zeta < 1$  the  $LCR$  circuit will oscillate and so the voltage and current only obey the equations above until the voltage on node  $n_1$  drops to zero. The inductor current is then snubbed via the flyback diode, obeying an  $LR$  decay characteristic

$$I_d(t) = I_0 e^{-\frac{R}{L}t}. \quad (4.12)$$

The cutoff time,  $t_c$ , between these solution regimes is found when

$$\cos(\omega_d t_c) + \frac{\zeta}{\sqrt{1 - \zeta^2}} \sin(\omega_d t_c) = 0 \quad (4.13)$$

for which the solution is

$$t_c = \frac{2}{\omega_d} \tan^{-1} \sqrt{\frac{1 + \zeta}{1 - \zeta}} \quad (4.14)$$

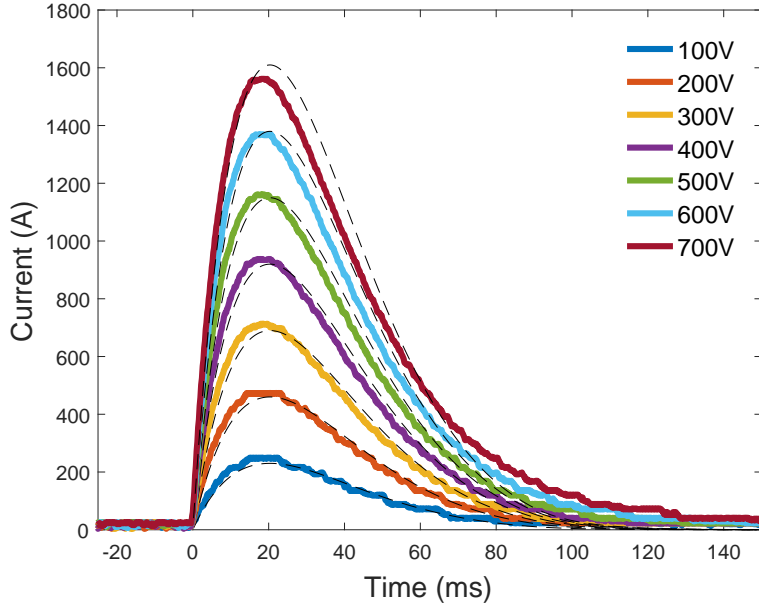


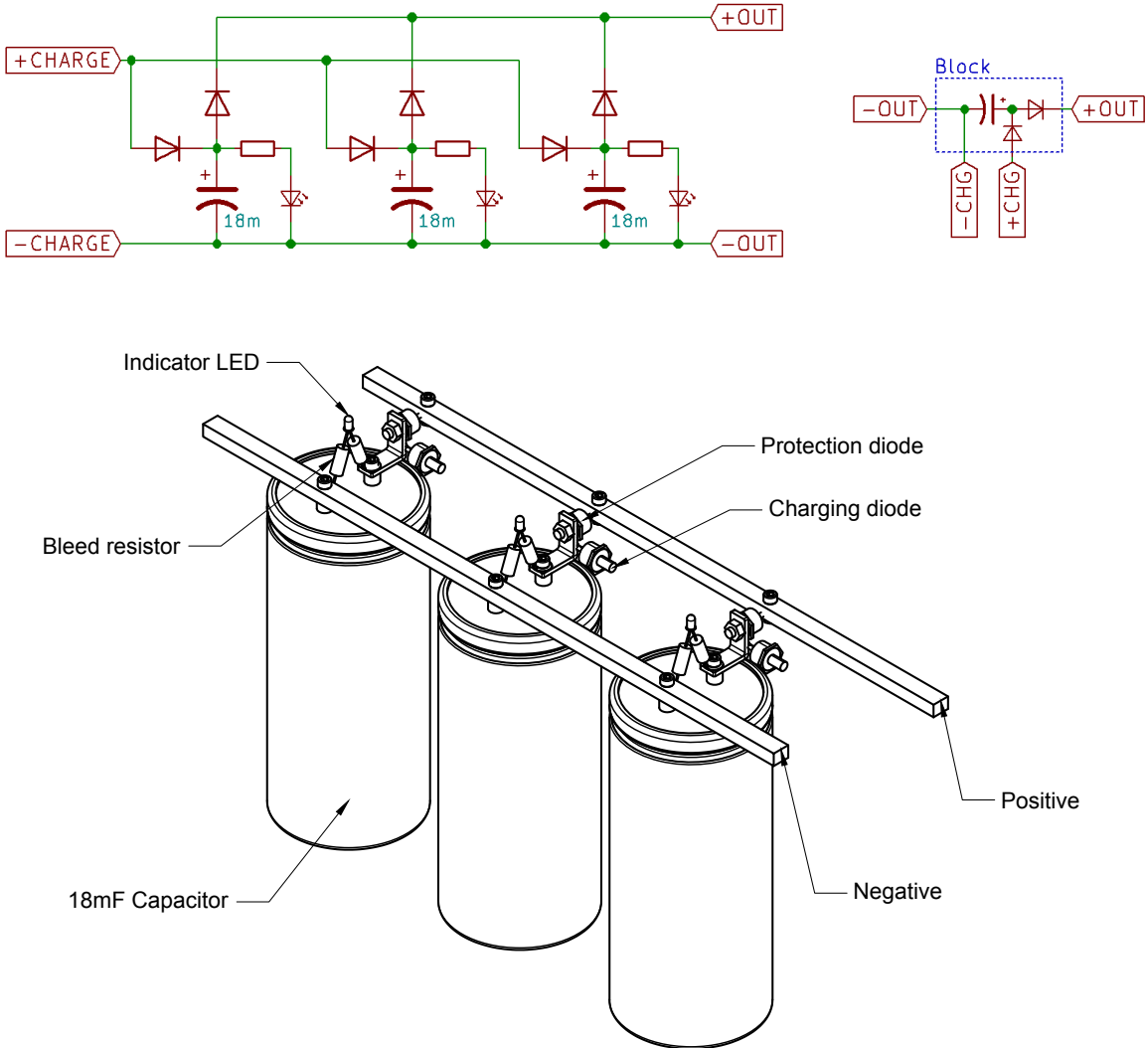
FIGURE 4.8: Coil current pulses in MCVC device for varying capacitor bank charge voltage.  
Dashed lines represent the theoretical pulse profiles.

Equating expressions 4.11 and 4.12 at  $t_c$  and solving for  $I_0$  completes the expression for the snubbed current pulse as

$$I(t) = \begin{cases} \frac{\omega_n C V_0}{\sqrt{1-\zeta^2}} e^{-\zeta \omega_n t} \sin(\omega_d t) & t \leq t_c \\ \omega_n C V_0 e^{\zeta \omega_n t_c} e^{-\frac{R}{L}t} & t > t_c. \end{cases} \quad (4.15)$$

450 V electrolytic capacitors are readily available [137] in large values ( $>10$  mF) which may be configured in parallel or series to obtain an appropriately specified capacitor bank. For safety reasons it was elected that the initial charging voltage should not exceed 900 V. Using the readily available sizes of copper wire Equation 4.15 was used in conjunction with Equations 4.1 and 4.2 to simulate hypothetical devices until a suitable set of coil parameters  $d, N$  and the required driving capacitance of  $C \sim 0.1$  F were obtained.

Coil current pulses are given in Figure 4.8 as a function of charging voltage. Dashed lines give the predicted pulses as computed by Equation 4.15. The total inductance of the device is slightly less than the simple sum of the two coils due to negative coupling between the coils. Likewise the resistance of the system is slightly larger due to non-zero resistance in other circuit components. Least squares fitting, using a Monte-Carlo Markov-Chain (MCMC) algorithm [138], of the experimentally determined pulses gives  $L = 3.0$  mH and  $R = 0.35$   $\Omega$ .

FIGURE 4.9: Capacitor Rail. 450 V, 57,000  $\mu$ F.

#### 4.1.1.2 Capacitor Bank Layout

The PCPS was composed of twenty-four 450 V, 18 mF (18,000  $\mu$ F) electrolytic capacitors [137]. Groups of three capacitors were configured in parallel to produce 57 mF ‘Rails’, so named for the 1/2”  $\times$  3/8” copper bus bars used to tie the capacitor terminals together. Protection diodes (800 V, 1500 A, [139]) on the output terminal of each capacitor prevented an uncontrolled discharge should a single capacitor fail closed circuit. Bleed resistors (20 k $\Omega$ ) and indicator LEDs also spanned the terminals of all capacitors. The layout of a single rail is given in Figure 4.9. Two shelves of capacitors contained 4 rails each arranged such that vertically aligned pairs of rails could be wired in series to produce a set of four 27,000  $\mu$ F, 900 V sub-banks. Each sub-bank was triggered independently with a silicon controlled rectifier (SCR) such that the PCPS acted as four smaller power supplies which could be used separately, together or in sequence to

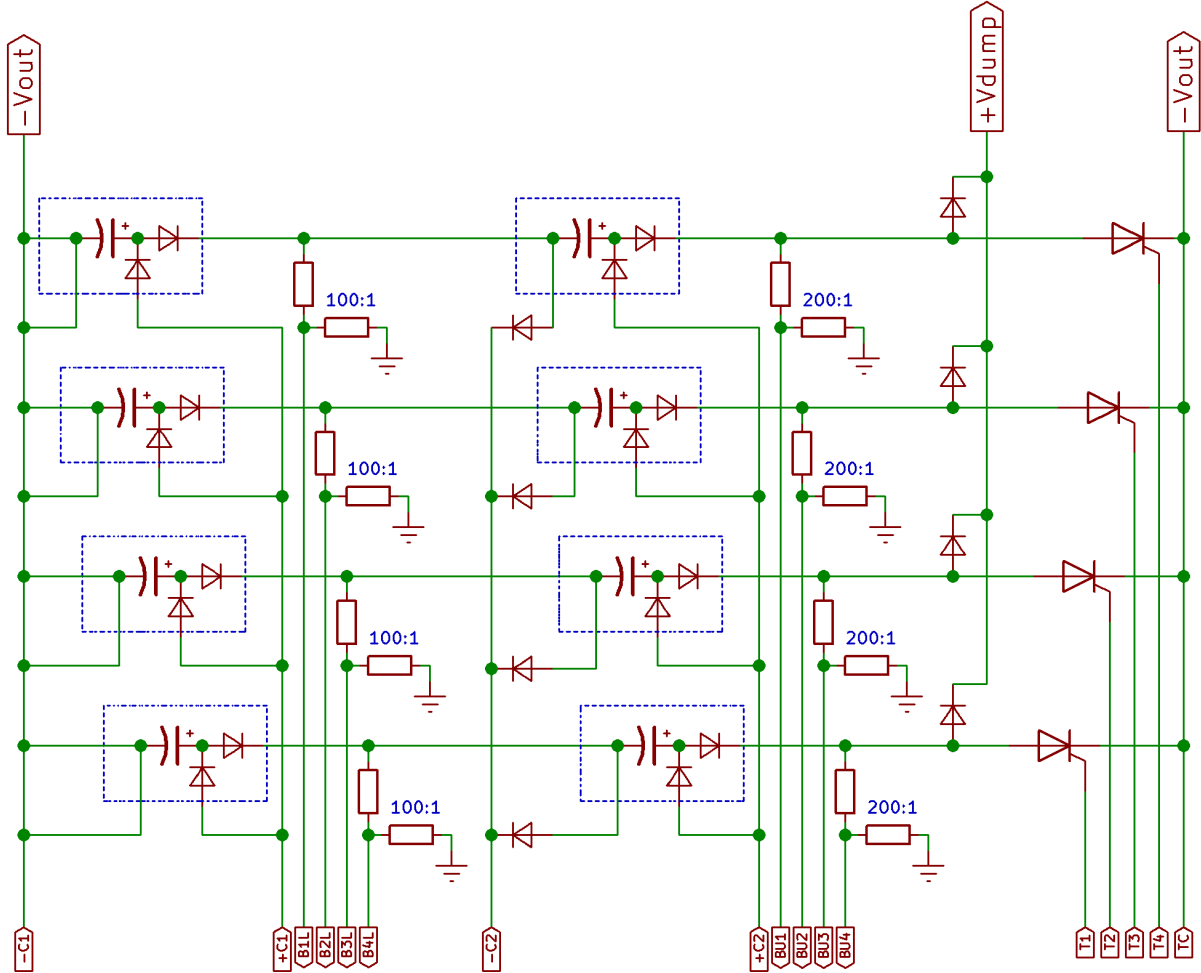


FIGURE 4.10: Capacitor bank layout.

produce the desired pulse heights and durations. The switching shelf was constructed according to Figure 4.11 with sections of  $50 \times 12$  mm aluminium flat bar serving as conductors. Four bus-bars receive input from the sub-banks and a single  $\Pi$  section serves as the main output bus. The SCR clamping structures bridge the gaps between input and output buses providing a convenient means for construction as well as large conducting contact areas. All high current connections were made using  $35 \text{ mm}^2$  welding cable. Pulse transformers for SCR triggering were located on the shelf directly above the SCRs. The main earth bus is aligned parallel to the output bus and was equipped with a pair of high voltage, high power diodes ( $4.2 \text{ kV}$ ,  $9 \text{ kA}$ ) which serve to snub any  $LC$  oscillation and prevent reverse polarisation of the electrolytic capacitors.

The capacitors were charged by two PAS398,  $450 \text{ V}$ ,  $2.5 \text{ A}$  floating power supplies [140]. The power supply for the upper rails was allowed to float on the positive terminal of the lower rails. Capacitor voltages were measured using  $100:1$  and  $200:1$  voltage dividers on the lower and upper rails respectively. Output currents were measured using a flux gate current transducer.

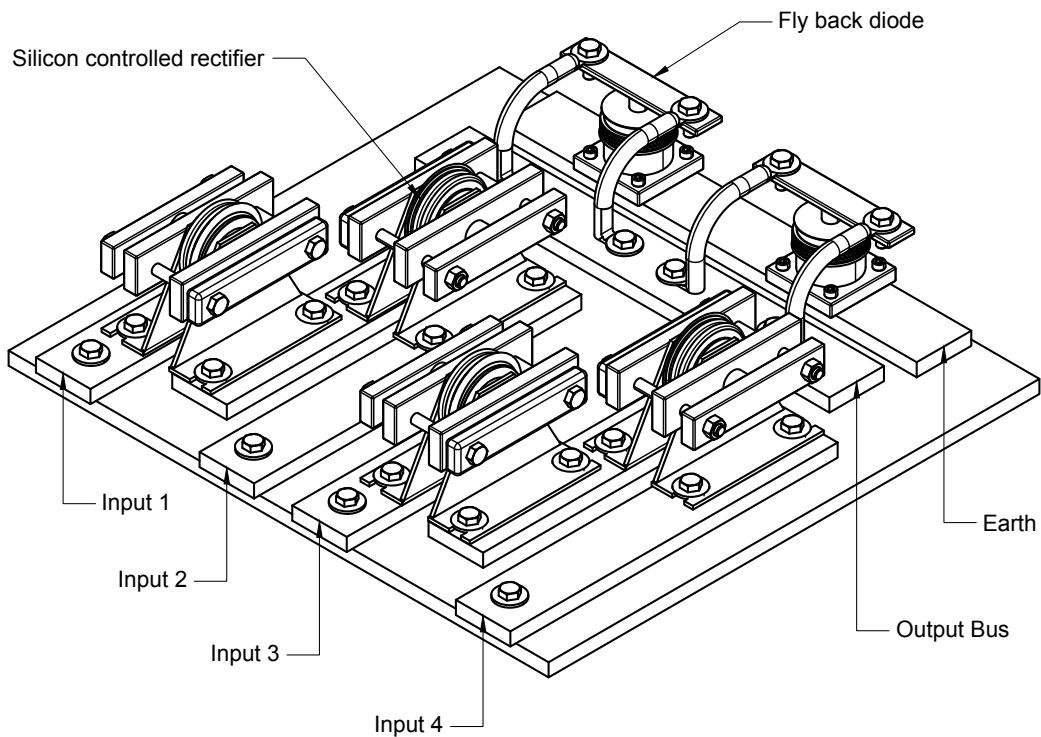


FIGURE 4.11: Configuration of the main switching shelf in the PCPS.

#### 4.1.1.3 Capacitor Bank Control and Automation

The associated PCPS control system is illustrated in Figure 4.12. The operation of the PCPS was characterised by five actions; They are *Arm*, *Charge Power*, *Enable*, *Charge* and *Trigger*. *Arm* disconnected the capacitors from the low resistance ( $2\Omega$ ) safety dump and was activated through application of system power. Cutting power by way of the emergency stop button would re-engage the dump circuit leading to a rapid discharge of the capacitors. *Charge Power* engaged mains power to the PAS395 charging power supplies and *Enable* disengaged the high resistance ( $330\Omega$ ) bleed circuit enabling bank charging. Finally the *Charge* action activated the charging relays, connecting the power supplies to the capacitors.

With the exception of *Arm*, each of the main bank operations could be configured into the MANUAL, AUTO and OFF states by way of mode select switches on the front panel. In the MANUAL state, the action could be activated directly via switches on the front panel. In the AUTO state control of the action was yielded to the system micro-controller. In the OFF state, the action was disabled entirely.

Automatic bank operation was controlled by a Controllino MEGA, an industrial micro-controller system based on the ATmega2560 [141, 142]. The device is equipped with large numbers of both

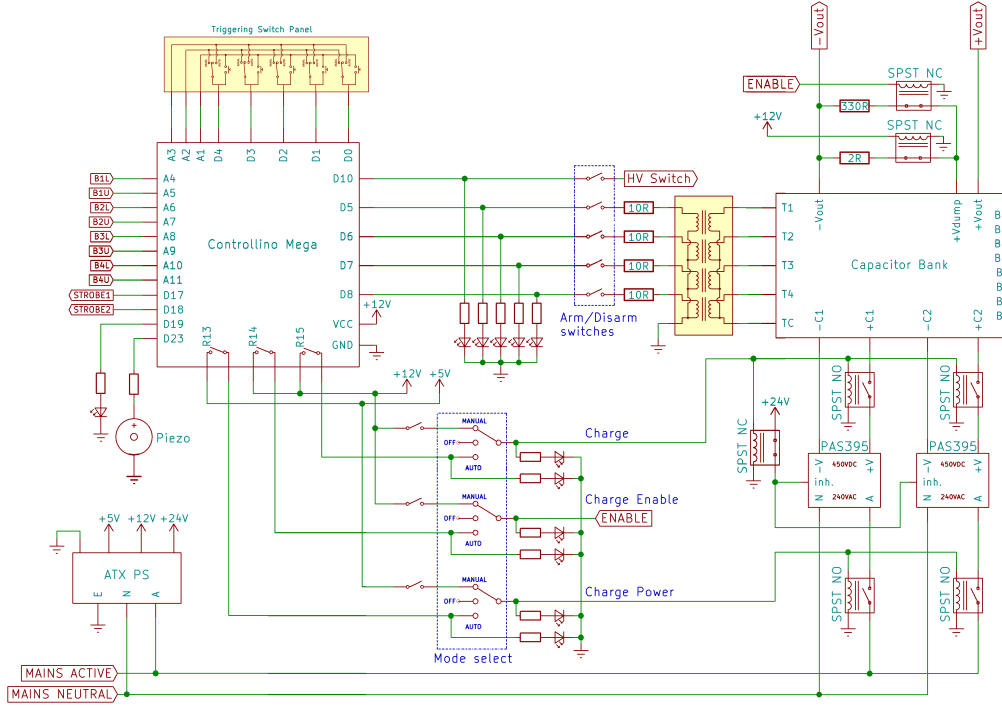


FIGURE 4.12: Pulsed capacitor bank power supply control system

digital and analogue inputs and outputs, as well as several built in relays capable of switching mains voltages at large currents (240V, 16A). The digital outputs are similarly capable of delivering output currents of up to 2 Amperes. Bank operations could be controlled by issuing commands to the Controllino via Ethernet, thereby permitting extended pulse sequences to be programmed.

Triggering pulses for the four sub-banks as well as the high voltage bias supply (see Section 4.1.2) were provided by the Controllino. Trigger timings could be uploaded to give arbitrary pulse configurations according to need. As above, the triggers could be placed in the MANUAL, AUTO and OFF states. In addition, *arm/disarm* switches were placed in series with each trigger.

Two strobe outputs were used to synchronise with other components of the MCVC system. The *System* strobe was used to activate the multi-channel pulse generator (See Section 4.3) and subsequently all sub-systems, while the *Acquisition* strobe was synchronised with the leading edge of the magnetic field pulse and was used to trigger oscilloscope capture.

#### 4.1.2 High Voltage Bias Power Supply

Bias voltages of up to 6 kV were applied to the coil cases. A 6 kV, 180  $\mu$ F capacitor was charged by an SPL300, 50 kV Spellman power supply, and switched to the device by a MOSFET based

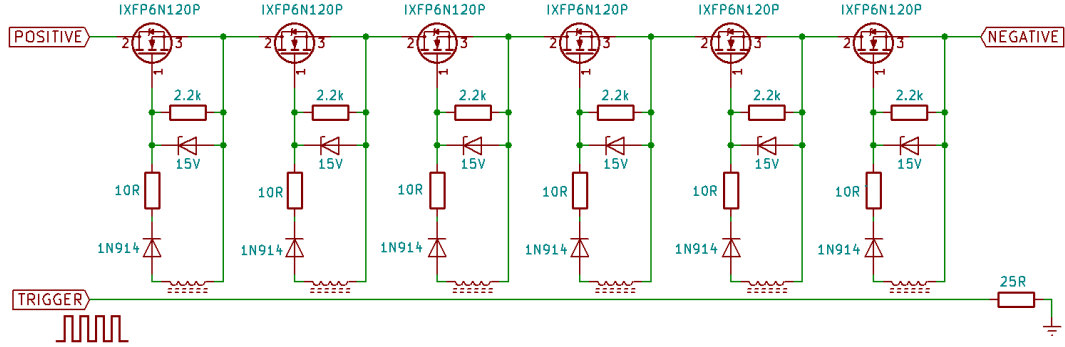


FIGURE 4.13: 7.2 kV MOSFET switch module

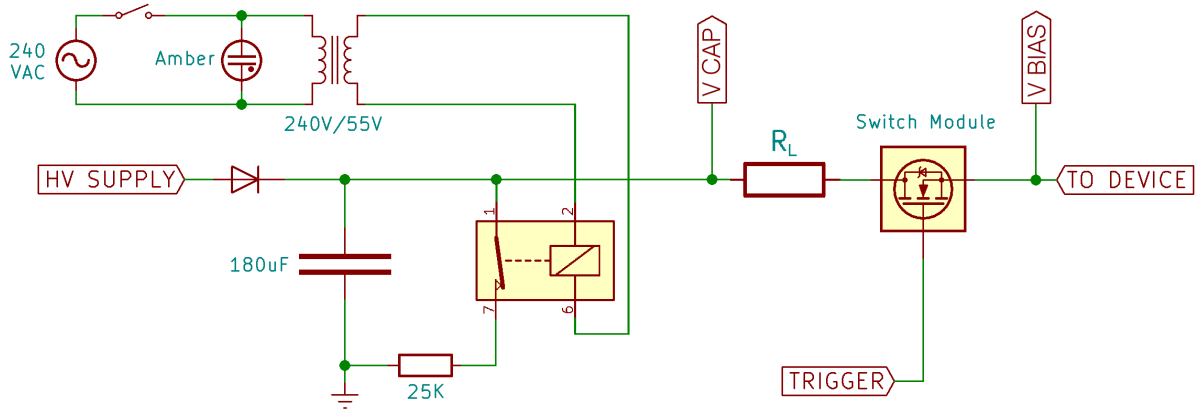


FIGURE 4.14: 6 kV bias power supply

switch. High voltage switching modules were constructed using groups of six IXFP6N120P FETs (1200 V, 6 A, [143]) configured in series to create 7.2 kV units. These could be further configured in series to increase the operating voltage. Half wave rectifiers configured between the gate and source of each FET allowed the devices to be switched while maintaining large voltage stand-off ( $>25$  kV) between the high voltage components and the triggering circuitry. The intrinsic gate capacitance of the FETs ( $\sim 10$  nF) was sufficient to smooth the rectified pulses. The devices were triggered simultaneously by way of a common primary, which was driven by a 200 kHz, 24 V pulse train. See Figure 4.13.

The capacitor could be discharged via a set of four parallel  $100\text{ k}\Omega$  dump resistors switched using a mechanical relay. An interchangeable load resistor,  $R_L$ , allowed the resistance of the plasma circuit to be adjusted. A schematic of the HV bias set up is given in Figure 4.14.

## 4.2 Coil Temperature Monitoring

The high power required to drive the MCVC magnetic field tended to lead to rapid heating of the field coils and so monitoring of the coil temperature was required to ensure that the

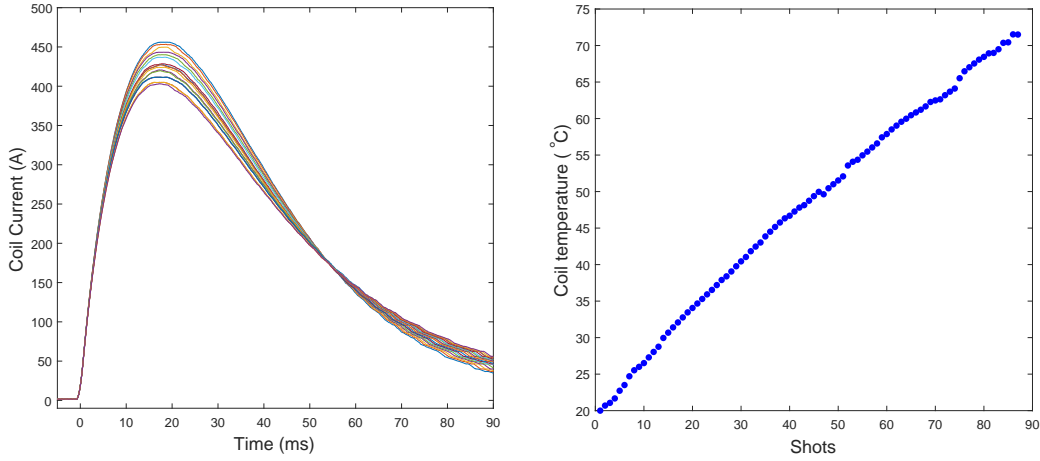


FIGURE 4.15: Changing current profiles (*Left*) and computed coil temperature (*Right*) over repeated shots. PCPS charge voltage = 200 V, Duty cycle = 30 seconds.

coils did not approach their maximum operating temperature of 200 °C. Further, increasing coil temperature led to alteration of the obtained current pulse, caused by changes in the coil resistance according to

$$R(T) = R(20^\circ\text{C}) [1 + \alpha (T - 20^\circ\text{C})] \quad (4.16)$$

where  $\alpha = 0.0039$  is the thermal coefficient of copper.

The expressions derived in Section 4.1.1 provided a convenient, non-intrusive means of monitoring the coil temperature without the need for additional sensors. Equation 4.15 was fitted to measured current pulses using the resistance as a fitting parameter and the coil temperature subsequently computed using Equation 4.16.

The left hand panel of Figure 4.15 illustrates how coil current profiles may vary over repeated shots. In this example the capacitor bank was charged to 200 V and the coils fired every 30 seconds. The right hand panel gives the computed coil temperature as a function of the number of pulses.

### 4.3 Programmable Pulse Generator

Operating of the MCVC apparatus involved the time-critical control of numerous sub-systems and data acquisition devices. The electron gun power supplies, gas puffing valve, optical shutter and spectrometer all required triggering pulses at appropriate times relative to the magnetic pulse of the main device. As such, it was convenient to build a multi-channel, arbitrarily programmable pulse generator that could be programmed with the required triggering sequences. An ATMega328 micro controller [144] was programmed to generate pulse sequences on 10 of its digital outputs. Simple buffers were then constructed such that the output channels could

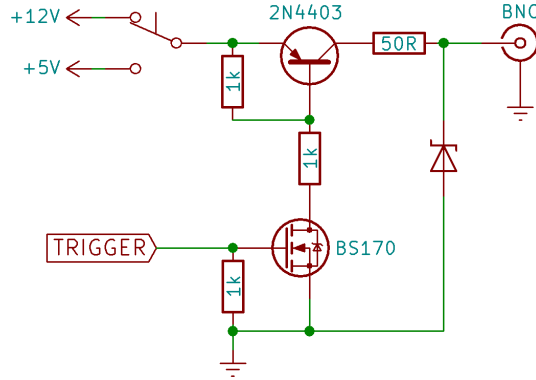


FIGURE 4.16: Pulse generator output stage.

provide sufficient current to activate solenoid relays. The outputs could also be independently configured to provide either 5 V or 12 V according to need. The output stage of a single pulse channel is given in Figure 4.16.

## 4.4 System Control Hierarchy

The MCVC-0 system control hierarchy is given in Figure 4.17. Digital data connections, such as Ethernet and USB-serial are given in blue. Analogue control signals, such as trigger pulses, voltage measurements and solenoid relay power are shown in red. Finally, direct power connections such as magnetic field coil power, electrode bias and stepper motor drive are shown in black. The system was operated from a dedicated server, able to issue commands to each of the sub devices in the hierarchy. User interfacing was permitted via a single lab PC where system actions could be executed via a text command line. All control software was coded in Python 3.0 or C++, and was written by Dr John Hedditch.

The configurations of the oscilloscopes, spectrometer, capacitor bank and pulse generator could all be adjusted remotely via the server, and extended experimental runs automated by the execution of a scripted sequence. Following each shot, the acquired data could be downloaded to the server and saved in the relevant sequence directories. An example trigger sequence for a shot of the MCVC system is given in Table 4.1.

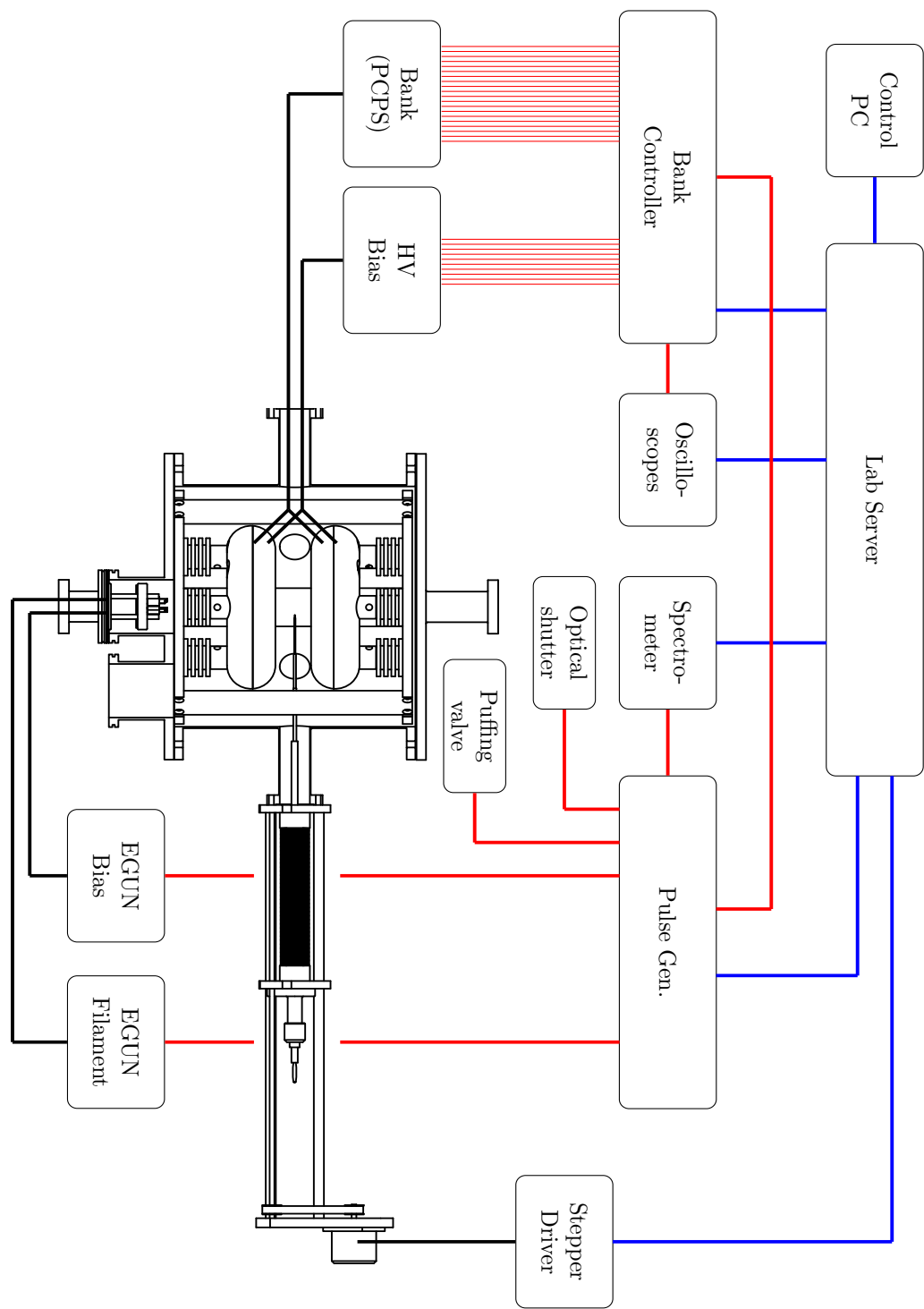


FIGURE 4.17: MCVC control system hierarchy. Digital data connections (USB Serial, Ethernet) are given in blue. Analogue data connections (trigger logic, solenoid relay power) are given in red and direct power connections are shown in black.

Time (ms)	Instruction From ...	To ...	Command
-3000	Server	Bank Controller	Pulse
-3000	Bank Controller	Pulse Generator	Trigger
-2500	Pulse Generator	Egun Filament	Activate
-500	Pulse Generator	Egun Bias	Activate
-50	Bank Controller	HV Bias	Trigger
0	Bank Controller	PCPS	Trigger
0	Bank Controller	Oscilloscopes	Trigger
20	Pulse Generator	Spectrometer	Trigger
200	Bank Controller	HV Bias	Deactivate
500	Pulse Generator	Egun Filament	Deactivate
500	Pulse Generator	Egun Bias	Deactivate
1000	Server	Oscilloscopes	Download Data
1000	Server	Spectrometer	Download Data
5000	Server	Stepper Driver	Translate Probe

TABLE 4.1: Example event time line during MCVC-0 plasma shot.

# Chapter 5

## Langmuir Probe Diagnostic

Critical to the operation of virtual cathode devices is the development of an electrostatic potential well at the core of the device. We therefore wish to monitor the plasma potential, or space potential  $V_s$  within MCVC-0 as a function of spacial position, as well as observe how the potential distribution evolves in time. In previous Polywell studies by Directed Technologies Inc. [83] and Cornish [92, 93], these measurements have been made through the use of emissive-capacitive probes, of the type described by Wang [145]. This style of probe has the advantage of being relatively simple to construct and has been shown to faithfully represent the space potential in fusion plasmas. However capacitive coupling lends itself only to time-varying systems, as limited by the time constant of the probe  $RC$  circuit. In the MCVC system the static electric field duration could exceed 100 ms and so capacitive diagnostics were avoided. Carr [90, 91, 94] constructed a low voltage, swept Langmuir probe capable of generating a single  $-150 \rightarrow +150$  V sweep over  $\sim 100 \mu\text{s}$ , and we elect to use a similar diagnostic here. Unlike Carr's probe however, which provided a snapshot into the state of the plasma at a specific time during a shot, we instead chose to operate a biased DC probe and obtain  $IV$  measurements over multiple successive shots. Moreover, DC operating permitted biasing over a wider range of values than the  $-150 \rightarrow +150$  V that is characteristic of swept probe instrumentation. In this chapter we discuss the relevant elements of biased Langmuir probe theory, as implemented later in Chapter 7, as well as provide detail into the mechanical and electrical aspects of the constructed equipment necessary to carry out Langmuir probe measurements.

### 5.1 Biased Langmuir Probe Theory

A Langmuir probe is a piece of conductive material inserted into a plasma. Electrons and ions are attracted or repelled from the probe tip as a function of the differential voltage between the probe and the plasma ( $V_p - V_s$ ), as well as their initial velocities upon encountering the probe.

The current collected for a given probe voltage is therefore dependent on the densities and energies of particles within the plasma and so may be used to diagnose the plasma potential, temperature and density. Mott-Smith and Langmuir developed a generalised theory for the collection of charged particles on biased probes by considering simple conservation laws within the vicinity of the probe tip [146]. The plasma is taken to be collisionless and the detailed trajectories of particles as they are attracted to the probe are not considered. Here we reproduce some key elements of their derivations.

Consider a cylindrical collector of radius  $r_p$  and length  $l_p$ , biased at a voltage of  $V_p$  and inserted into a plasma whose local space potential is  $V_s$ . There exists a transition region, or sheath, of radius  $a$  around the probe tip which determines the effective collection area of the probe. As an electron moves from the sheath edge to the probe surface conservation of energy and angular momentum dictate that

$$\begin{aligned} \frac{1}{2}m_e [u^2(a) + v^2(a)] &= \frac{1}{2}m_e [u^2(r_p) + v^2(r_p)] + e[V_p - V_s] \\ av(a) &= r_p v(r_p) \end{aligned} \quad (5.1)$$

where  $u$  and  $v$  are the radial and tangential velocities respectively,  $m_e$  is the electron mass and  $e$  is the fundamental charge.  $u$  is taken to be positive when approaching the probe. A particle only contributes to the current if  $u(a) > 0$  and  $u^2(r_p) > 0$  and so for an initial radial velocity the restriction on  $v(a)$  is given by

$$|v(a)| \leq v_1 = \sqrt{\frac{r_p^2}{a^2 - r_p^2} \left[ u^2(a) + \frac{2e(V_p - V_s)}{m_e} \right]} \quad (5.2)$$

In the case where the probe is repulsive to electrons, i.e.  $(V_p - V_s) < 0$ , then expression 5.2 becomes complex and we have an additional restriction on  $u(a)$  according to

$$u(a) \geq u_1 = \sqrt{\frac{2e(V_s - V_p)}{m_e}} \quad (5.3)$$

For an arbitrary velocity distribution function  $f(u, v)$  in the plasma, the flux of particles into the sheath per unit volume of velocity space is  $uf(u, v)dudv$ , and so we may obtain an expression for the collected current by integrating over those particles which are able to reach the probe surface. That is

$$I(V_p) = 2\pi a l_p e n_e \int_{0, u_1}^{\infty} \int_{-v_1}^{+v_1} u f(u, v) dudv. \quad (5.4)$$

In general, the sheath size  $a$  is unknown and so direct computation of Equation 5.4 is not possible. In the limit where  $a \gg r_p$  however, the expression may be shown to take a limiting

form. Application of L'Hôpital's rule gives

$$I_p(V_p) = 2\pi l_p e n_e \lim_{a \rightarrow \infty} \left[ -a^2 \frac{d}{da} \int_{0,u_1}^{\infty} \int_{-v_1}^{+v_1} u f(u, v) du dv \right] \quad (5.5)$$

which using Leibniz integration becomes

$$I_p(V_p) = 2\pi l_p e n_e \lim_{a \rightarrow \infty} \left[ -2a^2 \int_{0,u_1}^{\infty} u f(u, v_1) \frac{dv_1}{da} du dv \right]. \quad (5.6)$$

Finding the derivative of  $v_1$  and evaluating the limit yields the limiting current collected on the cylindrical probe as

$$I_p(V_p) = 4\pi r_p l_p e n_e \int_{0,u_1}^{\infty} u \left[ u^2 + \frac{2e}{m_e} (V_p - V_s) \right]^{\frac{1}{2}} f(u, 0) du \quad (5.7)$$

The corresponding expression for a spherical collector is

$$I_p(V_p) = 2\pi r_p^2 e n_e \int_{0,u_1}^{\infty} u \left[ u^2 + \frac{2e}{m_e} (V_p - V_s) \right] f(u, 0) du. \quad (5.8)$$

Mott-Smith and Langmuir also demonstrated that when the distribution  $f(u, v)$  is Maxwellian, the square of the current density collected on a cylindrical probe is linear with the applied probe voltage according to

$$J_p^2(V_p) = \left( \frac{I_p(V_p)}{2\pi r_p l_p} \right)^2 = \frac{2e^2 n_e^2 k_B T_e}{\pi^2 m_e} \left[ 1 + \frac{e}{k_B T_e} (V_p - V_s) \right]. \quad (5.9)$$

when the probe is biased positively with respect to the plasma potential. That is when  $V_p > V_s$ . The slope of Equation 5.9 is given by

$$S = \frac{2e^3}{\pi^2 m_e} \cdot n_e^2 \quad (5.10)$$

and so a plot of  $J_p^2(V_p)$  may be used to determine the electron density.

## 5.2 Langmuir Probe Construction

The langmuir probe was assembled from telescoping sections of alumina ceramic tubing and sealed using TorrSeal adhesive. The probe core consisted of a 5 mm diameter copper rod, threaded to accept an M3 screw. Interchangeable probe tips were constructed around 3×80 mm sections of brass rod. The rod ends were turned down to 1 mm and drilled to accept tungsten wire tips (50 - 200μm). The brass was then crimped to fix the tungsten in place and ensure a good electrical connection. Additional ceramic tubes were then used to shroud the brass, leaving

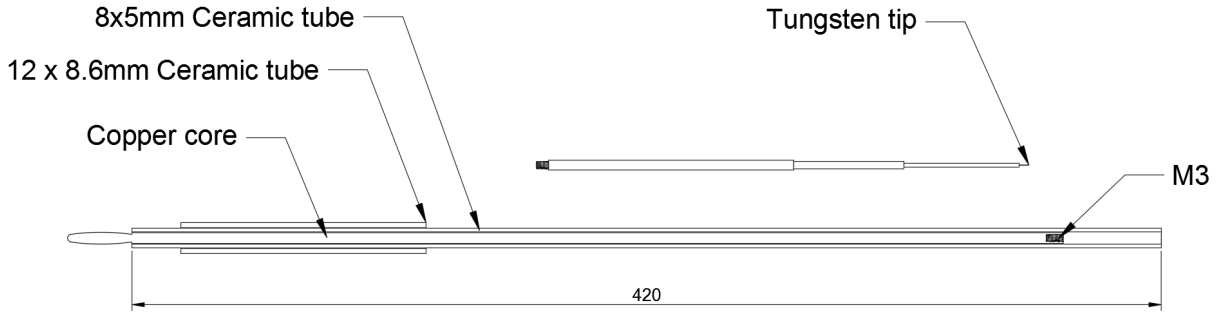


FIGURE 5.1: Langmuir probe body and interchangeable tip. All dimensions are in millimetres.

a small section of tungsten exposed to the plasma. In this way probe tips of varying size, length and angle could be created according to need. The probe was installed in the translational stage described in Section 2.2 such that it could be precisely positioned within the vacuum chamber.

### 5.2.1 High Impedance Floating Probe

The most basic method by which to measure the potential distribution within a plasma is the use of a floating probe. An electrically isolated conductor, placed within a plasma will collect charge until the electron and ion currents into the probe are equal. At this point the net current into the probe is zero and the equilibrium potential of the charged probe is referred to as the floating potential  $V_f$ . It is not possible, in practice, to realise such a device as the measurement of the probe voltage must necessarily draw a small net current. However it is possible to construct probes of sufficiently high impedance as to approximate the electrically isolated limit.

The floating potential is always smaller than the space potential and may be approximated as

$$V_f \approx V_s - \frac{k_B T_e}{2e} \ln \left( \frac{2m_i}{\pi m_e} \right) \quad (5.11)$$

where  $m_i$  is the ion mass [147]. For hydrogen and deuterium the logarithmic factor is about 7.1 and 7.7 respectively. The floating potential is therefore only a valid measure of the space potential in systems where the electron temperature,  $T_e$ , does not vary with time. If the electron velocity distribution contains a non-thermalised, high energy beam component then the measured floating potentials will be less reliable as an indicator of plasma potential. It is therefore important that floating probe measurements are validated against an additional reference diagnostic.

In the MCVC system, floating probe measurements were made by connecting the probe described in Section 5.2 directly to the oscilloscope via a large value load resistor, most commonly  $2\text{ G}\Omega$ . The scope channel is terminated via a  $1\text{ M}\Omega$  input impedance resulting in a 2001:1 voltage divider between the probe tip and ground.

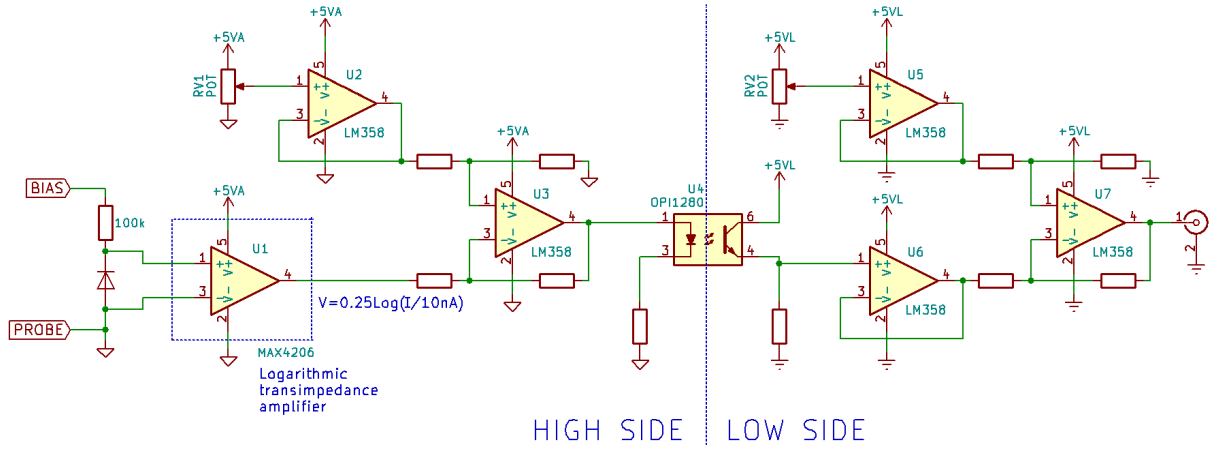


FIGURE 5.2: Simplified schematic of optically isolated current sense amplifier.  
 $V_{out} = 0.25 \log_{10} (I_p/10\text{nA})$

### 5.2.2 Biased Langmuir Probe

Detection of small collected probe currents presents a technical challenge, especially in the case where the order of magnitude of the expected current is unknown. It is convenient therefore, to make use of a detection device with a logarithmic response function. The MAX4206 is a precision, logarithmic, transimpedance amplifier capable of operating over five orders of magnitude (10 nA - 1 mA) and was used as the main current sensing component in biased probe experiments [148, 149]. The MAX4206 was configured for a gain of 0.25 V per decade and was allowed to float on the probe bias supply by way of analogue optical isolation as given in Figure 5.2. The gain and output offset of the MAX4206 were configured such that the optocouple remained in its linear regime. The high and low side circuits were both powered by 9 V batteries, regulated to 5 V by LM7805 linear regulators.

Due to the unipolar nature of the MAX4206, a diode was required across the inputs to protect the device against reverse biasing in the case where  $V_f > V_{bias}$ . The device is similarly protected from over-current by a 100 kΩ series resistor. The MAX4206 exhibits a 0.54 V forward voltage drop between its inputs and so probe current was only recorded when the probe voltage exceeds the floating potential by this value. In the case of forward conduction the voltage on the probe tip is

$$V_p = V_{bias} - I_p \times 100 \text{k}\Omega - 0.54 \quad (5.12)$$

DC bias voltages were applied to the probe and the collected current recorded over a shot. Varying the probe bias over repeated shots resulted in a family of current traces,  $I_p(t)$ , as well as probe voltages,  $V_p(t)$ , computed from Equation 5.12. An example family of current traces is given in Figure 5.3. Extracting temporal slices from the data results in standard  $IV$  curves as given in Figure 5.4.

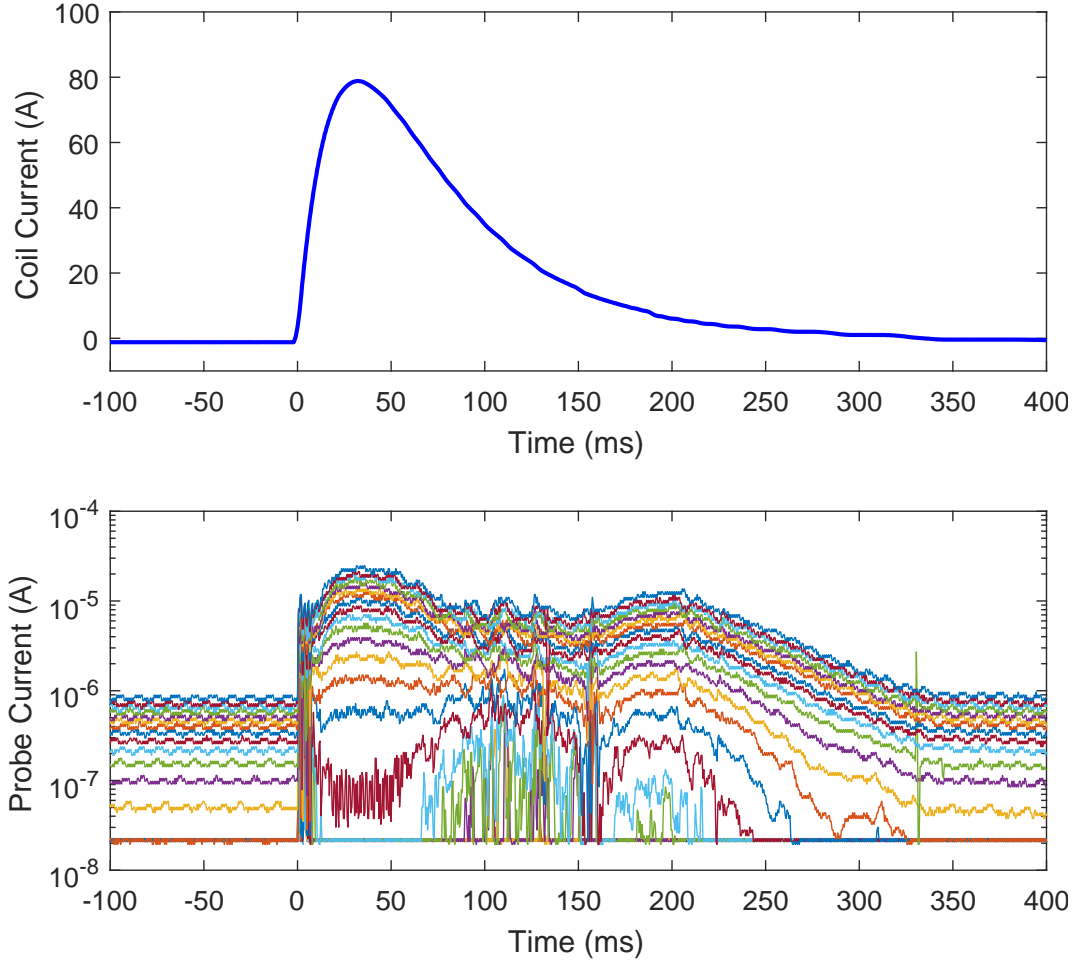


FIGURE 5.3: Indicative Langmuir probe current traces, obtained over multiple repeat shots for varying probe bias voltages. The magnetic field coil current is given in the top panel for reference.

The differential output stage of the current sense circuit (Figure 5.2) tended to sit at  $\sim 100$  mV above ground for zero input signal. As such, output signals of  $<100$  mV could not be measured, resulting in a minimum measurable Langmuir probe current of  $\sim 22$  nA. The recorded *IV* curves are therefore truncated at this value.

### 5.2.3 Current Sense Amplifier Offset

The current sense circuit described in Section 5.2.2 was initially powered directly from 9 V batteries. During the course of extended experimental runs, the drop in battery voltage led to drifts in the differential amplifier reference voltages and hence introduced a net offset to the output signal. This effect was later removed through the introduction of 5 V regulators, however the effect of offset on the measured data must be considered.

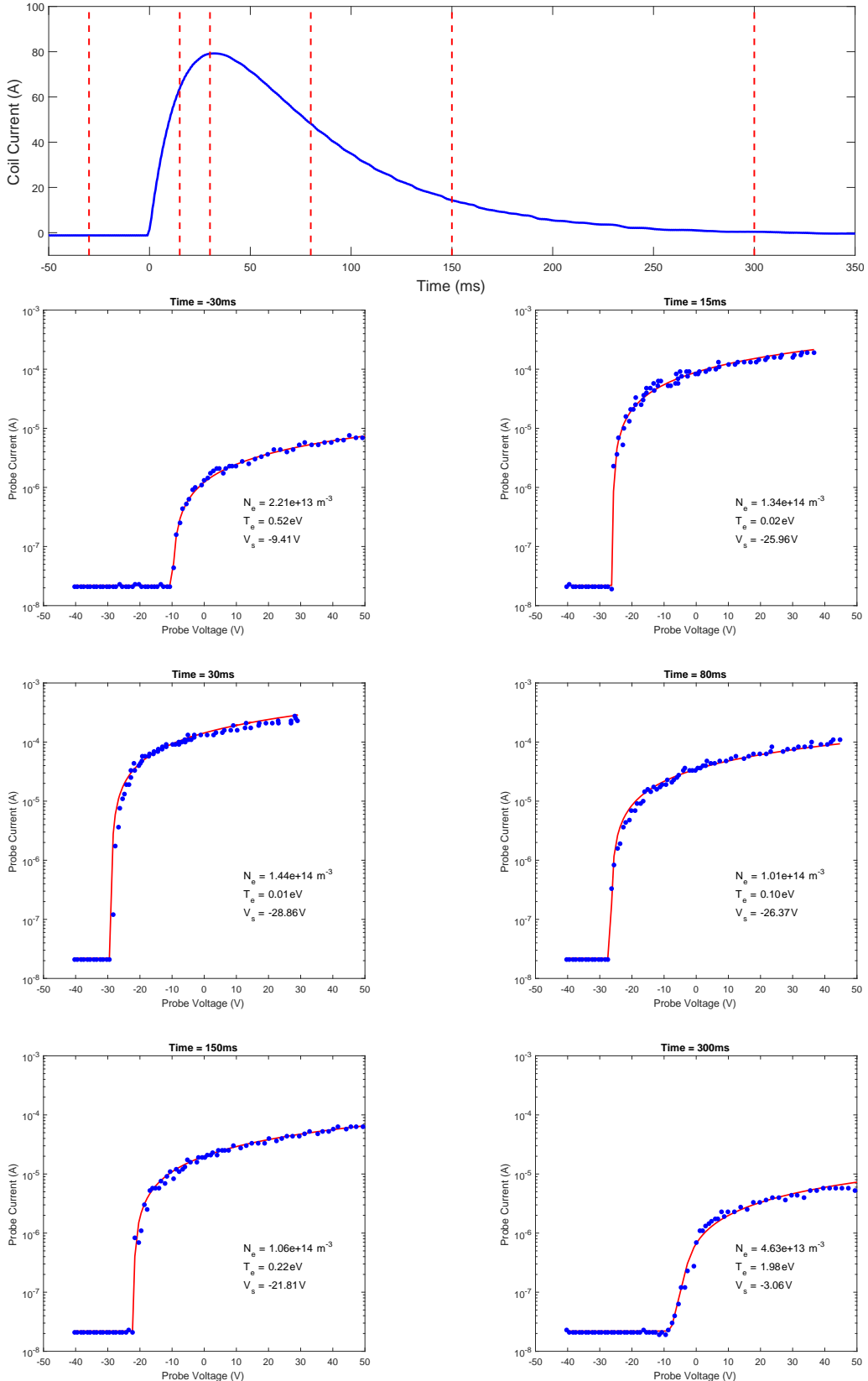


FIGURE 5.4: Example  $IV$  curve evolution during MCVC shot. The coil current is illustrated in the top panel, with dashed red lines representing the times at which  $IV$  curves are taken. The  $IV$  curves are fitted with the theoretical profiles for Maxwellian electron distributions and the computed density, temperature and space potential are given for each  $IV$  curve.

If we introduce a small offset voltage  $V_{off}$  to the signal of the current sense amplifier, the measured output signal becomes

$$V_{out} = 0.25 \log_{10} \left( \frac{I_p}{10 \text{ nA}} \right) + V_{off} \quad (5.13)$$

In this case, the computed probe current becomes

$$I_p = 10 \text{ nA} \cdot 10^{4V_{out}} \cdot 10^{-4V_{off}} \quad (5.14)$$

which is scaled by a quantity  $10^{-4V_{off}}$ . An offset of only 75 mV results in a halving of the apparent probe current and, via Equation 5.9, a subsequent halving of the measured plasma density. The absolute values of electron densities determined via Equation 5.9 should therefore be regarded with care, though the relationships between density measurements remain sound.

Of the other plasma parameters, the electron temperature is determined as  $T_e = 1/S$ , where  $S$  is the slope of the exponential region on a semilog plot. The slope is

$$S = \frac{d}{dV_p} (\ln(I_p)) = \frac{1}{I_p} \frac{dI_p}{dV_p} \quad (5.15)$$

and so arbitrarily scaling the current,  $I_p \rightarrow \kappa I_p$ , does not change the resulting temperature. Similarly, scaling the current does not move the inflection point in the  $IV$  curve and hence does not alter the space potential.

# Chapter 6

## Electro-Magnetic Fields In MCVC-0

The aim of this chapter is to characterise the spatial structure of the vacuum electric and magnetic fields within MCVC-0. A magnetic flux probe is described and the experimentally determined field profiles found to be in excellent agreement with the simulated results. Further, the induction of eddy currents in the metal components of the machine is examined and concluded to have negligible effect on the field profiles over the duration of a shot. Finally, a discrete Laplace equation solver is described and the vacuum potentials within MCVC-0 evaluated.

### 6.1 Magnetic Fields

#### 6.1.1 Simulated magnetic fields

The magnetic fields generated within the MCVC device were modelled using the superposition of the magnetic field contributions due to the individual wire turns of each coil. In a cylindrically symmetric system it is trivial to compute the magnetic vector potential of an axial coil, as  $\vec{A} \equiv A_\varphi \hat{\varphi}$  and so the vector potential may be treated as a two-dimensional scalar field. For a single current loop in the  $(x, y)$  plane, oriented such that its magnetic moment points along the  $z$  axis (see Figure 6.1), the  $\varphi$  component to the vector potential is given by [150]

$$A_\varphi(\rho, z) = \frac{\mu_0 I a}{4\pi} \int_0^{2\pi} \frac{\cos(\varphi') d\varphi'}{\sqrt{a^2 + \rho^2 + z^2 - 2a\rho \cos(\varphi')}} \quad (6.1)$$

where  $a$  is the loop radius,  $I$  is the current and  $(\rho, \varphi, z)$  are the normal cylindrical coordinates. Evaluating the integral gives

$$A_\varphi(\rho, z) = \frac{\mu_0 I a}{4\pi} \sqrt{\frac{a}{\rho}} \frac{1}{k} [(2 - k^2)K(k^2) - 2E(k^2)] \quad (6.2)$$

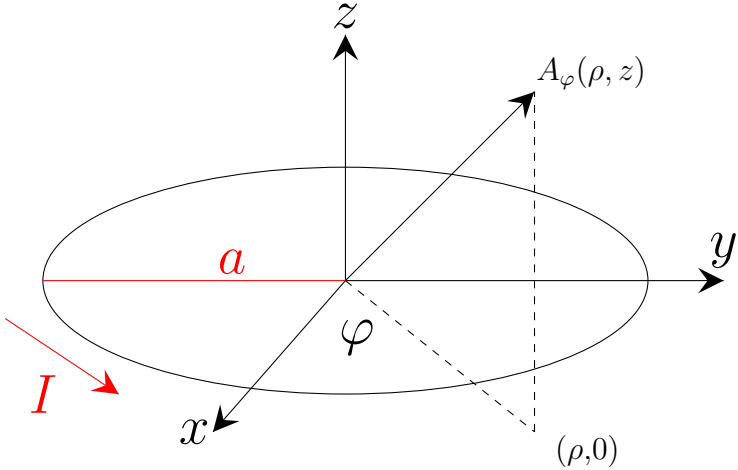


FIGURE 6.1: Single current loop

where

$$k^2 = \frac{4a\rho}{(a + \rho)^2 + z^2} \quad (6.3)$$

and  $K(k^2)$  and  $E(k^2)$  are the complete elliptic integrals of the first and second kinds respectively.

For a family of coils with radii  $a_i$  and axial positions  $z_i$ , the total vector potential may be computed through successive use of Equation 6.2. The radial and axial components of the magnetic field components are subsequently calculated as  $\vec{B} = \nabla \times \vec{A}$ , or more specifically for a cylindrical system

$$\begin{aligned} B_\rho &= -\frac{\partial}{\partial z} A_\varphi \\ B_z &= \frac{1}{\rho} \frac{\partial}{\partial \rho} (\rho A_\varphi). \end{aligned} \quad (6.4)$$

Outside of the magnetic field coils the current density,  $J$ , is zero and so we may also write the magnetic field as the gradient of a magnetic scalar potential  $\phi_m$ ,

$$\vec{B} = \nabla \phi_m = \frac{\partial \phi_m}{\partial \rho} \hat{\rho} + \frac{\partial \phi_m}{\partial z} \hat{z}. \quad (6.5)$$

The magnetic lines of force are everywhere perpendicular to the contours of  $\phi_m$  and so we define a stream function,  $\Psi(\rho, z)$ , such that the field lines are given by the contours of  $\Psi$ . The scalar potential and stream function are related by

$$\nabla \Psi \cdot \nabla \phi_m = \left( \frac{\partial \Psi}{\partial \rho} \right) \left( \frac{\partial \phi_m}{\partial \rho} \right) + \left( \frac{\partial \Psi}{\partial z} \right) \left( \frac{\partial \phi_m}{\partial z} \right) = 0. \quad (6.6)$$

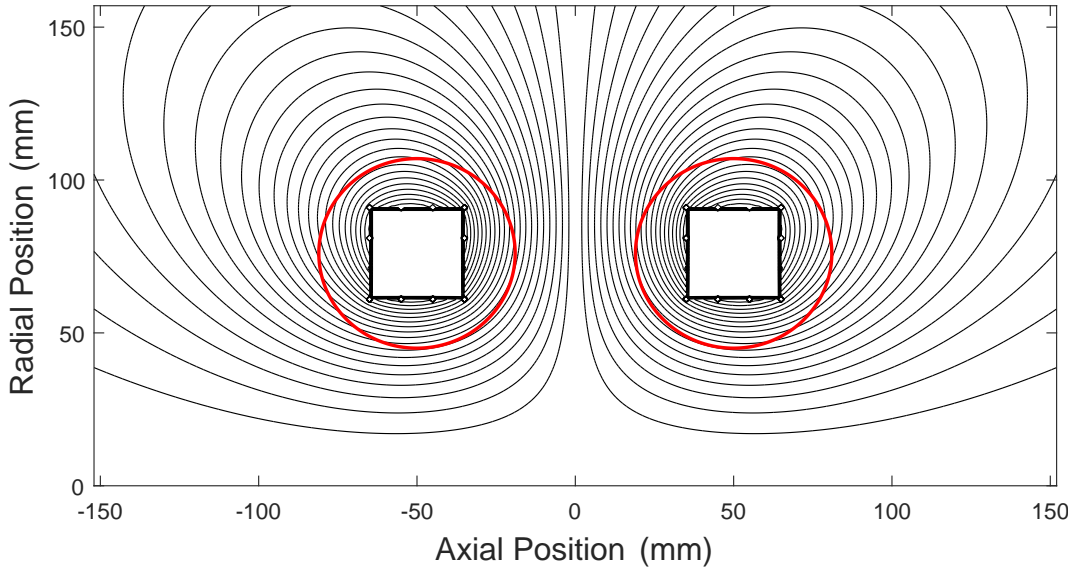


FIGURE 6.2: Magnetic lines of force in the MCVC device. Red circles indicate the surfaces of the coil cases. White rectangular regions correspond to the field coils.

Equating vector components in Equations 6.4 and 6.5 gives

$$-\left(\frac{\partial \Psi}{\partial \rho}\right)\left(\frac{\partial A_\varphi}{\partial z}\right) + \left(\frac{\partial \Psi}{\partial z}\right)\left(\frac{1}{\rho} \frac{\partial}{\partial \rho}(\rho A_\varphi)\right) = 0 \quad (6.7)$$

which has the solution

$$\Psi \equiv \rho A_\varphi \quad (6.8)$$

We therefore plot the magnetic field lines for the calculated fields as the contours of  $\rho A_\varphi$ , as given in Figure 6.2. The red circles denote the outer surfaces of the field coil casings. The coil spacing corresponds to 1.25 times the major radii of the coils. This configuration was chosen as it results in approximately equal field strengths in the point and line cusps, and hence a symmetric trapping volume. The contours of magnetic field strength are given in Figure 6.3.

### 6.1.2 Eddy Currents

The magnetic field computations conducted in the previous sections only account for fields due to static currents. The MCVC device, however, operates in pulsed mode and so currents induced in the coil cases and support structures as a result of time-varying magnetic fields must also be considered. The electric field induced about a closed flux loop is given by Faraday's law as

$$EMF = \oint_{\partial S} \vec{E} \cdot d\vec{l} = -\frac{d}{dt} \int_S \vec{B} \cdot d\vec{a} \quad (6.9)$$

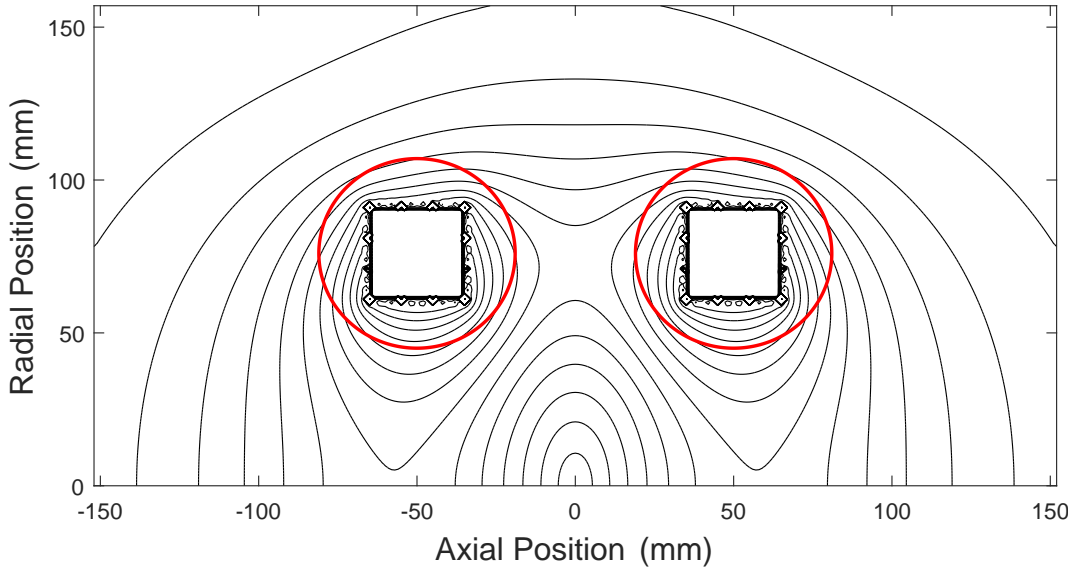


FIGURE 6.3: Contours of magnetic field strength in the MCVC device. Red circles indicate the surfaces of the coil cases. White rectangular regions correspond to the field coils.

where  $\partial\mathcal{S}$  is the boundary of surface  $\mathcal{S}$ . Applying ohms law,  $\vec{J} = \sigma\vec{E}$ , gives the induced eddy current density about circular loops in the  $(\rho, z)$  plane as

$$J_\varphi(\rho, z) = -\frac{\sigma}{\rho} \frac{dI}{dt} \int_0^\rho B_{z,1A}(\rho', z) \rho' d\rho'. \quad (6.10)$$

where  $B_{z,1A}(\rho', z)$  is the  $z$  component of the magnetic field computed for a coil current of 1 Ampere. Equation 6.10 was evaluated numerically using the electrical conductivity of 316 stainless steel,  $\sigma = 1.35 \times 10^6 \text{ S m}^{-1}$  [151] and the maximum achievable current gradient for our system  $\sim 1 \times 10^5 \text{ A s}^{-1}$ . Each cell in the square mesh was subsequently treated as an infinitesimal coil carrying a current  $I = h^2 J_\varphi$ , where  $h = 1 \times 10^{-3} \text{ m}$  is the grid spacing, and the individual field contributions summed as before. The magnitude of the eddy current densities, as well as the induced magnetic field lines are given in Figure 6.4. The magnetic field strength as a result of eddy currents was found to vary between  $\sim 1 - 5 \text{ mT}$  throughout the device. By contrast, the magnet coils generate fields on the order of  $\sim 0.5 - 1 \text{ mT A}^{-1}$ . Given that we have calculated the eddy currents in the most extreme case, and that the applied coil currents typically exceed 100 A, we conclude that induced eddy currents do not significantly perturb the magnetic field structure within the device.

### 6.1.3 EMF probe measurements

In order to profile the magnetic fields produced in the cusped system, an integrating magnetic flux probe was constructed. Four 10 turn pick-up coils, with 20 mm spacing, were wound around a section of half inch (12.7 mm) perspex tube. Shallow indents were filed into the tube

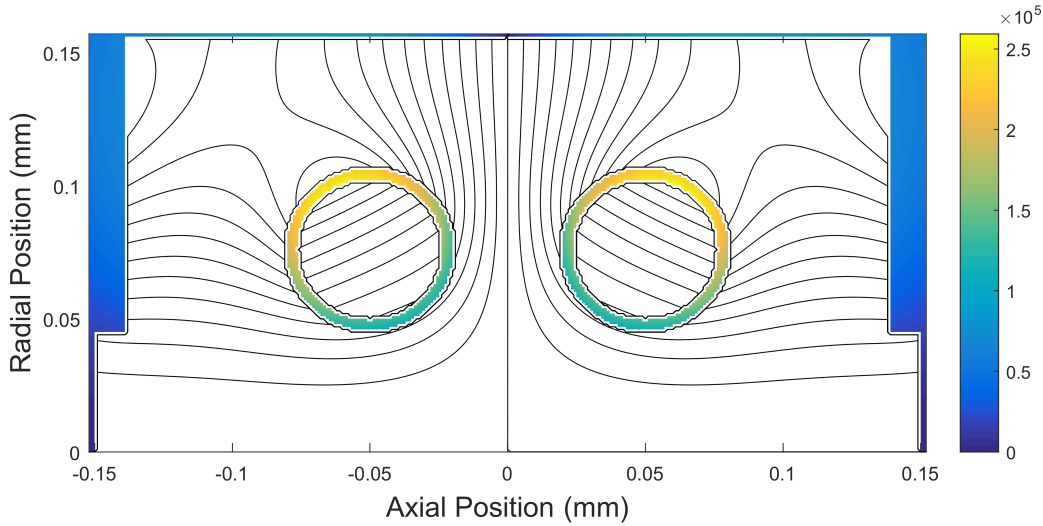


FIGURE 6.4: Computed eddy current densities ( $\text{A m}^{-2}$ ) in stainless steel structure. Eddies are calculated for the maximum obtainable  $dI/dt$  of  $\sim 1 \times 10^5 \text{ A s}^{-1}$ .

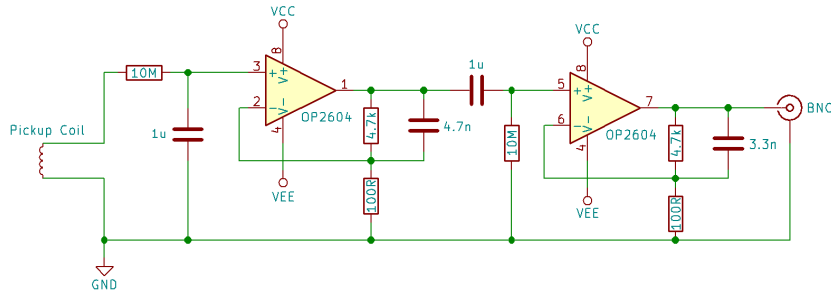


FIGURE 6.5: Single channel integrating amplifier for EMF magnetic field probe

so that the pick up coils would remain secure. A four channel integration amplifier was used to convert the EMF signals into proportional magnetic field measurements. A single channel of the integrator is given in Figure 6.5. The circuit consisted of an  $RC$  integration stage followed by two +33 dB amplification stages. An integrating response (-20 dB/Dec, -90°) was obtained between 0.2 Hz and 7 kHz. The magnetic flux probe was calibrated by placing it within the centre of a 135 mm solenoid ( $1.76 \times 10^{-2} \text{ T A}^{-1}$ ,  $9.2 \Omega$ ,  $45.9 \text{ mH}$ ) and applying current pulses of up to 80 A using the capacitor bank described in Section 4.1.1. The solenoid current was recorded as a voltage drop across a  $99 \text{ m}\Omega$  resistor placed in series. An example trace of both the solenoid current and probe responses is given in the left hand panel of Figure 6.6. The right hand panel gives response curves for the four pick up coils as a function of magnetic field strength. The calibration factor, averaged across the four pick up coils, was found to be  $0.24 \text{ V T}^{-1}$ . The flux probe was inserted into the translational stage described in Section 2.2 and was translated along the vertical axis and central plane of the device to profile the spacial variation in the magnetic field. The capacitor bank was repeatedly charged to  $\sim 300 \text{ V}$  resulting in current pulses of 800 A.

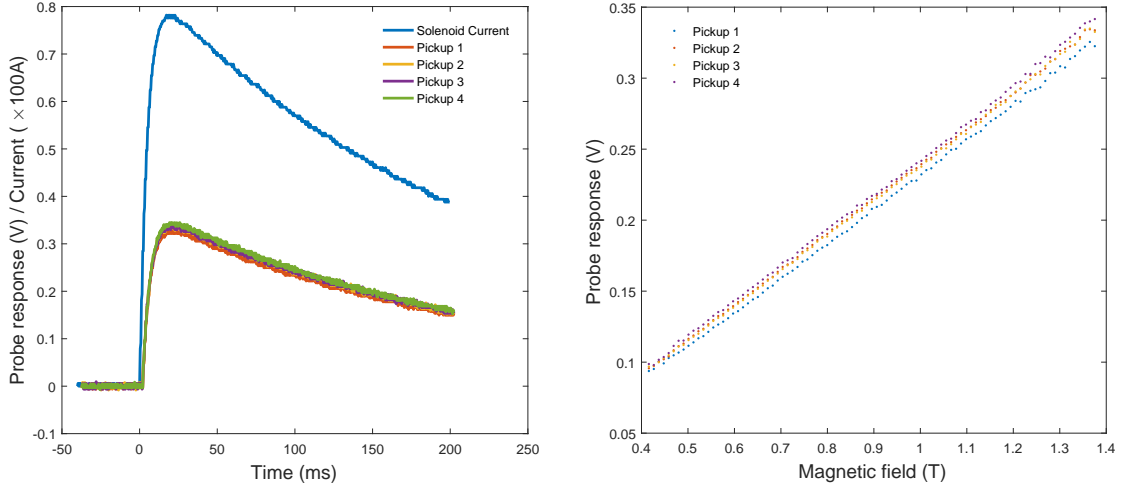


FIGURE 6.6: Example calibration shot (*Left*) and probe calibration curves (*Right*). Probe response factor =  $0.24 \text{ V T}^{-1}$

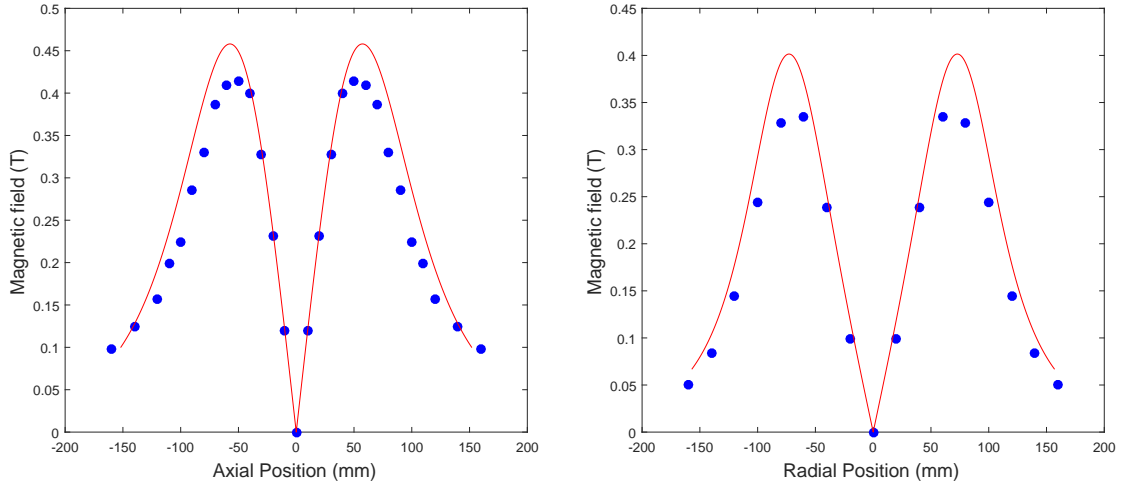


FIGURE 6.7: Axial (*left*) and radial (*right*) magnetic field strength. Simulated fields are given as solid lines.

The measured field strengths are given in Figure 6.7 where the theoretical results calculated in Section 6.1.1 are also shown as solid red lines. For each of the axial measurements the field strength was plotted against coil current, Figure 6.8. The high degree of linearity confirms the conclusion drawn in Section 6.1.2 that induced eddy currents do not significantly perturb the magnetic fields.

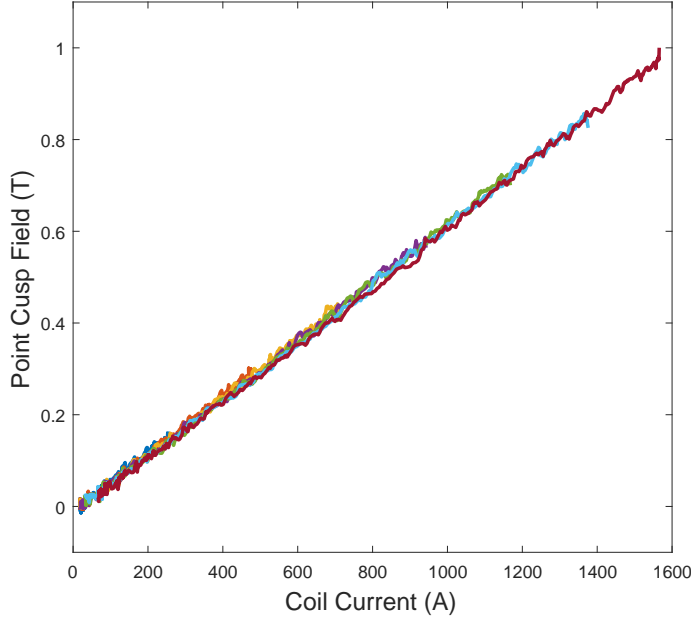


FIGURE 6.8: Point cusp magnetic field strength as a function of coil current.  
 $B_{cusp} \approx 5.8 \times 10^{-4} \text{ T A}^{-1}$ .

## 6.2 Electric Potential

### 6.2.1 Laplace Solver

The vacuum electric fields were computed in MatLab through the solution of the discrete Laplace equation via Jacobi relaxation [152–154]. The Laplace equation is

$$\nabla^2 \Phi(x, y, z) = 0 \quad (6.11)$$

where  $\Phi$  is the electrostatic potential and  $(x, y, z)$  are the normal Cartesian coordinates. Introducing a dummy time variable  $t$ , we may write Equation 6.11 in the form of a diffusion equation for which the equilibrium state is also the solution to the original Laplace equation:

$$\frac{\partial}{\partial t} \Phi(x, y, z, t) = \kappa \nabla^2 \Phi(x, y, z, t). \quad (6.12)$$

The spacial coordinates are expressed on a discrete square mesh using a finite step sizes  $h$  and the set of integer indices  $(i, j, k)$  which denote the location of a given point within the grid. The dummy time coordinate is similarly expressed in terms of the step size  $\tau$  and integer index  $n$ . The values of electric potential at the grid vertices are therefore denoted as

$$\begin{aligned} \Phi(x, y, z, t) &\rightarrow \Phi(ih, jh, kh, n\tau) \equiv \Phi_{i,j,k}^n \\ i, j, k, n \in \mathbb{Z}. \end{aligned} \quad (6.13)$$

In order to evaluate the potential at all points within the solution volume it is necessary to reformulate such that every point may be updated as a function of its nearest neighbours. Using the discrete approximations to the first and second derivatives

$$\begin{aligned}\frac{\partial}{\partial t} f(x, t) &\approx \frac{f(x, t + \tau) - f(x, t)}{\tau} \\ \frac{\partial}{\partial x} f(x, t) &\approx \frac{f(x + h, t) - f(x - h, t)}{2h} \\ \frac{\partial^2}{\partial x^2} f(x, t) &\approx \frac{f(x + h, t) - 2f(x, t) + f(x - h, t)}{h^2}\end{aligned}\quad (6.14)$$

yields the Jacobi update to the electric potential as

$$\Phi_{i,j,k}^{n+1} = \Phi + \frac{\kappa\tau}{h^2} \left[ \Phi_{i+1,j,k}^n + \Phi_{i-1,j,k}^n + \Phi_{i,j+1,k}^n + \Phi_{i,j-1,k}^n + \Phi_{i,j,k+1}^n + \Phi_{i,j,k-1}^n - 6\Phi_{i,j,k}^n \right]. \quad (6.15)$$

Von Neumann stability analysis may be used to show that most rapid convergence is obtained when the leading factor  $\kappa\tau/h^2 = 1/6$  and so the solution to Equation 6.11 is obtained through successive averaging of neighbouring points

$$\Phi^{n+1} = \frac{1}{6} \left[ \Phi_{i+1} + \Phi_{i-1} + \Phi_{j+1} + \Phi_{j-1} + \Phi_{k+1} + \Phi_{k-1} \right] \quad (6.16)$$

where un-shifted indices  $i, j, k, n$  have been omitted for clarity. Application of the same procedure in an azimuthally symmetric cylindrical coordinate system yields the corresponding update as

$$\Phi^{n+1} = \frac{1}{4} \left[ \left( \frac{i + \frac{1}{2}}{i} \right) \Phi_{i+1} + \left( \frac{i - \frac{1}{2}}{i} \right) \Phi_{i-1} + \Phi_{j+1} + \Phi_{j-1} \right] \quad (6.17)$$

where  $\Phi(\rho, z) \equiv \Phi(ih, jh)$  as before. Solutions were computed by initialising the potential matrix in which all elements were zero. Points within the matrix that corresponded to conductive boundaries were then located and assigned the required voltage value. Each point was then repeatedly updated using Equation 6.16 or Equation 6.17 as appropriate. During each update the voltages on the boundaries were also adjusted and so these points were restored by replacing the updated values with the boundary values. Iteration continued until the largest percentage update fell below some pre-specified limit  $\epsilon$ , or

$$100 \times \max \left| \frac{\Phi^{n+1} - \Phi^n}{\Phi^n} \right| \leq \epsilon. \quad (6.18)$$

In all cases we have used  $\epsilon = 0.1$ .

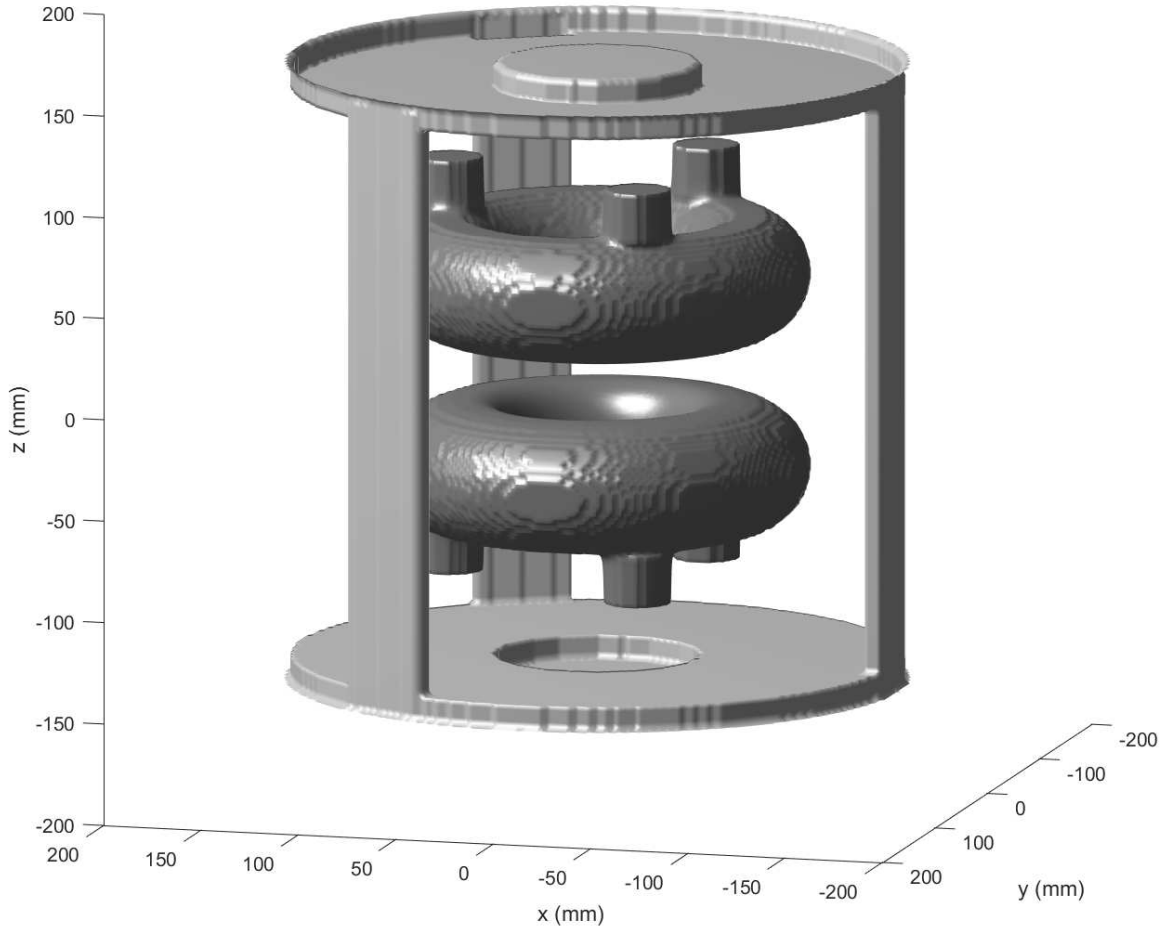


FIGURE 6.9: Boundary surfaces for the solution of the Poisson equation in the MCVC device.  
The cylindrical boundary corresponding to the vacuum chamber wall has been omitted.

### 6.2.2 MCVC potential

The implementation of the Jacobi scheme as described above required a faithful representation of the boundary conditions within the MCVC device. The presence of support structures breaks the cylindrical symmetry, instead resulting in a C3 rotational symmetry, and so we opt for a full Cartesian representation of the device rather than the simplified cylindrical model. The system was represented on a  $159 \times 159 \times 153$  element square mesh with a grid spacing  $h = 2$  mm. The metallic surfaces were defined in a matching boundary condition matrix by setting points within the metal surfaces to the appropriate values. Dielectrics were neglected. The chamber wall and support frame were set to 0 V and the potential solved for a coil bias of +1 V. In

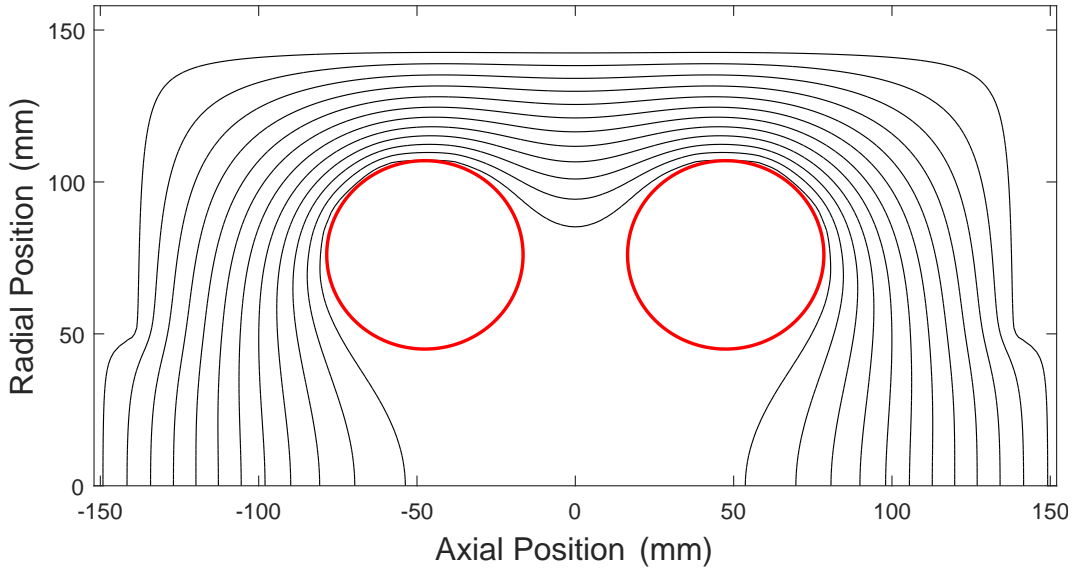


FIGURE 6.10: Contours of vacuum electric potential in the MCVC device. Red circles indicate the surfaces of the coil cases.

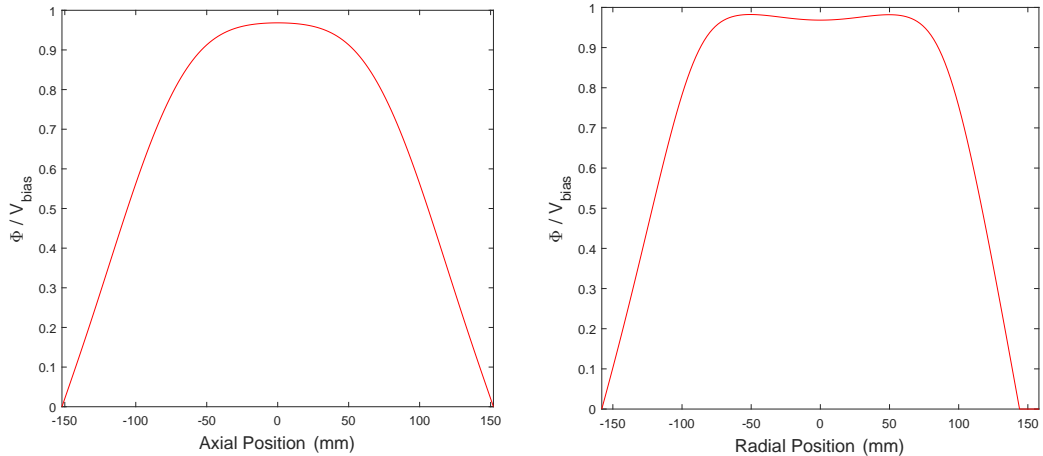


FIGURE 6.11: Axial (left) and radial (right) vacuum potential in the MCVC device. Potentials are normalised to the coil bias  $V_{bias}$ .

this way the solution could be arbitrarily scaled to any desired grid bias. The coil and frame boundary conditions are given as isosurfaces in Figure 6.9.

Figure 6.10 depicts the contours of the electric potential in the  $(\rho, z)$  plane. Figure 6.11 gives slices in the axial and radial directions, as normalised to the coil bias voltage. Note that the radial potential is asymmetric due to the presence of the vertical support strut at  $\rho = +145$  mm.

# Chapter 7

## Preliminary Plasma Studies in MCVC-0

In this chapter we describe preliminary experimental studies conducted in the MCVC device. Results are obtained for varying electron injection currents and grid biases, with spatial variation of the plasma potential, electron density and temperature examined. Initial results indicate negligible charge trapping with little to no potential well formation. Further, it is shown that the existence of potential wells reported in previous publications can be explained without the requirement of a virtual cathode produced by trapped electrons. Moreover, it is shown that potential wells, which produce electron confinement and heating from virtual cathodes, no longer exist with increasing plasma density.

### 7.1 Generalised Experimental Procedure

Prior to all experiments the MCVC-0 system was pumped down to its ultimate base pressure of  $\sim 1 \times 10^{-7}$  Torr. Although the chamber was baked at 165 °C for 72 hours during pump out, optical spectra obtained during plasma shots were dominated by strong  $H_\alpha - H_\epsilon$  Balmer lines, indicating significant contamination by residual atmospheric water. For this reason it was determined that initial experimental runs would be conducted without the addition of deuterium gas and hence all presented results were obtained using a system pressure of  $\sim 1 \times 10^{-7}$  Torr.

The PCPS was charged to values of 10-400 V, resulting in current pulses of  $\sim 20\text{-}1000$  A, or point cusp fields of up to  $\sim 0.6$  T. Biases of 0-6 kV were applied to the coil cases, and the collected plasma current recorded as a voltage drop across the load resistor  $R_L$  in Figure 4.14. Electron gun injection voltages of between -750 V and -1000 V, were used, with the filaments activated  $\sim 3$  seconds prior to the magnetic field shot to allow time for the thermionic current to stabilize.

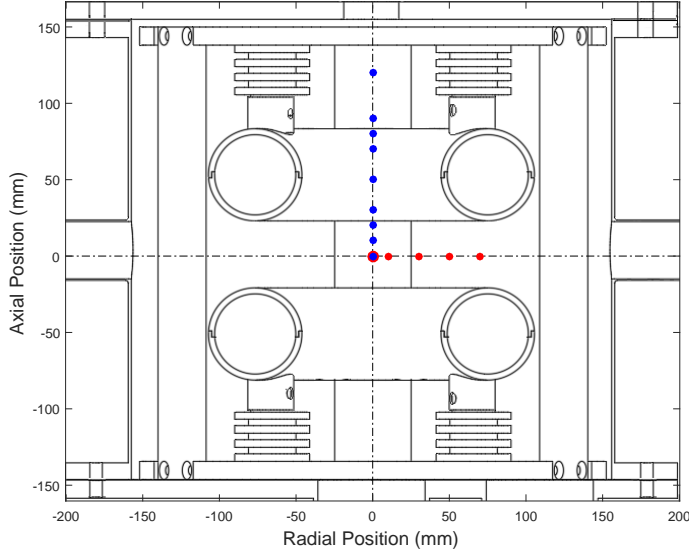


FIGURE 7.1: Spacial positions sampled within MCVC-0 during unbiased operation.

The emitted beam current was monitored by placing a current transducer around the filament supply cables and was varied through adjustment of the filament heating power. The Langmuir probe was fitted with a  $150\ \mu\text{m}$  diameter, 2 mm long cylindrical tip and was translated through the radial plane of the device, as well as along the central axis. Biased probe measurements were conducted in the low voltage ( $0\rightarrow 500\text{ V}$ ) regime and the resulting *IV* curves used to diagnose the plasma properties. In the high voltage regime ( $1\text{ kV}\rightarrow 6\text{ kV}$ ) electrostatic potential profiles were studied by way of resistive floating probe measurements.

## 7.2 Unbiased Operation

We wished to examine electron trapping within MCVC-0 in the absence of an externally applied bias, and in this way mimic the teflon polywell measurements as conducted by Carr [88]. The high voltage feed-through used to power the coil cases was disconnected from the high voltage supply and earthed directly to the vacuum chamber. A current transducer was placed around the earthing cable such that the collected coil current could still be measured. The duration of the magnetic pulse was extended by introducing an additional inductor ( $8.5\text{ mH}, 0.3\Omega$ ) in series with the field coils. Additionally, the added inductor served to reduce the power dissipation in the field coils and therefore reduce coil heating. Biased Langmuir probe measurements were conducted over the range  $-30\rightarrow+50\text{ V}$  at radial positions between 0 and 70 mm and axial positions between 0 and 120 mm as shown in Figure 7.1. In both cases 0 mm corresponds to the centre of the device. Electron gun currents of 10, 50 and 125 mA were used. Two processing methods were applied to the acquired Langmuir probe data. Firstly, the exponential and saturation regimes of the measured *IV* curves were linearly extrapolated (LE) on a semilog plot and their intersection

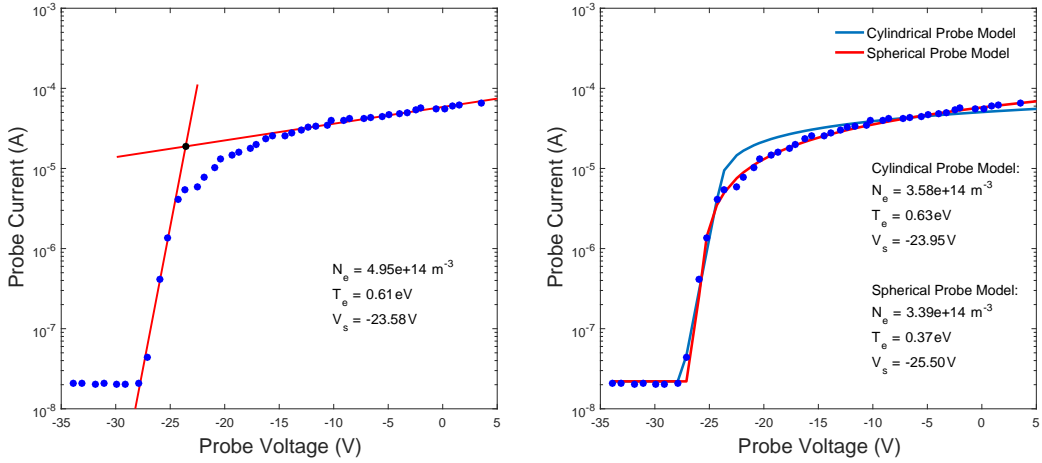


FIGURE 7.2: Methods of analysis applied to measured IV curves. Linear extrapolation (LE method) of the exponential and saturation regions (*Left*) and Monty-Carlo Markov-Chain fitting (Fit method) of the IV curves with analytical expressions (*Right*).

point used to determine  $V_s$ . Electron temperature was determined as the inverse of the slope of the exponential region while the electron density was derived from the saturation current as per Equation 5.9. The second method involved fitting the IV curve directly with the analytical expressions in Equations 5.7 and 5.8 assuming a Maxwell-Boltzmann velocity distribution. An example *IV* curve is given in Figure 7.2 along with the estimated values of  $N_e$ ,  $T_e$  and  $V_s$  resulting from each method. It is to be noted that the analytical expressions for a spherical collector proved to be a closer fit to the experimental data than those for the cylindrical probe. We address this by considering the Debye shielding length for the computed plasma parameters of  $T_e \approx 0.6 \text{ eV}$  and  $n_e \approx 3.5 \times 10^{14} \text{ m}^{-3}$ :

$$\lambda_D = \sqrt{\frac{\epsilon_0 k_B T_e}{e^2 n_e}} \approx 0.3 \text{ mm.} \quad (7.1)$$

Critical to the derivation of Equation 5.7 was the assumption that the sheath size  $a$  was much greater than the dimensions of the probe, and that  $r_p \ll l_p$ , such that the probe could be considered as an infinite cylinder. If we consider the sheath size to be  $a \approx 3\lambda_D$  we obtain

$$a/l_p \approx 0.5$$

$$a/r_p \approx 13$$

$$l_p/r_p \approx 26.$$

Similarly, if the sheath is taken to consist of a cylinder with a hemispherical cap, then we may compare the relative surface areas of the sheath components and assess whether collection at the end of the probe tip should be expected to significantly perturb the collected current. The area ratio is

$$\frac{2\pi a^2}{2\pi a l_p} = \frac{a}{l_p} = 0.5. \quad (7.2)$$

We therefore conclude that, despite its cylindrical construction, the probe tip does not fulfil the requirements of a truly cylindrical probe. The sheath structure, and therefore the collection area around the probe more closely resembles that of a spherical collector, and subsequently alters the observed *IV* curve. This presents difficulty in the analysis of such a probe, as the collection area is no longer well characterised. When fitting the spherical probe model to experimental data the probe was taken to be spherical with a surface area equal to that of the cylindrical probe used. That is, a sphere of radius

$$r_{sph} = \sqrt{\frac{r_{cyl} l_{cyl}}{2}} \quad (7.3)$$

The computed plasma properties during an example shot are given as functions of time in Figure 7.3. The probe was positioned in the centre of the device and the electron gun was operated at a current of 125 mA. Quantities derived from the linear extrapolation method are given as red crosses while fitted parameters are shown in blue. The extrapolation method required manual input from the user to designate the exponential and saturation regions of the *IV* curve and hence the resulting data points are of a much lower resolution than those obtained from the fully scripted Monte-Carlo method. The plasma potential and electron temperature are found to be consistent across the two methods, however the measured electron densities differ by a factor of  $\sim 3$ . It is expected that this difference is an artefact of both voltage offset in the current sense amplifier as addressed in Section 5.2.3, as well as the poorly characterised probe dimensions as discussed above.

A number of observations may be made. Firstly, the electron density is seen to rise by over an order of magnitude at the start of the magnetic field shot indicating electron confinement as well as increased ionisation of the background gas. Interestingly, the density does not appear to decay in proportionality with the magnetic field, instead maintaining a relatively constant level long after the magnetic field has decayed away. It is proposed that the residual magnetic field present in the tail of the pulse is sufficient to maintain the level of background gas ionisation and this would suggest that the background electron population is dominant over the beam population. Over the first 100 ms of the pulse however, the space potential within the core does drop as expected indicating the apparent formation of a negatively charged plasma. The absolute change is small however, amounting to only  $\approx 12$  V, despite injection of a 750 eV electron beam. As the magnetic field decays, the core potential is seen to rise, transitioning to a standard, positively charged discharge plasma at  $t \approx 110$  ms.

We may acquire an estimate for the non-neutral components of the electron density by computing the potential due to a small volume of charge within a grounded shell. If we take a sphere of charge with density  $\rho_0$  and radius  $R$ , residing within a grounded shell of radius  $R_s$ , then the

radial electric fields are given by Gauss's law as

$$E_r(r) = \begin{cases} \frac{\rho_0}{3\epsilon_0}r & r < R \\ \frac{\rho_0 R^3}{3\epsilon_0} \frac{1}{r^2} & R < r < R_s \end{cases} \quad (7.4)$$

Using the definition of the electric potential

$$-\frac{d}{dr}\Phi(r) = E_r(r) \quad (7.5)$$

along with the boundary conditions

$$\begin{aligned} \Phi_{inside}(R) &= \Phi_{outside}(R) \\ \Phi_{outside}(R_s) &= 0 \end{aligned}$$

results in the solution for the electrostatic potential throughout the volume as

$$\Phi(r) = \begin{cases} \left(\frac{\rho_0}{3\epsilon_0}\right) \left[ \frac{1}{2} (R^2 - r^2) + R^3 \left( \frac{1}{R} - \frac{1}{R_s} \right) \right] & r < R \\ \left(\frac{\rho_0 R^3}{3\epsilon_0}\right) \left[ \frac{1}{r} - \frac{1}{R_s} \right] & R < r < R_c. \end{cases} \quad (7.6)$$

Evaluating the potential for  $r = 0$  and  $\rho_0 = -en_e$  provides an estimate for the depth of the potential well as

$$\Phi_{well} = -\frac{en_e}{2\epsilon_0} R^2 \left[ 1 - \frac{2}{3} \frac{R}{R_s} \right]. \quad (7.7)$$

The inner surfaces of the toroidal coil cases circumscribe a sphere with a radius of approximately 60 mm and so we take this as our value for  $R_s$ . Assuming  $R \approx 0.5R_s$  and a central potential of -12 V as observed above, we compute an electron density of  $n_e \approx 2.2 \times 10^{12} \text{ m}^{-3}$ , two orders of magnitude less than our measured values. This confirms the hypothesis above that the neutral plasma contribution to the electron density dominates over the beam component.

### 7.2.1 Spatial Variation of Plasma Parameters

Figures 7.5, 7.6 and 7.7 give the spatial variation of the plasma potential, electron density and electron temperature respectively. Left hand panels correspond to the vertical axis of the device while right hand panels are radial slices through the central plane. The given data was averaged over a 15 ms window at the peak of the magnetic field pulse. Considering the radial variation in the space potential (Figure 7.5), we see the expected formation of a potential well. Differentials of up to 10 V are measured between the core of the device and the  $\rho = 30$  mm position. Contrary to expectation however, the largest differentials are observed when operating an electron beam

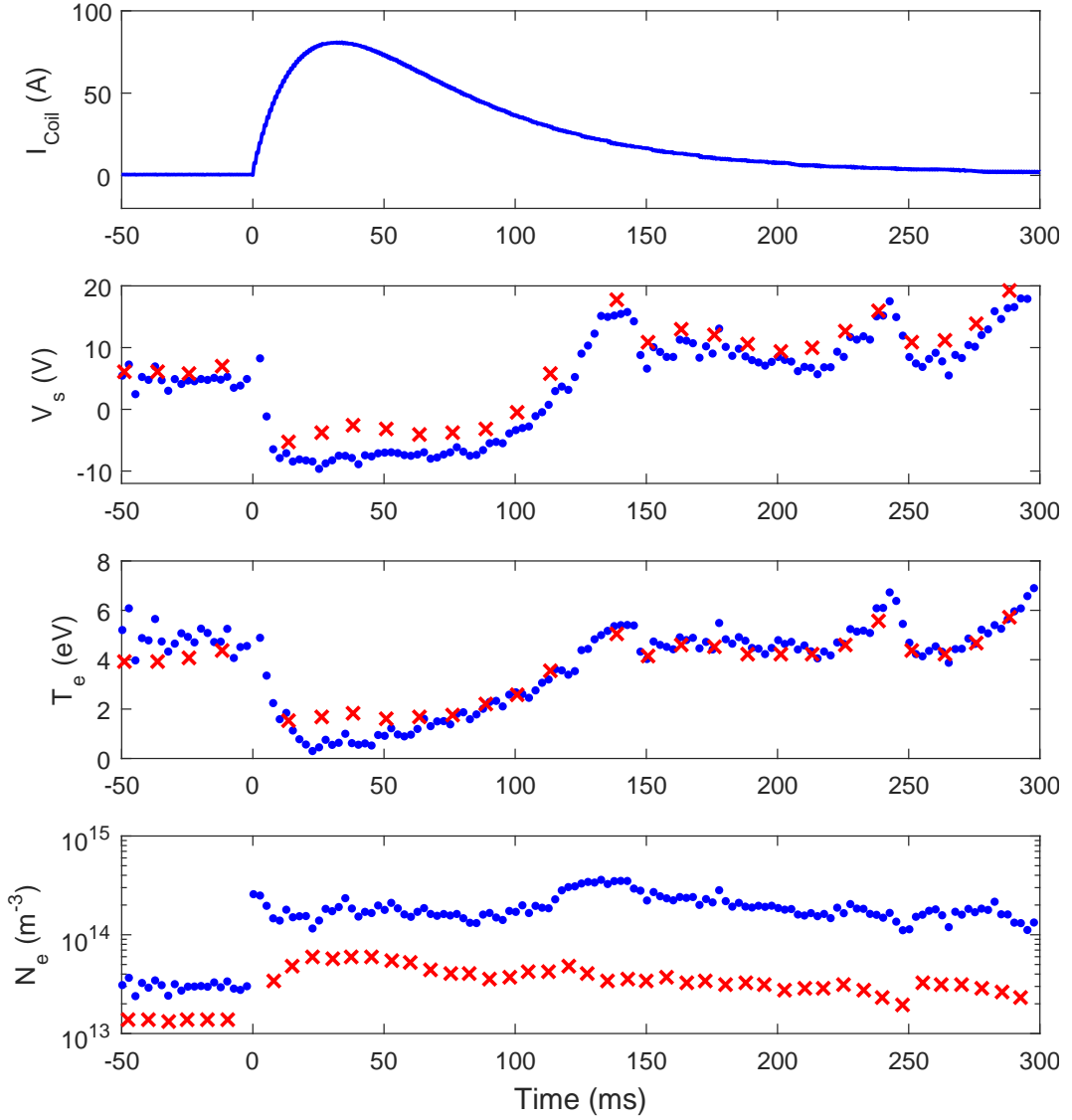


FIGURE 7.3: Computed plasma parameters as a function of time. Red crosses are derived from linear extrapolation of  $IV$  curve while blue data points result from MCMC fitting. Langmuir probe was positioned in the centre of the device; Electron gun current was 125 mA.

current of 10 mA, the smallest value used in this experiment. Similarly, the largest beam current used (125 mA) resulted in the shallowest potential well. This behaviour may be attributed to two factors

1. Increased ionisation of the background gas resulting in a cold population of electrons and ions that are able to “wash out” the formed potential well and
2. Higher beam densities in the outer region of the device resulting in space charge limited flow into the core and enhanced mirror reflection.

Point one may be addressed by considering a simple one dimensional magnetic trapping region, into which an electron beam of velocity  $v_b$  carrying a current  $I_b$  is injected. If the trapping

region has a cross sectional area  $A$  and the electrons complete, on average,  $\delta$  transits before being lost, then the trapped density of beam electrons may be approximated as

$$n_b \approx \frac{\delta I_b}{ev_b A}. \quad (7.8)$$

The production rate of cold electrons and ions within the volume through electron impact ionisation is therefore given by

$$+ \frac{d}{dt} n_{i,e} \approx n_n n_b v_b \sigma_{ei}(v_b) + n_n n_e < v \sigma_{ei} > \quad (7.9)$$

where  $n_n$  is the density of neutral gas molecules present within the trap and  $\sigma_{ei}(v)$  is the electron impact ionisation cross section for the given beam velocity. The second term describes ionisation events due to cold electron distribution. The new populations of cold electrons and ions will begin to escape the trap until the loss rate of both species is equal to Equation 7.9. Given their large mass differential the electrons will be more effectively confined by the magnetic field than the ions, however their correspondingly higher velocity means that an increased number of transits does not necessarily equate to longer trapping times. Berkowitz [15] estimated that for a cusp confined, mono-energetic distribution, the loss rate of electrons from the cusp could exceed that of the deuterium ions by a factor of 35. Thus, it is possible for the loss rate of electrons to exceed that of the ions resulting in a build up of positive space charge which serves to eliminate the potential well formed by the beam electrons.

The second point requires consideration of the interaction of the electron beam with its self generated electric fields. A propagating beam will produce fields that cause the beam to diverge, while simultaneously limiting the amount of current that can be conveyed. Child [155] derived expressions for the maximum current than can propagate across a parallel plate acceleration gap, the so called “space charge limit” of the system. In Child’s derivation the propagation of particles was limited only by the self induced electric fields, however in the case of MCVC-0 there is an additional magnetic component that restricts the flow of charge. In Section 1.2.1.1 we derived expressions for the reflection of electrons from regions of increasing magnetic field strength. In the MCVC device, electrons experience a magnetic ratio of  $B_m/B_0 \approx 7$  as they move from the electron gun to the face of the field coil, corresponding to a loss cone angle of  $\approx 22$  degrees. Due to the positioning of the electron gun, most electrons are injected almost parallel to the field lines, however electric field driven divergence of the beam will tend to drive electrons out of the loss cone region, thereby enhancing the mirror effect. Further, if Equation 1.20 is re-written as

$$\sin^2(\alpha) < R_m \left[ 1 + \frac{\Delta\Phi}{E} \right] \quad (7.10)$$

where  $E$  is the initial electron energy in eV, and  $\Delta\Phi$  is the change in the electrostatic potential along the path, then we see that for an injection energy of 750 eV, a potential barrier of only

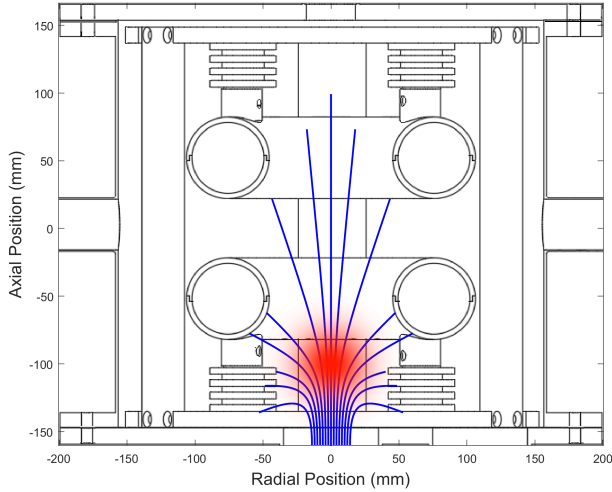


FIGURE 7.4: Magnetic mirror reflection of the electron gun beam from the outer face of the lower field coil. Space charge build up in this region, shown in red, results in divergence of the electron beam and subsequently enhances mirror reflection.

150 V is sufficient to close the loss cone further, to below 20 degrees. Figure 7.4 demonstrates how space charge build up, coupled with magnetic reflection, can limit electron beam propagation into the core.

A surprising feature in the axial measurements is that the minimum space potential is recorded at  $z = 80$  mm, well beyond the central plane of the magnetic field coil. This can likely be attributed to the presence of large quantities of dielectric materials in the  $z = 70 \rightarrow 150$  mm region of the device. Electrostatic charging of dielectric materials by electron beams is a well studied phenomenon [156, 157] and may be used to explain the observed potential profiles. During the pre-shot period the electron beam is able to freely traverse the vacuum chamber. Electrons collected on the surfaces of the PEEK support struts and their alumina ceramic protection sheaths charge these surfaces and generate new Dirichlet boundary conditions within the upper and lower regions of the device. It is noted that this effect was most pronounced when operating the electron gun at 50 mA and this is once again attributed to the space charge effect obstructing the beam. As all space potential measurements were conducted in the upper portion of the device, it is likely that the lower dielectrics, due to their proximity to the electron gun, are more highly charged than their upper counterparts. As such, the charged dielectrics form an additional electrostatic barrier to beam propagation into the central and upper reaches of the vacuum chamber.

We must also examine the reason behind the apparent formation of a potential well in the radial direction, while no equivalent well is seen in the axial direction. Consideration of the measured electron density profiles (Figure 7.6) provides insight, as the variation of electron density in the radial direction far exceeds that along the axis, thus resulting in a corresponding variation in the

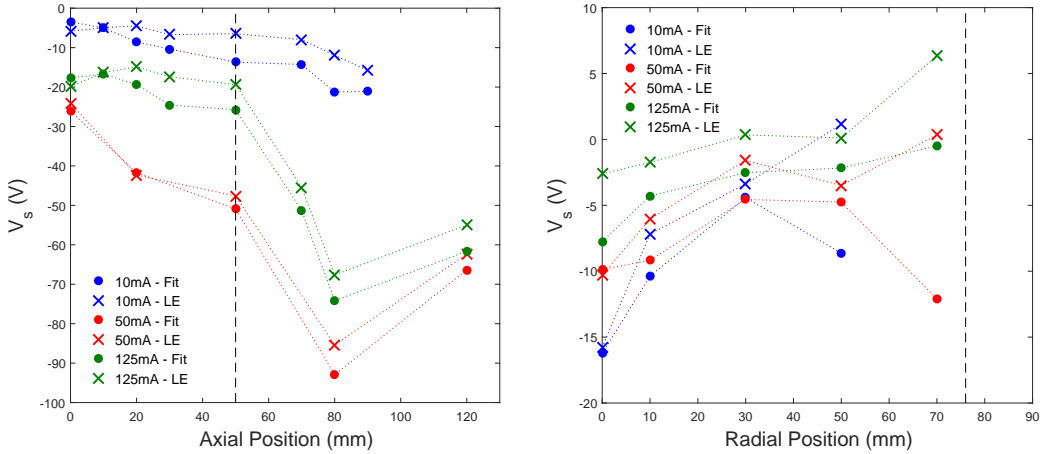


FIGURE 7.5: Plasma potential as a function of position in the axial (*Left*) and radial (*Right*) directions for varying electron beam currents. The results of the LE and Fit methods are given as crosses and points respectively. Dashed, vertical lines denote the spatial position of the magnetic field coils.

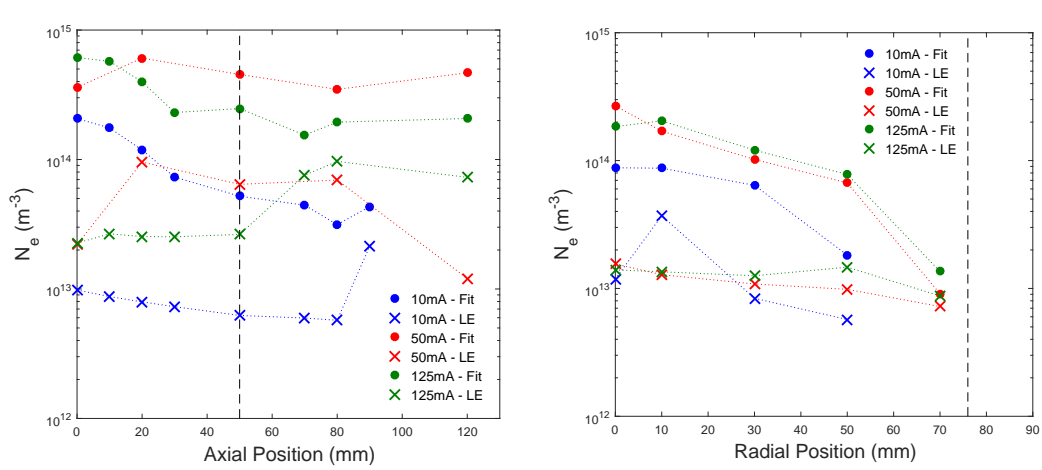


FIGURE 7.6: Electron density as a function of position in the axial (*Left*) and radial (*Right*) directions for varying electron beam currents. The results of the LE and Fit methods are given as crosses and points respectively. Dashed, vertical lines denote the spatial position of the magnetic field coils.

electric potential. A simple explanation for this observation is the system geometry, wherein an electron loss flux that leaves through the point cusps remains approximately cylindrical whereas the line cusp loss expands radially, corresponding to a  $1/\rho$  drop in particle density even in the absence of a confining force. Log-log plots of the radial density profiles result in slopes of approximately -0.6, rather than -1 as expected for divergent cylindrical flow and this suggests some small degree of confinement in the radial direction.

Finally, the electron temperature distributions in Figure 7.7 also display very little variation over the trapping volume, typically varying between 1-4 eV. It is expected that electrons with larger kinetic energies will populate the outer regions of the trapping volume and to an extent this effect is seen in the radial temperature distribution. It is hypothesised that the large jump

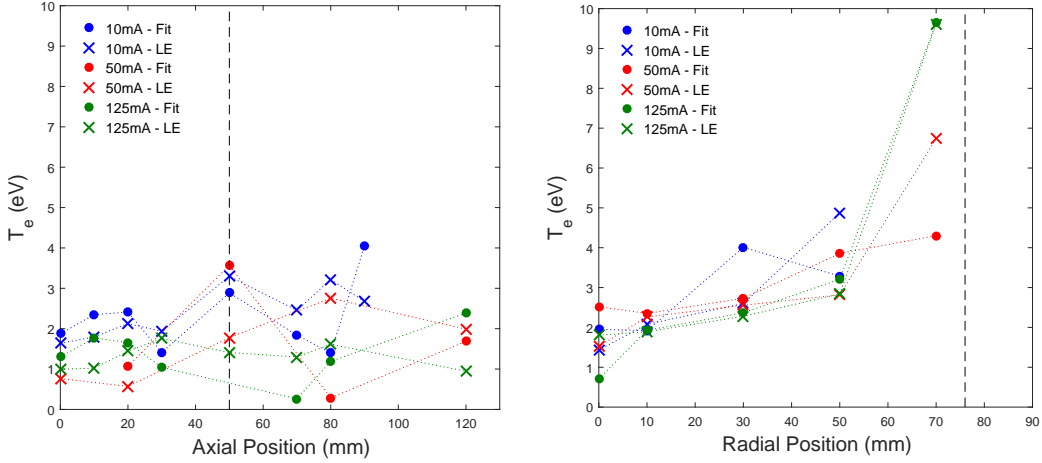


FIGURE 7.7: Electron temperature as a function of position in the axial (*Left*) and radial (*Right*) directions for varying electron beam currents. The results of the LE and Fit methods are given as crosses and points respectively. Dashed, vertical lines denote the spatial position of the magnetic field coils.

in the electron temperature at  $\rho = 70$  mm is the result of higher energy electron gun electrons that have traversed the region outside of the magnetic field coils. It is to be noted that the axial and radial data sets share a common value, at the  $\rho = z = 0$  mm position and it is expected that the measured plasma parameters at this point should be consistent across the two data sets. Significant discrepancy is found between the two datasets however, with as much as a factor of 2 variation between equivalent data points. Switching the translation axis of the Langmuir probe necessitated breaking vacuum and reconfiguring the vacuum chamber. It is therefore possible that the chamber conditions, in terms of vacuum cleanliness, differed between acquisition of the two data sets resulting in the observed inconsistencies. Further, gradual cleaning or coating of the Langmuir probe tip over successive shots would suitably account for variation in the measured plasma properties. Finally, it is not well understood the extent to which the position of the Langmuir probe itself perturbs the evolution of the plasma.

### 7.2.2 Electron Temperature from Variable Impedance Floating Probe

As discussed in Section 5.2.1, it is not possible to discern the true floating potential with a passive probe because the act of measuring the probe voltage results in a small net current being drawn from the plasma. The measured floating potential,  $V_{f,m}$ , is instead given by the point at which the collected probe current is equal to the leakage current being drawn by the measurement apparatus. That is

$$I_p(V_{f,m}) + \frac{V_{f,m}}{R_p} = 0 \quad (7.11)$$

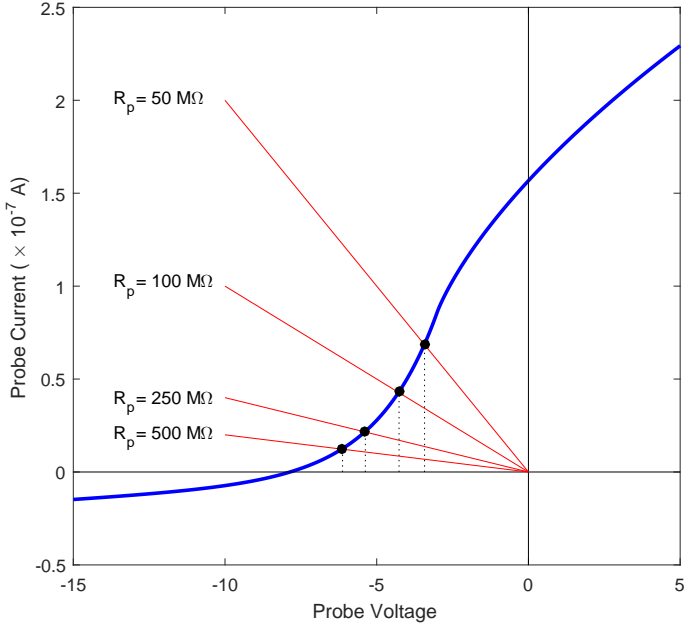


FIGURE 7.8: Illustration of resistive load lines for variable impedance floating probe. For each resistance the measured floating potential is given by the intersection of the plasma *IV* curve and corresponding load line.

where  $R_p$  is the series resistance of the probe and  $I_p(V_p)$  is the *IV* characteristic of the plasma. The measured equilibrium voltage will fall somewhere between the floating potential and the reference potential, usually ground.

In most cases the plasma potential and floating potential are positive relative to the vacuum apparatus. In this case  $0 < V_{f,m} < V_f$  and so the intersections between the *IV* curve and the resistive load lines lie on the ion collection part of the *IV* curve. In the case where the plasma potential is negative with respect to the apparatus however, the intersections lie on the exponential part of the electron collection curve and hence varying the probe resistance serves as a convenient means of sampling the *IV* curve without the need for additional power supplies and current sensing apparatus. An example *IV* is given in Figure 7.8 with the load lines for varying values of  $R_p$  given in red. For an electron beam current of 125 mA, the floating potential at the core of the device was measured using a set of large value resistors (60 M $\Omega$ , 250 M $\Omega$ , 500 M $\Omega$ , 2 G $\Omega$ ). The logarithms of the probe currents ( $I_p = V_{f,m}/R_p$ ) were plotted against the measured floating potentials and the gradients of the resulting curves used to compute the electron temperature. Figure 7.9 gives an example of one such plot, computed at the peak of the magnetic field pulse.

The electron temperature as a function of time was plotted alongside that determined from the *IV* curve fitting method, see Figure 7.10. The top panel of Figure 7.10 gives the plasma potential during the shot with dashed vertical lines denoting the region in which  $V_s < 0$ . It can be seen that the variable impedance probe measurements correlate closely with those obtained

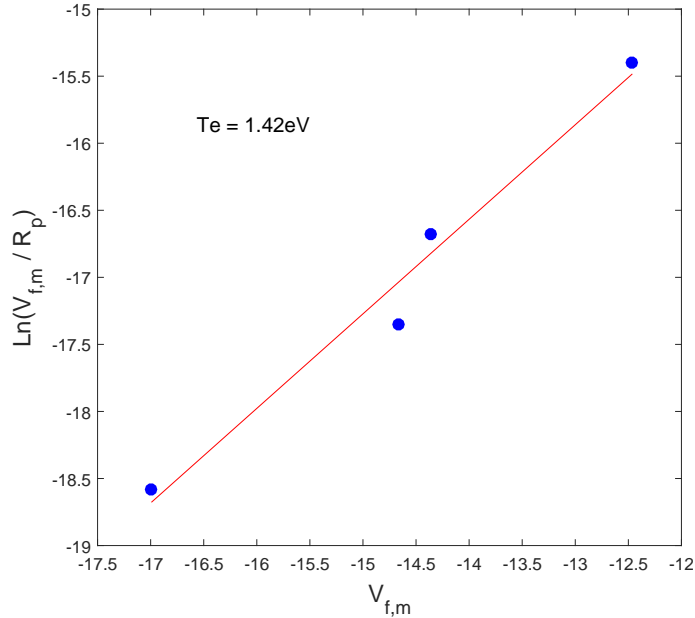


FIGURE 7.9: Example plot of the electron exponential region as determined through use of the variable impedance floating probe. The data corresponds to the peak of the magnetic field pulse and gives a computed electron temperature of 1.43 eV.

---

from the fitted *IV* curves, while requiring only 4 shots of the device as compared with  $\sim 75$  for the equivalent *IV* curve.

The data sets are seen to diverge at  $t \approx 90$  ms however, corresponding to the time at which the space potential begins to rise. It is expected that this is due to asymmetries in the probe response time as a result of the relative mobilities of electrons and ions. Charging the probe negatively involves collection of electrons while charging the probe positively requires the collection of ions or the emission of electrons from the probe surface. As the latter processes are limited by large ion masses and the low electron emissivity of tungsten probe tips there is a lag in the probe response in regions where  $dV_f/dt > 0$ . This delay results in a shift in the measured electron temperature and so such a method is best suited to slowly varying or DC systems such as traditional gridded IEC devices.

### 7.3 Low Voltage Operation (500V)

It has been established in Section 7.2 that operation of MCVC-0 in the absence of an applied coil bias does not result in the formation of any significant potential well, in direct contrast with comparable measurements observed in earlier polywell style devices. The most directly comparable experiment was that conducted by Carr [88] in which electrons were injected into an unbiased, teflon polywell. Floating potentials of approximately -100 V were obtained for modest injection currents of only 2 mA. Carr's electron injection however, came by way of a

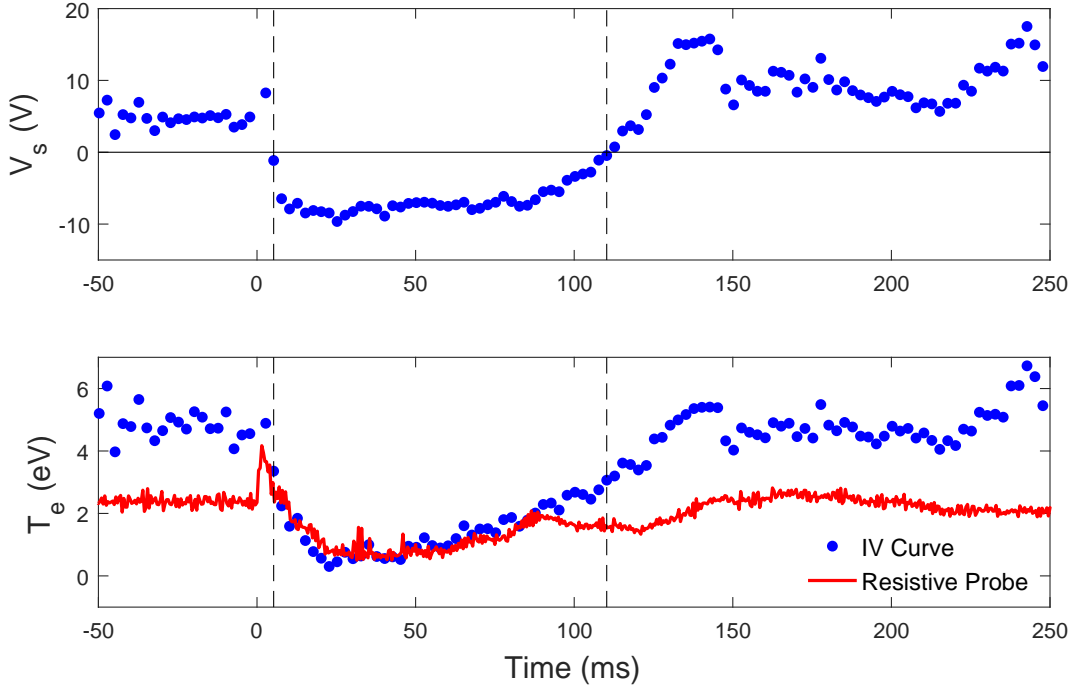


FIGURE 7.10: Comparison of measured electron temperatures as determined through the *IV* curve fitting and variable impedance floating probe methods. The top panel gives the plasma potential and dashed vertical lines denote the region where  $V_s < 0$ .

hollow cathode type electron gun [95] operating at voltages of 12-15 kV, well beyond that used in this experiment. If potential well depth is assumed to be proportional to electron injection energy then scaling Carr's results to our 750 eV injection energy we would infer expected well depths for our set up of  $\sim 5$  V.

In the absence of a high voltage gun for electron injection it is necessary to derive additional beam energy by using the MCVC-0 coils as an accelerating electrode. Further, in Section 1.2.1.1 we derived the corrected mirror ratio for a biased magnetic mirror and demonstrated that the application of a sufficiently large accelerating potential could reduce the reflection of the electron beam from the outer face of the magnetic field coil by expanding the loss cone angle. In this section we explore device operation in the low voltage regime, wherein a 500 V bias is applied to the field coil cases for the duration of the magnetic field shot. The bias was typically activated 50-100 ms prior to the shot and remained on for 200-400 ms. A series load ( $R_L$  in Figure 4.14) of  $9.4\text{ k}\Omega$  was used and the plasma current determined as the voltage differential between the capacitor ( $V_{cap}$ ) and the voltage developed on the coil cases ( $V_{bias}$ ).

The top panel in Figure 7.11 provides indicative time series for a biased shot. The coil current is given, as is the voltage on the bias capacitor. The magnetic coil current has been scaled for clarity. The coil voltage is given for varying values of electron beam current (2 mA, 20 mA and 120 mA). It is noted that the coil bias in the regions before and after the magnetic field shot is substantially attenuated relative to the driving bias capacitor and this is due to the collection

of the electron beam current on the coil surfaces:  $\Delta V = -I_b \text{ mA} \times 9400 \Omega$ . This is most obvious in the case where  $I_b = 120 \text{ mA}$ , as the voltage drop due to the collected current is larger than the maximum applied voltage of 500 V. The coil bias subsequently remains at ground until the magnetic field is activated and the electron current into the coil surface is mediated through magnetic shielding.

The remaining panels in Figure 7.11 give the calculated space potential and electron density and temperatures for the core of MCVC-0. The plasma properties have been derived from analytical fitting of the IV curves as discussed in the previous section. Unlike the previous measurements, the plasma potential (panel 2) is seen to drop significantly with the application of the magnetic field, reaching a minimum of +20 V while the coil bias was +450 V. This  $\approx 430 \text{ V}$  voltage differential between the centre of the plasma and the surrounding conductive surfaces appears to indicate the successful formation of a virtual cathode.

Figures 7.12, 7.13 and 7.14 once again give the spatial variation of the plasma parameters, averaged over the 15 ms window at the peak of the magnetic field pulse. The space potential profiles now appear to display the expected dependence on electron injection current, with increasing current resulting in lower core potentials. However the expected spatial structure remains absent, with very little absolute change in potential over the full span of the device.

It is noted that while the minimum in the axial direction is still beyond the limits of the magnetic field coils, the absolute drop in potential is far smaller than that observed in Figure 7.5. This is likely due to the fact that when the 500 V bias activates at  $t = -100 \text{ ms}$ , the electron beam is almost entirely captured on the coil shells. Charge previously collected on the dielectrics is therefore able to dissipate prior to the magnetic shot, thereby reducing the perturbation to the potential structure.

The absence of any significant potential well at the core is in contradiction to the apparent peak in electron density in the same region (Figure 7.13). We once again infer that the core plasma is therefore almost completely neutral, formed from the ionisation of the background gas. Such an observation is of interest however, due to the relatively low pressures under which the device was operated. The base operating pressure of the system was  $\approx 1 \times 10^{-7} \text{ Torr}$ , corresponding to a neutral particle density of  $\approx 3.2 \times 10^{15} \text{ m}^{-3}$ , the same order of magnitude as the measured electron densities. It is grossly unreasonable to suggest close to 100% gas ionisation in such a system due to insufficient heating power, however this observation does indicate a very high degree of background ionisation. For the duration of the shot it is likely that the system pressure was elevated to between  $1 \times 10^{-6} - 1 \times 10^{-5} \text{ Torr}$ , due to outgassing from the heated electron gun filaments, and this would correspond to a background ionisation fraction of between 1 and 10%. Such a high degree of ionisation is not unexpected from a system with strong electric and magnetic fields in a crossed configuration.

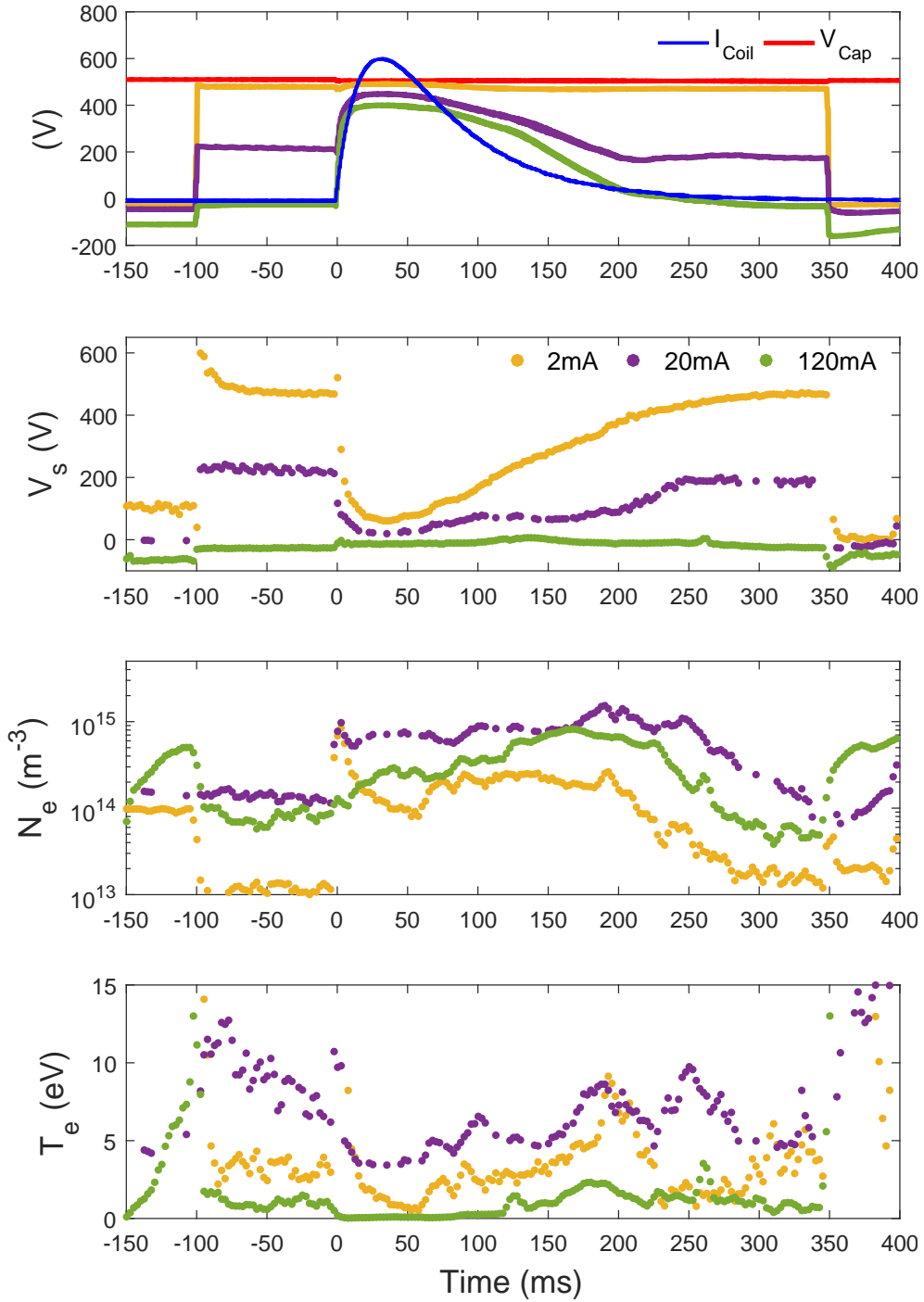


FIGURE 7.11: Computed plasma parameters, as a function of time, for MCVC-0 operation with low voltage (500V) biased coil cases. In the top panel the magnetic coil current is given in blue while the bias capacitor voltage is given in red. The remaining traces correspond to the coil bias voltage for varying electron gun currents of 2 mA, 20 mA and 120 mA. The second, third and fourth panels depict the plasma potential, density and temperature as computed via the *IV* curve fitting method.

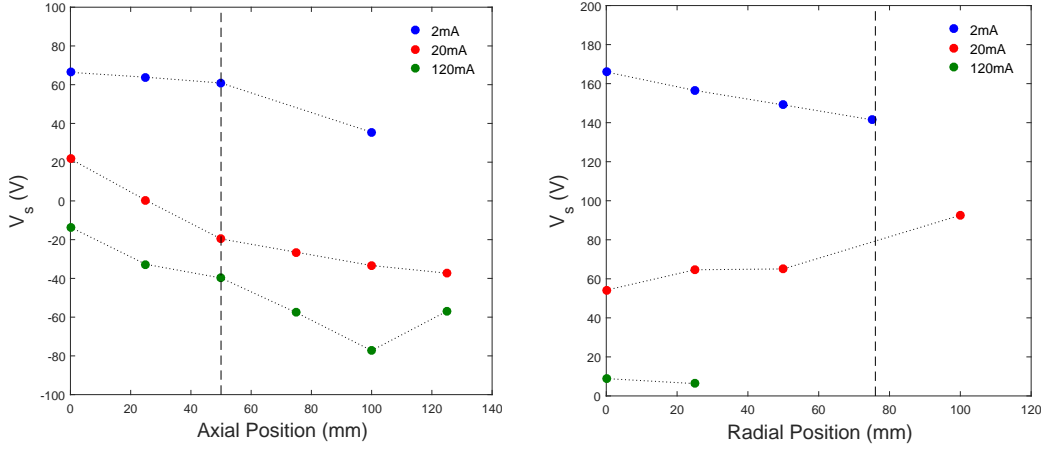


FIGURE 7.12: Plasma potential as a function of position in the axial (*Left*) and radial (*Right*) directions for varying electron beam currents. Dashed, vertical lines denote the spatial position of the magnetic field coils.

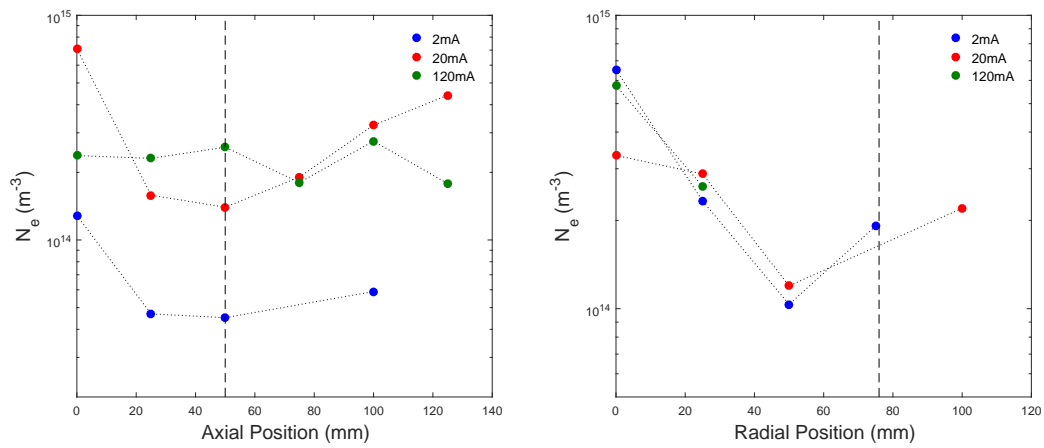


FIGURE 7.13: Electron density as a function of position in the axial (*Left*) and radial (*Right*) directions for varying electron beam currents. Dashed, vertical lines denote the spatial position of the magnetic field coils.

### 7.3.1 Potential Well Scaling with Magnetic Field Strength

It may be seen in Figures 7.3 and 7.10 that the space potential displays very little variation over the course of the magnetic field shot, even for large changes in magnetic field strength. It was found that increasing the peak field resulted only in excessively heating the magnetic field coils, with no apparent increase in the potential well depth. In biased operation (Figure 7.11) the core potential does obey an inverse relationship with magnetic field strength in time, though not in space. In order to verify that the absence of a potential well was not simply an artefact of insufficient magnetic field strength, a pair of *IV* curves were obtained at radial positions of 0 and 50 mm, using a PCPS charging voltage of 300 V. This corresponds to a four-fold increase in coil current over the previous sections.

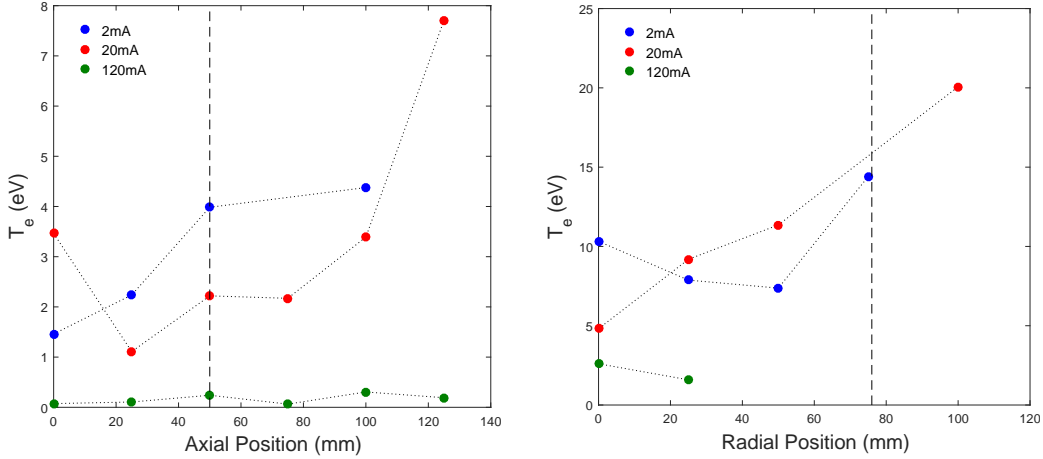


FIGURE 7.14: Electron temperature as a function of position in the axial (*Left*) and radial (*Right*) directions for varying electron beam currents. Dashed, vertical lines denote the spatial position of the magnetic field coils.

Figure 7.15 gives the measured potential difference between the  $\rho = 0$  mm and  $\rho = 50$  mm radial positions as a function of peak field strength. The potential is averaged over the 15 ms window at the peak of the current pulse and error bars correspond to the standard deviation over the same period. There was found to be negligible change in the well depth when compared to the statistical uncertainty. Indeed the larger magnetic field appears to have inverted the potential profile, resulting in a virtual *anode* in the core. It is hypothesised that this is due to increased ionisation of the core and subsequent ambipolar effects as discussed in Section 7.2.1. We therefore elected not to proceed with studies at increasingly elevated field strengths.

### 7.3.2 Off-Axis Langmuir Probe Measurements

It was demonstrated in the previous sections that the space potential does not vary significantly along either the central or horizontal axes of the MCVC-0 device, in direct contrast to the theoretical operation of the magnetically confined virtual cathode concept. The space potential in the plasma core is almost completely uniform, to within several tens of volts, and is approximately equal to the potential of the vacuum chamber walls (0 V). The coil cases however are held at close to 500 V for the duration of the shot and so there must exist a transition region, or sheath, between the main plasma volume and the biased coils.

We wished to examine the size of the transition region, as well as the potential drop across it and so a dog-leg Langmuir probe was constructed with the probe tip positioned 40 mm off axis. The closest approach between the probe tip and the coil case was approximately 5 mm. As the straight probe used in the previous sections violated the conditions for a “cylindrical” collector, the new tip was lengthened from 2 mm to 5 mm and reduced in diameter from 150  $\mu\text{m}$  to 50  $\mu\text{m}$ . The resulting probe had a length to radius ratio of 200, nearly ten times that of the previous

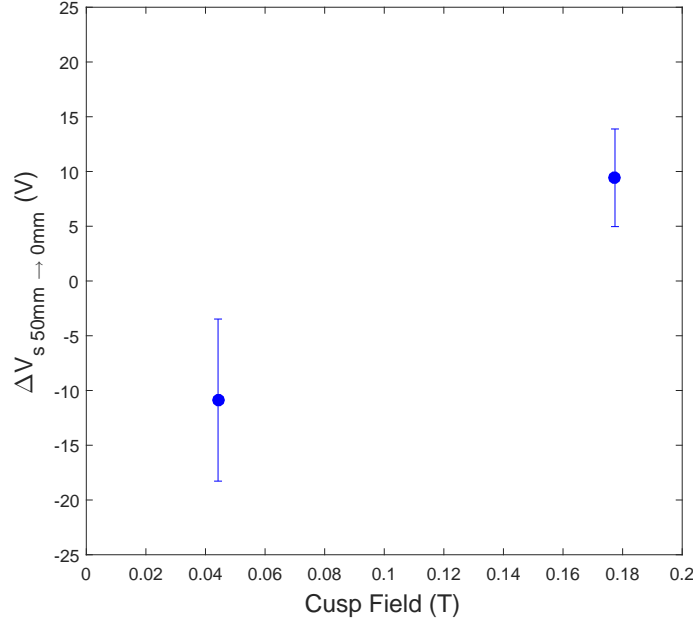


FIGURE 7.15: Potential differential between the  $\rho = 0$  mm and  $\rho = 50$  mm radial positions as a function of peak magnetic field strength. Data is averaged over 15 ms at the peak of the magnetic pulse. Error bars are given as the standard deviation of the potential over the averaging window.

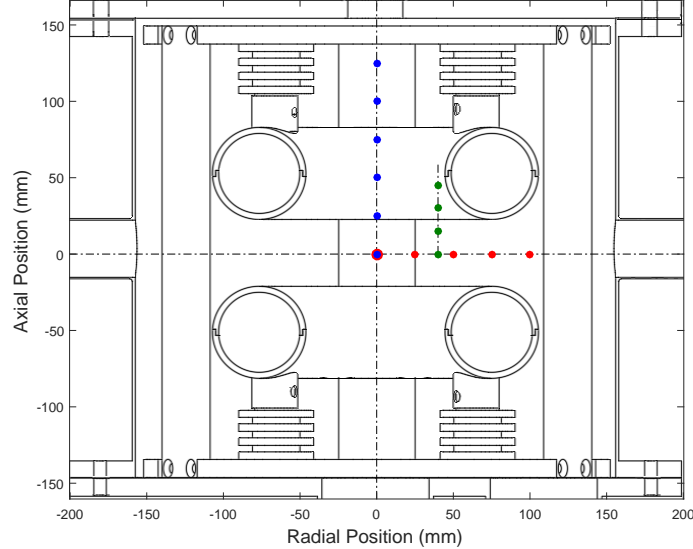


FIGURE 7.16: Spatial positions sampled within MCVC-0. Red and Blue data points are given in Figures 7.12 to 7.14. Green “dogleg” measurements are given in Figures 7.18 and 7.19.

probe. The dog-leg probe was positioned at the central plane of the device and translated vertically in 15 mm increments. The new sample locations are represented as green points in Figure 7.16. The axial and radial points sampled in previous sections are also shown in blue and red respectively. The electron gun current was set to 20 mA and the electrode bias was set to 500 V. As the series load of  $9.4 \text{ k}\Omega$  tended to curtail the maximum obtainable grid bias, even for modest collected currents (50 mA), in this section we have reduced the load to  $700\Omega$ , the

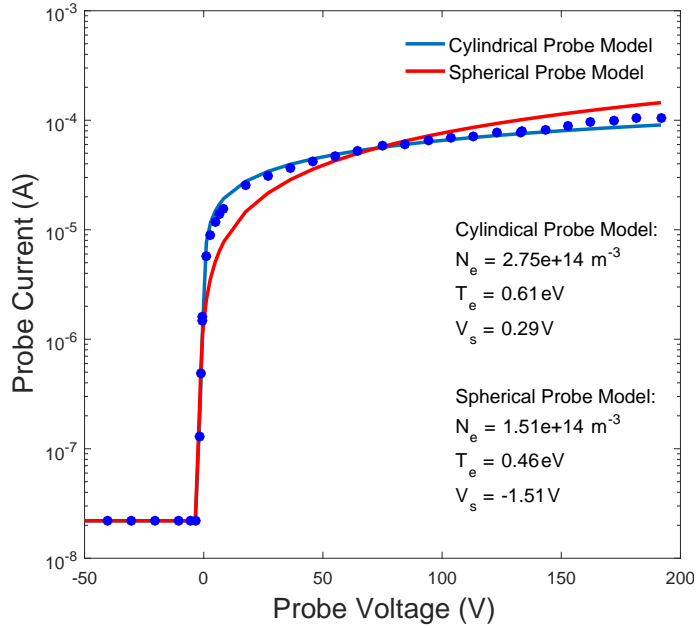


FIGURE 7.17: Example IV curve obtained using dogleg Langmuir probe. The data has been fitted with both cylindrical and spherical probe models and is found to be consistent with the theoretical cylindrical probe response.

minimum value for which uncontrolled gaseous breakdown did not occur. This value remained unchanged for the remainder of the work described in this thesis. Biased Langmuir probe measurements were made as previously described, with a typical IV curve shown in Figure 7.17. It is seen that the new probe tip behaves in a manner that is consistent with the derived theory for cylindrical probes. The density measurements obtained here therefore serve as a cross check for those values obtained previously. The time series obtained from the dog leg probe are shown in Figure 7.18. Significant variation in all parameters is now apparent, with a space potential drop of over 200 V across the points measured. Similarly, the electron density is seen to decay by over an order of magnitude when approaching the coil surface, accompanied with an increase in the electron temperature. Such observations are consistent with those expected from a plasma sheath. The probe positions  $(\rho, z)$  were converted to displacements  $dS$  from the surface of the electrode according to

$$dS = \sqrt{(76 - \rho)^2 + (z - 50)^2} - 30 \quad (7.12)$$

where all quantities are in millimetres. The numerical constants of 50, 30 and 76 correspond to the axial position of the coil and its minor and major radii respectively. The plasma parameters were then plotted as a function of  $dS$  as shown in Figure 7.19. Note that the measured values at the central plane of the cusp ( $dS = 32$  mm) are consistent with those obtained using the straight probe.

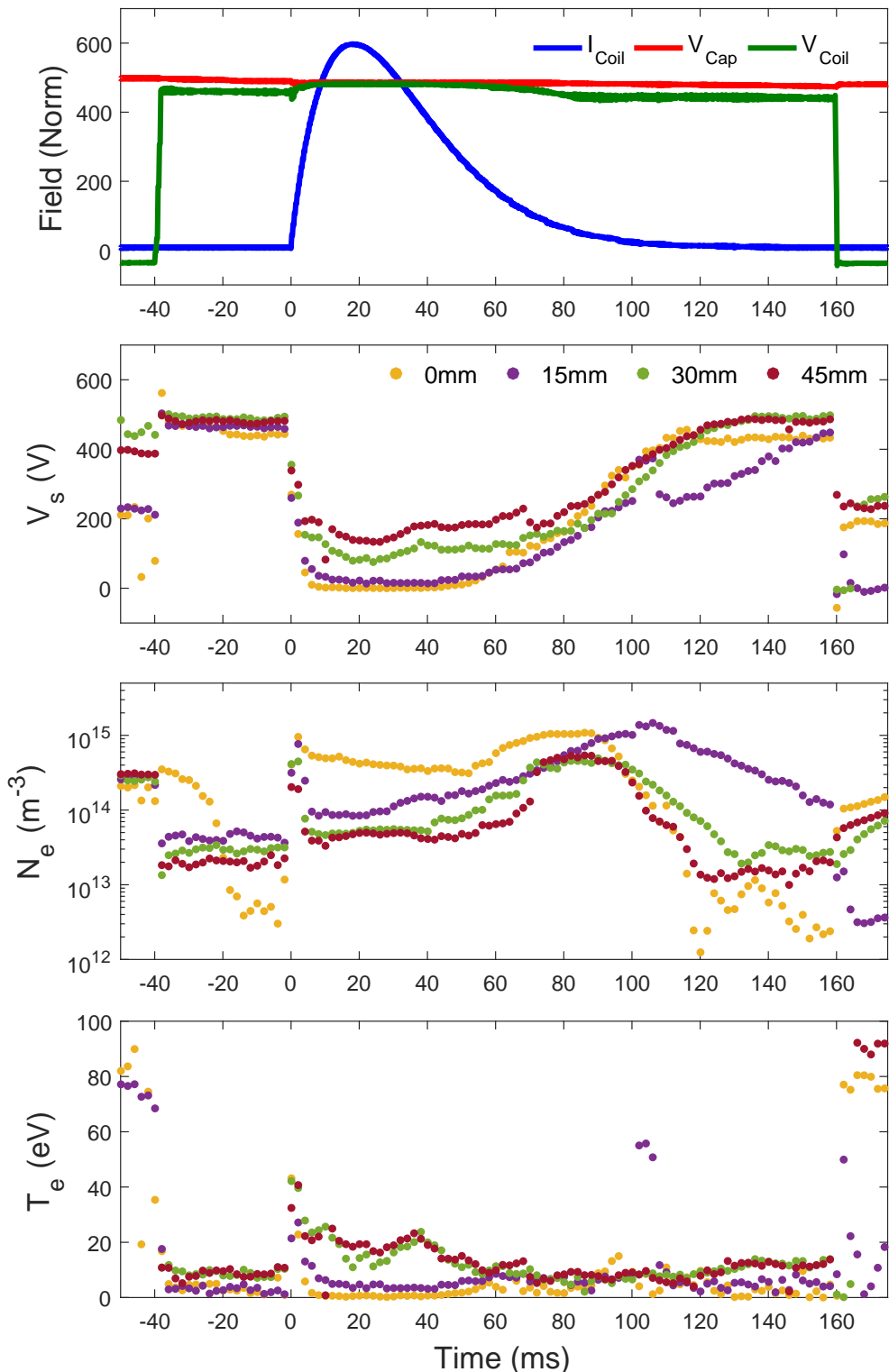
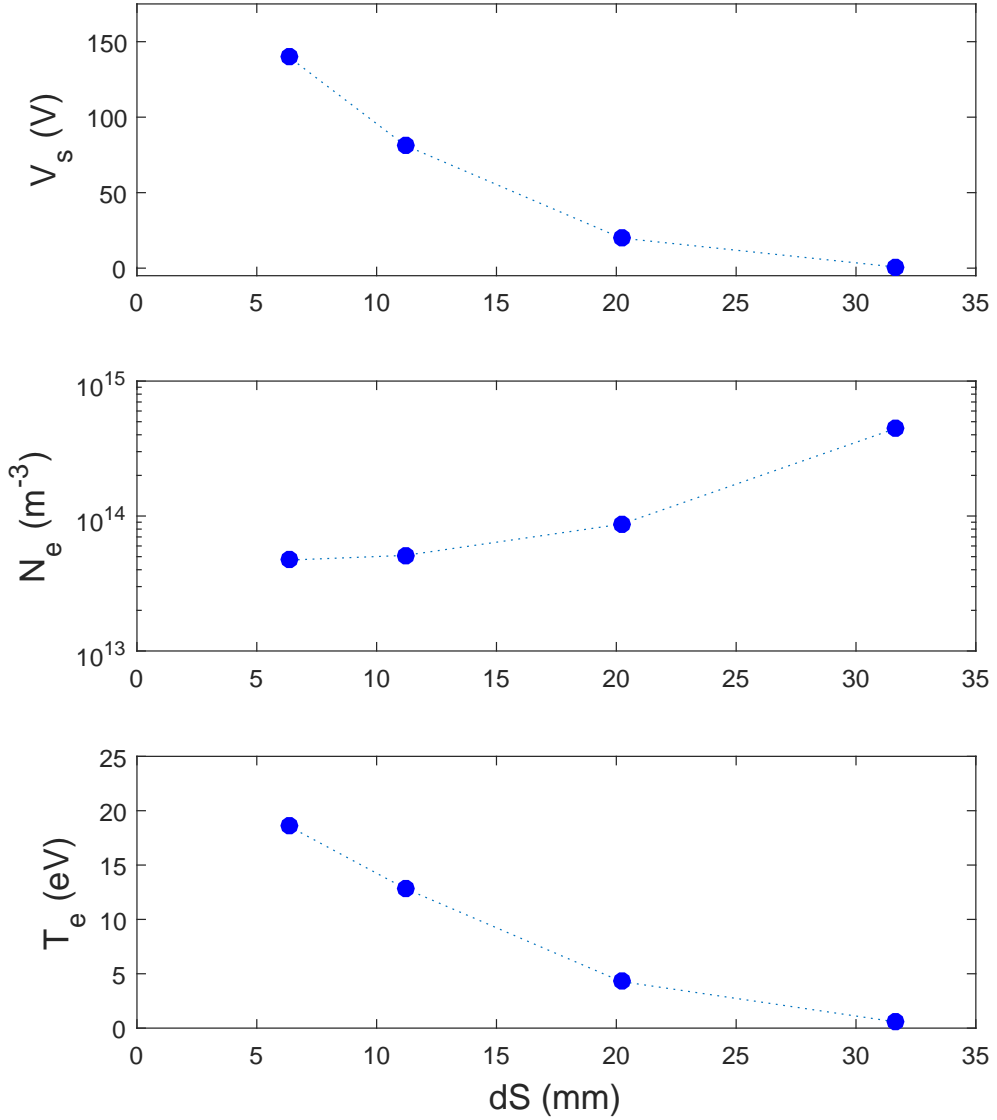


FIGURE 7.18: Temporal variation of plasma parameters at varying  $z$  positions for radial position of  $\rho = 40$  mm.

FIGURE 7.19: Plasma parameters as a function of displacement,  $dS$ , from electrode surface.

### 7.3.3 Validation of Floating Probe Diagnostic

Obtaining biased Langmuir probe measurements required extremely large numbers of pulses of the MCVC device in order to obtain even a single  $IV$  curve. This presented difficulties, not only in terms of long acquisition times, but also in terms of maintaining the system parameters over the course of an experiment. Heating of the magnetic field coils led to reductions in peak coil currents as well as raised system pressure. Further, over the duration of the shot, the space potential within the system varies from  $\sim 0$  V, to the applied coil bias voltage, and so it was necessary to sweep the probe voltage through all values  $0 \rightarrow V_{bias} + 100$  V in order to obtain complete  $IV$  curves for all time. For low voltage operating (500 V) this corresponds to 60-85 shots per  $IV$  curve, depending on the chosen resolution. For applied bias voltages above 1 kV however, this approach becomes impractical, not simply due to the excessive number of shots

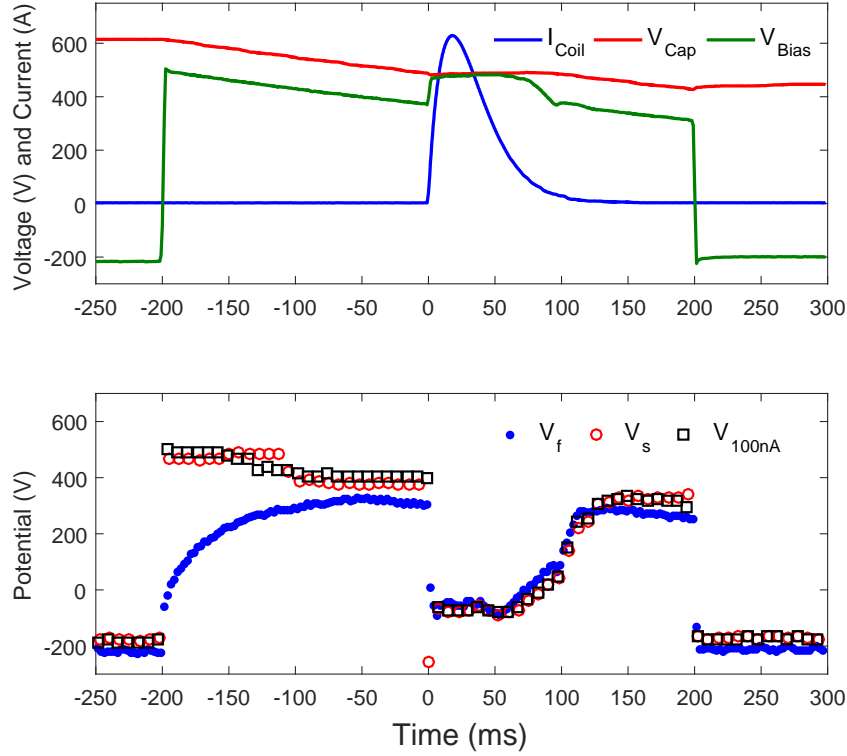


FIGURE 7.20: Comparison of floating and space potentials obtained from the high impedance floating probe and biased Langmuir probe measurement. The coil current has been scaled  $\times 4$  for clarity.

required, but also because arc breakdown on the probe tip often results in unusable data. The high impedance floating probe offers a convenient means to measure the space potential within the plasma without the need for large numbers of repeat pulses, however it was necessary to demonstrate that the measured floating potential  $V_f$  is a reliable indicator of the plasma space potential  $V_s$ . It is seen in the previous sections that the electron temperature appears to remain relatively constant over a shot, and hence according to Equation 5.11, it is expected that the space potential and floating voltage should agree within tens of volts.

The Langmuir probe was positioned in the centre of the device and the coil bias set to 500 V. The electron gun voltage and current were set to 1000 V and 150 mA respectively. The PCPS was charged to 75 V resulting in coil currents of  $\sim 120$  A. An  $IV$  curve was obtained over the range  $-200 \rightarrow 600$  V in 10 V increments and the space potential determined by fitting the expressions in Section 5.1 to the measured  $IV$  curve. A further estimate of the floating potential was obtained by locating the largest probe voltage for which  $I_p < 100$  nA. This method presents a significantly reduced computational burden and results in a cut-off voltage  $V_{100\text{nA}}$  that is constrained by  $V_f \leq V_{100\text{nA}} \leq V_s$ . Figure 7.20 shows the two  $IV$  curve estimates for the potential as compared with floating probe measurements. The coil current has been scaled for clarity.

Although the floating probe diagnostic displays an extremely long time constant in the pre-shot period (-200→-50 ms), likely due to the low electron density during this window, the three potential measurements show excellent agreement for the duration of the magnetic field pulse. We therefore conclude that the floating probe diagnostic is an appropriate tool for the measurement of the plasma space potential when operating the MCVC device in regimes where biased Langmuir probe measurements are impossible.

## 7.4 High Voltage Operation (1-6 kV)

Thus far we have considered both unbiased and low voltage operation of MCVC-0 resulting, in all cases, in a homogeneous, isothermal discharge plasma. This is likely attributable to the relatively small input powers ( $500\text{ V} \times 150\text{ mA} = 75\text{ W}$ ), as well as mirror reflection of the electron beam from the outer face of the cusp field. For the MCVC to operate as a fusion device the applied biases must be on the order of several kilovolts, with electron injection currents of many amperes. Using Equation 7.10 and our values of  $R_m \approx 1/7$  and  $E = 750\text{ V}$ , we find that the loss cone angle exceeds 90 degrees for an applied coil bias of  $\Delta\Phi = 4500\text{ V}$  and so we expect greatly improved electron injection above this voltage.

When operating at elevated bias voltages ( $>2\text{ kV}$ ) impurities present on the surface of the coils were liberated during the plasma shots and the resulting pressure spikes led to uncontrolled gaseous breakdown. It was therefore necessary to pre-condition the device prior to an experimental run. A cleaning routine was devised wherein the device was repeatedly pulsed at low power in order to sputter impurities off the electrode surfaces. The cleaning action was observed as a steady decline in the plasma current over successive shots until the discharge characteristic stabilised.

The high impedance floating probe was positioned in the centre of the MCVC-0 device and translated along the central axis in increments of 10 mm. At each spatial position the floating potential was recorded for varying magnetic field strengths by charging the PCPS between 0→150 V in increments of 10 V, resulting in point cusp field strengths of between 0 and 0.2 T. In all cases the electron gun current was set to its maximum value of 150 mA. The dog leg probe was installed and the procedure repeated. The spatial positions sampled by the straight and dogleg probes are indicated in Figure 7.21. Figure 7.22 provides floating potential traces, as measured at the core, for varying grid bias and field strength. In each panel the applied grid voltage is given as a dashed black line. We note that there is very little difference between the traces, even for very large changes in the applied bias. The core potentials rapidly saturate at  $\sim 0\text{ V}$ , even for weak magnetic fields.

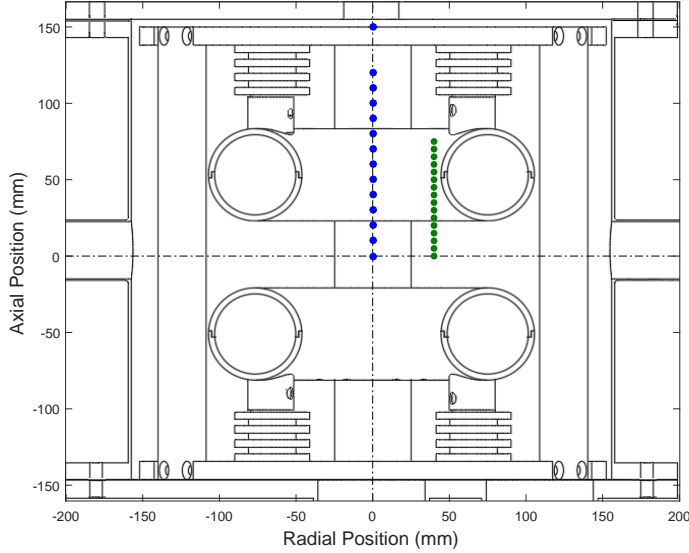


FIGURE 7.21: Spacial positions sampled within MCVC-0. Blue data points are given in Figure 7.24. Green “dogleg” measurements are given Figure 7.25.

By examining the orange traces in Figure 7.22 we may examine the response of the core potential when the smallest magnetic field is applied (18mT), corresponding to the lowest possible charge voltage of the PCPS (10 V). We see that for a coil bias of 500 V the core potential immediately saturates at its minimum value, while increased bias voltages result in a smaller drop in the core potential, relative to the coil voltage. Increasing the field strength to 26 mT and 40 mT (yellow and purple traces in Figure 7.22) results in further reduction of the core potential until the potential saturates, for all bias voltages, at fields above 100 mT. It is noted that further increasing the applied magnetic field does not result in a reduced core potential, but instead lengthens the time over which the minimum potential is obtained. The floating potential was averaged over 15 ms at the peak of the magnetic field shot and plotted against the field strength in the point cusp in Figure 7.23. There appears to be very little dependence on the applied bias voltage, with the core potential in all cases saturating at around 0.06 T. In an electron trapping model we would expect the injection energy to impact the effectiveness of electron trapping in the magnetic field. Gummersall [97] estimated the electron confinement time in a zero beta, six coil polywell machine to be given by

$$\tau \propto \frac{I_{coil}^{1/2} R_{coil}^{3/4}}{E^{3/4}} \quad (7.13)$$

where  $I_{coil}$  and  $R_{coil}$  are the coil current and radii respectively, and  $E$  is the electron energy. If we take the magnitude of the dip in the floating potential,  $|\Delta V_f|$ , to be proportional to the electron density, itself proportional to the confinement time, and assume that the cusp field is given approximately as

$$B_{cusp} \approx \frac{I_{coil}}{R_{coil}} \quad (7.14)$$

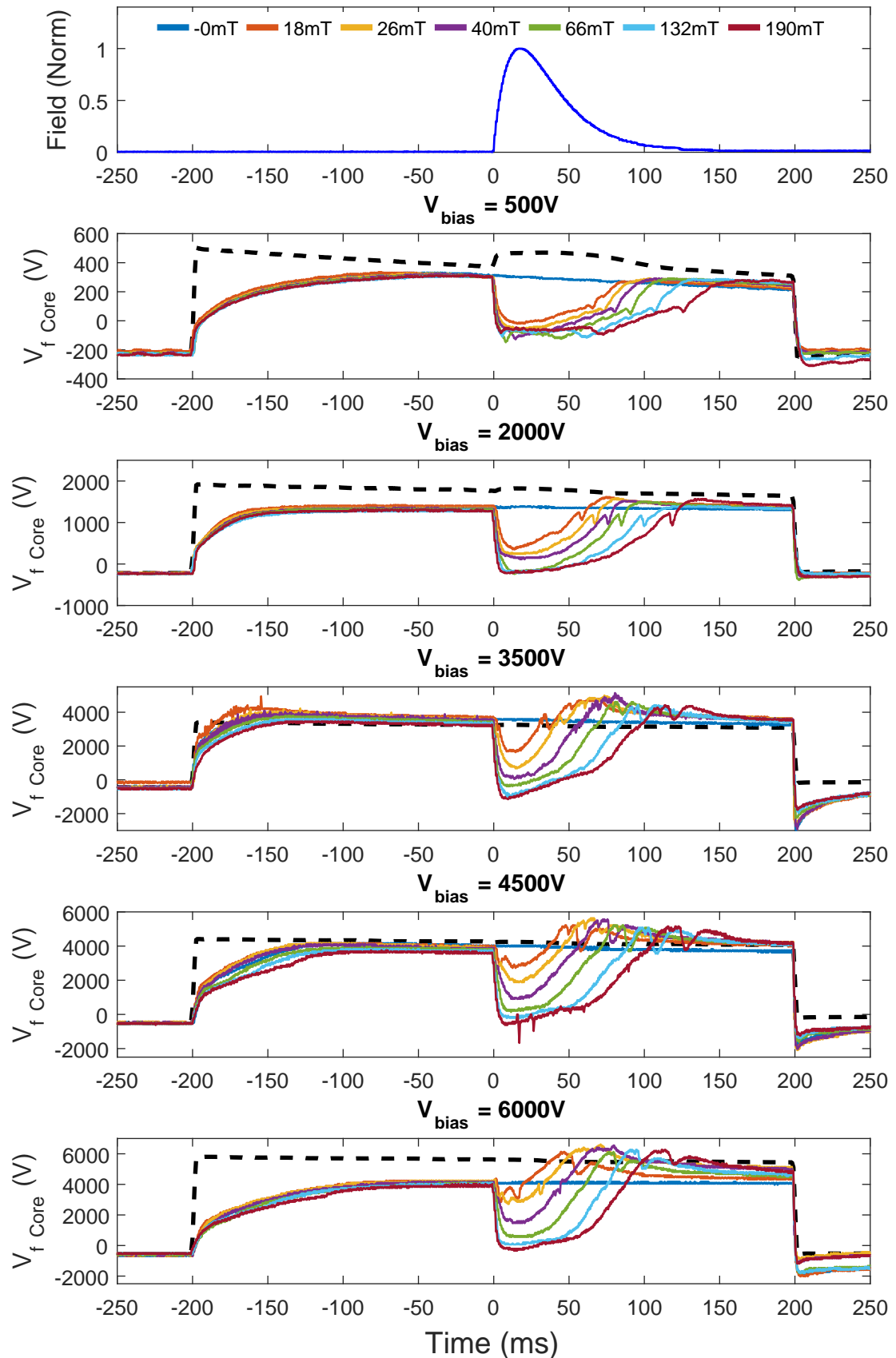


FIGURE 7.22: Core floating potential traces for varying values of grid bias voltage and magnetic field strength. The normalised magnetic field profile is given in the top panel, and the applied grid bias is shown in each panel as a dashed black line. The peak magnetic field strength for each trace is given in the top panel.

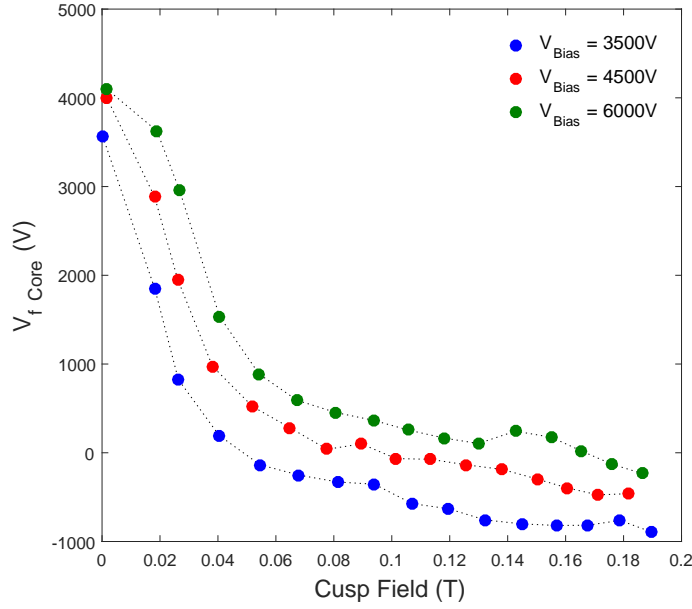


FIGURE 7.23: Floating potential in the core of MCVC-0 as a function of point cusp magnetic field strength for varying bias voltages.

then we find that

$$|\Delta V_f| \approx \frac{\sqrt{B_{cusp}} R_{coil}^2}{E^{3/4}} \quad (7.15)$$

The above expressions were formulated for a six coil cubic device, and so are not exact for our two coil system. They do, however, adequately demonstrate the expected behaviour of the potential dip as a function of magnetic field strength for varying electron energy. Computing the derivative of Equation 7.15 results in

$$\frac{d|\Delta V_f|}{dB_{cusp}} \approx \frac{1}{2} \frac{R_{coil}^2}{E^{3/4}} \frac{1}{\sqrt{B_{cusp}}} \quad (7.16)$$

and we note the dependence of the slope on the kinetic energy of the injected electrons. This is found to be inconsistent with the curves in Figure 7.23 which exhibit almost identical gradients in both the pre- and post- saturation regions. From this we again rule out any significant electron trapping. The floating potential as a function of axial position is shown in Figure 7.24 for varying field strengths, corresponding to the blue data points in Figure 7.21. We find that in the absence of any magnetic field the measured floating potentials approximate the computed vacuum solutions, given as solid red lines. With the application of increasing magnetic fields the profiles flatten until the floating potential is uniform from the core of the device to the chamber wall. Vertical black lines denote the central plane of the magnetic field coils and we see there is no distinction between the interior and exterior regions of the device. The off axis potentials, indicated by the green points in Figure 7.21, are shown in Figure 7.25 and exhibit considerably more structure. While the potentials at the  $z = 0$  mm position follow those in Figure 7.24, out of the central plane of the cusp we see the formation of a magnetic sheath with increasing field

strength. For the  $V_{bias} = 4\text{ kV}$  and  $6\text{ kV}$ , the maximum potential is observed in the central plane of the coil, at the point of closest approach to the high voltage surface. The size of the sheath region is found to be 25-30 mm, consistent with that measured in Section 7.3.2.

## 7.5 Summary

In this chapter we have presented the preliminary experimental findings from operation of MCVC-0 in each of the unbiased, low voltage and high voltage regimes. It is apparent from observations that the MCVC-0 machine is not operating according to the standard magnetically confined virtual cathode model, with negligible electron trapping observed and electric potential distributions which remain flat from the vacuum chamber wall to the plasma core. A valid criticism of the presented work is that the injected electron currents (150 mA) are very small relative to those in comparable Polywell machines. While insufficient electron current is a possible explanation for the observed behaviour, the injected currents are an order of magnitude larger than those used in smaller devices in which potential well formation was observed. Future work will be focused on upgrading the electron injection system such that multiple Amperes of injected current may be achieved.

In the following chapter we develop a model based on non-isotropic plasma conductivity and subsequently address the absence of potential well formation in MCVC-0. The model is further applied to two previously published Polywell machines and is shown to provide an alternative physical explanation for the observation of potential well structures in those devices.

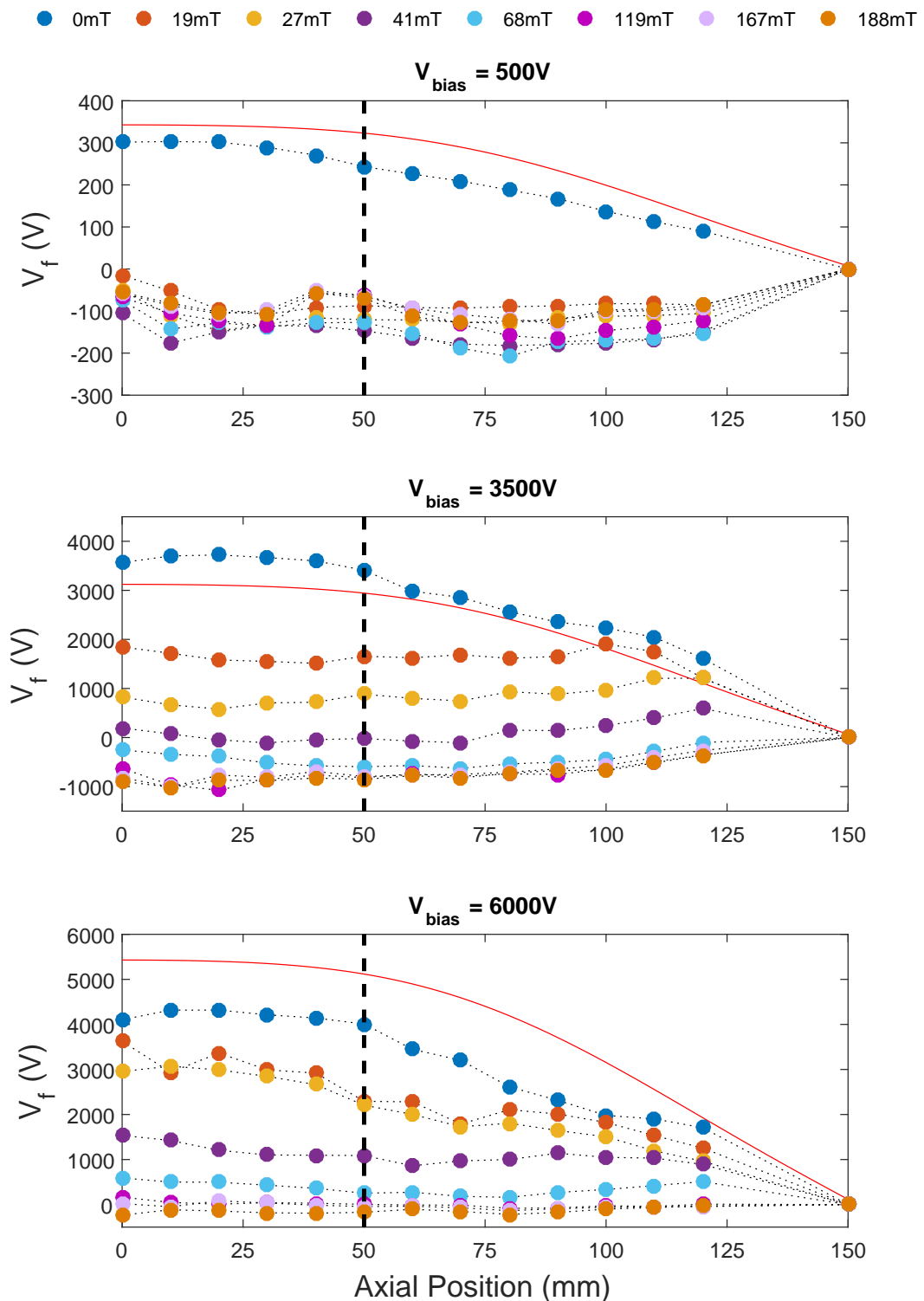


FIGURE 7.24: Floating potential as a function of axial position for varying magnetic field strength. Dashed vertical lines indicate the central plane of the magnetic field coils while solid red lines denote the theoretical vacuum potential in the absence of an applied magnetic field. At zero field the floating potential is approximately equal to the vacuum solution. The floating potential falls with increasing magnetic field until the potential is uniform.

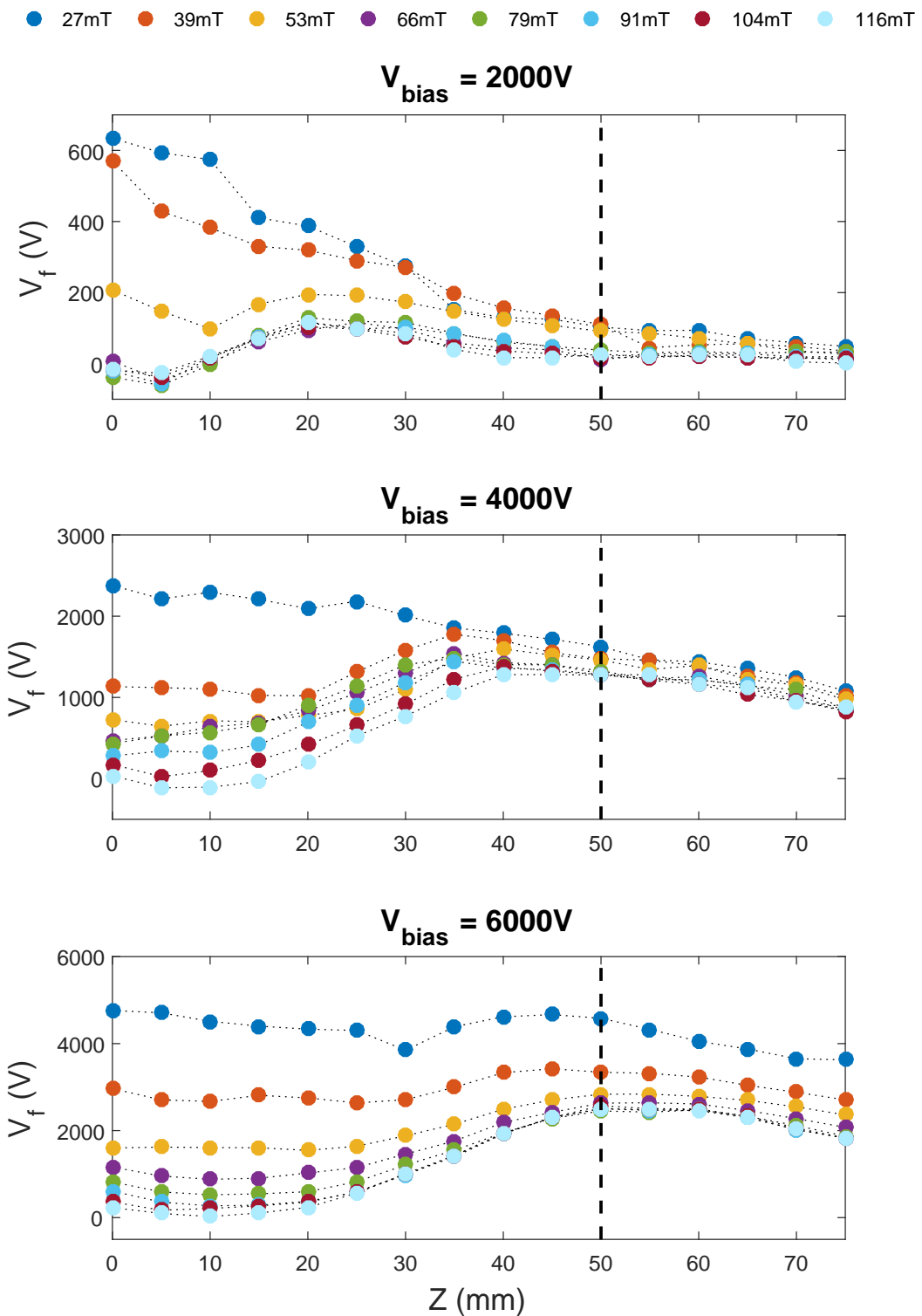


FIGURE 7.25: Off axis floating potential as a function of vertical position for varying magnetic field strength. Dashed vertical lines indicate the central plane of the magnetic field coils. Increasing magnetic field strength results in the formation of a magnetic sheath between the core and the biased coil.

## Chapter 8

# Plasma Conductivity in MCVC / Polywell Devices

In the previous chapter we have explored the operation of MCVC-0 and demonstrated, through the use of floating and biased Langmuir probe measurements, a complete absence of potential well formation. This outcome is puzzling when compared with previous Polywell machines operated at The University of Sydney [91, 93, 94] and DTI [83], all of which behaved in accordance with the Polywell theory. The biconic magnetic field configuration within MCVC-0 is expected to exhibit larger particle losses than a comparable six coil configuration, however this geometric difference is unlikely to account for such a large departure from the expected behaviour.

A common feature of hybrid electro-magnetic fusion devices, such as the Polywell, is the use of transverse magnetic fields to limit plasma conduction to electrode surfaces, so called “magnetic shielding”, with the view to reduce particle losses and therefore improve the energy efficiency of the machine. In this section we will demonstrate the importance of boundary conditions within magnetic virtual cathode devices and how complete magnetic shielding of electrode surfaces may prove to be deleterious in the formation of electrostatic potential wells. Further we cast a new physical interpretation on the results of earlier Polywell research, drawing into question the viability of magnetic virtual cathode systems as potential fusion sources.

### 8.1 Laplace Equation in Anisotropic Conductive Media

A common approach in plasma modelling is to first consider the vacuum fields caused by applied currents and electric boundaries and subsequently evaluate perturbations to those fields due to plasma currents and charges. In Section 6.2 we formulated a discrete form for the Laplace equation and solved the electric potential for the MCVC-0 device in the absence of a plasma and

the obtained potential is valid in all cases where the solution volume is filled with a medium of uniform electrical conductivity,  $\sigma$ . When a neutral plasma is introduced into the system however, the electrical conductivity becomes both non-zero and non-uniform and we wish to examine the resulting perturbation to the electric potential.

Consider a current flowing in a bulk conductor, written as a sum of source ( $J_s$ ) and conduction ( $J_c$ ) terms:

$$\vec{J} = \vec{J}_s + \vec{J}_c. \quad (8.1)$$

The conduction term is governed by Ohm's law such that

$$\vec{J}_c = \vec{\mathcal{S}} \cdot \vec{E} = -\vec{\mathcal{S}} \cdot \nabla \Phi \quad (8.2)$$

where  $\vec{\mathcal{S}}$  is called the conductivity dyad. From the principle of charge conservation we find that, in the steady state, the divergence of the current density must be zero. Taking the divergence of Equation 8.1 and substituting in 8.2 therefore yields

$$\nabla \cdot (\vec{\mathcal{S}} \cdot \nabla \Phi) = \nabla \cdot \vec{J}_s. \quad (8.3)$$

Equation 8.3 is a generalised form of the Poisson equation in the presence of conductive media. We shall now consider cases in which the source current is zero (Laplace equation) and  $\vec{\mathcal{S}}$  is both non-homogeneous and anisotropic. That is

$$\vec{\mathcal{S}} = \begin{pmatrix} \sigma_x(x, y, z) & 0 & 0 \\ 0 & \sigma_y(x, y, z) & 0 \\ 0 & 0 & \sigma_z(x, y, z) \end{pmatrix}. \quad (8.4)$$

Equation 8.3 may be reformulated in discrete form using the same approach described in Section 6.2 and expressed as a Jacobi relaxation update according to

$$\Phi^{n+1} = \mathcal{K}\Phi + \sum_{q=x,y,z} \mathcal{A}_q \Phi_{q+} + \mathcal{B}_q \Phi_{q-} \quad (8.5)$$

where  $q$  corresponds to each of the spacial indices and the coefficients  $\mathcal{K}$ ,  $\mathcal{A}_q$  and  $\mathcal{B}_q$  depend on the chosen coordinate system. Due to the large number of subscripts we have adopted the following shorthand notation: Un-shifted indices ( $i, j, k$ ) are omitted and positive and negative shifts are denoted  $q+$  and  $q-$  respectively, where  $q$  is the coordinate axis along which the shift occurs. In this way the discrete second derivative expression

$$\frac{\partial^2 \Phi}{\partial x^2} \Big|_{i,j,k} \approx \frac{\Phi_{i+1,j,k} - 2\Phi_{i,j,k} + \Phi_{i-1,j,k}}{\Delta x^2} \quad (8.6)$$

may be written more compactly as

$$\frac{\partial^2 \Phi}{\partial x^2} \Big|_{i,j,k} \approx \frac{\Phi_{x+} - 2\Phi + \Phi_{x-}}{\Delta x^2}. \quad (8.7)$$

In Cartesian coordinates, the coefficients in Equation 8.5 are given by

$$\begin{aligned} \mathcal{K} &= 1 - \frac{1}{3} \sum_q \sigma_q \\ \mathcal{A}_q &= \frac{1}{6} (\sigma_q + D_q) \\ \mathcal{B}_q &= \frac{1}{6} (\sigma_q - D_q) \\ D_q &= \frac{1}{4} (\sigma_{q,q+} - \sigma_{q,q-}) \end{aligned}$$

In Cylindrical coordinates, the equivalent expressions are

$$\begin{aligned} \Phi^{n+1} &= \mathcal{K}\Phi + \mathcal{A}_\rho\Phi_{\rho+} + \mathcal{B}_\rho\Phi_{\rho-} + \mathcal{A}_z\Phi_{z+} + \mathcal{B}_z\Phi_{z-} \\ \mathcal{K} &= \left(1 - \frac{1}{2}(\sigma_\rho + \sigma_z)\right) \\ \mathcal{A}_\rho &= \frac{1}{4} \left( \frac{\rho + \frac{1}{2}\Delta\rho}{\rho} \sigma_\rho + D_\rho \right) \\ \mathcal{B}_\rho &= \frac{1}{4} \left( \frac{\rho - \frac{1}{2}\Delta\rho}{\rho} \sigma_\rho - D_\rho \right) \\ \mathcal{A}_z &= \frac{1}{4} (\sigma_z + D_z) \\ \mathcal{B}_z &= \frac{1}{4} (\sigma_z - D_z) \\ D_\rho &= \frac{1}{4} (\sigma_{\rho,\rho+} - \sigma_{\rho,\rho-}) \\ D_z &= \frac{1}{4} (\sigma_{z,z+} - \sigma_{z,z-}) \end{aligned} \quad (8.8)$$

The largest anisotropy in plasma conductivity arises due to the presence of a magnetic field. For a magnetised plasma, in which the magnetic field is aligned with the  $z$  axis, the DC conductivity dyad is given by [22]

$$\vec{\mathcal{S}} = \frac{n_e e^2}{m_e \nu_c} \begin{pmatrix} \frac{\nu_c^2}{(\nu_c^2 + \Omega_e^2)} & -\frac{\nu_c \Omega_e}{(\nu_c^2 + \Omega_e^2)} & 0 \\ \frac{\nu_c \Omega_e}{(\nu_c^2 + \Omega_e^2)} & \frac{\nu_c^2}{(\nu_c^2 + \Omega_e^2)} & 0 \\ 0 & 0 & 1 \end{pmatrix} \quad (8.9)$$

where  $\nu_c$  is the collision frequency,  $\Omega_e$  is the electron cyclotron frequency and all other quantities

have their usual meaning. It is seen that Ohmic currents perpendicular to the magnetic field lines are suppressed relative to the parallel currents by a factor

$$\frac{\sigma_{\perp}}{\sigma_{\parallel}} = \frac{\nu_c^2}{(\nu_c^2 + \Omega_e^2)} \quad (8.10)$$

which is, in general, much less than unity. Miyamoto [158] found the electron-electron collision frequency to be

$$\nu_{ee} \approx \frac{n_e e^4}{6\pi\epsilon_0^2\sqrt{3m_e}(k_B T_e)^{3/2}} \ln \Lambda = 4.2 \times 10^{-12} n_e T_e [\text{eV}]^{-3/2} \ln \Lambda \quad (8.11)$$

and so using the experimentally determined parameters for our system:

$$n_e \approx 10^{14} - 10^{15} \text{ m}^{-3}$$

$$T_e \approx 1 - 10 \text{ eV}$$

$$B \approx 0.01 - 0.1 \text{ T}$$

$$\ln \Lambda \approx 15$$

we determine that

$$\frac{\sigma_{\perp}}{\sigma_{\parallel}} \approx 10^{-16} - 10^{-9}$$

The off diagonal terms in Equation 8.9 are known as the Hall conductivity,  $\sigma_H$ , and arise due to drift motion of charged particles in a direction perpendicular to both  $\vec{E}$  and  $\vec{B}$ . Comparing the diagonal and off diagonal terms in Equation 8.9 we see that the Hall currents are larger than Ohmic currents by a factor  $\Omega_e/\nu_{ee}$ , corresponding to  $\approx 10^5 - 10^6$  for our system, and so conduction transverse to magnetic field lines is dominated by this effect. Nonetheless, the relative magnitude of cross field conduction to parallel conduction remains vanishingly small

$$\frac{\sigma_H}{\sigma_{\parallel}} \approx 10^{-10} - 10^{-3}$$

The total conductivity transverse to the magnetic field is given as a combination of Ohmic and Hall terms. However as Hall conduction also occurs in a direction perpendicular to the electric field it is itself a function of the electric potential and hence solution of the potential inclusive of the off diagonal terms is necessarily a recursive process. We opt to neglect the Hall terms and instead adopt a simple phenomenological form for the elements in Equation 8.4 wherein the conductivity in a direction  $\hat{q}$  is given by

$$\sigma_q = (1 - \epsilon) \left| \hat{q} \cdot \hat{B} \right|^N + \epsilon \quad (8.12)$$

$q = x, y, z.$

The conductivity parallel to the magnetic field is taken to be uniformly 1, decaying with angle

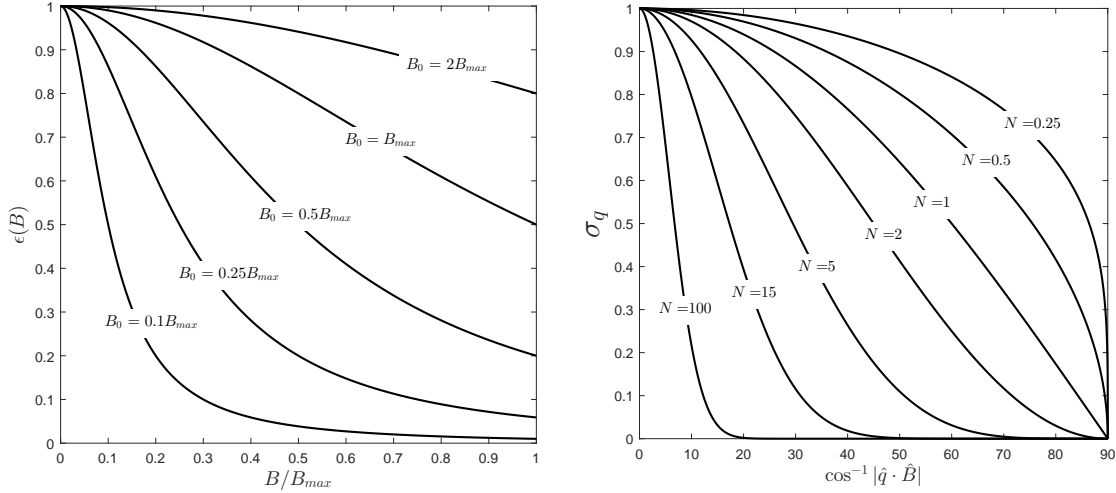


FIGURE 8.1: Relative transverse conductivity,  $\epsilon$ , as a function of magnetic field strength for varying values of  $B_0$  (Left) and roll-off of conductivity in a direction  $\hat{q}$  with increasing angle to the magnetic field line for varying values of  $N$  and  $\epsilon(B)$  taken to be zero. (Right)

until it reaches a minimum,  $\epsilon$ , at right angles to the field line. Through inspection of Equation 8.10 we approximate  $\epsilon$  to vary as a function of the magnetic field strength according to

$$\epsilon(B) \propto \frac{1}{1 + (B/B_0)^2} \quad (8.13)$$

such that the conductivity is approximately isotropic in regions where the magnetic field is small and maximally anisotropic where the field strength reaches its largest value. The left hand panel of Figure 8.1 gives  $\epsilon(B)$  for varying values of  $B_0$ . The free parameter  $N$  in Equation 8.12 may be used to adjust the rate of fall off of the conductivity with increasing angle to the magnetic field as shown in the right hand panel of Figure 8.1.

## 8.2 Anisotropic Laplace Equation in a Penning Trap

It is instructive to examine the solutions to Equation 8.8 in a simple geometry in which the magnetic field is uniform. We consider the case of a pair of disk shaped anodes placed at either end of a hollow cylinder cathode such that they form a Penning trap configuration. We take the inter-electrode volume to be filled with a homogeneous conductor with a magnetic field aligned along the  $z$  axis resulting in unequal axial,  $\sigma_z$ , and radial,  $\sigma_\rho$ , conductivities. Equation 8.8 was then solved for varying values of the ratio  $\sigma_\rho/\sigma_z$  and the resulting solutions are given as contour plots in Figure 8.2. As expected, we find that as the relative conductivity in the  $\rho$  direction is reduced the solution in the core is dominated by the voltage applied to the end plate electrodes, as seen by increased spacing between the contours in the  $z$  direction. Similarly, the dense packing of contours in the vicinity of the cathode indicates a steepening of the potential in this

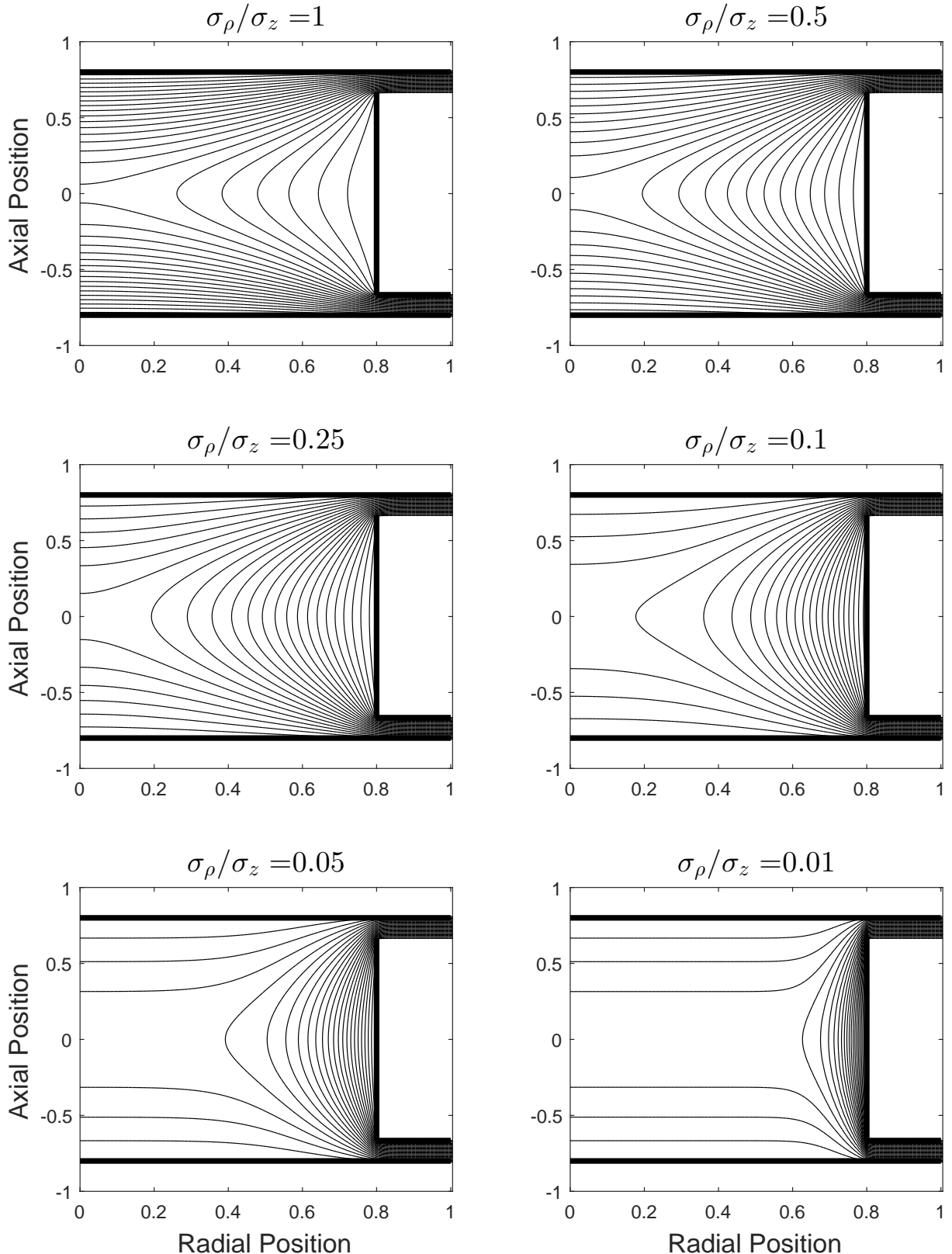


FIGURE 8.2: Equipotential contours of the computed solutions to the anisotropic Laplace equation, (Equation 8.8), in a Penning trap configuration, using varying values of  $\sigma_\rho/\sigma_z$ . In each panel the upper and lower rectangular regions denote the end plate anodes, while the right hand rectangle represents a cross section of the cylindrical cathode wall.

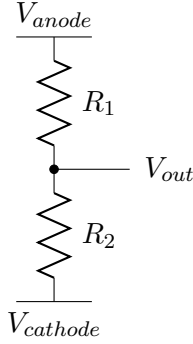


FIGURE 8.3: Resistive voltage divider

region. This effect is analogous to the simple resistive voltage divider, such as that given in Figure 8.3. The voltage expressed at  $V_{out}$  depends on the values of the resistors  $R_1$  and  $R_2$  such that

$$V_{out} = \left( \frac{R_2}{R_1 + R_2} \right) V_{anode} + \left( \frac{R_1}{R_1 + R_2} \right) V_{cathode}. \quad (8.14)$$

In the case where  $R_2 \gg R_1$ , the measured voltage is approximately given by  $V_{anode}$ , and conversely, when  $R_2 \ll R_1$  the output approaches  $V_{cathode}$ . By setting  $\sigma_\rho = 0.01\sigma_z$  we enforce the first case and thus the solution potential is dominated by the anodes. The result is generalised thus: In a medium with anisotropic electrical conductivity, as induced by a magnetic field, the solutions to the Laplace equation will tend to flatten along field lines and steepen across field lines. Such a result is of significance in any system in which the magnetic field lines intersect Dirichlet boundaries as the potential along the field line will tend towards that which is applied on the boundary.

### 8.3 Anisotropic Laplace Equation in MCVC-0

Considering the MCVC-0 machine using the same voltage divider analogy as discussed above we may envisage a mesh of resistive elements arranged along a magnetic field line as in Figure 8.4. The high voltage surface of the magnetic coil case is represented as a red circle, while the chamber walls are shown as bold black lines. The magnetic field lines are everywhere conformal to the coil cases which, with reference to Equation 8.14, may account for the uniformity in the electrostatic potential during a plasma shot. Due to the large size of the MCVC-0 coils relative to the vacuum chamber, a majority of the field lines directly intersect the vacuum chamber walls. Considering the large disparity between the plasma conductivity parallel and perpendicular to the magnetic field, discussed in Section 8.1, it is apparent why the potential profiles in Figure 7.24 converge to zero with increasing magnetic field strength. Increasing plasma density coupled with a high degree of anisotropy means that at elevated field strengths the effective values of  $R_\perp$  and  $R_\parallel$  in Figure 8.4 approach infinity and zero respectively. The measured voltages at all points within

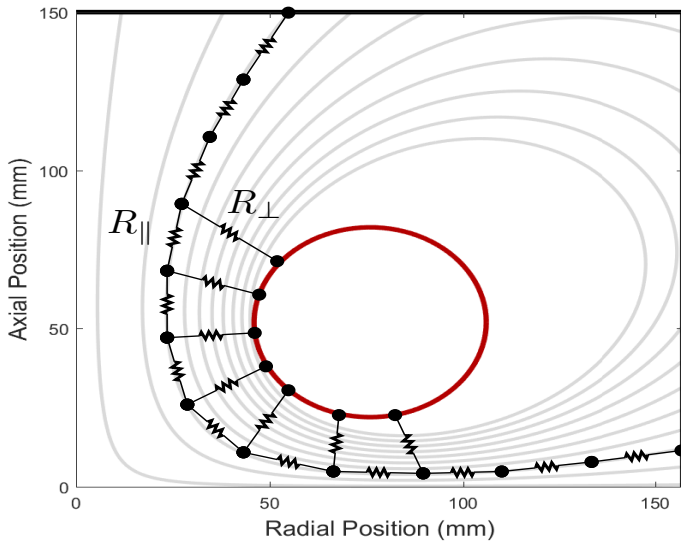


FIGURE 8.4: Resistive network in MCVC-0. The high voltage coil cases are represented in red while chamber walls are indicated as black lines.

the device therefore converge to the potential of the chamber wall. That is, zero. In order to demonstrate this effect numerically, the magnetic field profiles found in Section 6.1.1 were used in conjunction with Equations 8.12 and 8.13 to compute the axial and radial conductivity terms for varying values of  $N$  and  $B_0$ . The solutions to Equation 8.8 were then calculated as before and the resulting contours of electric potential are given in Figure 8.5. We note that in the case of subtle anisotropy ( $N = 1, B_0 = B_{max}$ ) the solutions are almost indistinguishable from the vacuum potentials in Section 6.2.2. As the degree of anisotropy is increased however (increasing  $N$ , decreasing  $B_0$ ) the electric potential between the magnetic field coils begins to flatten until the entire core region equilibrates with the outer grounded boundary. The most extreme case ( $N = 6, B_0 = 0.01B_{max}$ ) is shown in the lower right panel of Figure 8.5 in which the contours of electric potential are reminiscent of the magnetic field structure. We note however, that the minimum transverse conductivity in this case is approximately  $\epsilon = 1 \times 10^{-4}$ , which is still many orders of magnitude larger than our typical values of  $(\sigma_\perp/\sigma_\parallel)$  and  $(\sigma_H/\sigma_\parallel)$  computed in Section 8.1.

A vertical slice was taken through the  $N = 6, B_0 = 0.01B_{max}$  case at a radial position of  $\rho = 40$  mm, corresponding to the position of the dog-leg Langmuir probe described in Section 7.3.2. The saturated potential profiles measured in Figure 7.25 were plotted in Figure 8.6 with the equivalent simulated profile given as solid red lines. The experimental and computational results are found to be in reasonable agreement suggesting that the observed potential distributions measured in MCVC-0 are indeed a result of anisotropic plasma conductivity. Of great significance however, is the observation that well-like potential structures, such as those

shown in Figure 8.6, are achievable in *neutral systems* simply as an artefact of plasma anisotropy. This effect presents an alternative physical explanation for apparent potential well formation and must be considered in any experiment in which a magnetically confined virtual cathode is expected.

It is noted that as we increase the degree of anisotropy by varying the parameters in Equation 8.12 the potential begins to express the rectangular form of the solution mesh. This numerical artefact is caused by the difficulties associated with representing complex geometries on regular square grids and likely accounts for the sharper than expected transition region in Figure 8.6. Our solutions therefore depict the qualitative behaviour of the electric potential only, and should not be regarded as accurate representations. A more complete analysis needs to be conducted through the use of irregular adaptive mesh models [159], however such an analysis is beyond the scope of this work.

## 8.4 Imperfect Electrode Shielding in MCVC-0

In the above section we have addressed the poor performance of MCVC-0 as a virtual cathode device and demonstrated the effect of anisotropic conduction in magnetised plasmas with regard to how Dirichlet boundaries are expressed throughout the plasma volume. Within MCVC-0, almost all field lines intersect the grounded wall of the vacuum chamber and hence the electric potential throughout the machine is dominated by this boundary condition. In devices where magnetic field lines intersect both high and low voltage surfaces however, the resulting flux tubes represent conductive paths that may be considered using standard voltage divider equations. The emergence of potential gradients along such flux tubes may, in the appropriate conditions, be misinterpreted as evidence for a build up of net space charge within the magnetic trap. The validity of this conduction based model may be addressed experimentally by deliberately sabotaging the efficacy of the magnetic shielding in MCVC-0. Through the addition of biased surfaces that are non-conformal to the magnetic field, we are able to establish flux tubes from high to low voltage surfaces. Such an alteration would be expected to have a negative impact on the electron trapping properties of the device and adversely affect charge-induced virtual cathode formation. However if a conduction model applies, re-establishing a high voltage boundary condition will likely result in the formation of potential gradients reminiscent of the potential well expected in the MCVC model.

A set of 1.5 mm stainless steel wire interconnects were added between the magnetic coil cases such that they spanned the plane of the spindle cusp and intersect radial field lines. A total of three interconnects were added to the device, positioned at 120 degree intervals about the outer circumference of the electrodes as depicted in Figure 8.7. The combined area occluded by the interconnects accounts for only 0.7% of the total circumferential area. The floating Langmuir

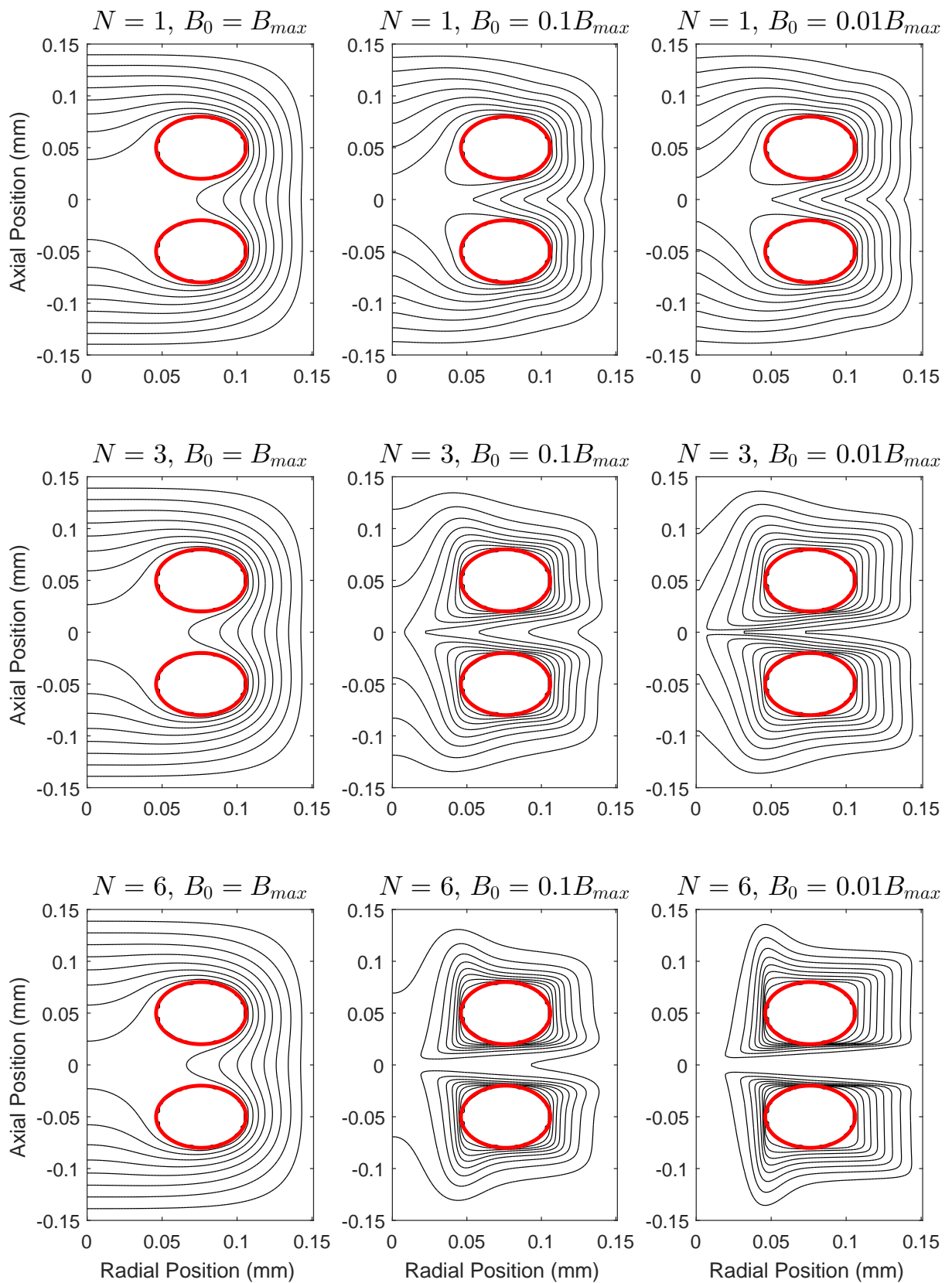


FIGURE 8.5: Electrostatic potential contours in MCVC-0 solved for varying values of  $N$  and  $B_0$  in Equations 8.12 and 8.13. Biased coil cases are represented as red circles.

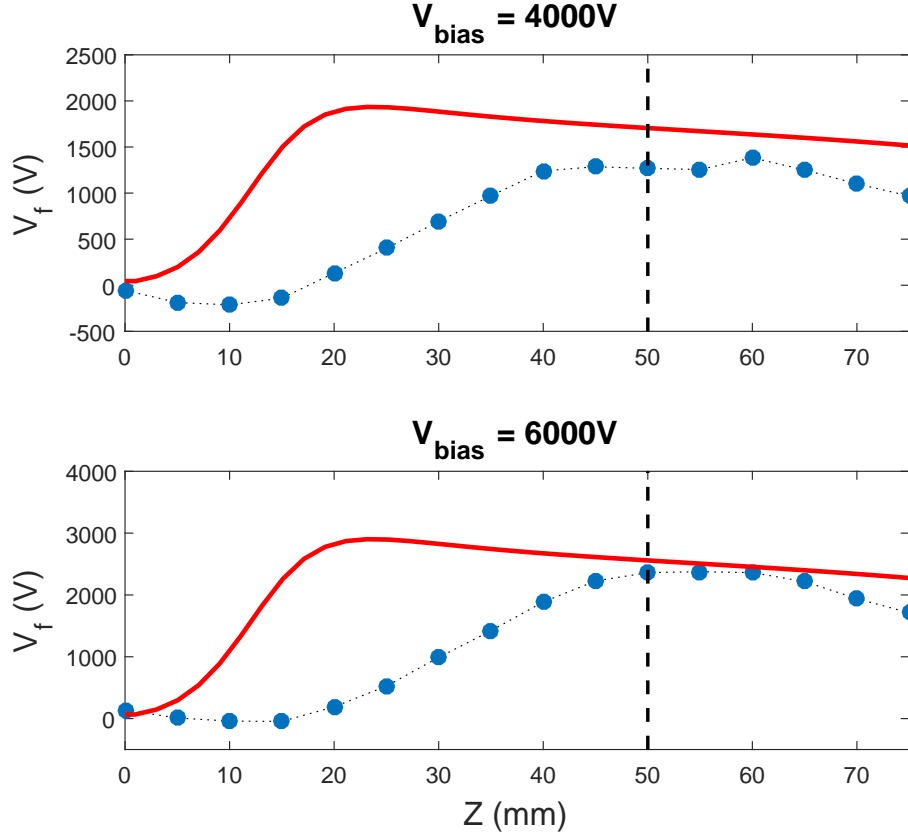


FIGURE 8.6: Saturated off axis potential profiles from Figure 7.25 as a function of axial position. Solid red lines represent the equivalent simulated potentials as shown in the bottom right panel of Figure 8.5.

probe was positioned in the central plane of the device and a radial sweep conducted in 10 mm intervals. The electron gun current was once again set to its maximum value of 150 mA and coil biases of 2000, 4000 and 6000 V were used. The PCPS was charged to values ranging 75-375 V resulting in point cusp field strengths of between 0.1-0.45 T. Figure 8.8 gives the floating potential at the core of the device as a function of cusp field strength, averaged over the 15 ms at peak field. Comparing against the equivalent measurements in Figure 7.23, we now find a strong dependence of the core potential on the coil bias. As per the theory discussed in Section 7.4, an MCVC / Polywell model of this result would attribute the observed behaviour to poorer magnetic trapping of electrons at elevated energies, leading to the need for larger field strengths with increasing bias. However we have demonstrated that such an explanation can not hold in this case as the particle confinement of the device has been compromised relative to that in Section 7.4 in which no potential wells were observed. We instead attribute the new behaviour to the relative degrees of conduction to the Dirichlet boundaries within the machine.

We take the plasma at the core of the magnetic cusp to be homogeneous and, due to the magnetic null, un-magnetised. The outer edge of the core is electrically connected to the walls of the chamber, as well as the interconnects, along radially divergent magnetic flux tubes,

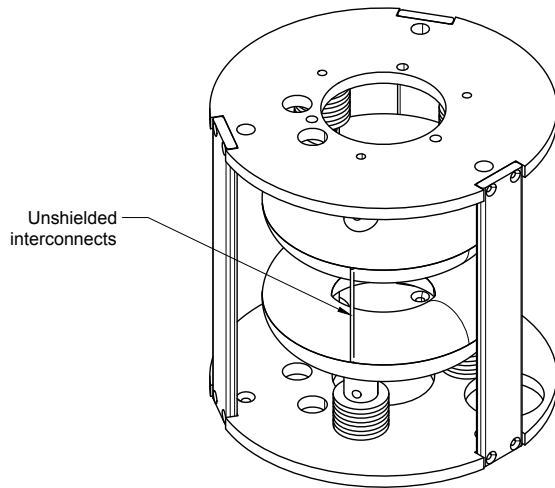


FIGURE 8.7: MCVC-0 device with unshielded interconnects spanning the spindle cusp. Interconnects are arranged at 120 degree intervals about the outer circumference of the field coil cases.

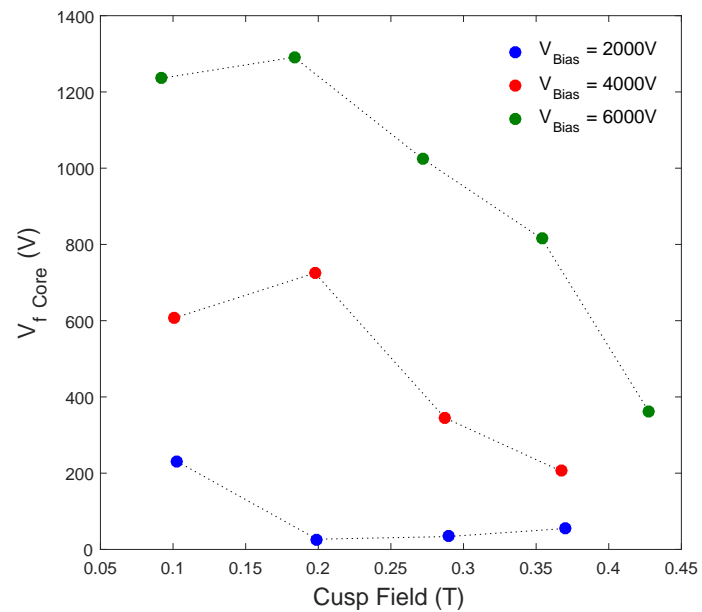


FIGURE 8.8: Core floating potential as a function of peak cusp field strength for imperfectly shielded electrodes.

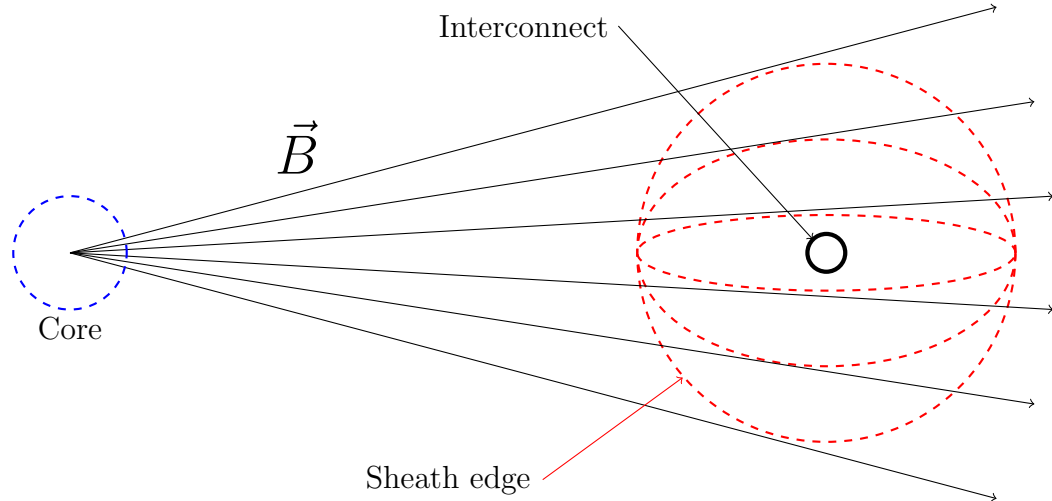


FIGURE 8.9: Plasma sheath around unshielded interconnect as viewed in the  $(r, \varphi)$  plane. Increasing magnetic field strength causes the sheath to contract in the direction transverse to the magnetic field lines until the effective collection area, as seen from the core, converges to the mechanical dimension of the interconnect.

with negligible conduction between adjacent tubes. The number of tubes that intersect the wall and the interconnects therefore determine the relative magnitudes of  $R_1$  and  $R_2$  in the resistive divider equation and hence the observed potential in the core. As with the cylindrical Langmuir probe discussed in Chapter 5, there exists a sheath region around the interconnects that determines their effective collection area and hence the number of flux tubes whose current is ultimately collected on the interconnect surfaces. In the absence of a magnetic field, this sheath is approximately circular, however with increasing field strength we expect the sheath to contract in the direction transverse to the field lines as particle motion in that direction is restricted. The effective collection area should therefore shrink until it is equal to the mechanical dimension of the interconnect, as shown in Figure 8.9. As the effective collection area of the interconnects shrink, the potential in the core becomes increasingly dominated by the chamber wall boundary condition and thus the core potential drops.

Figure 8.10 gives radial potential profiles for varying coil bias and field strength. As in Figure 7.24, the potential throughout the device is found to drop with increasing magnetic field strength, however we once again observe a significant departure from the previously measured behaviour. Distinct well-like structures have emerged, with potential differences of up to  $\sim 1500$  V obtained between the core and the radial dimension of the coils. The closest approach between the Langmuir probe tip and the interconnects is approximately 50 mm, occurring at a radial position of 90 mm. It is seen that the maximum in the measured floating potential occurs at this location in all datasets.

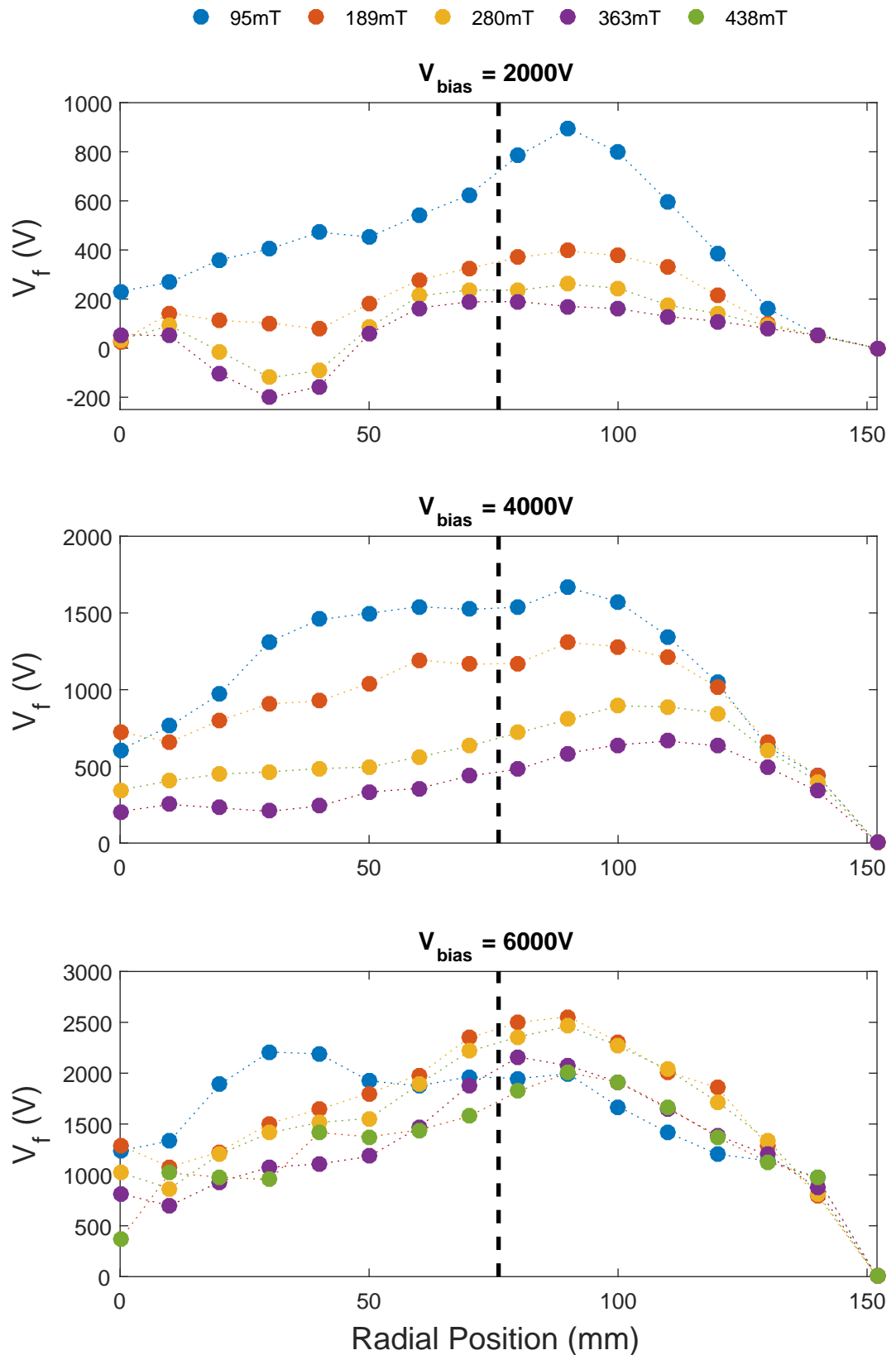


FIGURE 8.10: Radial floating potential profiles for varying grid bias and magnetic field strength.

## 8.5 Anisotropic Laplace Equation in Polywell Systems

In the previous section we verified, experimentally, that the formation of well-like structures in the electric potential is achievable simply through controlling the degree to which plasma may intercept high voltage and grounded surfaces. The expression of Dirichlet boundary conditions along magnetic field lines therefore provides an alternative explanation for observed potential well formation in previous Polywell experiments, especially in cases where field lines intercept both biased and grounded boundaries. In this section we apply the anisotropic Laplace equation, derived in Section 8.1, to two previously published Polywell devices; The University of Sydney’s WB6-Mini experiment, and EMC2’s High Energy Power Source (HEPS) machine. In both cases we find that the experimental results are adequately explained through a plasma conduction model, leading us to question the initial conclusions that the observed potential distributions were due to magnetic trapping of an electron rich plasma.

### 8.5.1 WB6-Mini

Polywell studies conducted by Carr [91] and Cornish [93] at the University of Sydney demonstrated successful potential well formation, consistent with Polywell theory. However both devices contained unshielded loss surfaces in the form of interconnects between the magnetic field coils, as seen in Figure 8.11. The field geometry within the Polywell is such that tubes of magnetic flux leave the device along the edges of the cube that is circumscribed by the coil faces and thus the magnetic shielding in both devices is severely compromised. In both experiments electron emitting filaments were placed in close proximity to the faces of one or more of the field coils and these low voltage elements present additional unshielded boundaries in the electrostatic system. The potential in the central plane of the Carr’s WB6-mini was modelled using Equation 8.5 on a  $201 \times 201$  square mesh. The device was operated in a cylindrical vacuum chamber with a radius of approximately 200 mm and consisted of 25 mm radius coils, which together formed a 75 mm cube. The magnetic field lines are given in Figure 8.12. The vacuum chamber wall is represented as a bold black circle and the rectangular protrusions denote the positions of the electron emitting filaments and their supporting structures. The filaments and chamber wall represent a  $\Phi = 0$  boundary, while the biased Polywell coils enforce  $\Phi \approx 100$  V. Carr used swept Langmuir probe measurements to determine the plasma potential as a function of position, with measurements conducted along a radial line oriented at 8 degrees to the coil axis, denoted as a red line in Figure 8.12.

As discussed briefly in Section 8.3, enforcing a large degree of anisotropy (large  $N$  and small  $B_0$  in Equation 8.12) results in an electric potential that tends to conform to the rectangular mesh used to compute the solution. This effect was dominated by the angular roll-off parameter ( $N$ ) and was further exacerbated by coarse grid resolutions. Due to the large size of the vacuum

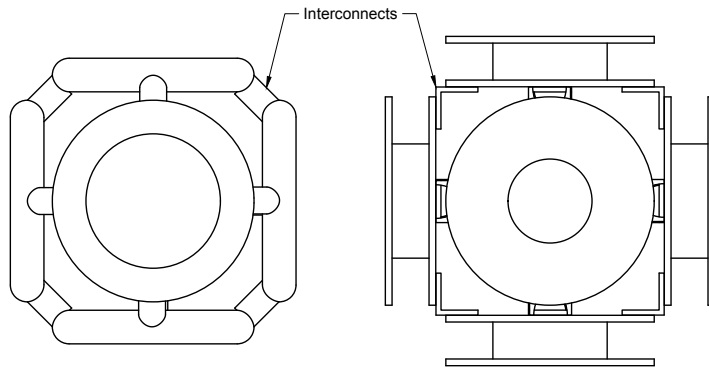


FIGURE 8.11: University of Sydney Polywells as constructed by Carr [91] (*Left*) and Cornish [93] (*Right*). Both devices contain unshielded interconnects between magnetic field coils that intercept lines of magnetic flux.

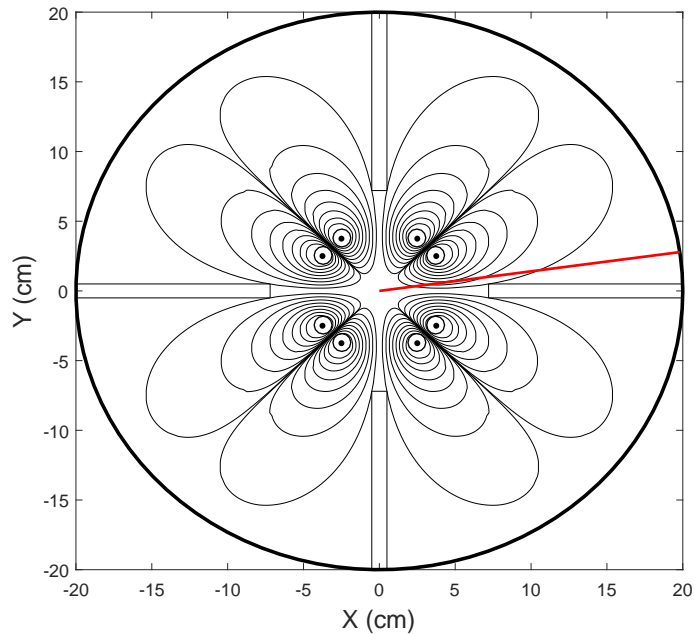


FIGURE 8.12: Magnetic field lines in the central plane of Carr's WB6-Mini. The black circle indicates the wall of the vacuum chamber while the position of electron emitting filaments and their supporting structures are shown as rectangular projections from the chamber wall. The chamber and filaments represent  $\Phi = 0$  boundaries while the coils of the Polywell are biased at  $\Phi \approx 100\text{ V}$ . Carr conducted biased Langmuir probe measurements along a radial line oriented at 8 degrees to the coil axis, as shown in red.

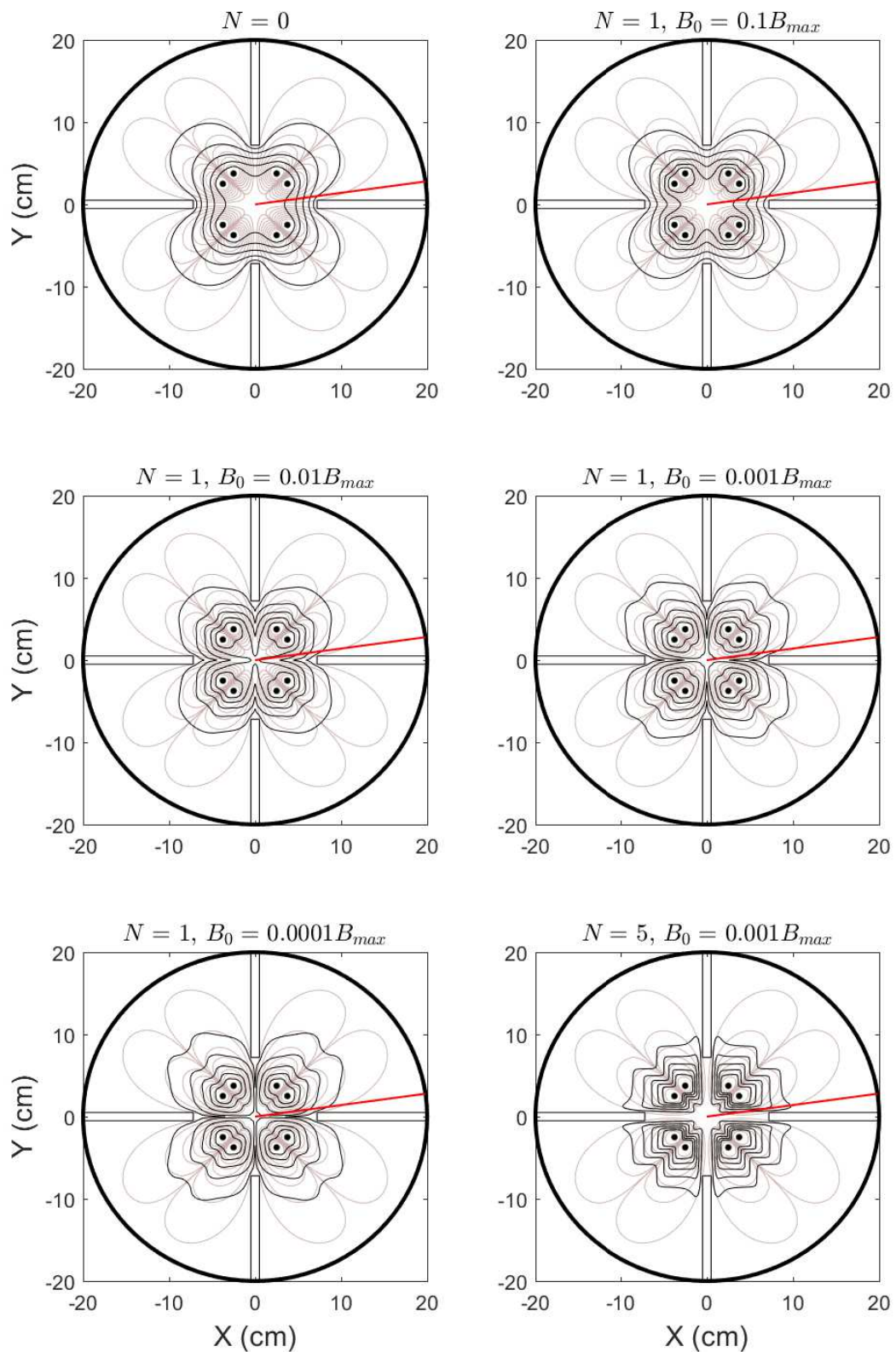


FIGURE 8.13: Electrostatic potential contours in Carr's WB6-Mini solved for varying values of  $N$  and  $B_0$ .

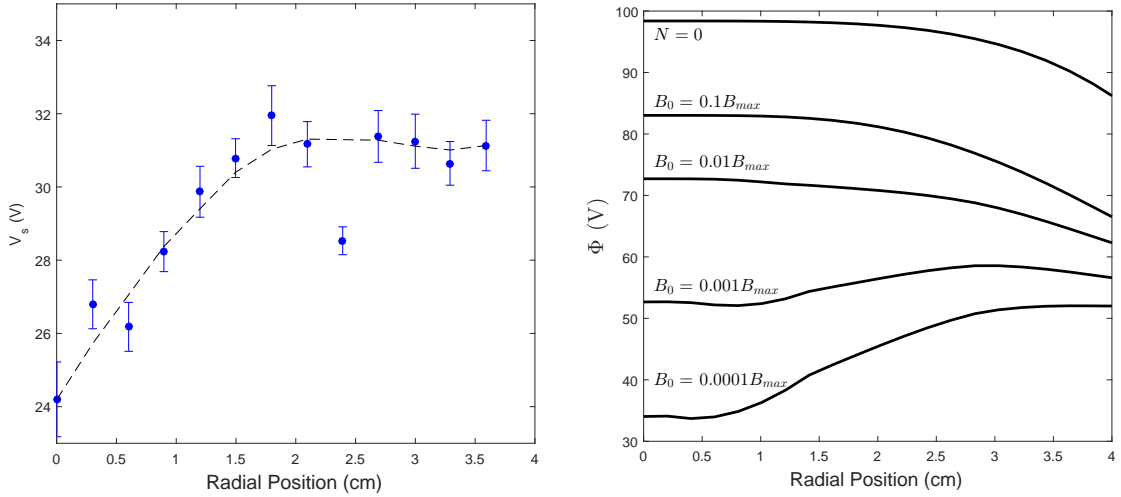


FIGURE 8.14: Plasma potential measurements obtained by Carr in WB6-Mini, reproduced from [91] (Left) and simulated potential for  $N = 1$  and varying values of  $B_0$  (Right). The  $N = 0$  case corresponds to the vacuum solution for the given electrostatic boundaries.

chamber relative to WB6-Mini, the number of grid points spanning the device was limited and so we have restricted our solutions to the  $N = 1$  case. This corresponds to a roll-off in conductivity given by the cosine of the angle between the conducting axis and the magnetic field line and is extremely conservative when compared to that in a magnetised plasma. Equation 8.5 was solved for varying values of  $B_0$  and the solutions are given in Figure 8.13. The top left panel gives the  $N = 0$  case, corresponding to the vacuum solution for the given boundaries. As the  $B_0$  parameter is reduced however, the potential along the axes of the device flattens, as indicated by a spreading of the contours, until the potential in the core is almost equal to that of the filaments. The structure of the magnetic cusps also becomes visible in the shape of the potential contours. The lower right panel gives an example of an extreme case in which the core is at a uniform zero volts, however in this case the geometry of the solution mesh is also apparent.

The potential well structure measured by Carr in WB6-Mini has been re-produced from [91] and is given in the left hand panel of Figure 8.14. Using a Polywell bias of 109 V and an electron injection current of  $\sim 3.5$  mA a potential difference of  $\sim 8$  V was obtained over a distance of 2cm. Our simulated potentials were interpolated along the 8 degree radial and plotted for comparison in the right hand panel of Figure 8.14. We note that as the anisotropy in the conductivity is increased, a potential well emerges that is similar to Carr's measurement. The simulated well has a magnitude of  $\sim 15$  V and also occurs over a distance of 2cm. It is proposed that the observation of the potential well was an artefact of the probe being translated *across* magnetic field lines. Had the probe been translated axially along a field line (as was done in MCVC-0) it is likely that no potential gradient would have been observed.

### 8.5.2 High Energy Power Source Experiment

The Polywell devices constructed at the University of Sydney have, by necessity, operated at very low power, with electron beam injection limited to units or tens of milliamperes. It is reasonable to suggest therefore that the studied devices did not operate in a power regime, with sufficient electron injection, where the virtual cathode effect could be realised. Although the observed potential wells in the USYD devices were likely an artefact of anisotropic plasma conductivity in a magnetic field, this result may not necessarily extend to machines operating at many kilovolts, with tens of amperes of electron current injection.

The “High Energy Power Source experiment” (HEPS), described in Section 1.5.1 represented a principle experiment in the development of the Polywell [83]. The device consisted of  $\sim 1.8\text{ m}$  diameter magnetic field coils arranged about a cubic vacuum chamber. Three 20 kV, 20 A electron guns were used to inject electrons into the core and the plasma potential was measured through the use of emissive capacitance probes. The HEPS magnetic coils were located outside of the vacuum chamber, and hence did not form electrostatic boundaries as with MCVC-0 or WB6-Mini. Instead the emissive cathodes inside the HEPS electron guns represent negatively biased boundaries within the machine. As with WB6-Mini, the HEPS electron guns were oriented such as to inject electrons along the line of a magnetic cusp. The DTI publication [83] does not specify whether the electron guns were positioned at the corners or faces of the Polywell cube, however based on a photograph of the HEPS machine in [85] we have assumed that injection occurred through the faces of the coils. In Section IV of [83], potential well formation was examined in the presence of a dense, radio frequency generated plasma. Three electron guns were used to produce a total injection current of 22 A at 9.2 kV. We assume that the electron beam is sufficiently conductive that the electric potential at the point where the beam enters the chamber is approximately equal to that applied to the emissive cathode. We therefore represent the incoming electron beams by assigning 2 cm intervals (the diameter of the beams) of the boundary wall a value of -9.2 kV. The magnetic field profile in HEPS is given in Figure 8.15, where the chamber walls are given as bold black lines and the electron beam entry locations are shown as red points. Potential profiles were measured along a radial line at 10 degrees to the coil axis, however no detail is given as to the relative position of this radial and the electron injection points. We therefore examine the radial profile in two directions, shown in Figure 8.15 as red and blue lines. The blue radial approaches a point of electron injection, while the red radial does not. The electric potential within HEPS was solved using Equation 8.5 on a  $251 \times 251$  square mesh, for  $N = 1$  and  $B_0 = 0.00001 \rightarrow 0.1$ . The contours of the resulting solutions are given in Figure 8.16. We note that for isotropic conductivity, the small sections of biased wall have negligible effect on the potential throughout the main volume of the device. As with the result in MCVC-0 and WB6-Mini, raising the degree of conductivity anisotropy results in the potential at the electron gun boundary extending radially inward along the cusp line into

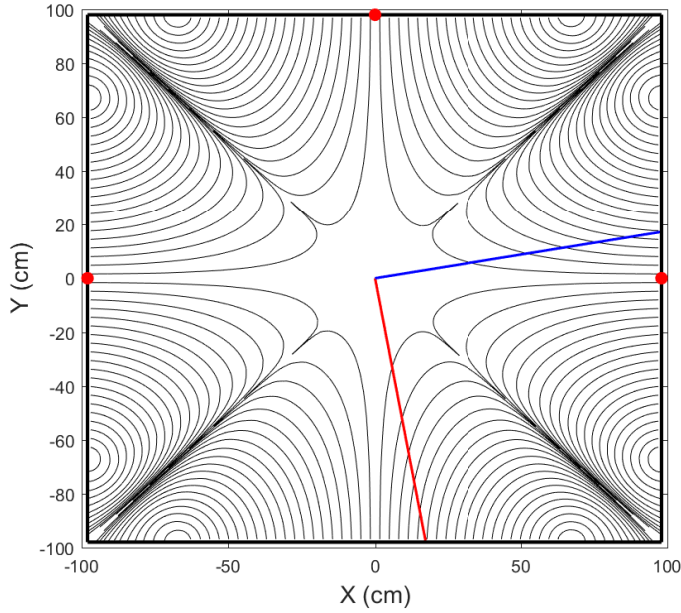


FIGURE 8.15: Magnetic field lines in DTI's HEPS machine. The bold black boarders denote the vacuum chamber walls and constitute a  $\Phi = 0$  boundary. Small, 2 cm intervals of the wall at coordinates  $(-100,0)$ ,  $(100,0)$  and  $(0,100)$  are assigned a potential of  $\Phi = -9.2$  kV, corresponding to the voltage applied to the emissive cathodes in the HEPS electron guns. These intervals are represented as gaps in the bold boundary. The red and blue lines are at 10 degrees to the coil axis and represent slices along which the electric potential was studied.

the core of the machine, as shown by the movement of the outer potential contour from the position of the electron gun. The dark region enclosed by this contour consists of a large number of closely spaced contours indicating large gradients in the potential. The left hand panel of Figure 8.17 was taken from [83] and shows the measured potential well in HEPS as a function of time. The potential well was initially found to reach -9 kV, approximately equal to the electron injection energy, before rapidly decaying to -4 kV. The right hand panel shows the simulated radial profiles where the red and blue lines correspond to the matching lines in Figure 8.15. We note that in the maximally anisotropic case the simulated potential is extremely close to the equilibrium profile as measured by DTI, both in shape and magnitude. This result provides a strong indication that the reported successful operation of the HEPS Polywell may have, in fact, been spurious.

## 8.6 Implications for Magnetic Virtual Cathode Machines

The primary operating principle of the Polywell and other MCVC style devices is the formation of an electrostatic potential well through the trapping of a *negatively charged plasma*. Using Equation 7.7 we find that for a 0.25 m radius sphere of plasma, residing inside a 1 m radius

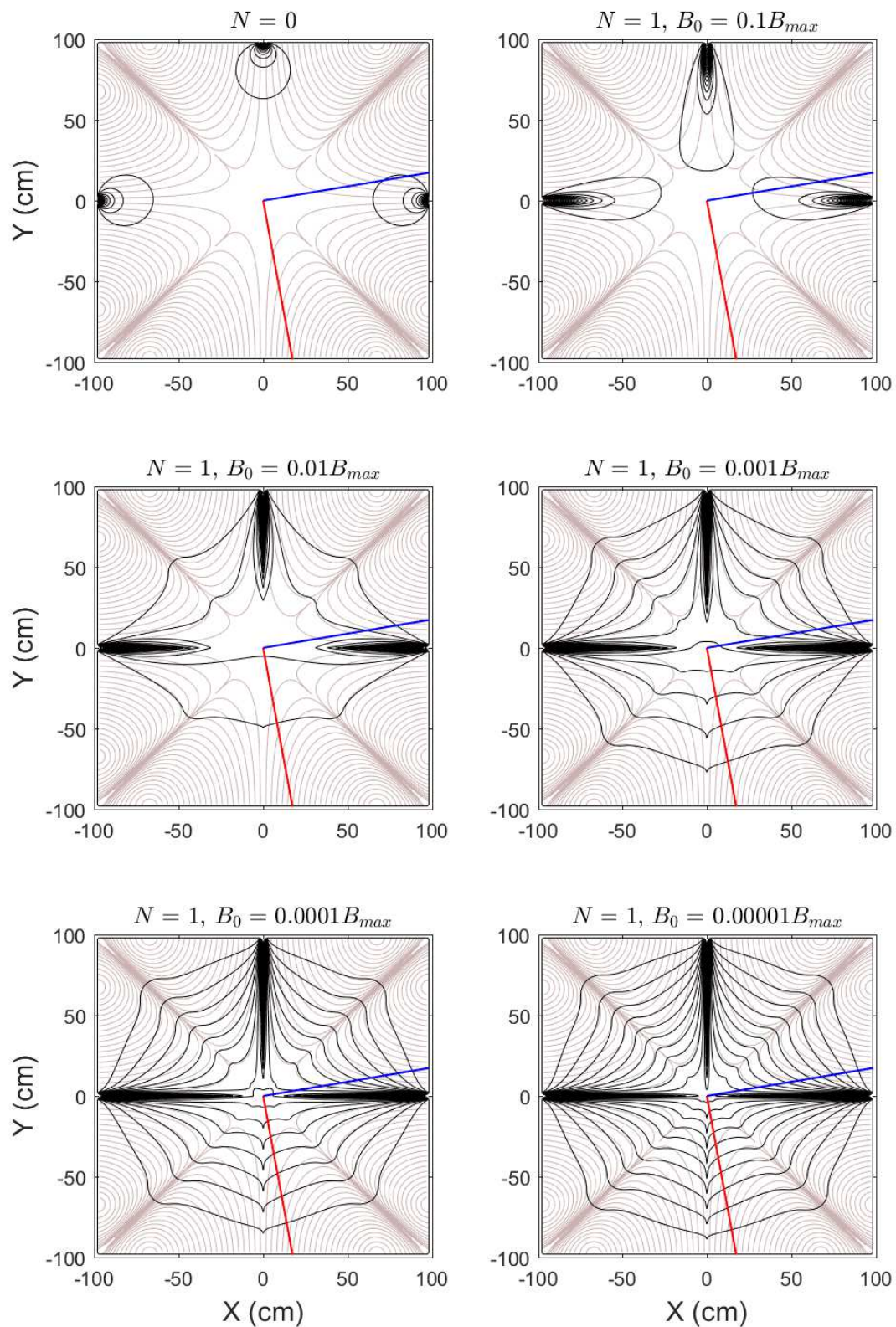


FIGURE 8.16: Electrostatic potential contours in DTI's HEPS machine solved for  $N = 1$  and varying values of  $B_0$ .

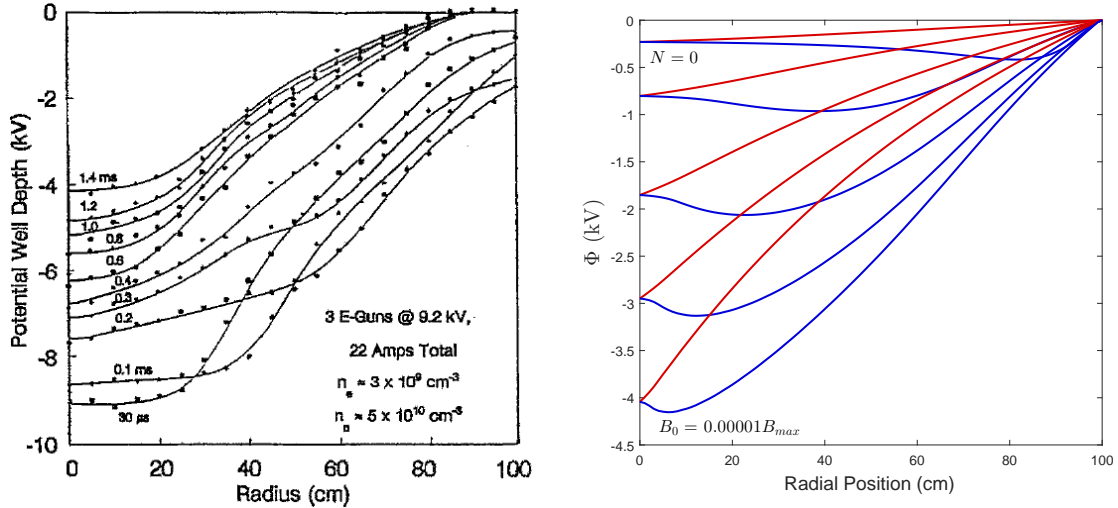


FIGURE 8.17: Potential well profiles as measured by DTI [83] in the HEPS experiment (*Left*) Simulated potential profiles as computed using Equation 8.5 for  $N = 1$  and varying values of  $B_0$  (*Right*). The observed well depth increases monotonically with decreasing  $B_0$ .

anode, the excess electron density required to produce a  $100\text{ kV}$  potential well is  $5.31 \times 10^{13} \text{ m}^{-3}$  which, assuming a typical thermonuclear plasma density of only  $1 \times 10^{20} \text{ m}^{-3}$ , corresponds to a departure from neutrality of  $\sim 5 \times 10^{-5}$  percent. Direct detection of such a small difference in electron and ion density is not possible using existing plasma diagnostics, leading previous authors to instead *infer* plasma non-neutrality from the measurement of potential wells. Through the application of a simple conductivity model we have computed theoretical electrostatic potentials in MCVC-0 and previously published Polywell devices. Because we have made use of *relative* rather than *absolute* values for the conductivity along and across field lines we are unable to compute the associated current densities consistent with our solution potentials. Such a computation requires detailed knowledge of the plasma properties so that the terms of  $\mathcal{S}$  may be determined, with the plasma currents subsequently given by Ohm's law,  $J_c = -\mathcal{S} \cdot \nabla \Phi$ . Further, we have assumed that the conducting medium throughout the solution volume is uniform, with inhomogeneity and anisotropy arising only due to the magnetic field. Additional factors, such as spacial variation in plasma density and temperature have been neglected. Finally, our solver exhibits numerical artefacts when imposing high degrees of field induced anisotropy, a property that is best addressed through implementation of adaptive mesh methods.

Nevertheless, the simulated electrostatic potentials were found to be in close agreement with their experimentally determined counterparts, with the observation of potential wells in the computed solutions having profound implications for all virtual cathode experiments: Namely that the observation of a potential well does not necessarily imply the existence of a non-neutral, electron rich plasma. We must therefore introduce nomenclature to denote the disparate forms a potential well may take: A *charge induced* well is one brought about through the confinement of negative space charge, while a *conduction induced* well arises in accordance with Ohm's

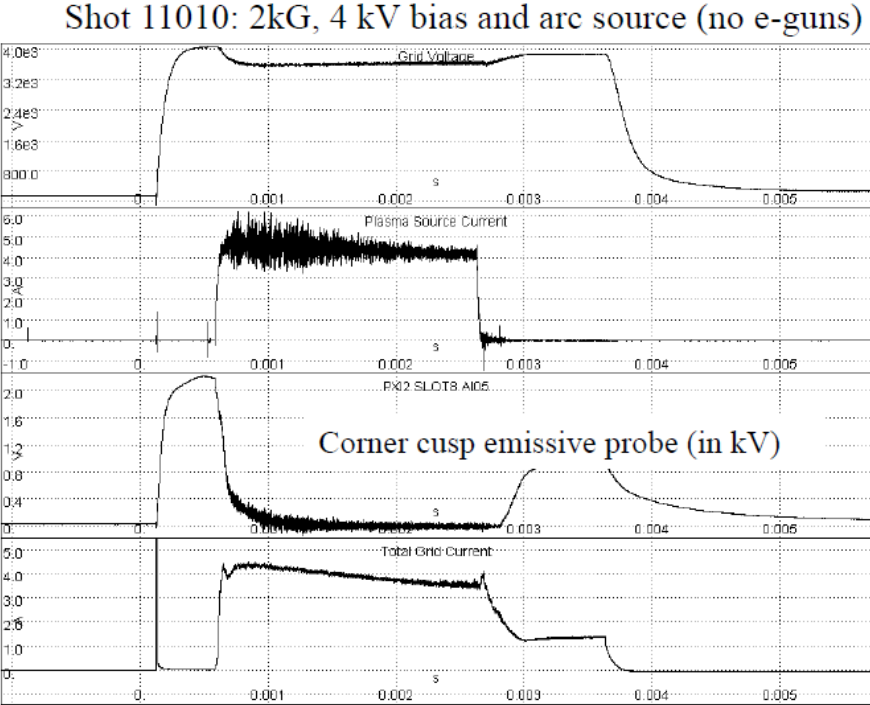


FIGURE 8.18: Plasma shot in WB8 polywell, presented by Park at the 16th US-Japan Workshop on Fusion Neutron Sources for Nuclear Assay and Alternate Applications [86]. The device was operated without external electron guns, drawing electron current instead from a dense background plasma.

law, due to the flow of a net current in an anisotropic medium. From the simulations in Section 8.5 it is likely that, in the case of WB6-Mini and HEPS, the observed wells were of the conduction variety. There is insufficient published data to properly assess the relative significance of charge or conduction potential well formation in EMC2’s WB1-WB7 devices, however we gain some insight into the operation of WB8 from the data in Figure 8.18, originally presented by EMC2 CEO Dr Jaeyoung Park at the 16th US-Japan Workshop on Fusion Neutron Sources for Nuclear Assay and Alternate Applications [86]. Figure 8.18 illustrates a shot of the WB8 machine in the absence of external electron injection, with electrons instead drawn from a dense background plasma through the application of a high voltage bias to the magnetic coils. The aim of the experiment was to determine whether coil biasing could achieve sufficient electron injection to establish a deep potential well. The third panel of Figure 8.18 gives the plasma potential as measured by an emissive probe positioned in the corner cusp of WB8. For the duration of the plasma shot the potential is uniformly zero, reminiscent of the results obtained in MCVC-0 (Figure 7.22). Park states that “*grid biasing does not look promising for potential well formation*” from which we infer that, as with MCVC-0, the entire core region was measured as being at, or near, 0 V, consistent with a conduction dominated system.

When WB8 is operated without additional electron injection, the negatively biased boundary

condition represented by the electron gun cathode is absent. The electrostatic system is therefore reduced to a simple two-electrode circuit in which the maximum and minimum potentials are defined by the biased coils and vacuum chamber respectively. As the Polywell field lines will always intercept the vacuum vessel at the point cusps, and due to the care taken to magnetically shield the WB8 coils, the resulting potential distributions are dominated exclusively by the grounded boundary. Although no published results were found describing potential well measurements in the presence of excess electron injection, it is deemed likely that any such wells resulted similarly from the expression of the cathode boundary condition rather than electron trapping.

The problem of plasma conductivity along magnetic field lines presents a critical obstacle to the formation of potential differentials in directions parallel to magnetic fields. The conductivity of a fully ionised, high temperature plasma ( $n_e = 1 \times 10^{20} \text{ m}^{-3}$ ,  $T_e = 10 \text{ keV}$ ), of the type required for fusion power generation, is estimated via Equations 8.9 and 8.11 to be

$$\sigma = \frac{n_e e^2}{m_e \nu_c} \approx 6500 \cdot \frac{T_e [\text{eV}]^{3/2}}{\ln \Lambda} = 6.5 \times 10^8 \Omega^{-1} \text{ m}^{-1} \quad (8.15)$$

which is more than an order of magnitude larger than that of copper [134]. As a confined region of negative space charge is expected to produce an approximately radial electric field, the magnetic field within a Polywell configuration contains 26 loss cusps (six faces, eight corners, twelve edges) along which the electric and magnetic field lines are parallel to one another. It is apparent from Equation 8.15, in conjunction with Ohm's law ( $\vec{J} = \sigma \vec{E}$ ), that for commonly quoted potential well depths of 100-200 kV the resulting loss currents would be prohibitively large. To demonstrate this we evaluate the equivalent series resistance of a single loss cusp by modelling it as a 1 metre long, thin resistive wire. A common estimate for the loss diameter of a point cusp is approximately two gyro-radii [14, 15] which, for an electron with a transverse velocity of  $v_\perp = 1 \times 10^7 \text{ m s}^{-1} \approx 300 \text{ eV}$  in a 10 T field, corresponds to  $2r_g \approx 12 \mu\text{m}$ . Taking the conductivity value from Equation 8.15 and using the standard formula for the value of a resistive element gives

$$R_{cusp} \approx \frac{1}{\pi r_g^2 \sigma} = 13.6 \Omega \text{ m}^{-1} \quad (8.16)$$

corresponding to a cusp loss current of  $\sim 7300 \text{ A}$  at 100 kV. As the lost electrons must be continually replenished via beam injection, and given that a typical Polywell has 26 such loss paths, we estimate that the electron gun current required to maintain the well depth to be somewhere in the vicinity of 200 kA. Further, the “two gyro-radii” approximation determined by Grad and Berkowitz [14, 15] was derived in the absence of a parallel electric field which will tend to drive electrons into the cusp and further enhance losses. We therefore regard the estimates above as very conservative, rendering the required electrical power implausibly large (20 GW).

It remains to be seen whether potential wells of the conduction variety are sufficient to achieve

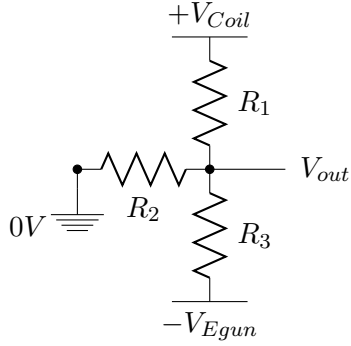


FIGURE 8.19: Resistive voltage divider in three electrode MCVC system.

the desired ion confinement. In an MCVC system that includes both biased coils and negative emissive cathodes, there exists three electrostatic boundaries, simplified as a resistor tree in Figure 8.19. The electrons injected along a magnetic cusp ( $R_3$ ) are either lost to the chamber wall along another cusp ( $R_2$ ) or else collected on the biased coils ( $R_1$ ). If the coils of the device are magnetically shielded, as with WB8 or MCVC-0, then the value of  $R_1$  goes to infinity and the primary conducting pathway for the injected electron current consists of  $R_2$  and  $R_3$ , both of which are parallel to the magnetic field. This may account for anomalously high electron loss from the core of Polywell machines as electron current is simply conducted along field lines from the source to the chamber wall. In WB8, only 8 of the 26 cusps terminate at an electron gun cathode, while the remaining 18 intersect the vacuum vessel. These conduction losses could possibly be reduced by removing the grounded boundary, ensuring instead that all magnetic cusps intersect surfaces of equal electric potential to the electron gun cathodes. In this way cusp losses no longer constitute a net current and it is possible to impose a negative bias on the entire plasma volume. A similar scheme has previously been described by Grad [14]. Such a configuration is not dissimilar to that already observed in MCVC-0 and WB8, however in those cases the potential of the plasma volume was determined by the grounded chamber wall rather than a set of biased cathodes. By implementing plasma biasing it is possible to establish much larger electric fields between the plasma and the shielded magnetic coils as all loss current is now conducted in a direction transverse to the magnetic field. While a conduction based potential well provides desirable ion confinement properties, the spatially uniform potential within the biased plasma eliminates any possibility of electrostatic ion heating. Conventional radio frequency and neutral beam methods would need to be applied in order to achieve fusion relevant plasma temperatures.

### 8.6.1 Summary

A plasma conductivity model has been described and used to address the absence of electrostatic potential well formation in MCVC-0. The anisotropic and inhomogeneous nature of

electrical conductivity in a magnetised plasma discharge was found to sufficiently account for the observed behaviour, with simulated electrostatic potentials closely resembling their experimentally determined counterparts. It was hypothesised therefore, that the formation of potential well structures in MCVC devices is strongly dependent on the relationship between the magnetic field and biased electrostatic boundaries. An experimental verification of the hypothesis was carried out by deliberately sabotaging the magnetic shielding of the MCVC-0 coils to allow field lines to intercept high voltage surfaces. Re-establishing electrical contact between the plasma and the high voltage boundary condition resulted in potential well formation, with well depths of up to  $\sim 1500$  V obtained while operating at 6 kV. The plasma conductivity model was subsequently applied to two previously published Polywell devices, The University of Sydney's WB6-Mini and DTI's HEPS machine, and in both cases the simulated electric potentials closely matched the published results.

A principle finding of the presented work, with regards to future MCVC / Polywell experiments, is that the measurement of potential well like structures *does not necessarily imply* the confinement of a net negative space charge. Anisotropic plasma conductivity provides an alternative physical explanation for the observed behaviour of experimental Polywell machines, referred to here as *conduction induced* well formation, as distinct from the expected *charge induced* well. From the consideration of plasma conductivity however, it is deemed implausible that a conduction based potential well of sufficient depth could be established to heat a dense plasma to fusion temperatures without expending an unacceptable quantity of electrical power. Care must therefore be taken in all future MCVC work to rigorously distinguish between conduction and charge induced potential wells, such that the successful operation of new devices is not overstated. Particular attention must be paid to the identifying features of charge based potential wells, namely that the well is spherical symmetric, and that potential gradients are observed in directions *parallel* to the magnetic cusps.

## Chapter 9

# Conclusions and Future Work

An experimental study was carried out on inertial electrostatic confinement devices in both gridded electrode and virtual cathode forms. A deuterium fuelled, gridded IEC machine was used to study the phenomenon of “surface fusion”, wherein fusion reactions occur between energetic ions and neutral gas molecules adsorbed on the cathode surface. The system was subjected to step function adjustments to the background gas pressure in order to promote adsorption or desorption of deuterium molecules from the cathode surface. The measured fusion rate was found to display significant hysteresis following changes in pressure, consistent with a system in which the fusion events are dominated by interactions between ions and surface bound targets. Equilibrium fusion rates as a function of pressure were found to take the form of a “Langmuir Isotherm”, which describes the fraction of surface binding sites that are occupied for a given gas pressure, providing further evidence of a surface fusion dominated system. It is estimated that surface bound interactions may account for up to 80% of the observed fusion rate when operating IEC grids at low power.

The dependency of fusion rate on cathode material was also examined through the use of a selection of planar cathodes made from stainless steel, copper, molybdenum, silver, titanium and graphite. Graphite was found to perform exceptionally well when compared to the transition metal targets, producing a fusion rate almost an order of magnitude larger than that of silver, the highest performing metal. A factor of 60 was observed between graphite and the poorest performing metal, stainless steel. The principle factor determining cathode performance was found to be the susceptibility of surface bound deuterium to thermally induced desorption. Graphite, well known for its hydrogen retention properties, exhibits enhanced target density at elevated temperatures and thus out-performs equivalent metal cathodes. This effect was demonstrated through the operation of a set of otherwise identical gridded IEC cathodes constructed from stainless steel and graphite. The fusion output as a function of power for the stainless steel cathode was found to plateau for cathode temperatures above  $\sim 350\text{ K}$ , whereas the graphite

grid exhibited a linear trend up to  $\sim 450$  K. In this way, the operation temperature, or equivalently the power per unit area deposited into the cathode by the discharge, is an important factor in the development of high performance, high efficiency IEC machines. The work indicates that great improvements in efficiency are possible in existing, high power, IEC machines through strategies aimed at preventing over-heating of gridded cathodes. Incandescent operation, where cathode temperatures exceed 1000 K, should be avoided, with grid temperatures instead maintained below the characteristic deuterium desorption temperature of the chosen cathode material. Through the use of cathode materials with large deuterium binding energies, as well as the implementation of active cathode cooling, it is suggested that increases in fusion rate of up to a factor of five are possible.

The design and construction of MCVC-0, a successor to earlier Polywell style devices at The University of Sydney, was described. The machine consisted of a pair of magnetic field coils arranged in a biconic cusp configuration and aimed to produce a virtual cathode through the magnetic confinement of injected electrons. Biased and floating Langmuir probe measurements were used to conduct preliminary plasma measurements within the new machine, with particular attention paid to electron trapping and virtual cathode formation. Contrary to expectation however, no virtual cathode was observed, with uniform electric potentials measured from the core to the periphery of the device. The unexpected behaviour of MCVC-0 was addressed through the development of a conductivity based model, in which the Laplace equation was solved in the presence of a non-isotropic volume conductor. In this way the perturbation to the vacuum electric potential due to the presence of a magnetised discharge plasma could be studied. It was found that non-isotropic plasma conductivity along and across magnetic field lines suitably accounted for the observed electric distributions within MCVC-0, with the simulated potentials closely matching the experimentally determined values. The potential profiles were found to flatten along the direction of the magnetic field and steepen in the direction perpendicular to the field. Where a field line directly intersected a biased or grounded boundary, the potential along this field line was dominated by the prescribed voltage on the boundary. It was experimentally demonstrated that when field lines are allowed to intersect surfaces at both high voltage and ground, potential well like structures may be formed even in the absence of a net negative space charge. In light of this, the conduction model was similarly applied to two previously published Polywell experiments and the simulated potentials found to be in excellent agreement with the literature results. The observation of potential wells in *neutral* systems, both experimental and simulated, raises questions with regards to the validity of the virtual cathode concept as a potential source of fusion energy. Care must be taken in future work to ensure that measured potential wells are indeed the result of confined negative space charge and not merely the expression of Dirichlet boundaries along magnetic field lines.

While the electric potentials obtained from the non-isotropic conduction model display good qualitative agreement with the experimental measurements, limitations in the existing solver

make an explorative study of possible electromagnetic configurations impossible. Firstly, the parallel and transverse electrical conductivities were computed using a phenomenological model only. The work must therefore be extended to include conductivities determined from real plasma parameters, including spacial variation in the particle density and temperature. Further, the use of a square mesh discretisation of the solution domain proved unsuitable for the representation of complex geometries and led to numerical artefacts when imposing a high degree of plasma anisotropy. It is proposed to build an adaptive mesh solver in which the coordinate mesh is defined along magnetic field lines. In this way the definition of parallel and transverse conductivities becomes trivial. It is hoped that through such a scheme it will become possible to examine how the manipulation of boundary conditions may be used to enhance plasma confinement in hybrid electro-magnetic systems.

Continued development of MCVC-0 is required in order to properly rule out the possibility of charge induced potential well formation. Owing to the poor confinement properties of the biconic cusp when compared with the Polywell configuration, it is possible that the observed behaviour is an artefact of insufficient electron injection current. High rates of electron loss through the large equatorial line cusp prevents the trapping of an excess electron population and hence the formation of a virtual cathode. Future studies in MCVC-0 will aim to increase the available electron beam current from its present limit of 150 mA to 1-10 Amperes, similar to comparable Polywell machines. Proposed upgrades to the device also include raising the applied coil bias from 6 kV to 25 kV, as well as the implementation of 2.45 GHz microwave heating as a means of improving the ionisation fraction. It is hoped that the above upgrades will result in a machine that is capable of generating measurable deuterium-deuterium fusion.

# Bibliography

- [1] Department of Economic and Social Affairs. The world population situation in 2014. *United Nations*, 2014.
- [2] Alan Pasternak. *Global Energy Futures and Human Development: A Framework for Analysis*. Lawrence Livermore National Laboratory, October 2000.
- [3] Amie Gaye. *Access to Energy and Human Development*. United Nations Development Programme, 2008.
- [4] Cesar Pasten and Juan Carlos Santamarina. Energy and quality of life. *Energy Policy*, 49:468 – 476, 2012. ISSN 0301-4215. doi: <https://doi.org/10.1016/j.enpol.2012.06.051>. URL <http://www.sciencedirect.com/science/article/pii/S0301421512005617>.
- [5] Chronic Poverty Advisory Network. The chronic poverty report: The road to zero extreme poverty. 2015.
- [6] International Energy Agency. *World Energy Outlook 2018*. 2018. doi: <https://doi.org/https://doi.org/10.1787/weo-2018-en>. URL <https://www.oecd-ilibrary.org/content/publication/weo-2018-en>.
- [7] International Atomic Energy Agency. *Fusion Physics*. 2012. ISBN ISBN:978-92-0-130410-0.
- [8] Jeffrey P. Freidberg. *Plasma physics and fusion energy*. Cambridge University Press, Cambridge, 2007. ISBN 9780521851077;0521851076;.
- [9] J D Huba. *NRL PLASMA FORMULARY Supported by The Office of Naval Research*. Naval Research Laboratory, Washington, DC, 2013. ISBN 9781234126070. URL <http://wwwppd.nrl.navy.mil/nrlformulary/>.
- [10] H.-S Bosch and G.M Hale. Improved formulas for fusion cross-sections and thermal reactivities. *Nuclear Fusion*, 32(4):611–631, apr 1992. doi: 10.1088/0029-5515/32/4/i07. URL <https://doi.org/10.1088%2F0029-5515%2F32%2F4%2Fi07>.

- [11] H.-S Bosch and G.M Hale. Improved formulas for fusion cross-sections and thermal reactivities. *Nuclear Fusion*, 33(12):1919–1919, dec 1993. doi: 10.1088/0029-5515/33/12/513. URL <https://doi.org/10.1088%2F0029-5515%2F33%2F12%2F513>.
- [12] R.F. Post. The magnetic mirror approach to fusion. *Nuclear Fusion*, 27(10):1579–1739, oct 1987. doi: 10.1088/0029-5515/27/10/001. URL <https://doi.org/10.1088%2F0029-5515%2F27%2F10%2F001>.
- [13] Thomas Dolan. Magnetic electrostatic plasma confinement. *Plasma Physics and Controlled Fusion*, 36:1539, 01 1999. doi: 10.1088/0741-3335/36/10/001.
- [14] H Grad. *Theory of Cusped Geometries I: General Theory*. New York: Courant Institute of Mathematical Sciences, New York University, 1957.
- [15] J Berkowitz. *Theory of Cusped Geometries II: Particle Losses*. New York: Courant Institute of Mathematical Sciences, New York University, 1959.
- [16] H Grad. *Thermonuclear Plasma Containment in Open-Ended Systems*. New York: Courant Institute of Mathematical Sciences, New York University, 1960.
- [17] H Grad. *Containment in cusped plasma systems*. New York: Courant Institute of Mathematical Sciences, New York University, 1961.
- [18] M Keilhacker, A Gibson, C Gormezano, and P.H Rebut. The scientific success of JET. *Nuclear Fusion*, 41(12):1925–1966, dec 2001. doi: 10.1088/0029-5515/41/12/217. URL <https://doi.org/10.1088%2F0029-5515%2F41%2F12%2F217>.
- [19] Mitsuru Kikuchi. The large tokamak jt-60: a history of the fight to achieve the japanese fusion research mission. *The European Physical Journal H*, 43(4):551–577, Dec 2018.
- [20] ITR-18-003. ITER research plan within the staged approach. *ITER Organization*, 2018.
- [21] F.F. Chen. *Introduction to Plasma Physics*. Springer US, 2012. ISBN 9781475704594. URL <https://books.google.com.au/books?id=Z1rtBwAAQBAJ>.
- [22] J.A. Bittencourt. *Fundamentals of Plasma Physics*. Elsevier Science, 2013. ISBN 9781483293196. URL <https://books.google.com.au/books?id=4vBGBQAAQBAJ>.
- [23] International Atomic Energy Agency. *Safe Handling of Tritium*. 1991.
- [24] US Department of Energy. *Tritium handling and safe strorage*. 2015.
- [25] T Tanabe, N Bekris, P Coad, C.H Skinner, M Glugla, and N Miya. Tritium retention of plasma facing components in tokamaks. *Journal of Nuclear Materials*, 313-316:478 – 490, 2003. ISSN 0022-3115. doi: [https://doi.org/10.1016/S0022-3115\(02\)01377-6](https://doi.org/10.1016/S0022-3115(02)01377-6). URL <http://www.sciencedirect.com/science/article/pii/S0022311502013776>. Plasma-Surface Interactions in Controlled Fusion Devices 15.

- [26] Yi-Kang Lee. Analysis of the tritium breeding ratio benchmark experiments using the monte carlo code tripoli-4. *Fusion Engineering and Design*, 85(7):1125 – 1128, 2010. ISSN 0920-3796. doi: <https://doi.org/10.1016/j.fusengdes.2010.02.032>. URL <http://www.sciencedirect.com/science/article/pii/S092037961000058X>. Proceedings of the Ninth International Symposium on Fusion Nuclear Technology.
- [27] Y. Wu. Design analysis of the china dual-functional lithium lead (dfll) test blanket module in iter. *Fusion Engineering and Design*, 82(15):1893 – 1903, 2007. ISSN 0920-3796. doi: <https://doi.org/10.1016/j.fusengdes.2007.08.012>. URL <http://www.sciencedirect.com/science/article/pii/S092037960700419X>. Proceedings of the 24th Symposium on Fusion Technology.
- [28] M.Z Youssef and M.A Abdou. Heat deposition, damage, and tritium breeding characteristics in thick liquid wall blanket concepts. *Fusion Engineering and Design*, 49-50:719 – 725, 2000. ISSN 0920-3796. doi: [https://doi.org/10.1016/S0920-3796\(00\)00179-4](https://doi.org/10.1016/S0920-3796(00)00179-4). URL <http://www.sciencedirect.com/science/article/pii/S0920379600001794>.
- [29] R.G. Jr. Alsmiller, R.T. Santoro, J Barish, and Tony Gabriel. Comparison of the cross-section sensitivity of the tritium breeding ratio in various fusion-reactor blankets. *Nucl. Sci. Eng.*, v. 57, no. 2, pp. 122-128, 57, 06 1975. doi: 10.13182/NSE75-A27340.
- [30] Behrooz Soltani and Morteza Habibi. Tritium breeding ratio calculation for iter tokamak using developed helium cooled pebble bed blanket (hcpb). *Journal of Fusion Energy*, 34 (3):604–607, Jun 2015.
- [31] Yoshiyuki Asaoka, Kunihiko Okano, Tomoaki Yoshida, and Ken Tomabechi. Requirements of tritium breeding ratio for early fusion power reactors. *Fusion Technology*, 30, 12 1996.
- [32] S. Zheng, D.B. King, L. Garzotti, E. Surrey, and T.N. Todd. Fusion reactor start-up without an external tritium source. *Fusion Engineering and Design*, 103(C):13–20, 2016. doi: 10.1016/j.fusengdes.2015.11.034.
- [33] S. Konishi, R. Kasada, and F. Okino. Myth of initial loading tritium for demo—modelling of fuel system and operation scenario. *Fusion Engineering and Design*, 121:111 – 116, 2017. ISSN 0920-3796. doi: <https://doi.org/10.1016/j.fusengdes.2017.05.138>. URL <http://www.sciencedirect.com/science/article/pii/S092037961730697X>.
- [34] A.I. Miller. Heavy water: A manufacturers’ guide for the hydrogen century. *Canadian Nuclear Society Bulletin*, 22(1), February 2001.
- [35] G. Gorelik and A.W. Bouis. *The World of Andrei Sakharov: A Russian Physicists Path to Freedom*. Oxford University Press, 2005. ISBN 9780190288778. URL <https://books.google.com.au/books?id=7tsJCAAQBAJ>.

- [36] Lavrent'ev's proposal forwarded to the CPSU Central Committee on July 29, 1950. *Physics-Uspekhi*, 44:862, 2001.
- [37] O. A. Lavrent'ev. *Ukr. Fiz. Zh.*, 8:440, 1963.
- [38] O A. Lavrent'ev. *Annals of the New York Academy of Sciences*, pages 152–178, 1975.
- [39] P.T. Farnsworth. Method and apparatus for producing nuclear-fusion reactions. June 4 1968. URL <https://www.google.com.au/patents/US3386883>. US Patent 3,386,883.
- [40] Robert L. Hirsch. Inertial electrostatic confinement of ionized fusion gases. *Journal of Applied Physics*, 38(11), 1967.
- [41] R.L. Hirsch. Apparatus for generating fusion reactions. 1970. URL <https://patents.google.com/patent/US3530036>. US Patent 3530036A.
- [42] R.L. Hirsch and Meeks G.A. Apparatus for generating fusion reactions. 1970. URL <https://patents.google.com/patent/US3530497>. US Patent 3530497A.
- [43] S. Krupakar Murali, G. A. Emmert, J. F. Santarius, and G. L. Kulcinski. *Physics of Plasmas*, 17(10):102701, 2010. doi: 10.1063/1.3484224.
- [44] D. C. Donovan, D. R. Boris, G. L. Kulcinski, J. F. Santarius, and G. R. Piefer. 84(3): 033501, 2013. doi: 10.1063/1.4793771.
- [45] E.C.Alderson. Experimental and theoretical characterisation of deuterium ion distributions in a gridded inertial electrostatic confinement devices. PhD Thesis - University of Wisconsin, 2012.
- [46] D.R.Boris. Novel diagnostic approaches to characterising the performance of the wisconsin inertial electrostatic confinement plasma. PhD Thesis - University of Wisconsin, 2009.
- [47] B.B.Cipiti. The fusion of advanced fuels to produce medical isotopes using inertial electrostatic confinement. PhD Thesis - University of Wisconsin, 2004.
- [48] G. H. Miley, J. Javedani, Y. Yamamoto, R. Nebel, J. Nadler, Y. Gu, A. Satsangi, and P. Heck. Inertial electrostatic confinement neutron/proton source. *AIP Conference Proceedings*, 299(1):675–689, 1994. doi: 10.1063/1.2949222. URL <https://aip.scitation.org/doi/abs/10.1063/1.2949222>.
- [49] G. H. Miley, J. Javedani, Y. Yamamoto, R. , J. Nadler, Y. Gu, A. Satsangi, and P. Heck. *AIP Conference Proceedings*, 299(1):675–689, 1994.
- [50] T. Takamatsu, K. Masuda, T. Kyunai, H. Toku, and K. Yoshikawa. *Nuclear Fusion*, 46 (1):142, 2006. URL <http://stacks.iop.org/0029-5515/46/i=1/a=016>.

- [51] K. Nobe, H. Imaji, K. Nanjo, W. Ngamdee, M. Watanabe, and E. Hotta. *14th US-Japan workshop on IECF*, 2012.
- [52] K. Noborio, Y. Yamamoto, and S. Konishi. *Fusion Science and Technology*, 52(4):1105–1109, 2007. doi: 10.13182/FST07-A1645.
- [53] K. Noborio, S. Konishi, T. Maegawa, and Y. Yamamoto. Numerical calculation of reactions on electrode surfaces and in a volume of a discharge type fusion neutron source. In *2011 IEEE/NPSS 24th Symposium on Fusion Engineering*, pages 1–5, June 2011. doi: 10.1109/SOFE.2011.6052315.
- [54] Kai Masuda, Takeshi Fujimoto, Tomoya Nakagawa, Heishun Zen, Taiju Kajiwara, Kazunobu Nagasaki, and Kiyoji Yoshikawa. *Fusion Science and Technology*, 56(1):528–532, 2009. doi: 10.13182/FST09-A8957. URL <https://doi.org/10.13182/FST09-A8957>.
- [55] J Khachan and S Collis. Measurements of ion energy distributions by doppler shift spectroscopy in an inertial-electrostatic confinement device. *Physics of Plasmas (1994-present)*, 8(4):1299–1304, 2001.
- [56] J. Kipritidis, J. Khachan, M. Fitzgerald, and O. Shrier. Absolute densities of energetic hydrogen ion species in an abnormal hollow cathode discharge. *Phys. Rev. E*, 77:066405, Jun 2008. doi: 10.1103/PhysRevE.77.066405. URL <http://link.aps.org/doi/10.1103/PhysRevE.77.066405>.
- [57] J Kipritidis and J Khachan. Application of doppler spectroscopy in h 2 to the prediction of experimental d (d, n) 3 he reaction rates in an inertial electrostatic confinement device. *Physical Review E*, 79(2):026403, 2009.
- [58] Lachlan Blackhall and Joe Khachan. A simple electric thruster based on ion charge exchange. *Journal of Physics D: Applied Physics*, 40(8):2491, 2007.
- [59] Jan-Philipp Wulfkühler and Martin Tajmar. AIAA-2016-4777. *52nd AIAA/SAE/ASEE Joint Propulsion Conference*, Jul 2016. doi: 10.2514/6.2016-4777. URL <https://doi.org/10.2514/6.2016-4777>.
- [60] Hermans E.C.G. The design and optimization of an inertial electrostatic confinement fusion device. Masters Thesis - Eindhoven University of Technology.
- [61] Mahdi Yousefi, Vahid Damideh, and Hamid Ghomi. Low-energy electron beam extraction from spherical discharge. *IEEE Transactions on Plasma Science*, 39(11):2554, 2011.
- [62] V. Damideh, A. Sadighzadeh, A. Koohi, A. Aslezaeem, A. Heidarnia, N. Abdollahi, F. Abbasi Davani, and R. Damideh. Experimental study of the iranian inertial electrostatic confinement fusion device as a continuous neutron generator. *Journal of Fusion*

- Energy*, 31(2):109–111, 2012. ISSN 1572-9591. doi: 10.1007/s10894-011-9438-8. URL <http://dx.doi.org/10.1007/s10894-011-9438-8>.
- [63] E. Haji Ebrahimi, R. Amrollahi, A. Sadighzadeh, M. Torabi, M. Sedaghat, R. Sabri, B. Pourshahab, and V. Damideh. The influence of cathode voltage and discharge current on neutron production rate of inertial electrostatic confinement fusion (ir-iecf). *Journal of Fusion Energy*, 32(1):62–65, 2013. ISSN 1572-9591. doi: 10.1007/s10894-012-9524-6. URL <http://dx.doi.org/10.1007/s10894-012-9524-6>.
- [64] AS Böyükdemir, Y Akgün, and A Alaçakır. Preliminary results of experimental studies from low pressure inertial electrostatic confinement device. *Journal of Fusion Energy*, 32(5):561–565, 2013.
- [65] Robert L. Hirsch. Experimental studies of a deep, negative, electrostatic potential well in spherical geometry. *Physics of Fluids*, 11(11), 1968.
- [66] John Hedditch, Richard Bowden-Reid, and Joe Khachan. Fusion energy in an inertial electrostatic confinement device using a magnetically shielded grid. *Physics of Plasmas*, 22(10):102705, 2015. doi: <http://dx.doi.org/10.1063/1.4933213>. URL <http://scitation.aip.org/content/aip/journal/pop/22/10/10.1063/1.4933213>.
- [67] Park J Murali K, Nebel R. Carbon nanotubes in iec fusion reactors. In *In: ANS 2006 annual meeting*, June 2006.
- [68] M.L. Sztejnberg Gonçalves-Carralves and M.E. Miller. Neutron flux assessment of a neutron irradiation facility based on inertial electrostatic confinement fusion. *Applied Radiation and Isotopes*, 106:95 – 100, 2015. ISSN 0969-8043. doi: <https://doi.org/10.1016/j.apradiso.2015.06.017>. URL <http://www.sciencedirect.com/science/article/pii/S0969804315300609>. The 16th International Congress on Neutron Capture Therapy (ICNCT-16). Representative person of the Organizing Committee: Dr Hanna Koivunoro (Secretary general of the ICNCT-16).
- [69] A.L. Wehmeyer. The detection of explosives using an inertial electrostatic confinement D-D fusion device. Masters Thesis - University of Wisconsin, 2005.
- [70] Fusion Energy Sciences Advisory Committee (FESAC). Non-electric application of fusion of the electrostatic confinement fusion concept. 2003.
- [71] William C. Elmore, James L. Tuck, and Kenneth M. Watson. On the inertial electrostatic confinement of a plasma. *Physics of Fluids*, 2(3), 1959.
- [72] P.T. Farnsworth. Electric discharge device for producing interactions between nuclei. June 28 1966. URL <http://www.google.com/patents/US3258402>. US Patent 3,258,402.

- [73] D. A. Swanson, B. E. Cherrington, and J. T. Verdeyen. Theory of the negative electrostatic potential well in spherical geometry. *The Physics of Fluids*, 17(6):1269–1274, 1974. doi: 10.1063/1.1694877. URL <https://aip.scitation.org/doi/abs/10.1063/1.1694877>.
- [74] J. Park, R. A. Nebel, S. Stange, and S. Krupakar Murali. Periodically oscillating plasma sphere. *Physics of Plasmas*, 12(5):056315, 2005. doi: 10.1063/1.1888822. URL <https://doi.org/10.1063/1.1888822>.
- [75] J. Park, R. A. Nebel, S. Stange, and S. Krupakar Murali. Experimental observation of a periodically oscillating plasma sphere in a gridded inertial electrostatic confinement device. *Phys. Rev. Lett.*, 95:015003, Jun 2005. doi: 10.1103/PhysRevLett.95.015003. URL <https://link.aps.org/doi/10.1103/PhysRevLett.95.015003>.
- [76] Colin Tuft and Joe Khachan. Spherical plasma oscillations in a reversed-polarity inertial-electrostatic confinement device. *Physics of Plasmas (1994-present)*, 17(11):112117, 2010.
- [77] R Bandara and J Khachan. Spherical ion oscillations in a positive polarity gridded inertial-electrostatic confinement device. *Physics of Plasmas (1994-present)*, 20(7):072705, 2013.
- [78] R Bandara and J Khachan. Nonlinear saturation of the ion-electron buneman instability in a spherical positively pulsed gridded inertial electrostatic confinement device. *Physics of Plasmas (1994-present)*, 22(8):082701, 2015.
- [79] Robert W. Bussard. Some physics considerations of magnetic inertial-electrostatic confinement: A new concept for spherical converging-flow fusion. *Fusion Technology*, 19(2):273–293, 1991. doi: 10.13182/FST91-A29364. URL <https://doi.org/10.13182/FST91-A29364>.
- [80] Nicholas A. Krall. The polywell<sup>TM</sup>: A spherically convergent ion focus concept. *Fusion Technology*, 22(1):42–49, 1992. doi: 10.13182/FST92-A30052. URL <https://doi.org/10.13182/FST92-A30052>.
- [81] Robert W. Bussard. Method and apparatus for controlling charged particles. May 2 1989. URL <https://patents.google.com/patent/US4826646A/en?oq=US4826646A>. US Patent: 4,826,646.
- [82] Robert W. Bussard. Method and apparatus for creating and controlling nuclear fusion reactions. November 3 1992. URL <https://patents.google.com/patent/US5160695A/en?oq=US5160695A>. US Patent: 5,160,695.
- [83] Nicholas A. Krall, M. Coleman, K. Maffei, J. Lovberg, R. Jacobsen, and R. W. Bussard. Forming and maintaining a potential well in a quasispherical magnetic trap. *Physics of Plasmas*, 2(1):146–158, 1995. doi: 10.1063/1.871103. URL <https://doi.org/10.1063/1.871103>.

- [84] Jaeyoung Park, Nicholas A. Krall, Paul E. Sieck, Dustin T. Offermann, Michael Skillicorn, Andrew Sanchez, Kevin Davis, Eric Alderson, and Giovanni Lapenta. High-energy electron confinement in a magnetic cusp configuration. *Phys. Rev. X*, 5:021024, Jun 2015. doi: 10.1103/PhysRevX.5.021024. URL <https://link.aps.org/doi/10.1103/PhysRevX.5.021024>.
- [85] Robert W. Bussard. *Should Google Go Nuclear?* Google Tech Talk, 2006.
- [86] Jaeyoung Park. Polywell - a path to electrostatic fusion. 16th US-Japan Workshop on Fusion Neutron Sources for Nuclear Assay and Alternate Applications, 2014.
- [87] Energy matter conversion corporation. URL <http://www.emc2fusion.org/>.
- [88] Matthew Carr and Joe Khachan. The dependence of the virtual cathode in a polywell<sup>TM</sup> on the coil current and background gas pressure. *Physics of Plasmas*, 17(5):052510, 2010. doi: 10.1063/1.3428744. URL <https://doi.org/10.1063/1.3428744>.
- [89] Matthew Carr, David Gummersall, Scott Cornish, and Joe Khachan. Low beta confinement in a polywell modelled with conventional point cusp theories. *Physics of Plasmas*, 18(11):112501, 2011. doi: 10.1063/1.3655446. URL <https://doi.org/10.1063/1.3655446>.
- [90] Matthew Carr and Joe Khachan. A biased probe analysis of potential well formation in an electron only, low beta polywell magnetic field. *Physics of Plasmas*, 20(5):052504, 2013. doi: 10.1063/1.4804279. URL <https://doi.org/10.1063/1.4804279>.
- [91] Matthew Carr. Electrostatic potential measurements and point cusp theories applied to a low beta polywell fusion device. PhD Thesis - University of Sydney, 2013.
- [92] S. Cornish, D. Gummersall, M. Carr, and J. Khachan. The dependence of potential well formation on the magnetic field strength and electron injection current in a polywell device. *Physics of Plasmas*, 21(9):092502, 2014. doi: 10.1063/1.4894475. URL <https://doi.org/10.1063/1.4894475>.
- [93] Scott Cornish. A study of scaling physics in a polywell device. PhD Thesis - University of Sydney, 2016.
- [94] Dominic Poznic, Johnson Ren, and Joe Khachan. Electron density and velocity functions in a low beta polywell. *Physics of Plasmas*, 26(2):022703, 2019. doi: 10.1063/1.5049865. URL <https://doi.org/10.1063/1.5049865>.
- [95] S. Cornish and J. Khachan. The use of an electron microchannel as a self-extracting and focusing plasma cathode electron gun. *Plasma Science and Technology*, 18(2):138–142, feb 2016. doi: 10.1088/1009-0630/18/2/07. URL <https://doi.org/10.1088%2F1009-0630%2F18%2F2%2F07>.

- [96] F. Kazemyzade, H. Mahdipoor, A. Bagheri, S. Khademzade, E. Hajiebrahimi, Z. Gheisari, A. Sadighzadeh, and V. Damideh. Dependence of potential well depth on the magnetic field intensity in a polywell reactor. *Journal of Fusion Energy*, 31(4):341–345, Aug 2012. ISSN 1572-9591. doi: 10.1007/s10894-011-9474-4. URL <https://doi.org/10.1007/s10894-011-9474-4>.
- [97] David V. Gummersall, Matthew Carr, Scott Cornish, and Joe Kachan. Scaling law of electron confinement in a zero beta polywell device. *Physics of Plasmas*, 20(10):102701, 2013. doi: 10.1063/1.4824005. URL <https://doi.org/10.1063/1.4824005>.
- [98] Jeff Kollasch, Carl Sovinec, and John Santarius. Vlasov-poisson calculations of electron confinement times in polywell devices using a steady-state particle-in-cell method. 16th US-Japan Workshop on Fusion Neutron Sources for Nuclear Assay and Alternate Applications, 2014.
- [99] Joel Rogers. Two-dimensional particle-in-cell simulation of polywell. 11th US-Japan Workshop on Fusion Neutron Sources for Nuclear Assay and Alternate Applications, 2009.
- [100] Joel Rogers. Evaluation of net power polywell designs. 12th US-Japan Workshop on Fusion Neutron Sources for Nuclear Assay and Alternate Applications, 2010.
- [101] Joel Rogers. A polywell p+11b power reactor. 13th US-Japan Workshop on Fusion Neutron Sources for Nuclear Assay and Alternate Applications, 2011.
- [102] Joel Rogers. Designing a small-scale d+d reactor. 14th US-Japan Workshop on Fusion Neutron Sources for Nuclear Assay and Alternate Applications, 2012.
- [103] Product datasheet - halostar 50w 12v gy6.35. URL <https://docs-emea.rs-online.com/webdocs/1282/0900766b81282896.pdf>.
- [104] M. Awschalom and R.S. Sanna. Applications of bonner sphere detectors in neutron field dosimetry. *Radiation Protection Dosimetry*, 10(1-4):89, 1985. doi: 10.1093/oxfordjournals.rpd.a079413. URL <http://dx.doi.org/10.1093/oxfordjournals.rpd.a079413>.
- [105] Richard L. Bramblett, Ronald I. Ewing, and T.W. Bonner. A new type of neutron spectrometer. *Nuclear Instruments and Methods*, 9(1):1 – 12, 1960. ISSN 0029-554X. doi: [http://dx.doi.org/10.1016/0029-554X\(60\)90043-4](http://dx.doi.org/10.1016/0029-554X(60)90043-4). URL <http://www.sciencedirect.com/science/article/pii/0029554X60900434>.
- [106] Vladimir Mares and Hans Schraube. *Nuclear Instruments and Methods in Physics Research Section A: Accelerators, Spectrometers, Detectors and Associated Equipment*, 337(2):461 – 473, 1994. ISSN 0168-9002.

- [107] J.E. Strain, G.W. Leddicotte, and Oak Ridge National Laboratory. Analytical Chemistry Division. *The preparation, properties, and uses of americium-241, alpha-, gamma-, and neutron sources*. U.S. Atomic Energy Commission, 1962. URL <https://books.google.com.au/books?id=31SRFeysm8UC>.
- [108] Horizon fuel cell technologies - product data sheet: Hydro-fill. URL [http://www.udomi.de/downloads/HydroFill%20Pro\\_UM.pdf](http://www.udomi.de/downloads/HydroFill%20Pro_UM.pdf).
- [109] J. Kipritidis and J. Khachan. *Phys. Rev. E*, 79:026403, Feb 2009. doi: 10.1103/PhysRevE.79.026403. URL <https://link.aps.org/doi/10.1103/PhysRevE.79.026403>.
- [110] V. Damideh, A. Sadighzadeh, A. Koohi, A. Aslezaeem, A. Heidarnia, N. Abdollahi, F. Abbasi Davani, and R. Damideh. *Journal of Fusion Energy*, 31(2):109–111, Apr 2012. doi: 10.1007/s10894-011-9438-8. URL <https://doi.org/10.1007/s10894-011-9438-8>.
- [111] E. Haji Ebrahimi, R. Amrollahi, A. Sadighzadeh, M. Torabi, M. Sedaghat, R. Sabri, B. Pourshahab, and V. Damideh. 32(1):62–65, Feb 2013.
- [112] J. H. Nadler, Y. B. Gu, and G. H. Miley. *Review of Scientific Instruments*, 63(10):4810–4812, 1992.
- [113] A. S. Bölükdemir, Y. Akgün, and A. Alaçakır. *Journal of Fusion Energy*, 32(5):561–565, 2013.
- [114] J. Khachan and S. Collis. *Physics of Plasmas*, 8(4):1299–1304, 2001. doi: 10.1063/1.1349875.
- [115] J. Khachan, D. Moore, and S. Bosi. *Phys. Plasmas*, 10:596, 2003.
- [116] O. Shrier, J. Khachan, S. Bosi, M. Fitzgerald, and N. Evans. *Phys. Plasmas*, 13:012703, 2006.
- [117] J. Kipritidis, J. Khachan, M. Fitzgerald, and O. Shrier. *Phys. Rev. E*, 77:066405, Jun 2008. doi: 10.1103/PhysRevE.77.066405. URL <https://link.aps.org/doi/10.1103/PhysRevE.77.066405>.
- [118] K. Christmann, O. Schober, G. Ertl, and M. Neumann. *The Journal of Chemical Physics*, 60(11):4528–4540, 1974. doi: 10.1063/1.1680935.
- [119] P. W. Tamm and L. D. Schmidt. *The Journal of Chemical Physics*, 55(9):4253–4259, 1971. doi: 10.1063/1.1676743.
- [120] S. M. Ko and L. D. Schmidt. *Surface Science*, 42:508–524, 1974. doi: 10.1063/1.1676743.
- [121] A. Yu. Didyk, R. Wiśniewski, K. Kitowski, V. Kulikauskas, T. Wilczynska, A. Hofman, A. A. Shiryaev, and Ya. V. Zubavichus. *Physics of Particles and Nuclei Letters*, 9(1):86–95, 2012.

- [122] I. Langmuir. The adsorption of gases on plane surfaces of glass, mica and platinum. *J. Am. Chem. Soc.*, 40:1361–1403, 1918. doi: 10.1021/ja02242a004.
- [123] E. Tal-Gutelmacher, D. Eliezer, and E. Abramov. *Materials Science and Engineering: A*, 445-446:625 – 631, 2007. ISSN 0921-509.
- [124] L B Begrambekov, A A Ayrapetov, Ya A Sadovskiy, and P A Shigin. Hydrogen trapping in graphite materials in various conditions. *Journal of Physics: Conference Series*, 669: 012003, jan 2016. doi: 10.1088/1742-6596/669/1/012003. URL <https://doi.org/10.1088%2F1742-6596%2F669%2F1%2F012003>.
- [125] Simone Casolo, Ole Martin Løvvik, Rocco Martinazzo, and Gian Franco Tantardini. Understanding adsorption of hydrogen atoms on graphene. *The Journal of Chemical Physics*, 130(5):054704, 2009. doi: 10.1063/1.3072333. URL <https://doi.org/10.1063/1.3072333>.
- [126] Joseph Builth-Williams. Geometrically and reflectively enhanced embedded fusion. Unpublished PhD Thesis - University of Sydney, 2019.
- [127] P. Nordlander, S. Holloway, and J.K. Nørskov. Hydrogen adsorption on metal surfaces. *Surface Science*, 136(1):59 – 81, 1984. ISSN 0039-6028. doi: [https://doi.org/10.1016/0039-6028\(84\)90655-1](https://doi.org/10.1016/0039-6028(84)90655-1). URL <http://www.sciencedirect.com/science/article/pii/0039602884906551>.
- [128] Karl W. Frese. Calculation of surface binding energy for hydrogen, oxygen, and carbon atoms on metallic surfaces. *Surface Science*, 182(1):85 – 97, 1987. ISSN 0039-6028. doi: [https://doi.org/10.1016/0039-6028\(87\)90090-2](https://doi.org/10.1016/0039-6028(87)90090-2). URL <http://www.sciencedirect.com/science/article/pii/0039602887900902>.
- [129] Jeff Greeley and Manos Mavrikakis. Surface and subsurface hydrogen: Adsorption properties on transition metals and near-surface alloys. *The Journal of Physical Chemistry B*, 109(8):3460–3471, 2005. doi: 10.1021/jp046540q. URL <https://doi.org/10.1021/jp046540q>. PMID: 16851380.
- [130] D. Vasić, Z. Ristanović, I. Pašti, and S. Mentus. Systematic dft-gga study of hydrogen adsorption on transition metals. *Russian Journal of Physical Chemistry A*, 85(13):2373–2379, Dec 2011. doi: 10.1134/S0036024411130334. URL <https://doi.org/10.1134/S0036024411130334>.
- [131] Hydrogen adsorption, absorption and diffusion on and in transition metal surfaces: A dft study. *Surface Science*, 606(7):679 – 689, 2012. ISSN 0039-6028. doi: <https://doi.org/10.1016/j.susc.2011.12.017>.

- [132] P.C. Zalm and L.J. Beckers. Secondary electron yields from clean polycrystalline metal surfaces bombarded by 5-20 kev hydrogen or noble gas ions. *Philips Journal of Research*, 39:61–76, 01 1984.
- [133] American Radio Relay League. *The ARRL Handbook for Radio Communications*. Publication no. 6 of the Radio amateur's library. ARRL, 2003. URL [https://books.google.com.au/books?id=Dk\\_inQEACAAJ](https://books.google.com.au/books?id=Dk_inQEACAAJ).
- [134] Lavuta oxygen free copper - product datasheet. URL [https://www.luvata.com/Documents/Oxygen-free%20copper%20and%20special%20alloy%20data%20sheets/Oxygen-free%20Copper\\_OF-OK\\_ENG.pdf](https://www.luvata.com/Documents/Oxygen-free%20copper%20and%20special%20alloy%20data%20sheets/Oxygen-free%20Copper_OF-OK_ENG.pdf).
- [135] R Calder and G Lewin. Reduction of stainless-steel outgassing in ultra-high vacuum. *British Journal of Applied Physics*, 18(10):1459–1472, oct 1967. doi: 10.1088/0508-3443/18/10/313. URL <https://doi.org/10.1088/0508-3443/2F18%2F10%2F313>.
- [136] V.D. Toro. *Electrical engineering fundamentals*. Prentice-Hall, 1972. URL <https://books.google.com.au/books?id=7-NSAAAAMAAJ>.
- [137] Cd 137 px series electrolytic capacitors. URL <http://www.jianghai.com/pdf/CD137.pdf>.
- [138] S. Brooks, A. Gelman, G. Jones, and X.L. Meng. *Handbook of Markov Chain Monte Carlo*. Chapman & Hall/CRC Handbooks of Modern Statistical Methods. CRC Press, 2011. ISBN 9781420079425. URL <https://books.google.com.au/books?id=qfRsAIKZ4rIC>.
- [139] Vishay vs-80pfr80 power diode. URL <http://www.mouser.com/ds/2/427/vs-80pfrseries-86949.pdf>.
- [140] Puls - product data sheet: Pas395 power supply. URL <https://www.pulspower.com/fileadmin/Dateien/pdf/pas395.pdf>.
- [141] Product datasheet - controllino mega. URL [http://www.controllino.biz/wp-content/uploads/2017/03/MEGA\\_DATASHEET-19-04-20161.pdf](http://www.controllino.biz/wp-content/uploads/2017/03/MEGA_DATASHEET-19-04-20161.pdf).
- [142] Atmel Corporation. Product datasheet - atmega2560 micro controller, . URL [http://ww1.microchip.com/downloads/en/devicedoc/atmel-2549-8-bit-avr-microcontroller-atmega640-1280-1281-2560-2561\\_datasheet.pdf](http://ww1.microchip.com/downloads/en/devicedoc/atmel-2549-8-bit-avr-microcontroller-atmega640-1280-1281-2560-2561_datasheet.pdf).
- [143] Ixys - product data sheet: Ixfp6n120p n-channel mosfet. URL <https://au.mouser.com/datasheet/2/205/Viewer-765452.pdf>.
- [144] Atmel Corporation. Product datasheet - atmega328 micro controller, . URL <https://www.sparkfun.com/datasheets/Components/SMD/ATMega328.pdf>.

- [145] En Yao Wang, N. Hershkowitz, D. Diebold, T. Intrator, R. Majeski, H. Persing, G. Severn, B. Nelson, and Y. J. Wen. Secondary electron emission-capacitive probes for plasma potential measurements in plasmas with hot electrons. *Journal of Applied Physics*, 61(10): 4786–4790, 1987. doi: 10.1063/1.338338. URL <https://doi.org/10.1063/1.338338>.
- [146] H. M. Mott-Smith and Irving Langmuir. The theory of collectors in gaseous discharges. *Phys. Rev.*, 28:727–763, Oct 1926. doi: 10.1103/PhysRev.28.727. URL <https://link.aps.org/doi/10.1103/PhysRev.28.727>.
- [147] F.Chen. Langmuir probe diagnostics. Lecture Notes - Electrical Engineering Department, University of California, Los Angeles, 2012.
- [148] MAXIM Integrated Products. Product datasheet - max4206, . URL <https://datasheets.maximintegrated.com/en/ds/MAX4206.pdf>.
- [149] MAXIM Integrated Products. Product datasheet - max4206 evaluation kit, . URL <https://datasheets.maximintegrated.com/en/ds/MAX4206EVKIT.pdf>.
- [150] J.D. Jackson. *Classical electrodynamics*. Wiley, 1962. URL <https://books.google.com.au/books?id=QuANAQAAIAAJ>.
- [151] Atlas steels - grade data sheet. URL [http://www.atlassteels.com.au/documents/Atlas\\_Grade\\_datasheet\\_316\\_rev\\_Jan\\_2011.pdf](http://www.atlassteels.com.au/documents/Atlas_Grade_datasheet_316_rev_Jan_2011.pdf).
- [152] E. Isaacson and H.B. Keller. *Analysis of Numerical Methods*. Dover Books on Mathematics. Dover Publications, 1994. ISBN 9780486680293. URL <https://books.google.com.au/books?id=y77n2ySMJHUC>.
- [153] Y. Saad. *Iterative Methods for Sparse Linear Systems: Second Edition*. Other Titles in Applied Mathematics. Society for Industrial and Applied Mathematics, 2003. ISBN 9780898715347. URL <https://books.google.com.au/books?id=ZdLeBlqYeF8C>.
- [154] H.K. Dass. *Advanced Engineering Mathematics*. S. Chand Limited, 2008. ISBN 9788121903455. URL <https://books.google.com.au/books?id=IkZLAgAAQBAJ>.
- [155] C. D. Child. Discharge from hot cao. *Phys. Rev. (Series I)*, 32:492–511, May 1911. doi: 10.1103/PhysRevSeriesI.32.492. URL <https://link.aps.org/doi/10.1103/PhysRevSeriesI.32.492>.
- [156] V. Y. Upatov. Dielectric charging by an electron beam. *Journal of Applied Physics*, 80(4): 2453–2457, 1996. doi: 10.1063/1.363081. URL <https://doi.org/10.1063/1.363081>.
- [157] E.I. Rau, A.A. Tatarintsev, and E.Yu. Zykova. Influence of ion implantation and electron pre-irradiation on charging of dielectrics under electron beam irradiation: Application to sio2. *Nuclear Instruments and Methods in Physics Research Section B*:

- Beam Interactions with Materials and Atoms*, 2019. ISSN 0168-583X. doi: <https://doi.org/10.1016/j.nimb.2018.12.030>. URL <http://www.sciencedirect.com/science/article/pii/S0168583X18307419>.
- [158] K. Miyamoto. *Fundamentals of Plasma Physics and Controlled Fusion*. NIFS PROC.: Kakuyūgō-Kagaku-Kenkyūsho. K. Miyamoto, 2001. URL <https://books.google.com.au/books?id=wcQkNQAACAAJ>.
- [159] Alan M Winslow. Numerical solution of the quasilinear poisson equation in a nonuniform triangle mesh. *Journal of Computational Physics*, 1(2):149 – 172, 1966. ISSN 0021-9991. doi: [https://doi.org/10.1016/0021-9991\(66\)90001-5](https://doi.org/10.1016/0021-9991(66)90001-5). URL <http://www.sciencedirect.com/science/article/pii/0021999166900015>.